

Magnetic pulse crimping of mechanical joints

Matthias Van Wonterghem, Pieter Vanhulsel

Promotor: prof. dr. ir. Wim De Waele

Begeleider: Koen Faes (BIL)

Masterproef ingediend tot het behalen van de academische graad van
Master in de ingenieurswetenschappen: werktuigkunde-elektrotechniek

Vakgroep Mechanische Constructie en Productie
Voorzitter: prof. dr. ir. Patrick De Baets
Faculteit Ingenieurswetenschappen en Architectuur
Academiejaar 2010-2011



Magnetic pulse crimping of mechanical joints

Matthias Van Wonterghem, Pieter Vanhulsel

Promotor: prof. dr. ir. Wim De Waele

Begeleider: Koen Faes (BIL)

Masterproef ingediend tot het behalen van de academische graad van
Master in de ingenieurswetenschappen: werktuigkunde-elektrotechniek

Vakgroep Mechanische Constructie en Productie
Voorzitter: prof. dr. ir. Patrick De Baets
Faculteit Ingenieurswetenschappen en Architectuur
Academiejaar 2010-2011



Acknowledgments

The last words of the master thesis are almost completed. It was a pleasure for us to be able to perform experimental research on this interesting innovative technology. With the promising results obtained in this work, we are glad to complete our studies. We like to express our gratitude to several people who helped us during the year.

First of all, we like to express our sincere gratitude to our supervisor prof. dr. ir. Wim De Waele and our mentor ir. Koen Faes. They assisted us, despite their busy schedules, and they pushed us in the right direction. We thank them for the effort they put into revising the several drafts of this work.

Also, we would like to thank the Belgian Welding Institute, and in particular Philip De Baere, for his technical advice and for making all the parts we needed. Also, we would like to thank Oleg Zaitov for helping us with making several cross sections of our workpieces.

Further, we very much appreciate the effort and time ir. Matthias Verstraete has put into helping us with our finite element simulations in Abaqus and with the Design of Experiments. Also, the help of Stijn Hertelé with the Digital Image Correlation experiments is very much appreciated.

Last but not least, we would like to thank our parents for offering us the opportunity to complete these studies and for their support throughout the years.

Pieter Vanhulsel
Matthias Van Wonterghem
Ghent, 6 June 2011

The author(s) give permission to make this master dissertation available for consultation and to copy parts of this master dissertation for personal use. In the case of any other use, the limitations of the copyright have to be respected, in particular with regard to the obligation to state expressly the source when quoting results from this master dissertation.

Ghent, June 2011

Supervisor

prof.dr.ir. W. De Waele,

Mentor

ir. K. Faes,

Authors

Matthias Van Wonterghem,

Pieter Vanhulsel,

Magnetic pulse crimping of mechanical joints

by

Matthias Van Wonterghem
Pieter Vanhulsel

Master thesis presented in fulfilment of the requirements for the degree of
MASTER OF ELECTROMECHICAL ENGINEERING

Academic year 2010-2011

Supervisor: prof. dr. ir. Wim De Waele
Mentor: ir. Koen Faes (BIL)

Faculty of Engineering
Ghent Univerisity
Department of Mechanical Construction and Production
Chairman: prof. dr. ir. Patric De Baets

Synopsis

Electromagnetic pulse crimping of form fit joints for single and double grooves was investigated in this work.

For a single groove, the radial inward displacement of the tube into the groove and the necking of the tube at the groove edge were studied. It was concluded that the relationship between the groove width and the radial inward displacement is directly proportional and that an increase of the charging voltage leads to a larger radial inward displacement. A larger necking was observed when the groove edge radius is smaller and when the voltage is higher. It was also observed that initially the necking increases to a maximum as the groove width increases. As the groove gets wider, the necking starts to decline. This was explained by looking at the ratio of shearing and bending.

Preliminary experiments were performed on a double groove design and it was concluded that higher tensile strengths could be achieved than with a single groove design. The Design of Experiments method was used to optimise the double groove design. An optimal double groove design was proposed which has a statistically expected tensile strength equal to the tensile strength of the base material of the tube. The optimal design includes a shallow, long first groove with sharp edges, a sunk collar and a long second groove with sharp edges. Designs which have seven out of eight optimal parameters in common with the optimal design were tested during the DoE experiments and these resulted in tensile strengths relative to the tensile strength of the base material of more than 90%, which is very promising. Also, the deformation behaviour of a double groove design during a tensile test was studied by using the Digital Image Correlation technique. It was noted that there are 3 main failure modes and these 3 were discussed in detail.

Keywords

electromagnetic pulse crimping, form fit joints, optimal groove design, Design of Experiments, failure behaviour.

Magnetic pulse crimping of mechanical joints

Pieter Vanhulsel, Matthias Van Wonterghem

Supervisors: Wim De Waele, Koen Faes

Abstract Electromagnetic pulse crimping can be a valuable alternative for electromagnetic pulse welding. However, most research done until now was focused on the latter one. In this master thesis, electromagnetic pulse crimping is investigated. The incentive for this is the fact that electromagnetic pulse crimping has some major advantages compared to electromagnetic pulse welding: it is possible to join materials which cannot be joined by electromagnetic pulse welding (low conductive materials and high strength materials), the needed energy level is lower and larger diameter parts (for tubular joints) can be joined. More knowledge was gathered about the deformation behaviour, by performing experiments on both single and double grooves. The double groove design was optimised by using the Design of Experiments method and three main failure modes have been noted and discussed by using the Digital Image Correlation technique.

Keywords electromagnetic pulse crimping, form fit joints, optimal groove design, Design of Experiments, failure behaviour

I. INTRODUCTION

The electromagnetic pulse technology uses magnetic forces to deform or join workpieces. The energy stored in a capacitor bank is discharged rapidly through a magnetic coil. Typically a ring-shaped coil is placed over a tubular workpiece. The magnetic field produced by the coil generates eddy currents in the tube. These currents, in turn, produce their own magnetic field. The forces generated by the two opposed magnetic fields result in a repelling force between the coil and the tube. As a consequence, the tube collapses onto the internal workpiece, creating a crimp joint. This process was used in this work to create form-fit crimp joints with a single groove and a double groove design, which are subjected to an axial load.

II. EXPERIMENTS ON A SINGLE GROOVE DESIGN

During the experiments performed in an industrial case study on a single groove design, it was observed that it is a challenge to determine the appropriate charging voltage to be applied when a certain groove design is given: a too low voltage level will result in hardly any deformation of the tube into the groove. A too high voltage level will cause the internal workpiece to act as a 'cutting tool'. Therefore, it would be helpful to have graphs which, for a certain groove design, link the radial inward tube displacement and necking occurring at the groove edges with the applied voltage. To obtain these graphs, free deformation experiments were performed.

P. Vanhulsel and M. Van Wonterghem are with the Department of Mechanical Construction and Production, Ghent University (UGent), Gent, Belgium.

E-mail: pieter.vanhulsel@ugent.be

E-mail: matthias.vanwongerghem@ugent.be

A. Free deformation experiments

A cylinder system, inspired on [1], which allows to simulate rectangular grooves (which will result in the highest strength according to the literature [1]) with low material resources and with low processing and evaluation time, was designed and built (see Figure 1).



Figure 1 Cylinder system used for the free deformation experiments.

It consists of two steel cylinders S235 with an internal screw thread which are screwed on a threaded rod. The groove edge radii are simulated by the groove edge radii of both cylinders. The groove width can be simulated by placing a correct number of metal rings between both cylinders. It should be noted that the outer diameter of the metal rings is small enough, in order not to interfere with the inward deformation of the tube (cfr. 'free deformation'). Aluminum EN AW-6060 T6 tubes (see Table 1) with a wall thickness of 1.5 mm and an outer diameter of 50 mm are used. After the crimping process, the cylinders are recovered and the deformed tube (see Figure 2) was cross sectioned to perform measurements.

Table 1 Properties of EN AW-6060 T6 at 20°C [2]

Electrical conductivity [MS/m]	Elasticity modulus [GPa]	Shear modulus [GPa]	Tensile strength [MPa]
34-38	69.5	26.1	min. 190



Figure 2 The resulting deformed tube.

For each of the 132 deformed tubes, the largest radial inward displacement and the necking at the edges were measured. Graphs were generated which link the groove width and edge radii, the charging voltage and the measured values.

It was observed that an increase of the charging voltage leads to a larger radial inward displacement. The relationship between the groove width and the radial inward displacement is directly proportional: a larger radial inward displacement is

measured when the groove width is larger. It was also observed that the groove edge radius has a very limited influence on the radial inward displacement.

On the other hand, the groove edge radius has a significant influence on the amount of necking: a smaller groove edge radius causes more necking. A larger necking of the deformed tube at the groove edge is also observed when the charging voltage is increased. A remarkable trend was observed when relating the amount of necking to the groove width. At first necking increases gradually with the groove width. It reaches a maximum and then the necking starts to decline as the groove width increases further (while the radial inward displacement linearly increases as the groove width further increases). This could be explained by looking at the ratio of shearing and bending: the radial inward displacement will for the most part be achieved by shearing at the groove edges when the groove width is small. This causes fairly large necking for a relatively small radial inward displacement. If the groove width increases, a part of the radial inward displacement into the groove is realised by bending, which does not cause necking at the groove edges. The remaining radial inward displacement is realised by shearing at the groove edges (see Figure 3). As the groove width increases, a greater part of the radial inward displacement is achieved by bending and a smaller part by shearing at the edges. This explains the decrease in necking while the radial inward displacement increases.

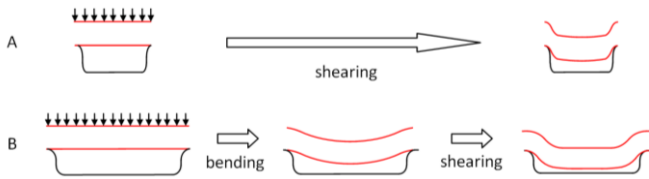


Figure 3 A. Mainly shearing for a small groove width, B. A combination of bending and shearing for a larger groove width.

III. EXPERIMENTS ON A DOUBLE GROOVE DESIGN

In the literature it is noted that additional grooves should improve the strength of the crimp joint [1]. Therefore, preliminary experiments were performed on a double groove design for an axial loaded crimp joint and it was observed that a higher tensile strength could be achieved compared to a single groove design. In order to optimise this double groove design in a structured way, and to minimise the amount of experiments needed, the Design of Experiments method was used.

A. Design of Experiments (DoE)

In general, to investigate the influence of parameters at two levels, 2^n experiments are required. DoE takes out a subset, reducing the number of experiments. This causes a certain loss of information, but it is still possible to draw statistically sound conclusions if the subset is well chosen [3].

A fractional factorial design was used on 8 parameters. These parameters were selected and values were assigned to them based on the knowledge acquired during the previous experiments (see Figure 4). A test-matrix with 64 experiments was generated, and all the experiments were repeated once in order to reduce scatter. The tensile strength of the crimp joint relative to the tensile strength of the base material of the tube was chosen to be the evaluation parameter. The experiments were performed on aluminium EN AW-6060 T6 tubes (see

Table 1 for the properties) with a wall thickness of 1.5 mm and an outer diameter of 50 mm.

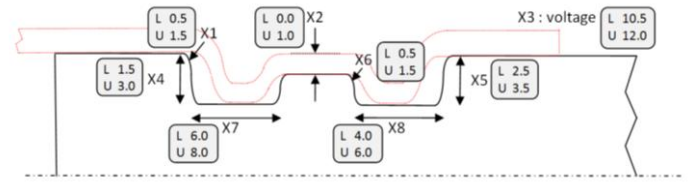


Figure 4 The eight selected parameters with the lower- (L) and the upper- (U) values expressed in mm and in kV (only for the charging voltage X3).

The results from the executed DoE led to an optimal design which should provide a joint strength as strong as the base material (see Figure 5). The actual optimal design was not included in the test matrix, but designs which have seven out of eight optimal parameters in common with the optimal design were tested. These designs had a relative tensile strength more than 90%, and two of these samples sheared completely in the base material while the actual joint remained undamaged. These results are very promising.

It should be noted that the DoE-analysis only included geometrical parameters (besides the voltage) and therefore it is material independent. The results can be used for other material combinations, if an appropriate charging voltage is used.

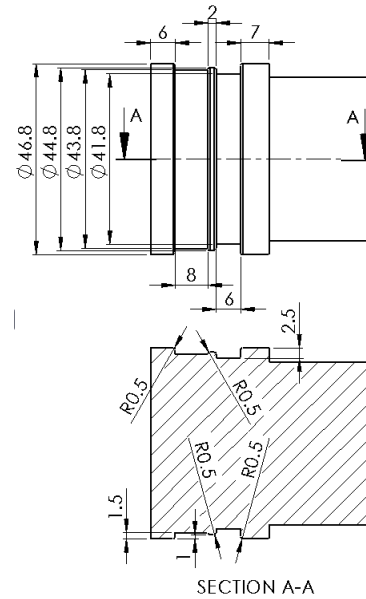


Figure 5 The optimal double groove design resulting from the DoE.

B. Digital Image Correlation (DIC)

The idea behind the DIC technique is to infer the material displacement during testing by tracking the deformation of a random speckle pattern in digital images acquired during the testing. The image analysis process is based on a pattern recognition technique. By using two synchronised cameras which acquire images of the loaded specimen from different viewing angles, it is possible to determine both the three-dimensional displacement and three-dimensional deformation [4].

The DIC technique was used to perform an in depth study on the failure behaviour of the crimp joints from the DoE: the distribution, the location and the magnitude of strains during tensile testing of the crimp joint were determined. Since strain

is linked to load, this also allowed to investigate the load distribution among the 2 grooves. Three main failure modes were distinguished:

Failure mode 1: The tube tears at edge 1₁ at the complete circumference.

Failure mode 2: The tube tears at edge 2₁ at the complete circumference.

Failure mode 3: The tube gets pulled of the internal workpiece and no tearing occurs.

The average relative tensile strength and the percentage of occurrence for these main failure can be found in Table 2. The nomenclature for the double groove design can be found in Figure 6. It should be noted that the tube will get pulled to the left on Figure 6 when a tensile test is performed.

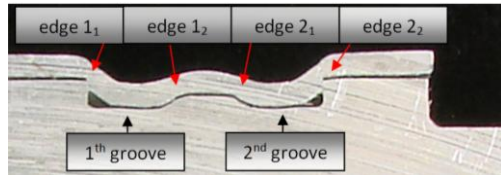


Figure 6 Nomenclature for the double groove design.

In failure mode 1, the necking near groove edge 1₁ and the amount of load taken up by the second groove determine the tensile strength of the joint. After the tube tears at edge 1₁, the joint can no longer bear a load. It was observed that failure mode 1 could be divided into 3 subgroups, based on the design of the first groove and the collar depth (a sunk collar will allow the second groove to absorb a larger amount of the load). A design, close to the optimal design belongs to subgroup 3. A typical DIC image of the strain-distribution in the axial direction right before failure occurs in a sample from subgroup 3 is shown in Figure 7.

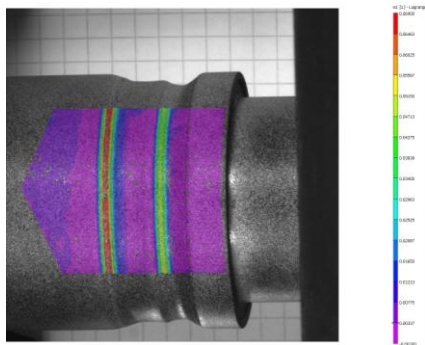


Figure 7 At edge 1₁ and edge 2₁ a strain in the axial direction of respectively 6.9% and 5.2% is observed.

In failure mode 2, the thinning of the tube wall near the groove edge 2₁ determines the tensile strength until the tube tears at that edge. It was observed that the connection still has some strength after tearing occurred. This is because the tube needs to be pushed out of the first groove, and thus a load is absorbed. The remaining strength is determined by the radial inward tube displacement into the first groove in combination with the axial displacement at the edge 1₁ of the internal workpiece relative to the tube which is of importance.

In failure mode 3 no tearing occurs; Therefore, it is the radial inward tube displacement into both grooves in combination with the axial displacement of the internal workpiece relative to the tube which is of importance. Some applications demand this type of failure because a warning can be given during the pull out of the tube.

Table 2 Comparison of relative tensile strength and the occurrence of the 3 failure modes.

Failure behaviour	Average relative tensile strength [%]	Percentage of occurrence [%]
Failure mode 1	81.7	63.0
Subgroup 1	74.0	16.8
Subgroup 2	80.0	29.4
Subgroup 3	91.0	16.8
Failure mode 2	75.3	12.0
Failure mode 3	66.4	14.0

IV. CONCLUSION

Electromagnetic pulse crimping of form fit joints was investigated in this work. The deformation behaviour for a single groove design was studied by making use of a cylinder system which allowed to simulate a large amount of grooves. It was concluded that the relationship between the groove width and the radial inward displacement is directly proportional and that an increase of the charging voltage leads to a larger radial inward displacement. A larger necking was observed when the groove edge radius is smaller and when the voltage is higher. A remarkable trend was observed when relating the amount of necking to the groove width: initially the necking increases, but as the groove gets wider, the necking starts to decline. This was explained by looking at the ratio of shearing and bending.

After preliminary experiments performed on a double groove design, it was concluded that higher tensile strengths could be achieved than with a single groove design. The Design of Experiments method was used to optimise the double groove design. An optimal double groove design was proposed which has a statistically expected tensile strength equal to the tensile strength of the base material of the tube. The optimal design includes a shallow, long first groove with sharp edges, a sunk collar and a long second groove with sharp edges. Designs which have seven out of eight optimal parameters in common with the optimal design were tested during the DoE experiments and these resulted in tensile strengths relative to the tensile strength of the base material of more than 90%, which is very promising. Also, the deformation behaviour of a double groove design during a tensile test was studied by using the Digital Image Correlation technique. It was noted that there are 3 main failure modes and these 3 were discussed in detail. The failure mode in which the tube tears at the first edge of the first groove (failure mode 1) is the one according to which the optimal design is predicted to fail. This failure mode occurred the most during the performed experiments and it resulted in the highest average tensile strength.

V. REFERENCES

- [1] Weddeling, C., Woodward, S., Marré, M., Nellesen, J., Psyk, V., Tekkaya, E., Tillmann, W., *Influence of groove characteristics on strength of form-fit joints*. Journal of Materials Processing Technology, 2010.
- [2] *Material Data Sheet EN AW-6060*.
- [3] Schmidt, S., Launsby, R., *Understanding Industrial Designed Experiments*. 4th ed.
- [4] Lichtenberger, R., Schreier, H., *Efficient Optimization of Airbags by the Measurement of the Time Resolved Strain Distribution on Airbag Covers*.

Magnetic pulse crimping of mechanical joints (Nederlandstalige samenvatting)

1 Inleiding

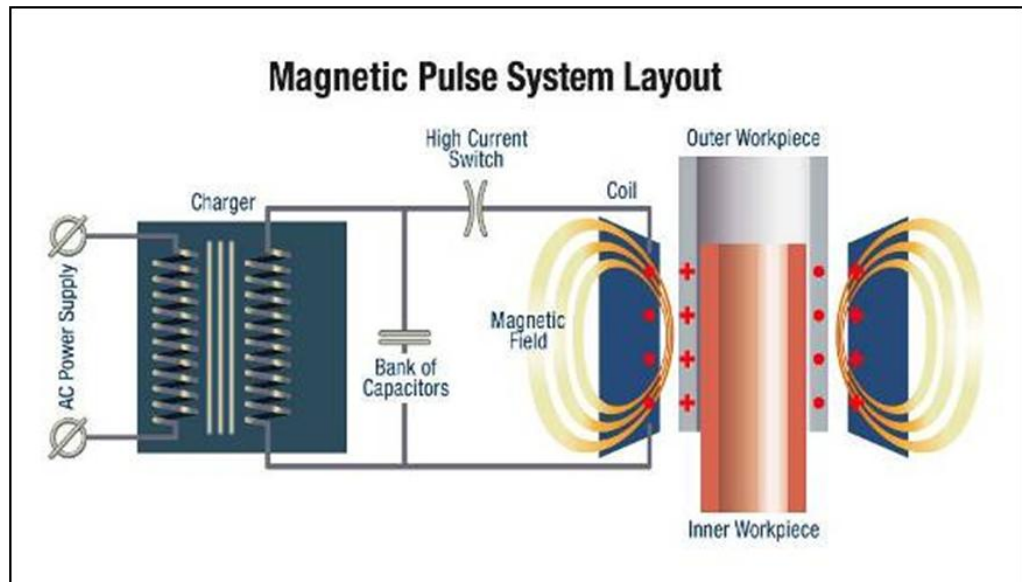
In dit werk wordt het realiseren van krimpverbindingen door gebruik te maken van het (elektro)magnetisch pulskrimp proces onderzocht. Het werk kadert in het onderzoeksproject "PULSCRIMP" dat ondersteund wordt door het IWT (het agentschap voor Innovatie door Wetenschap en Technologie) [1]. Het project wordt uitgevoerd door het Belgisch Instituut voor Lastechniek (BIL), Labo Soete (Universiteit Gent), het opleidings- en onderzoekcentrum voor lassen SLV (München) en OCAS. Eén van de hoofddoelstellingen van het project is het ontwerpen van een sterke krimpverbinding die als waardig alternatief voor lasverbindingen kan gebruikt worden.

2 Het elektromagnetisch pulskrimp proces

Het (elektro)magnetisch pulskrimp proces gebruikt magnetische kracht om een werkstuk te vervormen. Een schematische voorstelling van de belangrijkste componenten van de machine is weergegeven in Figuur 1. De energievoorziening van de machine laadt een condensatorbank op tot een gewenst energieniveau bereikt is. Nadien wordt de condensatorbank in verbinding gebracht met het ontladingscircuit door het sluiten van een schakelaar. In het ontladingscircuit loopt de wisselstroom doorheen een primaire spoel en wekt daarin een magnetisch veld op. Een elektrisch geleidend werkstuk dat zich binnen het wisselend magnetisch veld bevindt, zal volgens de wet van Lenz geïnduceerde wervelstromen ontwikkelen in een oppervlaktelaag. De dikte van deze laag wordt bepaald door het zogenaamde 'skin effect'. Doordat het werkstuk op zijn beurt een tegengesteld magnetisch veld ontwikkelt, ontstaat er een verschil tussen het magnetisch veld binnen en buiten het werkstuk. Door dit verschil zal er volgens het principe van de Lorentz kracht, een radiaal inwaarts gerichte kracht uitgeoefend worden. Het ontstane magnetische veld in de primaire spoel, kan nog geconcentreerd worden op een beperkte axiale lengte met behulp van een zogenaamde field shaper. Dit resulteert in een hogere magnetische druk. De field shaper is vervaardigd uit een goed elektrisch geleidend en mechanisch sterk materiaal, gewoonlijk een koperlegering. Dit onderdeel vangt ook de grote magnetische krachten op en beschermt daardoor de kwetsbare primaire spoel.

Door de buis die men wil krimpen te laten vervormen in aangebrachte groeven op een inwendig werkstuk, kan men een vormvaste verbinding realiseren. Groeven met verscheidene geometrieën (cirkelvormige -, driehoekige - en rechthoekige groeven) werden reeds onderzocht [2] en er werd besloten dat rechthoekige groeven altijd de sterkste verbinding creëerden.

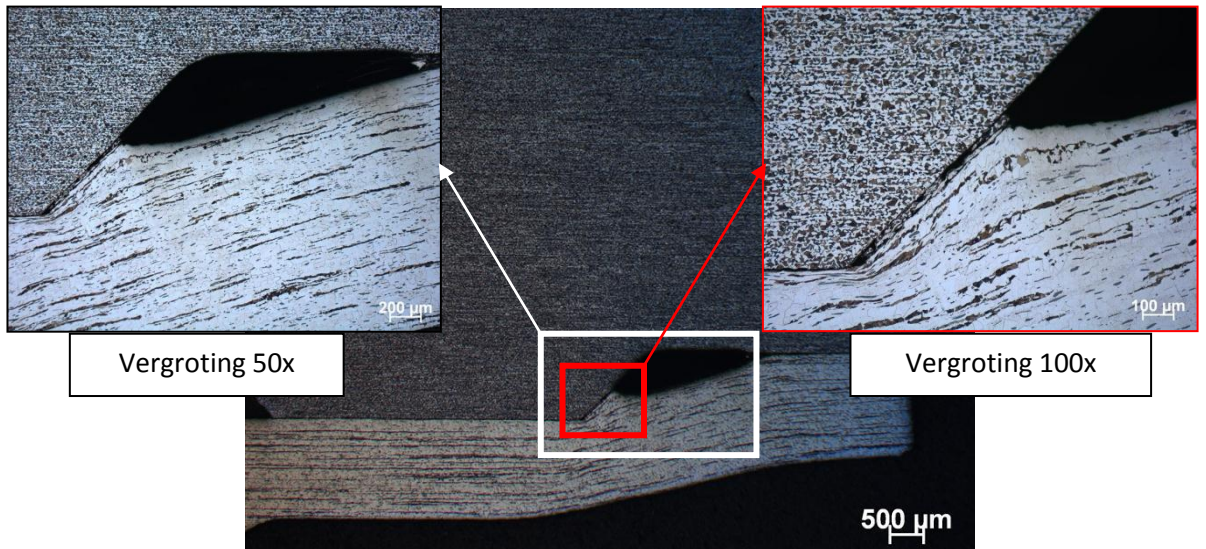
Een tweede mechanisme dat de 2 stukken samenhoudt is de wrijving. Doordat de buis met grote kracht en snelheid tegen het binnenstuk botst, zullen beide onderdelen elastisch/plastisch vervormen. Beide onderdelen zullen elastisch terugveren na de botsing en er ontstaan residuele spanningen aan het grensooppervlak tussen beide onderdelen. De sterkte van de perspassing die hierbij ontstaat, hangt af van de wrijvingscoëfficiënt en van de grootte van de residuele spanningen.



Figuur 1: Schematische voorstelling van de belangrijkste componenten van de EMP krimp machine [3].

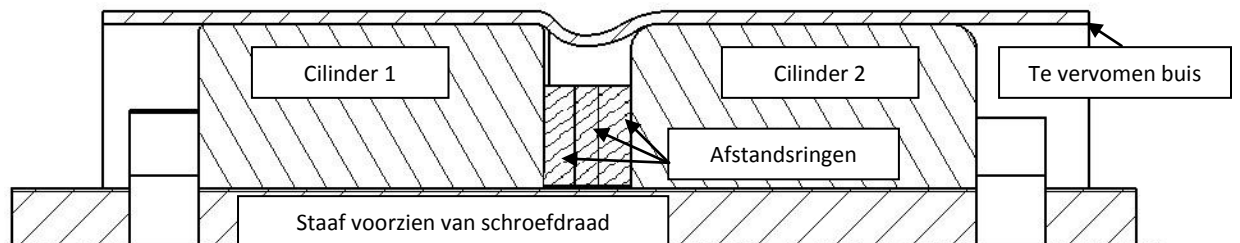
3 Onderzoek voor een enkele groef

Er werden enkele experimenten uitgevoerd in opdracht van een bedrijf om voeling te krijgen met het proces. Een stalen buis (11SMn30K) werd gekrompen op een stalen binnenstuk (gewoon koolstofstaal). Er werden trekproeven uitgevoerd om de sterkte te testen, doorsneden (zie Figuur 2) gemaakt om de vervorming te onderzoeken en excentriciteitstesten uitgevoerd om de rondheid van de gekrompen verbinding te bepalen. Er werd vastgesteld dat het een uitdaging is om een correcte laadspanning aan te leggen. Indien het voltage te laag is, zal de buis nauwelijks vervormen in de groef. Indien het voltage te hoog is, zal de insnoering van de buis op de groefrand (zie Figuur 2) aanzienlijk zijn waardoor de sterkte van de krimpverbinding significant daalt.



Figuur 2: Doorsnede van een krimpvverbinding waarop men duidelijk kan zien dat de buis zal afschuiven (en bijgevolg insnoeren) op een scherpe hoek van de groefrand.

Er werd daarom een opstelling ontwikkeld waarbij men op een goedkope manier en met weinig materiaal het vervormen van een buis in een groef kan bestuderen. Dit zogenaamde cilindersysteem bestaat uit 2 cilinders met bepaalde afronding op de hoeken en een inwendige schroefdraad, een staaf voorzien van schroefdraad, en enkele afstandsringen. Figuur 3 toont een schematische voorstelling van een longitudinale doorsnede van het cilindersysteem. Groeven met een bepaalde axiale lengte en bepaalde hoekradii, maar zonder groefdiepte (vandaar 'vrije vervorming'), werden gesimuleerd.



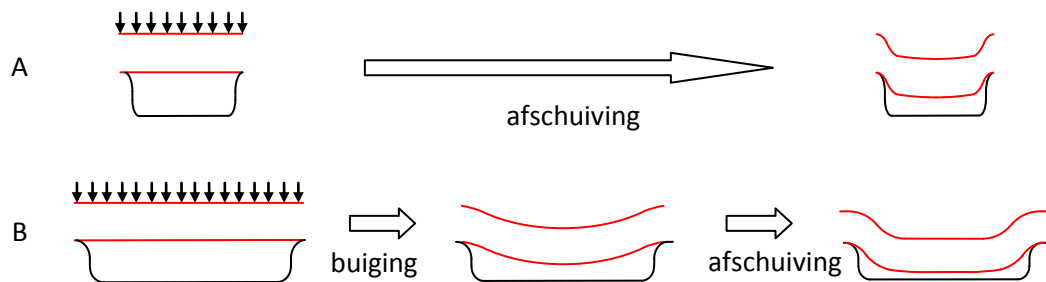
Figuur 3: schematische voorstelling van het cilindersysteem voor vrije vervormingsexperimenten.

Na de vrije vervorming van de buis in de gesimuleerde groef konden de buis en de cilinders opnieuw van elkaar gescheiden worden en het systeem kon terug hergebruikt worden. Verschillende combinaties van groeflengte en groefradii werden onderzocht en grafieken werden opgesteld. Uit de grafieken die de radiale inwaartse verplaatsing van de buis uitzetten in functie van de groefdiepte voor een bepaalde laadspanning kon men besluiten dat de inwaartse verplaatsing proportioneel stijgt met een stijging van de groeflengte. Hoe groter de aangelegde laadspanning, hoe groter de radiale verplaatsing en hoe groter de evenredigheidsconstante werd. De afrondingsstraal van de groefranden had slechts een beperkte invloed op de maximale inwaartse radiale verplaatsing.

De grafieken die de insnoering van de wanddikte ter hoogte van de groefrand in functie van de groeflengte weergeven voor een bepaald voltage, vertoonden een stijgend verloop tot aan een maximum insnoering voor een welbepaalde groeflengte. Eens de groef nog langer werd daalde dit verloop. De verklaring hiervoor is te zien in Figuur 4: men kan de buis die vervormt in een groef onder de magnetische druk voorstellen als een opgelegde balk met 2 steunpunten waarop een gelijkmatig verdeelde belasting wordt uitgeoefend. De belasting induceert een dwarskracht en een buigend moment. Wanneer men werkt met een kleine groeflengte (korte afstand tussen de oplegpunten van de balk), zal de dwarskracht domineren en de buis zal afschuiven in de groef, zie Figuur 4.A. Dit zorgt voor grote insnoering van de buis aan de wanden. Wanneer een lange groeflengte (lange afstand tussen de oplegpunten) aanwezig is, zal er eerst een buigend moment plaatsvinden (wat niet voor een insnoering van de buiswanddikte zorgt) en vervolgens zal de buis pas gaan afschuiven, wat resulteert in een kleinere insnoering van de buis aan de wanden, zie Figuur 4.B.

De afrondingsstraal van de groefranden heeft een grote invloed op de hoeveelheid insnoering: hoe scherper de rand, hoe meer de rand van het inwendige stuk in het buismateriaal zal 'snijden'. Wanneer een voldoende scherpe hoek gebruikt wordt in combinatie met een groot voltage, zal de buis volledig doorsneden worden (cfr. elektromagnetisch ponsen [4]).

De vrije vervorming experimenten werden (net als de hierop volgende experimenten) uitgevoerd met aluminium EN AW-6060 buizen met een wanddikte van 1,5 mm en een uitwendige diameter van 50 mm. De maximale inwaartse verplaatsing die werd opgemeten tijdens de experimenten zonder dat de buis gescheurd was, bedroeg 6,5 mm. De wanddikte aan de randen bedroeg in dat geval nog 0,5 mm. Dit stemt overeen met een radiaal inwaartse verplaatsing van 27,8% van de diameter en een daling van de wanddikte van 34%.



Figuur 4: A. Afschuiving treedt op bij een kleine groeflengte, B. Een combinatie van buigen en afschuiving treedt op bij een lange groef.

Er werden 3-D grafieken ontworpen die toestaan om een voorspelling te maken van de radiaal inwaartse verplaatsing en de insnoering aan de wanden, indien laadspanning en groeflengte opgegeven zijn. Deze grafieken kunnen dienen als een leidraad bij een eerste ontwerp van een groef.

Er werden 2 verschillende enkelvoudige groefontwerpen gekrompen en er werd een trektest op uitgevoerd. De behaalde treksterktes, relatief ten opzichte van de treksterkte van het

basismateriaal, bedroegen maximaal 74.5%. Dit resultaat is niet slecht, maar het moet mogelijk zijn om grotere treksterktes te bereiken bij een ontwerp met een dubbele groef [2,5].

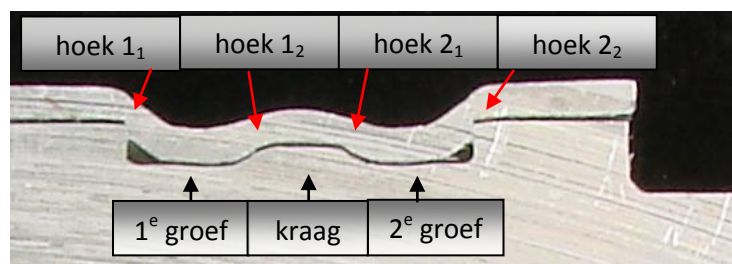
4 Ontwerp voor een dubbele groef

4.1 Verkennende experimenten

Om voeling te krijgen met de optredende vervorming, de nodige laadspanning, de optredende insnoering,... werden enkele verkennende experimenten uitgevoerd. Acht reeksen werden onderzocht, waarin telkens 4 dezelfde ontwerpen gekrompen werden. Drie daarvan werden op 3 verschillende laadspanningen gekrompen en werden longitudinaal doorgeslepen om de vervorming van de buis, de hoeveelheid insnoering en eventuele zones van plastische vervorming te onderzoeken. Een vierde proefstuk werd voor alle testseries op eenzelfde laadspanning gekrompen en werd onderworpen aan een trekproef.

Een eerste belangrijke resultaat was dat de buis geen materiaal 'voedde' in de groef tijdens de vervorming. Het hoge snelheidsvervormen gebeurt enkel daar waar vervorming mogelijk is, namelijk ter hoogte van de groef. Net zoals bij de experimenten van vrije vervorming, resulteren scherpe randen in een grote insnoering en soms zelfs in het snijden van de buis. Daarentegen resulteert de combinatie van een scherpe groefrand en een ondiepe groef in een sterke verbinding.

De insnoering van de buis aan de randen van de groef werd kleiner indien een verlaagde centrale kraag tussen beide groeven aanwezig was. Indien hoge laadspanningen aangelegd werden, was er veel plastische vervorming van de kraag zichtbaar. Dit is omdat de buis tegen grote impactsnelheid de kraag bereikt en zijn energie deels doorgeeft aan de kraag, die op zijn beurt plastisch zal vervormen. In sommige teststukken (zie Figuur 5), werd de kraag volledig platgedrukt.



Figuur 5: Doorsnede met naamgeving van een dubbele groef krimpverbinding. Op de figuur is ook te zien dat de centrale kraag volledig platgedrukt is.

Bij de trekproeven scheurden alle krimpverbindingen (op 1 na) ter hoogte van hoek 1₁. Dit werd reeds voorspeld door eindige elementen simulaties in Abaqus. Bij de simulatie van een trekproef op een krimpverbinding met dubbele groef, werd waargenomen dat de hoogste trekspanningen zich bevinden ter hoogte van hoek 1₁. De buis werd lichtjes uit de groef getrokken en ervaart in de kritische zone ter hoogte van hoek 1₁ een maximale trekspanning. Een maximale drukspanning werd waargenomen ter hoogte van hoek 2₁.

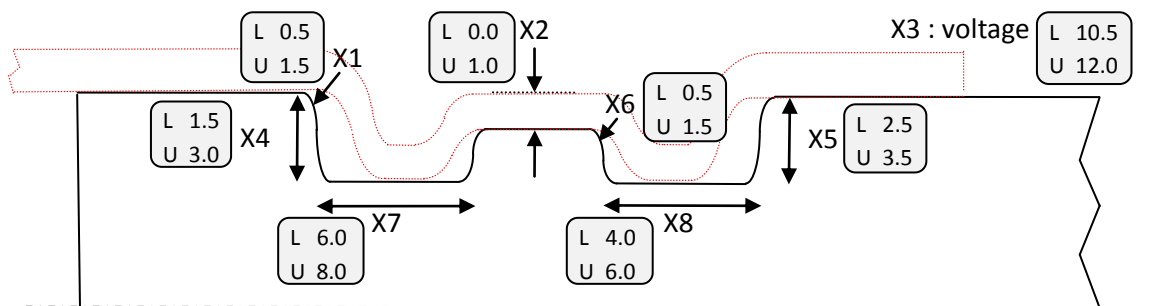
De waarde voor de treksterkte van de laatste krimpverbinding van de verkennende experimenten was 96% van de treksterkte van het basismateriaal. Men stelde voorop dat het mogelijk moest zijn om een optimale verbinding te ontwerpen met een sterkte die even hoog is als de sterkte van het basismateriaal.

4.2 Design of Experiments (DoE)

Het optimaliseren van een ontwerp van een dubbele groef werd gedaan aan de hand van de 'Design of Experiments'-methode (DoE) op 2 niveaus. Algemeen, zijn er voor een onderzoek naar n parameters op 2 niveaus, 2^n experimenten nodig. DoE selecteert een weloverwogen deel van die experimenten, zodanig dat veel minder experimenten moeten uitgevoerd worden. Er is uiteraard een verlies aan informatie, maar het is nog steeds mogelijk om statistisch verantwoorde conclusies te trekken (op voorwaarde dat de deelverzameling goed gekozen is).

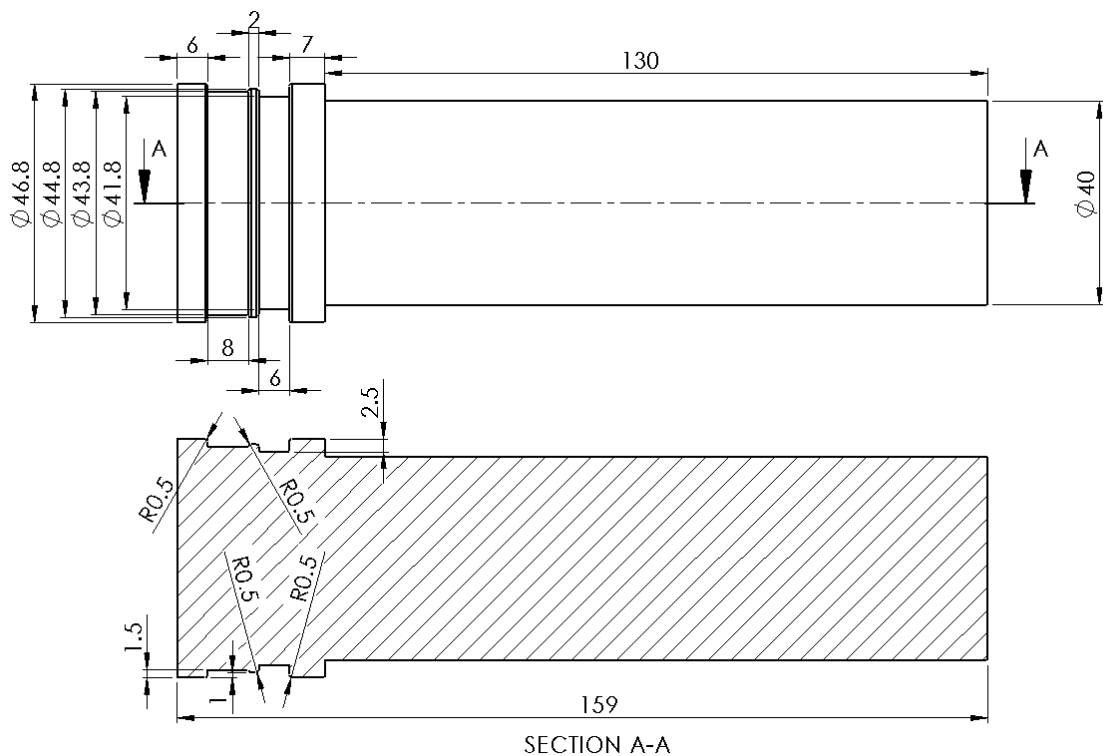
In het design voor een dubbele groef werden acht parameters geselecteerd en er werd aan elk van deze 2 waarden toegekend: een bovenwaarde en een onderwaarde. Een testmatrix van 64 experimenten werd ontwikkeld en alle experimenten werden twee keer uitgevoerd om een idee te hebben van de spreiding op de resultaten. De experimenten werden uitgevoerd met hetzelfde materiaal en met dezelfde afmetingen van de buis als in de verkennende experimenten (aluminium EN AW-6060).

Figuur 6 toont de gekozen parameters, alsook de waarden die werden geselecteerd voor die parameters.



Figuur 6: Keuze van de parameters (X1 tot X8) en de waarden in mm en in kV (enkel parameter X3). De 'L' staat voor de 'lower value' (onderwaarde) en de 'U' staat voor de 'upper value' (bovenwaarde).

De resultaten van de DoE leiden tot een optimaal ontwerp van een krimpverbinding die even sterk is als het basismateriaal. Het optimale ontwerp is voorgesteld in Figuur 7. Het bevat scherpe hoeken voor zowel hoek 1_1 als hoek 2_1 , die voor voldoende vormvastheid zorgen. Scherpe randen resulteren ook in veel insnoering, daarom dat de andere parameters in het optimale ontwerp zo zijn ingesteld dat die insnoering toch beperkt blijft. Een ondiepe eerste groef zorgt voor geringe verdunning van de wanddikte van de buis op groefrand 1_1 . Een zekere kraagdiepte is belangrijk om de insnoering op groefranden 1_1 en 2_2 te minimaliseren. Een lange eerste groef zorgt voor een grote contactzone tussen de vervormde buis en de groefbodem. Dit contact resulteert in een wrijvingseffect die de sterkte ten goede komt.



Figuur 7: Het optimaal ontwerp bekomen met de DoE.

Enkel geometrische parameters (en de laadspanning) werden gebruikt in de DoE-analyse. Dit betekent dat het optimale ontwerp materiaalafhankelijk is.

4.3 Digitale Beeld Correlatie (DIC)

Een deel van de trekproeven die uitgevoerd zijn tijdens de DoE, werden onderzocht op hun faalgedrag. Tijdens de verkennende experimenten zag men dat het merendeel van de krimpverbindingen scheurde ter hoogte van hoek 1_1 , in overeenstemming met de resultaten van de eindige elementen. Niettemin faalde een groot deel van de krimpverbindingen bij de DoE op andere manieren. Met behulp van de Digital Image Correlation (DIC)-techniek werden deze faalmodes onderzocht.

De DIC-techniek maakt gebruik van twee gesynchroniseerde camera's die foto's trekken van een werkstuk onder belasting op discrete tijdstippen. Op het werkstuk zijn zwarte spikkels op een witte achtergrond aangebracht met een spuitbus. Aan de hand van het vervormingspatroon van deze spikkels tijdens de belasting, is het mogelijk om verplaatsingen te bepalen en hieruit rekken af te leiden.

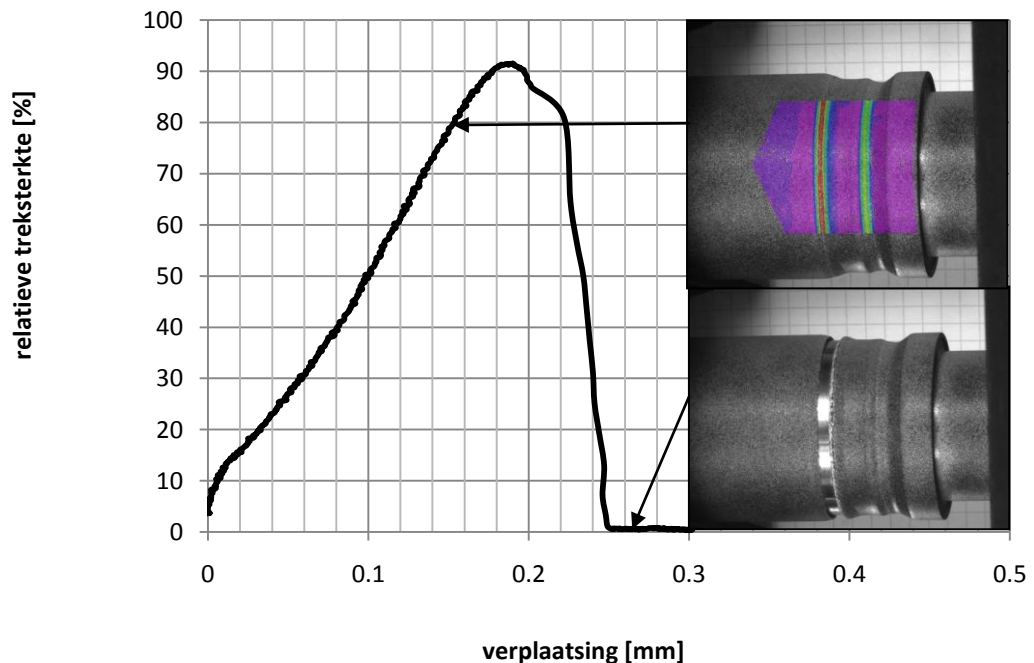
De verdeling, de plaats en de grootte van de rekken tijdens een trekproef op een krimpverbinding werden bekeken en er werden 3 hoofd faalmodes onderscheiden:

- ✓ **1^e faalmode:** de buis scheurt over de gehele omtrek aan hoek 1_1 .
- ✓ **2^e faalmode:** de buis scheurt over de gehele omtrek in de zone van hoek 2_1 .
- ✓ **3^e faalmode:** de buis scheurt niet, maar het binnenstuk en het buitenstuk wordt uit het buitenstuk getrokken.

De eerste faalmode komt het meest voor en de sterkte van de verbinding wordt bepaald door de verdeling van de opgenomen kracht over de twee groeven. Deze faalmode kan bijgevolg onderverdeeld worden in 3 subcategorieën:

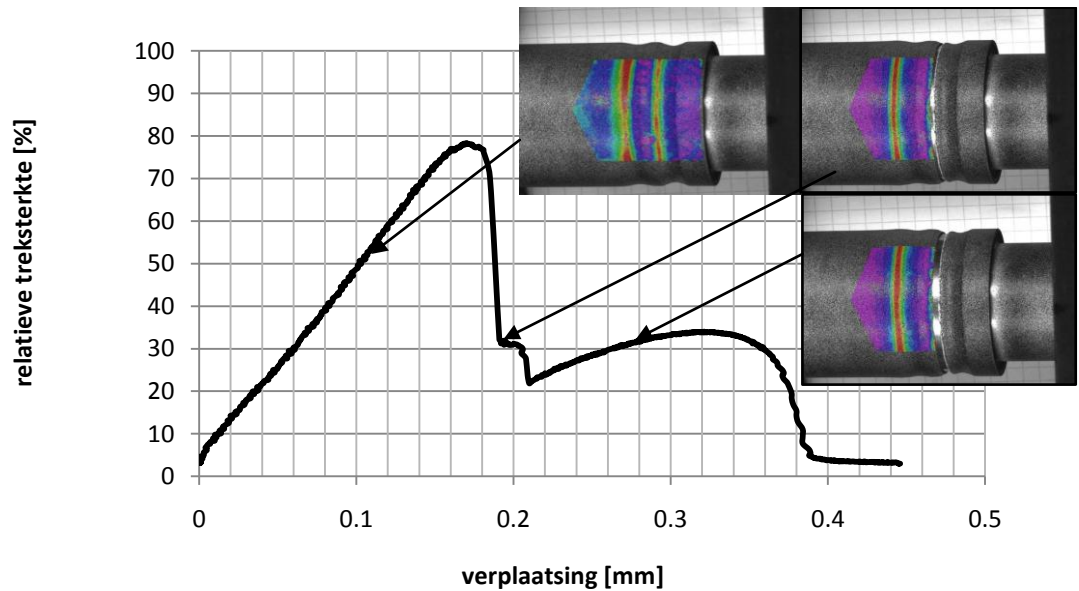
- ✓ **Subcategorie 1:** deze hebben vanwege een slecht ontwerp van de eerste groef, reeds veel insnoering van de buis op de groefrand 1_1 . Zoals aangehaald in de DoE moet de insnoering op de groefrand 1_1 sterk vermeden worden. Door hun extreme verzwakking op de eerste rand, zal de tweede groef bijna niets van kracht opnemen bij een trekproef.
- ✓ **Subcategorie 2:** de tweede groef neemt geringe kracht op en er is geen kraagdiepte aanwezig.
- ✓ **Subcategorie 3:** de tweede groef neemt veel kracht op en er is een kraagdiepte aanwezig. Deze zorgt voor een minimalisatie van de insnoering op rand 1_1 en een betere overbrenging van de kracht naar de tweede groef bij een trekproef. Deze categorie bereikt de hoogste sterktes.

In Figuur 8 is de treksterkte, relatief t.o.v. het basismateriaal, uitgezet in functie van de verplaatsing gedurende de trekproef. De DIC-afbeeldingen die de verschillende zones op de grafiek aanduiden, tonen de Lagrange rek. De zones waar de grootste rek optreedt, zal de meeste kracht opnemen.



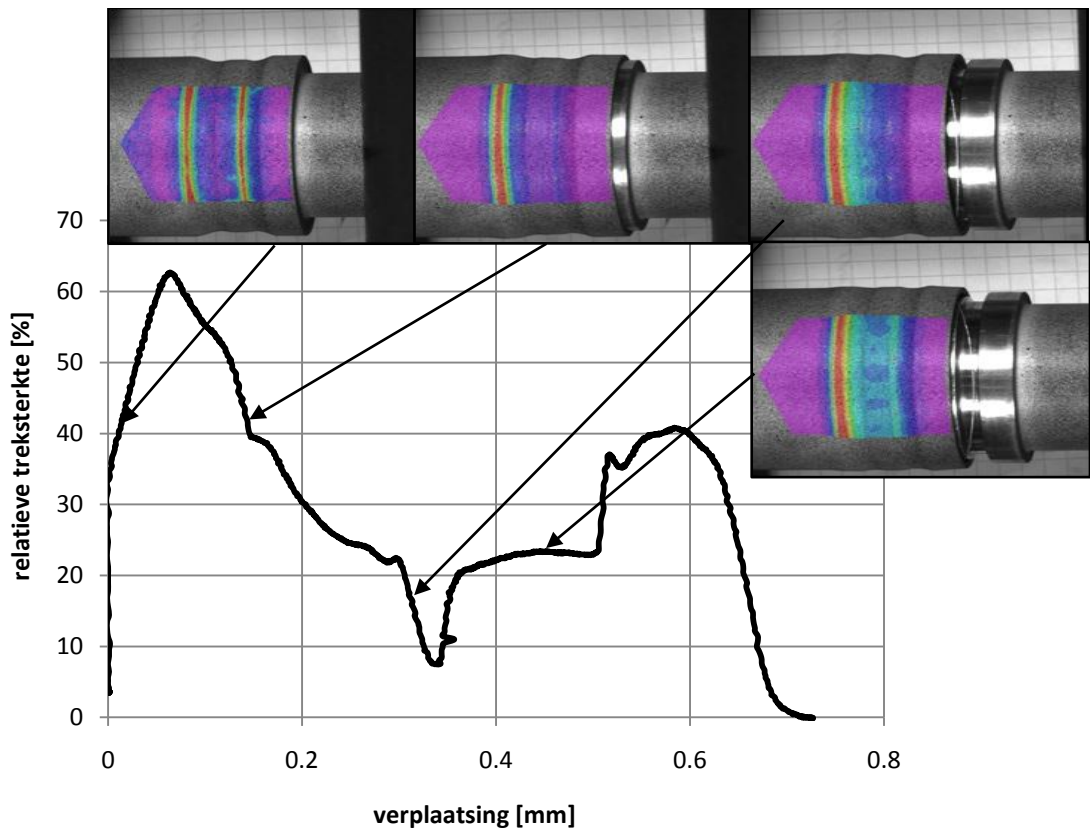
Figuur 8: Relatieve treksterkte in functie van verplaatsing voor een proefstuk met hoge sterkte (eerste faalmode, subcategorie 3) met bijhorende figuren van de DIC waarop zones van hoge concentraties aan rek zichtbaar zijn.

In de tweede faalmode is de bepalende factor voor de sterkte de insnoering van de buis aan de groefrand 2_1 van het interne stuk. In tegenstelling tot de 1^{ste} faalmode heeft de verbinding nog sterkte nadat de buis gescheurd is over de gehele omtrek. Dit komt omdat de buis nog vervormd zit in de eerste groef. Bij een verdere verplaatsing zal de vervormde buis uit de groef getrokken worden. De sterkte is dan afhankelijk van de combinatie van de maximale inwaartse vervorming van de buis in de groef en de axiale verplaatsing van de buis t.o.v. de groefrand 1_1 . Figuur 9 toont een typische curve van de relatieve treksterkte t.o.v. verplaatsing met figuren van de DIC.



Figuur 9: Relatieve treksterkte in functie van verplaatsing voor een proefstuk met tweede faalmode met bijhorende figuren van de DIC waarop zones van hoge concentraties aan rek zichtbaar zijn.

De curve van de treksterkte in functie van de verplaatsing voor een proefstuk dat faalt volgens de derde faalmode ('pull out') heeft heel uiteenlopende vormen. De sterkte is afhankelijk van de vervorming van de buis in beide groeven in combinatie met de axiale verplaatsing van de buis t.o.v. het binnenstuk. Een voorbeeld wordt getoond in Figuur 10.



Figuur 10: Relatieve treksterkte in functie van verplaatsing voor een proefstuk met derde faalmode met bijhorende figuren van de DIC waarop zones van hoge concentraties aan rek zichtbaar zijn.

Tabel 1 somt de gemiddelde relatieve treksterktes op van de verschillende faalmodes. De eerste faalmode komt het meeste voor en resulteert ook in de hoogste sterktes. Voor sommige toepassingen (waar bijvoorbeeld een waarschuwing moet zijn als de buis het begint te begeven) is faalmode 3 meer geschikt dan bijvoorbeeld faalmode 1, die plots doorschiet.

Faalmode	Gemiddelde relatieve treksterkte [%]	Voorkomen [%]
Faalmode 1	81.7	63.0
Subcategorie 1	74.0	16.8
Subcategorie 2	80.0	29.4
Subcategorie 3	91.0	16.8
Faalmode 2	75.3	12.0
Faalmode 3	66.4	14.0

Tabel 1: Vergelijking van de relatieve treksterkte en het procentuele voorkomen van de 3 faalmodes.

5 Aanbevelingen voor verder onderzoek

Op het einde van dit werk zijn enkele concrete voorstellen en aanbevelingen geformuleerd voor verder onderzoek. Eén van de belangrijkste toekomstige doelstellingen zal zijn om de krimpverbinding die geoptimaliseerd werd qua sterkte, ook lekdicht te maken.

- [1] *PULSCRIMP - Investigations on magnetic pulse crimping of tubular overlap joints with and without filler material.* available from: <http://www.innovatienetwerk.be/projects/1551>.
- [2] Weddeling, C., Woodward,S.,Marré,M.,Nellesen,J.,Psyk,V.,Tekkaya,E.,Tillmann,W., *Influence of groove characteristics on strength of form-fit joints.* Journal of Materials Processing Technology, 2010.
- [3] Shribman, V., *Magnetic pulse technology for improved tube joining and forming.* Tube & Pipe Technology, November/December 2006: p. 91-95.
- [4] Broekaert, F., De Ketele,M., *An exploratory study into the feasibility of magnetic pulse forming,* in *Mechanical construction and production.* 2009, Gent. p. 284.
- [5] Park, Y., Kim, H. , Oh, S., *Design of axial/torque joints made by electromagnetic forming.* Thin-walled structures 43, 2005: p. 826-844.

Table of contents

Chapter 1: Introduction

1.1	General.....	1
1.2	Objectives.....	2
1.3	Brief overview of the chapter content.....	3

Chapter 2: Literature review

2.1	General principle of the electromagnetic pulse process	4
2.2	Advantages of electromagnetic pulse forming	8
2.3	Disadvantages and limitations of EMP forming.....	9
2.4	Field shaper	10
2.5	Connection mechanisms.....	15
2.5.1	Interference fits	15
2.5.1.1	Remaining residual stresses in the contact zone	15
2.5.1.2	Friction coefficient between the outer tube and the internal part	16
2.5.1.3	Area of contact zone	17
2.5.2	Form fits	19
2.6	Conclusions	22

Chapter 3: Industrial case study

3.1	Introduction	24
3.2	Experimental data.....	24
3.2.1	Materials	24
3.2.2	Test setup.....	26
3.2.3	Field shaper	27
3.3	Measurement methods	27
3.4	Results and discussion	28
3.5	Conclusion.....	32

Chapter 4: Free deformation experiments

4.1	Introduction	32
4.2	Material properties	32
4.3	Experimental test setup	33
4.4	Positioning.....	35
4.5	Test matrix and measurement methods	36
4.6	Results and discussion	38
4.6.1	Radial inward displacement as a function of the groove width and the charging voltage	40
4.6.1.1	Two-dimensional graphs.....	40
4.6.1.2	Three-dimensional graphs and equations	41
4.6.1.3	Discussion.....	42
4.6.2	Necking at the groove edge as a function of the groove width and the charging voltage	44
4.6.2.1	Two-dimensional graphs.....	44
4.6.2.2	Three-dimensional graphs and equations	45
4.6.2.3	Discussion.....	46
4.6.3	Effect of the radial cut in the field shaper	49
4.7	Conclusions	50

Chapter 5: Preliminary experiments

5.1	Introduction	51
5.2	Finite element simulations.....	52
5.3	Experimental data	54
5.3.1	Materials	54
5.3.2	Test setup.....	55
5.3.3	Field shaper	55
5.3.4	Process parameters.....	56
5.4	Results and discussion	57
5.4.1	Single groove strength	57
5.4.2	Test series A & B.....	58
5.4.2.1	Design and setup.....	58
5.4.2.2	Results.....	59
5.4.3	Test series C	61

5.4.3.1	Design and setup.....	61
5.4.3.2	Results.....	62
5.4.4	Test series D.....	63
5.4.4.1	Design and setup.....	63
5.4.4.2	Results.....	64
5.4.5	Test series E & F.....	65
5.4.5.1	Design and setup.....	65
5.4.5.2	Results.....	66
5.4.6	Test series G.....	67
5.4.6.1	Design and setup.....	67
5.4.6.2	Results.....	68
5.4.7	Test series H.....	69
5.4.7.1	Design and setup.....	69
5.4.7.2	Results.....	70
5.5	CONCLUSION.....	71

Chapter 6: Design of Experiments

6.1	Introduction.....	73
6.2	Test setup.....	73
6.2.1	Choosing the parameters for DoE.....	73
6.2.2	Parameter values.....	74
6.2.3	Test-matrix.....	77
6.3	Discussion of the experiments.....	80
6.3.1	Analytical background of the evaluation method.....	80
6.3.2	Scatter on the DoE.....	82
6.3.3	Results.....	85
6.4	Discussion of the results.....	91
6.4.1	Second groove width (X8).....	91
6.4.2	Edge 1 ₁ (X1).....	92
6.4.3	Collar depth (X2).....	92
6.4.4	Depth of the first groove (X4).....	93
6.4.5	Edge 2 ₁ (X6).....	94
6.4.6	Collar depth and applied voltage (X2*X3).....	94
6.4.7	Collar depth and width of second groove (X2*X8).....	94

6.4.8	Voltage and depth of first groove (X3*X4)	94
6.4.9	Voltage (X3).....	95
6.4.10	Collar depth and width of first groove (X2*X7)	95
6.4.11	Depth of first groove and width of second groove (X4*X8)	95
6.4.12	Depth of first groove and width of first groove (X4*X7).....	95
6.4.13	Depth of first groove and edge 2_1 (X4*X6)	96
6.4.14	Estimating the maximal relative tensile strength	96
6.5	Optimal design according to DoE.....	96
6.6	Remarks and evaluation of the methodology	98
6.6.1	A design with other diameters.....	98
6.6.1	A design with other diameters.....	98

Chapter 7: Digital Image Correlation

7.1	Introduction	100
7.2	The Digital Image Correlation technique	100
7.3	Lagrange strain.....	103
7.4	Analysing the different failure modes	104
7.4.1	Failure mode 1	105
7.4.2	Failure mode 2	110
7.4.3	Failure mode 3	114
7.4.3.1	Discussion on crimp joint 8	115
7.4.3.2	Discussion on crimp joints 34 and 36.....	115
7.4.3.3	Discussion on crimp joint 50, 53 and 56	117
7.5	Conclusions	121

Chapter 8: Conclusions and recommendations

8.1	Single groove crimp joints.....	123
8.2	Double groove crimp joints.....	124
8.3	Recommendation for future work.....	127
8.3.1	Further work on DoE.....	127
8.3.2	Leakproofness	128
8.3.3	Further work on free deformation.....	130
8.3.3.1	Validating the conclusions of the free deformation experiments	130
8.3.3.2	Influence of the groove depth	131

8.3.3.3	Evaluating a double groove design	131
8.3.4	Finite element simulations of joint strength.....	132
8.3.5	Torque joints	132
8.3.6	Hollow internal workpiece.....	133
8.3.1	Field shaper design	135

Abbreviations

BWI	Belgian Welding Institute
SLV	Schweißtechnische Lehr- und Versuchsanstalt
IWT	Agency for Innovation by Science and Technology of the Flemish Region
EMP	Electromagnetic pulse
EMPC	Electromagnetic pulse crimping
DOE	Design of Experiments
DIC	Digital Image Correlation

Chapter 1: Introduction

1.1 General

The electromagnetic pulse technology uses magnetic forces to deform or join workpieces. The energy stored in a capacitor bank is discharged rapidly through a magnetic coil. Typically a ring-shaped coil is placed over a tubular workpiece. The magnetic field produced by the coil generates eddy currents in the tube. These currents, in turn, produce their own magnetic field. The forces generated by the two magnetic fields oppose each other. Consequently, a repelling force between the coil and the tube is created. As a consequence, the tube is collapsed onto the internal workpiece, creating a crimp joint or a welded joint.

The main difference between the both is that in electromagnetic pulse crimping process an atomic bond is not realised. These joints obtain their strength from the combination of an interference and a form fit. In this case, a special profiled internal workpiece is used, as shown in **Fout! Verwijzingsbron niet gevonden..**



Figure 1.1: Electromagnetic crimp joints obtain their strength from the combination of an interference and a form fit.

Most of the research concerning the electromagnetic pulse technology until now focussed on electromagnetic pulse welding. In this master thesis however, electromagnetic pulse crimping will be investigated.

The incentive to perform research on electromagnetic pulse crimping is the fact that electromagnetic pulse crimping has some major advantages compared to electromagnetic pulse welding [1]:

- ✓ It is possible to join materials which cannot be joined using magnetic pulse welding: low electric conductive materials and higher strength materials.
- ✓ The needed energy level is lower for electromagnetic pulse crimping and therefore smaller and less expensive pulse generators can be used.
- ✓ It is possible to join larger diameter parts (for tubular joints).
- ✓ The quality of magnetic pulse welds is very dependent on the surface preparation and cleanliness. This is not the case for magnetic pulse crimping.
- ✓ The quality of the electromagnetic crimped connections is depends less on the parameters than for electromagnetic welded connections.

This master thesis is performed within the framework of the Cornett project “PULSCRIMP Investigations on magnetic pulse crimping of tubular overlap joints with and without filler material”. This is a collective research project aimed at acquiring technological knowledge useful for industrial applications. The partners in this project are the Belgian Welding Institute (BWI), Labo Soete (Ghent University), OCAS, SLV (München) and a group of companies which have interest in the technique. The project is supported by IWT – Agency for Innovation by Science and Technology of the Flemish Region [2].



Figure 1.2: Partners of the PULSCRIMP project.

The target sectors of the PULSCRIMP project are air-conditioning & cooling applications, automotive, aluminium and steel processing companies.

One of the main goal is to evidence that that magnetic pulse crimping can create strong joints and that it is a valuable alternative for magnetic pulse welding.



Figure 1.3: Example of an application of the electromagnetic pulse crimping [3].

1.2 Objectives

The objectives which were set for this thesis work are:

- ✓ Gather more knowledge about the deformation behaviour in crimp joints, more specific for a single groove and a double groove design of the internal workpiece.
- ✓ Execute an industrial case study for a company which is involved in the PULSCRIMP project.
- ✓ Determine the parameters which have an important influence on the strength of axial joints, using a double groove design.

- ✓ Determine an optimal design for a double groove internal workpiece of a crimp joint and demonstrate that magnetic pulse crimping is a valuable alternative for magnetic pulse welding.
- ✓ Gather more knowledge on the failure behaviour of the crimp joints.

1.3 Brief overview of the chapter content

To guide the reader through this master thesis, a brief overview of the chapter content is given below.

Chapter 2 contains a literature review in which the general principles of electromagnetic pulse forming and its advantages/disadvantages are discussed. Also, the field shaper design and the interference and form fit mechanisms which are of importance for crimp joints are described.

In **chapter 3**, an industrial case study using a single groove design is presented. From this case study, it will be concluded that it is difficult to determine an appropriate capacitor charging voltage for a certain groove design.

Therefore, in **chapter 4**, an experimental research is presented, which links the charging voltage and single groove design parameters to the global deformation capacity and localised necking of aluminium tubes. The experimental results provide practical guidance for groove design and increased knowledge on the deformation behaviour during magnetic pulse crimping.

In **chapter 5**, preliminary experiments on a double groove design are presented. This task is motivated by literature reports on the limited strength of single groove joints and the possible beneficial influence of a second groove. Additionally, finite element simulations of a tensile test performed on a double groove crimp joint were performed to get more insight in the stress distribution throughout the joint. Both the preliminary experiments and the finite element simulations provide more insight in the deformation behaviour for a double groove design.

The preliminary experiments confirmed that higher tensile strengths could be reached with a double groove design, and therefore in **chapter 6** an in depth study on a double groove design for an axial loaded joint is presented. In order to do this in a structured way, and to minimise the amount of experiments needed, the Design of Experiments method is used. Results of tensile tests on the crimp joints allow to determine the most important parameters for the groove design. Based on these observations an optimal double groove joint design is proposed.

The deformation and failure behaviour of several crimp joints were experimentally studied in detail in **chapter 7**. The digital image correlation technique was used during tensile tests on crimp joints to measure the local and global deformation of the joint. Failure mechanisms include pull-out, local shearing and fracture of the tube.

Chapter 8 is a summary of the most important conclusions from the previous chapters and includes recommendations for future work.

Chapter 2: Literature review

In this master thesis, electromagnetic pulse crimp joining will be investigated in detail, with the emphasis on tubular joints loaded with an axial force.

In order to get acquainted with the subject, a literature review was performed. The topics investigated in this literature review are:

- ✓ The general principle of electromagnetic pulse forming
- ✓ Design of a field shaper
- ✓ Advantages and disadvantages of the electromagnetic pulse technique
- ✓ Joint mechanism

The most important observations and conclusions of the literature review are discussed in the paragraphs below.

2.1 General principle of the electromagnetic pulse process

In Figure 2.1, a schematic representation of a typical electromagnetic pulse (EMP) system layout is shown. The system consists of a power supply, a bank of capacitors to store the energy, a control unit to operate the machine (not shown on the figure), a high current switch, a coil and a field shaper. The latter one is not depicted and is discussed in detail in the next paragraph.

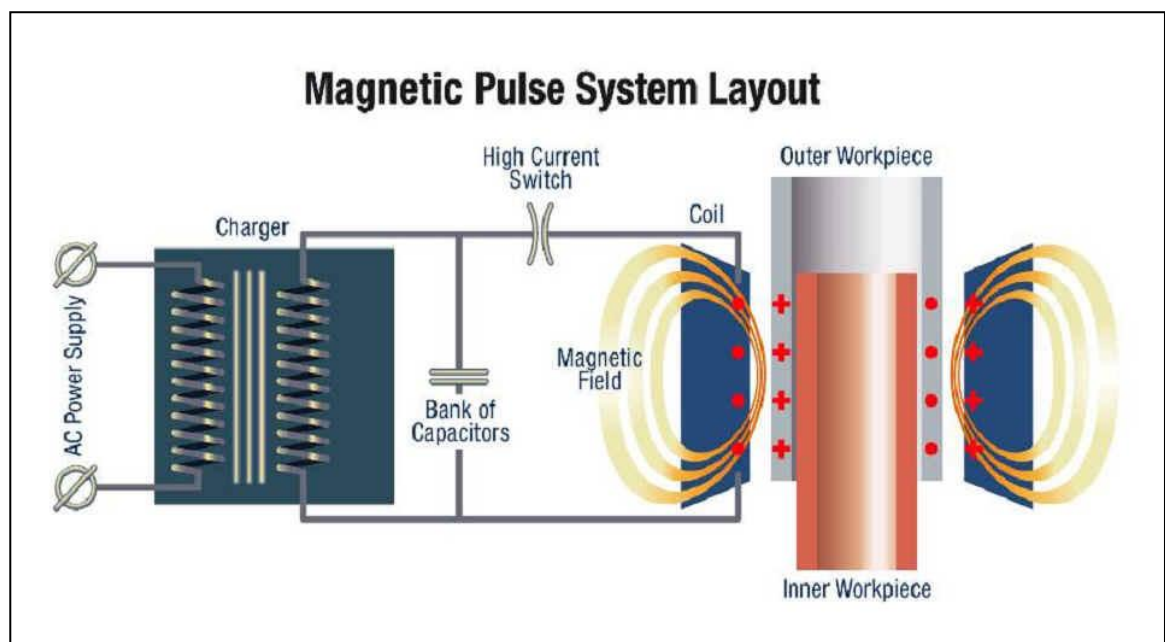


Figure 2.1: Layout of an electromagnetic pulse system [4].

The capacitor bank is charged to the desired energy level by setting the correct charging voltage of the capacitors on the machine's control unit. The energised capacitor bank is then discharged

by operating a high current switch . This results in a damped oscillating current, which flows through the coil, generating an intense transient magnetic field inside the coil.

According to Lenz's law, eddy currents are induced in the workpiece outer surface layer. This is the so-called skin effect. The skin depth is the depth below the surface of the conductor inside the coil at which the current density decays to $\frac{1}{e}$ of the current density at the surface. The skin depth can be calculated as:

$$\delta = \sqrt{\frac{2\rho}{\omega\mu}} \quad (2.1)$$

With: ρ : resistivity of conductor [$\Omega \cdot m$]
 ω : angular frequency of the current [rad/s]
 μ : absolute magnetic permeability of the conductor [H/m]

As can be seen from the above equation, the skin depth varies with the inverse square root of the angular frequency of the current. When hollow workpieces are used, it is important that the frequency is high enough, so that the skin depth is smaller than the tube wall thickness. If this is not the case, part of the current would have no material to flow in, causing a less effective induced magnetic field and therefore less effective pressure and deformation (see further).

The skin depth also varies with the square root of the resistivity of the conductive material, implying that less conductive materials (having a higher resistivity) have a larger skin depth. Especially for those materials, it is important that the frequency is high enough. In Figure 2.2, the skin depth of several materials as a function of current frequency is shown [1].

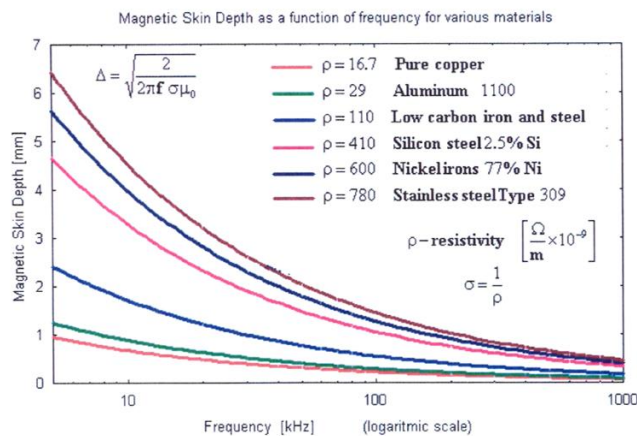


Figure 2.2: Skin depth as a function of the frequency for several materials [6].

The eddy currents flow in such a direction that an induced magnetic field is created, which initially shields the workpiece from the magnetic field inside the coil. Figure 2.3 shows a typical graph of the current inside the coil and the induced current in the workpiece. Both currents are nearly into anti-phase, because of Lenz's law.

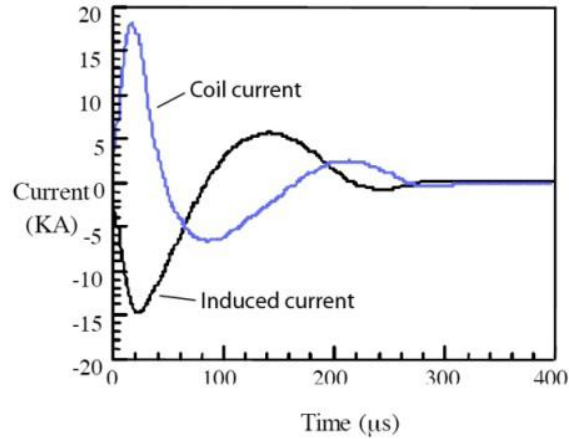


Figure 2.3: Current in the coil and current induced in the workpiece [7].

During the proceeding of the process, the magnetic field penetrates the workpiece wall. The resulting pressure pulse acts orthogonally on the magnetic field inside the coil, and the Lorentz repulsion force causes the tube to repel away from the coil. When this force is greater than the workpiece material's yield strength, permanent plastic deformation occurs [2-4].

The magnetic pressure $p(t, r, z)$ during the deformation process can be calculated using the magnetic field outside the workpiece $H_a(t, r, z)$, the penetrating magnetic field $H_i(t, r, z)$ and the permeability μ_0 of vacuum [5] (see Figure 2.4 for the interpretation of t , r and z):

$$p(t, r, z) = \frac{1}{2} \mu_0 (H_a^2(t, r, z) - H_i^2(t, r, z)) \quad (2.2)$$

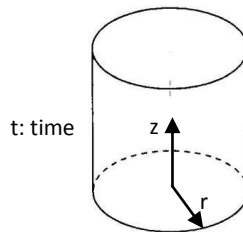


Figure 2.4: Parameters of the magnetic pressure.

Experimental investigations as well as analytical calculations of the magnetic pressure [6] proved that the equation (2.2) can be simplified if the ratio of the skin depth to the tube's inner radius is less than 0.2 and the ratio of the wall thickness to the skin depth is greater than 2:

$$p(t, r, z) = \frac{1}{2} \mu_0 H_a^2(t, r, z) \quad (2.3)$$

If the movement of the workpiece is neglected, the magnetic field can be approximated by using equation (3) [8]:

$$H_a(t, r, z) = \frac{n I(t)}{l_{coil}} k_H(z) \quad (2.4)$$

With: l_{coil} : unit length of the coil [mm]
 n : number of turns per l_{coil} [-]
 $I(t)$: current in the coil [A]
 $k_H(z)$: axial distribution of the magnetic field [-]

The current in the coil can be measured using a Rogowski coil. By combining equations (2.3) and (2.4), the magnetic pressure can be estimated based on the measured current.

In Figure 2.5, a typical graph of the current in the coil as well as the resulting pressure is shown [13]. It can be observed that almost all of the deformation will occur during the first peak and that this peak only takes approximately 20 μ s.

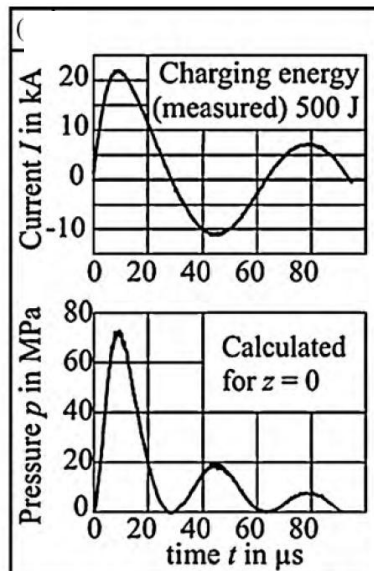


Figure 2.5: Current inside the coil and the magnetic pressure during the process [14].

The machine used for the experiments performed in this thesis is the Pulsar's MPW 50/25 magnetic pulse system (see Figure 2.6). The specifications of this machine can be found in Appendix A.

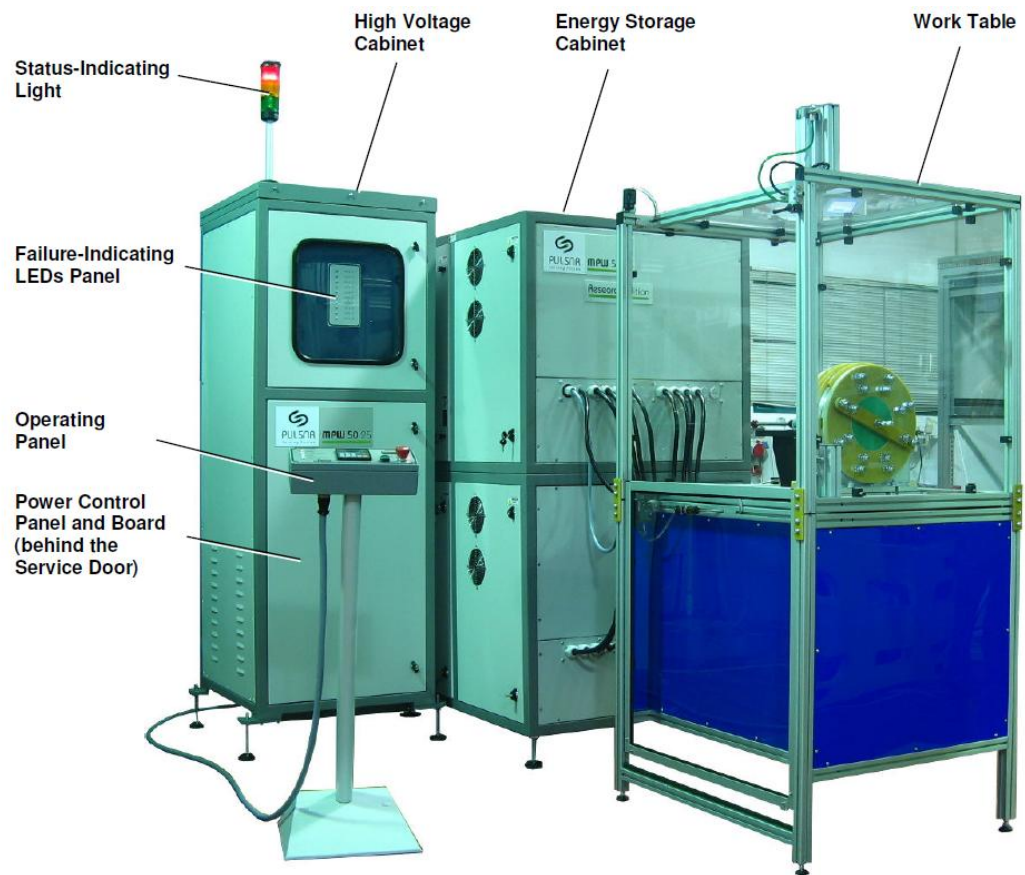


Figure 2.6: Pulsar's MPW 50/25 magnetic pulse system [6].

2.2 Advantages of electromagnetic pulse forming

The EMP forming process has several advantages compared to conventional mechanical forming processes. The most important advantages are listed below. Some of the advantages are common to all high speed forming process, others are unique to EMP forming.

- ✓ The workpiece velocities are 100 to 1,000 times higher compared to conventional forming processes. By forming at high velocities, the failure strain (this is the strain at which a material breaks or fails) is significantly increased and an increased formability can be obtained. Many of the metals used in industry (aluminum alloys, steel, magnesium) have demonstrated an increased formability of 100% or more, when formed at high velocity (> 50 m/s) [10].
- ✓ In ring compression, wrinkling is caused by the non-uniform compression of the ring. Forming at high velocities reduces wrinkling. This was demonstrated in a series of experiments [15]: aluminum and copper rings with various heights were compressed onto a internal part using a single turn coil. In both types of experiments, the tendency for wrinkling reduced as the discharge energy of the capacitor bank increased. In other words, high velocities tend to suppress wrinkling.

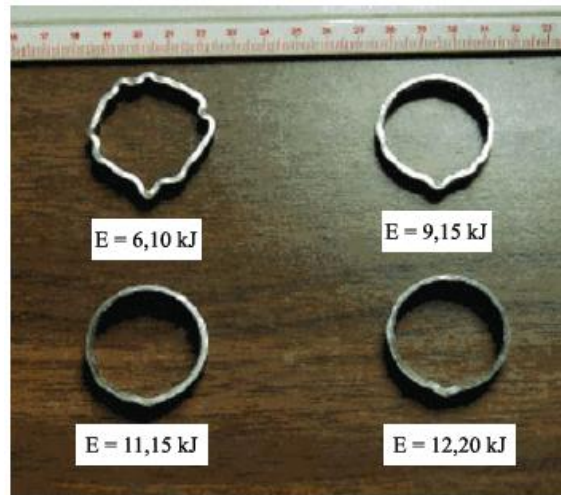


Figure 2.7: Wrinkling is reduced when deformation is performed at high velocities [15].

- ✓ When a material is formed, it is stretched both plastically and elastically. After the removal of the deforming force, the elastic part of the strain is recovered causing a change in the shape of the product. This is called springback. Springback has a significant effect on the product accuracy. It also reduces the strength of mechanically joined products. Electromagnetically formed products show less springback compared to conventional formed products, thus creating workpieces with a better accuracy [10].
- ✓ Possibility to join dissimilar materials [4].
- ✓ A workpiece surface finish can be executed before forming, since there is no mechanical contact during the process.
- ✓ The system requires low maintenance and short setup times.
- ✓ Low workmanship skills are required.
- ✓ The large amount of energy is released very quickly, and as a consequence the actual energy expenditure is up to 10 times less than in conventional processes [6].
- ✓ The workpiece surface does not need to be machined to tight tolerances before crimping.
- ✓ The process is environmentally friendly [Pulsar Ltd., MPW 50 25 Magnetic Pulse System, user guide].

2.3 Disadvantages and limitations of EMP forming

The EMP process also has its disadvantages and limitations. The most important are listed below.

- ✓ Only electrically conductive materials can be formed directly. Non-conductive materials can also be formed, but a conductive driver must be attached to the material [10].
- ✓ The size of the tubes is limited. For EMP welding, the company Magneform mentions possible diameters ranging from 0.64 cm to 25.4 cm [16]. The required energy to crimp is lower than to weld, and as a consequence the maximum diameter possible will be larger, but is still very limited. The high voltages and currents involved require careful safety considerations. The process is not suitable for in-field applications.

2.4 Field shaper

For the generation of a magnetic field, either a single-turn coil or a multi-turn coil can be used. Each of them has its own advantages.

In case of a single-turn coil there is no need to use a field shaper as the current flows close to the work zone of the coil. This zone can be shaped according to the needs. Also, the single-turn coil can be manufactured as a solid component to resist the acting forces.

In case of a multi-turn coil, a field shaper can be used to focus the widely spread current from many windings onto a small work-zone, and to gain the advantage of the high current generated by several windings, to offset the large amount of current dissipation inherent to all field shapers [17]. The positioning of the field shaper in the machine can be seen in Figure 2.8.

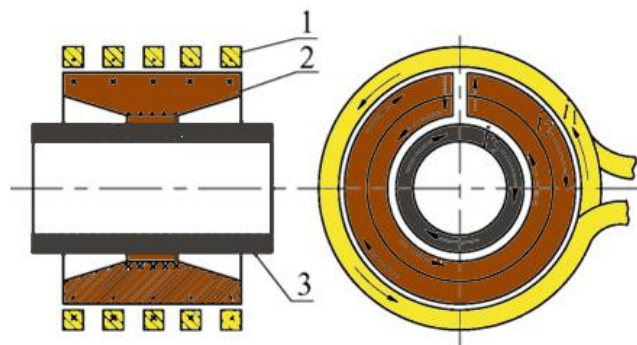


Figure 2.8: 1=A multi-turn coil, 2=field shaper and 3=workpiece [18].

Field shapers can prolong the coil lifetime, can be machined according to the shape of the workpiece and can carry out batch production [18]. They can also easily increase the magnetic pressure with a factor 2 or more [19].

To design a field shaper, 2 important parameters have to be considered, which are the material and the geometry. The field shaper material needs to combine a good electrical conductivity and a strong mechanical endurance against pulse loads and thermal shocks. There is of course also the issue of cost: tantalum (Ta), for example, has better properties than copper-beryllium, but the cost of CuBe_2 will be much lower and offset more the slightly lower service life.

As for the geometry, the design is more complicated. The aspects which should be taken into account are:

- ✓ The desired shape of the work zone based on the diameter of the workpiece, the width of the affected zone and tailoring the magnetic profile.
- ✓ The inner diameter and axial length of the multi-turn coil to be used.
- ✓ The efficiency of the field shaper, based on minimising current loss in transformation and minimising eddy currents and field-shaper heating.
- ✓ Durability of the field-shaper (minimising mechanical and thermal stresses)

An optimum shape has to be found for the chosen material and for a given geometry of the test set up. For industrial applications, optimisation of the efficiency is very important for reducing the energy costs. For the laboratory experiments, optimisation of the efficiency was not really

required because the main goal of the thesis was to investigate the possibilities of the magnetic pulse crimping process [17].

Since the current has to flow as close as possible to the part to be deformed, a radial cut is foreseen in the field shaper. This is because the induced current only flows at the surface of the workpiece inside the coil. Figure 2.9 shows the cross-section of a field shaper with (A) and without (B) a radial cut. Also the path of the current is plotted in the figure [19].

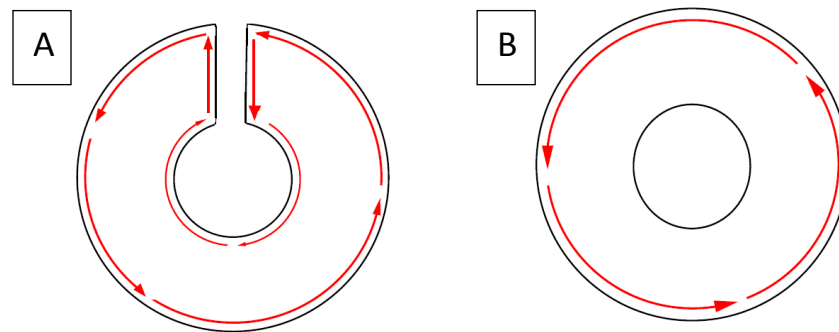


Figure 2.9: Cross section of a field shaper with (A) and without (B) radial cut [10].

The main disadvantage of a field shaper is the low energy-transfer efficiency. The losses can be divided into 3 types:

- ✓ Thermal losses due to resistive dissipation
- ✓ Inductive energy losses caused by poor coupling between primary and secondary coil
- ✓ Inductive energy losses caused by the shape of the field shaper [17]

For reducing the thermal losses due to resistive dissipation, good conducting materials have to be used. The coupling between the primary and secondary coil (secondary coil is the field shaper) depends on the mutual inductance. The ideal situation would be to integrate the primary coil into grooves on the outer surface of the field shaper.

Despite unavoidable losses, the field shaper is shaped to suit a specific diameter of the parts to be deformed. The shaping results from electro-magnetic force considerations. The electromagnetic field produced by the field shaper in the work zone is stronger than the electromagnetic field produced by the primary coil. This implies an increase in surface current density, due to the decrease of the axial length of the field shaper. Unfortunately this also implies a decrease of efficiency. It should be noted that the frequency of the current is lower when a field shaper is used (due to mutual inductance between the primary coil and the field shaper). A lower frequency implies a larger skin depth and less shielding (see equation 2.1), which results in a lower magnetic pressure. Despite this lower magnetic pressure due to the decrease in frequency of the current, the net result is that the field shaper increases the magnetic pressure.

When designing a field shaper, there are some fixed parameters such as the primary coil length (depends on the pulse equipment), the axial and radial dimensions of the working area. In Figure 2.10, several possible shapes of the field shaper are shown.

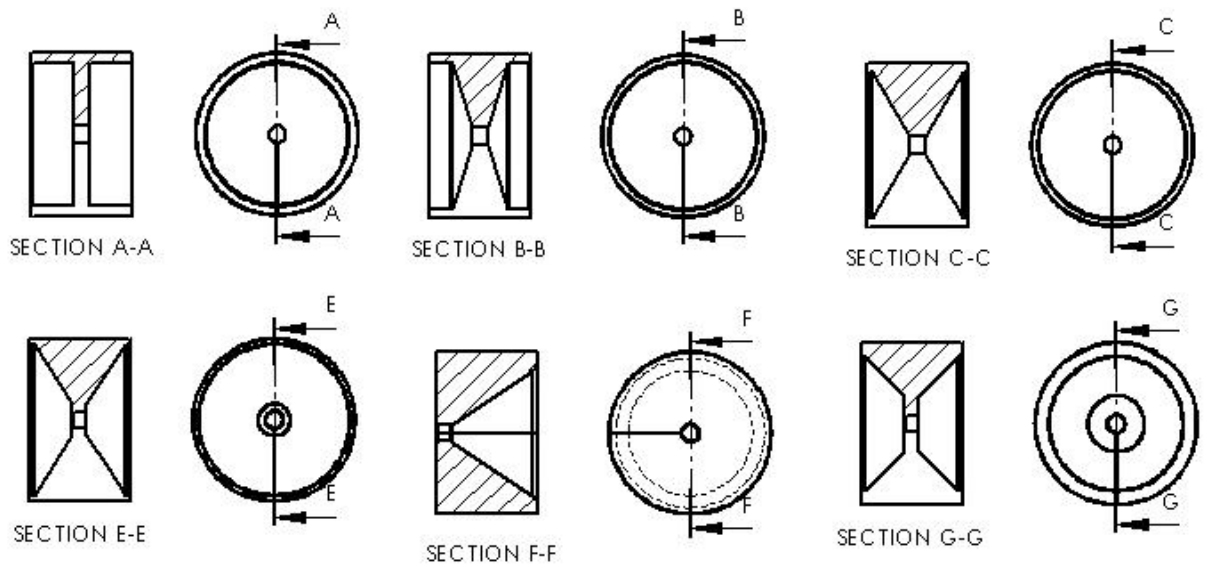


Figure 2.10: Cross section of possible shapes of a field shaper
From step-shaped FS (A-A') to conical-shaped FS with straight ends (G-G').

Research has been performed on the design of field shapers [18-20]. It was found that the step-shaped field shaper has the best efficiency, but this design was the worst from a mechanical viewpoint because the primary windings failed due to high forces (radial and axial). This was not the case for a slightly conical field shaper. The difference in efficiency between the step-shaped and the conical-shaped field shaper was not more than 5%.

The reason for these high forces acting on the primary coil is the magnetic field distribution in the radial cut. With the step-shaped field shaper, large radial as well as axial forces exist whereas the current density in the slot increased slightly in the case of a simple conical model [17].

Without field shaper, the coil is larger than the workpiece and therefore there are magnetic field components acting on the ends of the tube so we have an axially downward oriented pressure. The field shaper homogenizes the magnetic pressure acting on the tube and the uniform force area is being enlarged, as can be seen in Figure 2.11. The magnetic field is also strengthened by using a field shaper. The field shaper thus contributes to the increase and uniform distribution of magnetic pressure and weakens the end-effect of the tube.

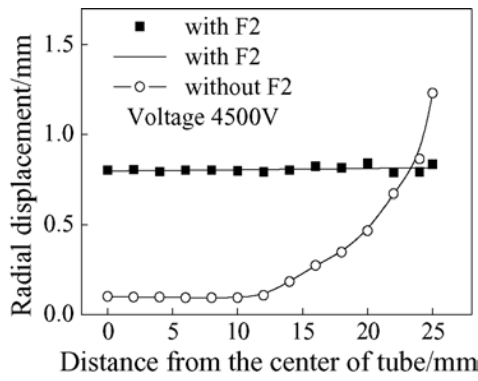


Figure 2.11: Radial displacement distribution [18].

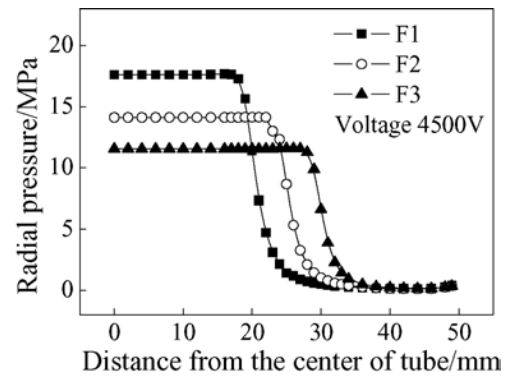


Figure 2.12: Radial pressure distribution [18].

The effective area of a field shaper is the area enclosed by its inner surface. The larger this effective area of the field shaper, the bigger the uniform force area is, but the magnetic pressure decreases (see Figure 2.12). This statement can also be applied to field shapers with multiple nodes (see Figure 2.13) considering the effective area as the sum of each node-area.

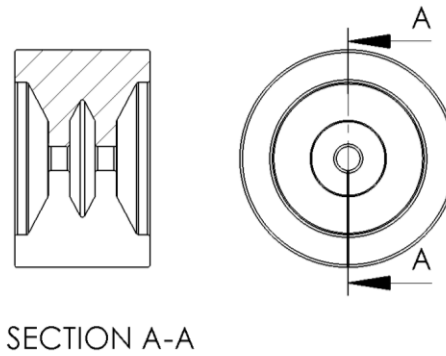


Figure 2.13: Field shaper with two nodes.

The magnetic pressure decreases with the increase of the relative diameter of the field shaper (see Figure 2.14).

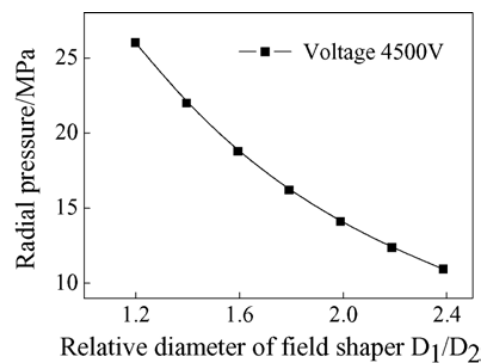


Figure 2.14: Radial pressure as a function of relative diameter [18].

The electromagnetic pulse crimping process can also be investigated using finite element simulations. The advantage of such simulations is that, without having costs for experimental

testing the effects of different parameters can be evaluated. One of the drawbacks of finite element models is that there is a high computational cost and that the result is not always accurate enough. The conditions of the real operation can differ from the (often perfect) conditions assumed by the models.

The development of such a finite element simulation model is based on complex analytical formulas describing coupled mechanical, thermal and electromagnetic phenomena. In the past, many models were tested for evaluation of the MPC process [20-21]. Most of these models have found good agreement with reality in their (narrow) working area. However, note for example that in [20] the authors found that with a 3D simulation, the maximum magnetic field increases with 15% as compared to 2D models. This indicates a lack of accuracy in the 2D models.

The magnetic field distribution is found to be proportional to the current amplitude [21]. This means that the field distribution can be predicted if the different current peaks are measured. The change in geometry during the mechanical deformation of the workpiece has an impact on the magnetic flux distribution. The air gap increases in case of electromagnetic compression.

$$\vec{B} = KI f(A_{effective}) \quad (2.5)$$

With: \vec{B} : magnetic flux density on the node(s) of the field shaper [Wb]

$A_{effective}$: effective area [mm²]

I : amplitude of the pulsed current [A]

K : constant depending on other geometrical parameters, material properties and characteristics of the electrical circuit [-]

f : enhancement factor of the magnetic flux density [-]

Figure 2.15 shows the enhancement factor of the magnetic flux density (f) as a function of the ratio of axial length of the field shaper (= width of the nodule) to the whole length of the primary coil for different radii of the primary coil. To determine the value of the proportional factor K , only one experiment is needed. The magnetic flux density and the current can be measured. The effective area can be calculated and the enhancement factor can be read from Figure 2.15. Once the proportional factor K is known, it is possible to determine the current amplitude needed to achieve the desired magnetic pressure at the region of interest [20].

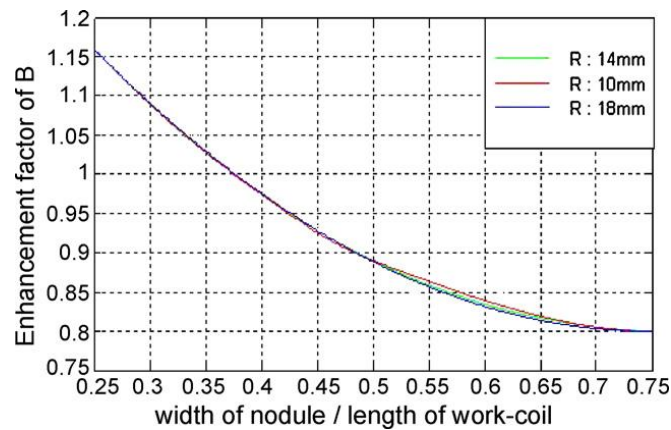


Figure 2.15: Enhancement factor of B for various field-shapers with three different internal radii of the coil or field shaper [20].

2.5 Connection mechanisms

Electromagnetic joining of tubular workpieces can be classified into three main categories, according to the dominating mechanism:

- ✓ **Interference fits:** the outer tube undergoes plastic deformation and the internal part deforms purely elastic. After forming is completed and the forces decrease, the internal part wants to return to its original shape (elastic relaxation) but is being restrained by the plastically deformed outer tube. As a result, interference stresses are generated between both joining partners.
- ✓ **Form fits:** an undercut (e.g. a groove) is applied in the internal part and the other tube is deformed into this undercut, thus creating mechanical interlock
- ✓ **Welded joints:** are attached on a micro-structural level.

For electromagnetic compression, interference and form fits are of importance. These will be discussed in detail in what follows.

2.5.1 Interference fits

The strength of interference fits strongly depends on 3 factors: remaining residual stresses in the contact zone, the friction coefficient and the area of the contact zone.

2.5.1.1 Remaining residual stresses in the contact zone

On the one hand, the remaining stresses depend on the material properties of both components being joined, more specific the strength as well as the stiffness.

It is favourable to use a internal part material of higher strength and stiffness than the tube material, because the elastic recovery of the internal part is higher, which leads to a higher radial reaction force and a higher pull-out load [9].

On the other hand, the remaining stresses also depend on the compression velocity. A higher velocity will lead to a higher kinetic energy at the time of impact, and the internal part will thus experience a higher impact force. A higher force will lead to a larger (elastic) compression of the

internal part, which increases the radial reaction force and therefore realises a higher pull-out load.

The compression velocity can be varied by changing the charging energy or by varying the initial gap between both joining partners. An increase of the charging energy will naturally result in an increase of the compression velocity. As for the initial gap: during the deformation process the velocity shows an acceleration and a deceleration part. By increasing the initial gap, the velocity will be higher. But it must be noted that when the initial gap is too large, it is possible that the tube will already decelerate significantly before the internal part is hit, and therefore the joint strength will be lower.

The influence of the charging energy and the initial gap on the residual stresses can be seen in Figure 2.16, which is the graphical representation of experiments performed on aluminum tubes and internal parts (the alloy of both of the components was EN AW-6060). The initial gap was varied (1, 1.5 and 2 mm) and also the charging energy (10% and 20% of the maximum energy of the device used for the experiments, equal to 32 kJ) [14].

It can be noted that the combination of an initial gap of 2 mm and 10% of the maximal charging energy of the machine leads to low residual stress values. This can be explained by the fact that the charging energy wasn't high enough to reach a complete constriction of the tubular component.

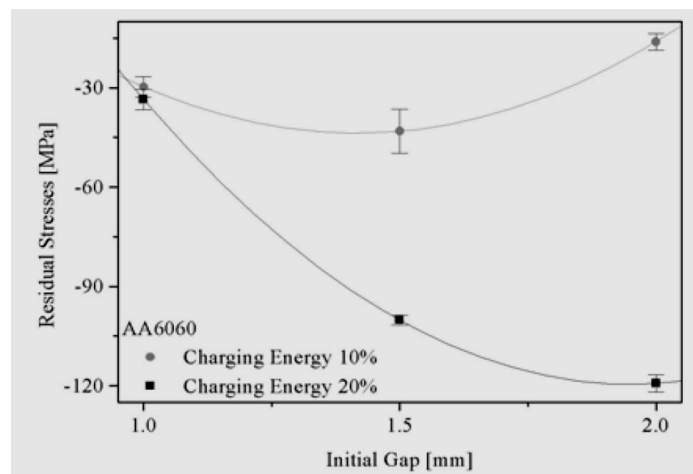


Figure 2.16: Influence of the charging energy and the initial gap on the residual stresses [14].

2.5.1.2 Friction coefficient between the outer tube and the internal part

The second factor which is of importance for the interference fit is the friction coefficient between the outer tube material and the internal part. There are two different types of friction coefficients: the static friction coefficient μ_s is the ratio between the friction force and the applied normal force when the surfaces are stationary and the dynamic friction coefficient μ_d is the ratio between the two when the surfaces are moving. Higher values for the friction coefficient will create a stronger interference fit. The failure mechanism of the joint determines which friction coefficient is of importance: if the tube gets pulled off the internal part, μ_d is of importance, otherwise it is μ_s which is of importance.

The value of the friction coefficient only depends on the two materials that are used. In Table 2.1, some values are given for combinations which are of importance for electromagnetic forming [3].

Correlating materials	μ_s	μ_d
Steel-steel	0.74	0.57
Aluminum - Aluminum	1.05-1.35	1.4
Aluminum-steel	0.61	0.47
Copper-steel	0.53	0.36

Table 2.1: Overview of friction coefficients for various material combinations [23].

2.5.1.3 Area of contact zone

The third factor which is of importance for the interference fit is the area of the contact zone. Two aspects are important: the roughness and the size of the contact zone.

An increasing roughness of the surfaces will lead to a micro form fit and a higher percentage of contact area in the joints and consequently higher pull-out forces. The internal part's surface can be treated, because it is easier accessible than the inside surface of the outer tube. Shot peening with glass beads and Al_2O_3 was investigated, as well as 5-axis milling [1]. The increase of the pull-out forces achieved with Al_2O_3 particles is much more pronounced than with the glass beads. This can be explained by the surface morphology after the shot peening operation. Peening with Al_2O_3 particles leads to a much more edged surface, which leads to better micro form fits and a higher percentage of contact area. Also, increasing the shot pressure at which the shot peening is done will lead to a higher pull-out load (see Figure 2.17).

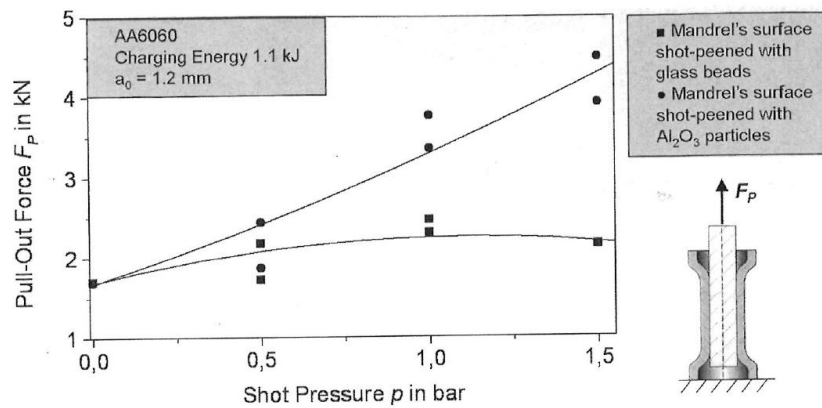


Figure 2.17: Influence of a treatment of the internal part surface on the pull-out force of the connection [9].

Preparing the surface of the internal part by milling is even more effective than shot peening, because a much larger range of roughness values is achievable (for shot peening the average roughness that can be obtained is $R_z=12\ \mu\text{m}$ to $R_z=18\ \mu\text{m}$, whereas the average roughness by milling can be up to $34\ \mu\text{m}$) The effect on the pull-out force is significant: there is a factor 2 difference.

A larger area will lead to stronger joints. For tubular joints, the diameter of the internal part and the length of the contact zone determine the size of the contact area. The diameter of the

internal part is in most cases a fixed parameter that is determined by the application, but the length of the contact zone (the overlap length) is a parameter which can be varied when designing connections. A large length is desirable, but of course a good balance needs to be found between increasing the length (leading to a higher pull-out force) and the higher cost involved (more material, larger machine, more energy). To estimate the expected pull-out force of a connection realised purely by the interference fit (no form fit is taken in account), the equation below can be used.

$$F = -\pi d l \sigma_{rad} \mu \quad (2.6)$$

With: F : expected pull-out force [N]
 d : internal part's diameter [mm]
 l : joining zone's length [mm]
 σ_{rad} : residual radial stresses [N/mm²]
 μ : friction coefficient [-]

To determine σ_{rad} , the x-ray diffraction method can be used. A detailed description of this technique can be found in [24].

It is important to know that the calculated pull-out loads will be much higher than the measured loads. This is because the calculations are performed assuming an ideal contact between tube and internal part. In [14] it was found that after microscopic inspecting that the real contact is far from perfect. Only in few zones direct contact could be determined and the remaining gap is not uniform around the circumference. In total, the remaining gap between the outer tube and the internal part after compression seems to be decreasing with decreasing initial gap and increasing charging energy [14].

The characteristic of force vs. displacement in tensile tests on interference fits has a typical shape, as can be seen in Figure 2.18. The force increases and then suddenly drops. After this, the tube starts to slip off the internal part and a "seizing effect" takes place: the tube takes off some material from the internal part and increases the contact surface between the tube and the internal part. Because of this, there is a continuous increase of the total contact surface and the pull-out force increases again until the outer tube is pulled off the internal part. So the ultimate failure does not occur abruptly and it is possible to optically detect this seizing effect, which is very positive with regards to safety measures (visual inspection).

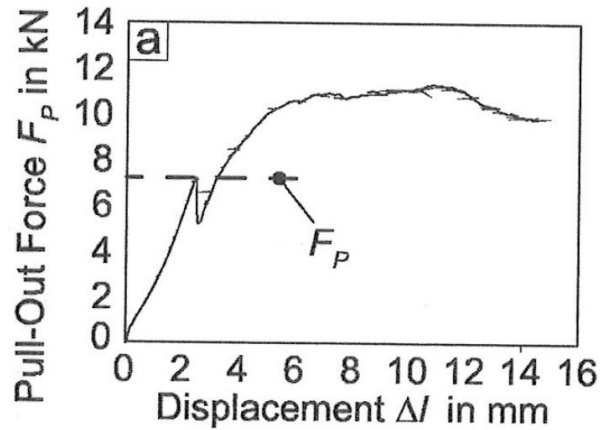


Figure 2.18: Typical characteristic for an interference fit [9].

Another positive effect of an interference fit developed by impact is that it eliminates the potential for fretting (=microscopic movements caused by deformations in the interference fit during the operation).

2.5.2 Form fits

To determine the best shape of the groove in the internal part, three options were investigated in detail in literature: triangular, circular and rectangular grooves (see Figure 2.19) [4].

Joints with triangular grooves are always the weakest. The explanation for this is that for triangular grooves the angle α (see the radioscopic images after deformation in Figure 2.19) is greater than for rectangular or circular grooves. This results in a lower degree of deformation at the groove edge, and thus a smaller tensile force is required to initiate pull-out of the tube from the groove.

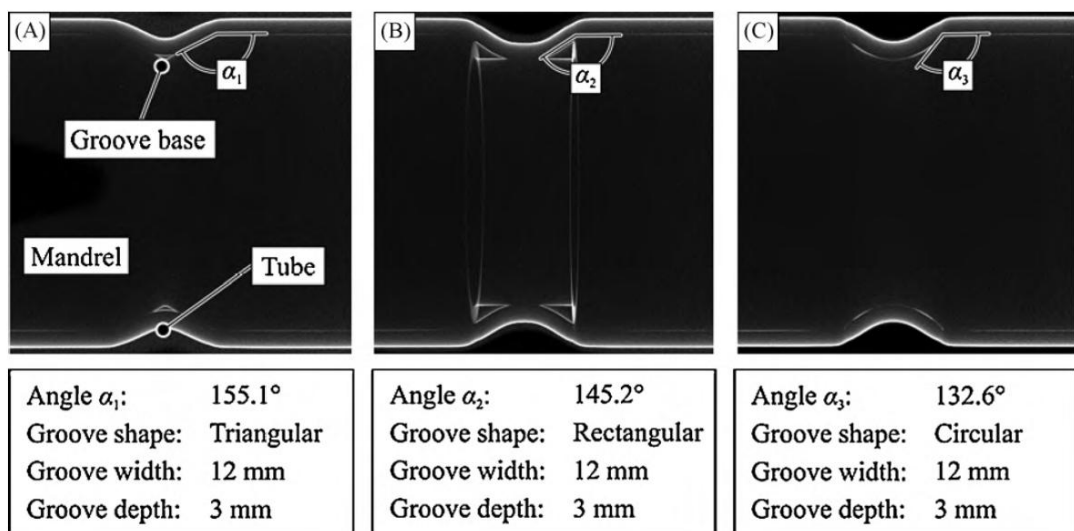


Figure 2.19: Radioscopic images after deformation [13].

The circular grooves have a smaller resulting angle α than the rectangular, but the rectangular grooves still have a larger pull-out force because of the larger amount of shearing of the tube into the rectangular groove. This better locks the tube in place.

Joints formed with rectangular grooves will always exhibit the highest joint strength, which was experimentally verified [13].

The strength of the rectangular groove of form fits strongly depends on three factors which determine the groove geometry: its depth and width and the radius at the groove edges (see Figure 2.20).

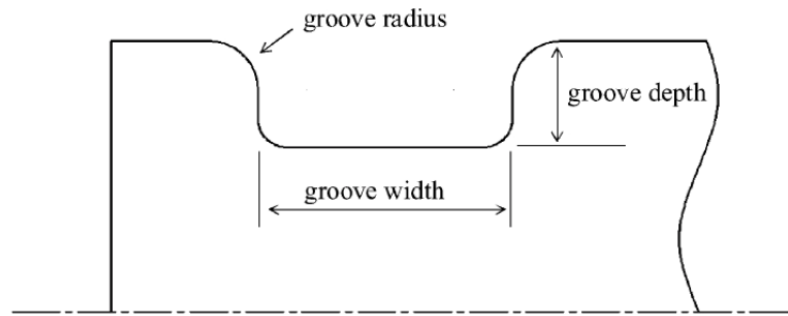


Figure 2.20: The three parameters which determine the groove geometry for a rectangular groove [25].

Deeper grooves will lead to higher joint strengths [26-27], but increasing the groove depth too much leads to a decrease in strength as a result of intense shearing at the groove edges during forming [28].

For the groove width, it was first believed that a narrower groove would lead to higher joint strengths [26-27], but this was later revised because an increasing groove width leads to a larger contact area at the groove base, which leads to a larger interference fit and a stronger joint strength. Again, it may not be increased too much, because this could lead to wrinkling which has a negative effect on the joint strength [28]. Furthermore an economical factor comes into play here, because a larger width requires more overlap (more material) and a higher energy.

A smaller edge radius leads to a higher joint strength, but a too small radius leads to an increase of shearing at the groove edge during forming and negatively affects the joint strength [28].

To find the proper magnetic pressure which is required to fill a groove, a combination of an analytical model and experimental data can be used. The methodology will be explained below.

In the first part of the methodology, the analytical model is used to determine the minimum magnetic pressure required to initiate plastic deformation of a tube into a groove, based on assumptions of ideal plastic material behaviour and plain strain [29].

The bending moment M_b at the groove edge (see Figure 2.21) is described by:

$$M_b = \frac{w}{12} (p_{min} \cdot R \cdot d\beta \cdot w - 2 \cdot \sigma_t \cdot s \cdot w \cdot \frac{d\beta}{2}) \quad (2.7)$$

With: M_b : bending moment at the groove edge [N.mm]
 w : groove width [mm]
 p_{min} : minimum magnetic pressure [N/mm²]
 R : inside radius of the tube [mm]
 s : wall thickness of the tube [mm]
 σ_t : principal tube stress in tangential direction [N/mm²]

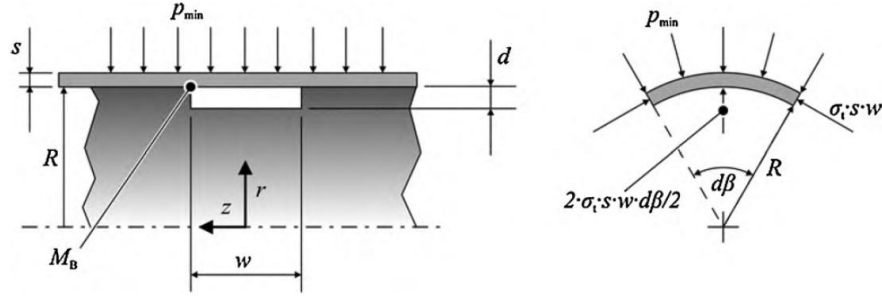


Figure 2.21: Geometrical model to determine the bending moment at the groove edge [13].

This equation can be simplified using the Tresca yield criterion. It can be assumed that the principal stress in the radial direction is significantly lower than the principal stress in the tangential direction. Therefore σ_r can be set to zero and σ_t can be approximated as the tube yield strength σ_y . This assumption is justified because the outer tube can be considered thin-walled [9] which leads to the equation below.

$$M_b = \frac{w^2}{12} \cdot R \cdot d\beta \cdot \left(p_{min} - \sigma_y \cdot \frac{s}{R} \right) \quad (2.8)$$

Under the consideration of ideal plastic material behaviour and pure bending, a second equation for the bending moment required for the onset of plastic deformation is found [8]:

$$M_b = \frac{3}{2} \cdot R \cdot d\beta \cdot \sigma_y \cdot \frac{s^2}{6} \quad (2.9)$$

By now combining the two equations above and solving for p_{min} , the expression below is found.

$$p_{min} = \sigma_y \left[3 \cdot \left(\frac{s}{w} \right)^2 + \frac{s}{R} \right] \quad (2.10)$$

The expression for p_{min} generates an approximate starting point for the second step in the methodology: using experimental optimisation to determine the exact magnetic pressure that is required to fill a groove of any desired dimensions.

The experimental data were obtained by inserting two greased steel cylinders inside the outer tube instead of the internal part [13]. The cylinders were connected in such a way that they could

be separated at a desired distance, thus creating the possibility to test for any groove width. For a certain groove width, the magnetic pressure was varied and the corresponding depth was measured.

For each gap width, the necessary magnetic pressure increases linearly with the groove depth. It is therefore possible to measure a discrete amount of points and fit a (linear) regression curve through these points, hence creating a graph from which the necessary magnetic pressure for any groove depth can be read. An example of such a graph can be seen in Figure 2.22. From Figure 2.22, it can also be noted that the analytically calculated values for p_{min} are a lot smaller than the values that could be derived from the experimental results. This is due to the simplifications and assumptions that are used in the analytical model (ideal plastic material behaviour and plain strain, $\sigma_r=0$, pure bending). The usability of the analytical calculation can therefore be questioned.

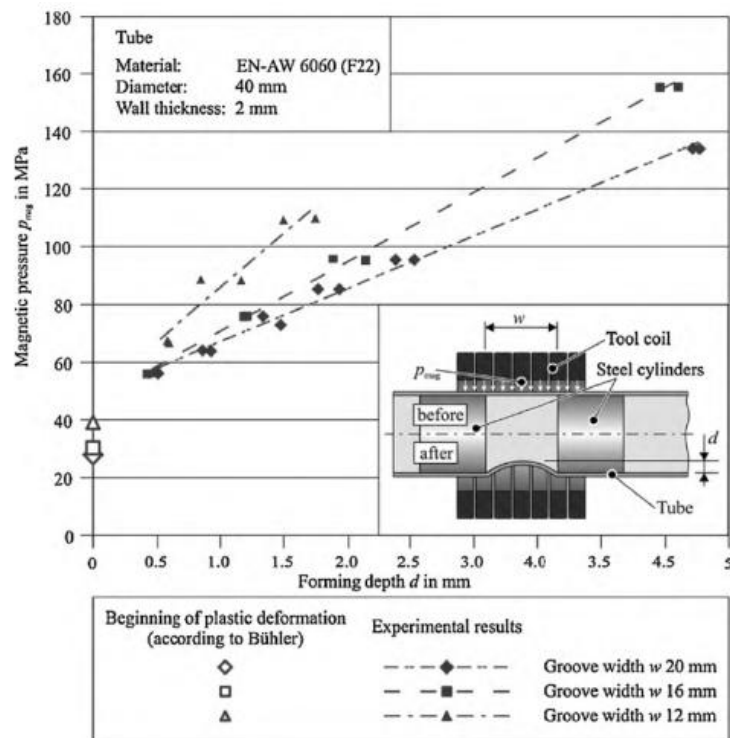


Figure 2.22: Magnetic pressure as a function of the groove depth [13].

Also, additional grooves in the joining zone could significantly increase the strength of a form-fit connection [13]. This statement was confirmed by some preliminary experiments performed in a preceding thesis, where a geometry with 2 grooves was tested for joining steel parts [10].

2.6 Conclusions

The general principle of the electromagnetic pulse process was studied. It is important to know that the frequency must be high enough when using hollow outer workpieces, so that the skin depth is smaller than the wall thickness of the outer tube, and the process is used in an efficient

way. It was observed that the magnetic pressure has a sinusoidal distribution in time and that almost all of the deformation occurs during the first peak, which only takes about 20 μ s.

Advantages and disadvantages and limitations of the EMP forming process were discussed.

When using a multi-turn coil, a field shaper can be used to focus the widely spread current from many windings onto a small work-zone. Field shapers prolong the life of a coil and can easily increase the magnetic pressure by a factor 2 or more.

Considerations on the designs of field shapers were made.

The connection mechanisms for crimp joints that are of importance are an interference fit and a form fit. A stronger interference fit is realised when the internal part material has a higher strength and stiffness than the tube material. A higher charging energy and a larger initial gap will lead to a higher compression velocity and this will also create a stronger interference fit. Of course the friction coefficient between the two materials which are joined is of importance. A last factor which determines the strength of the interference fit is the area of the contact zone: a larger and rougher contact zone will lead to a stronger interference fit.

It was noted that an interference fit developed by impact eliminates the potential for fretting.

For the form fit, it was concluded that rectangular grooves will exhibit the highest joint strength. The form fit will be stronger when the groove edge radius is small, the groove depth is deep and the groove width is large.

Additional grooves in the joining zone could significantly increase the strength of a form-fit connection.

Equations to determine the (minimal needed) magnetic pressure and to estimate the pull-out force realised purely by an interference fit were derived. However these equations do not take the effect of a field shaper into account and they result in values which vary significantly from experimental values. Therefore, more fundamental research seems commendable. This should then allow to determine more precise equations.

Chapter 3: Industrial case study

3.1 Introduction

The electromagnetic crimping process can be used for several applications. Some diverse examples are: an automotive steering axle coupling (Figure 3.1.A), high voltage fuses, lighting reflectors, munitions (Figure 3.1.B), shock absorbers, water separators, aluminum on a plastic medical inhaler (Figure 3.1.C), etc.



Figure 3.1: Some industrial applications where electromagnetic pulse crimping is used [31].

To get acquainted with the electromagnetic pulse crimp process, an industrial case study was performed. Due to strict confidentiality, it will not be mentioned for which company nor which application the following design is intended.

The axial crimp joint design studied in this chapter is a steel to steel joint based on a single groove design. At the moment, the connection between the steel internal workpiece and the steel outer tube is made using a welding technique. However, an electromagnetic pulse crimping operation could be a cleaner and more reliable alternative.

The groove design can vary but needs to satisfy certain constraints regarding dimensions. The crimp joints need to deliver a certain axial load during application. Therefore, the joined specimens will be tensile tested. Also, the eccentricity needs to be tested.

3.2 Experimental data

3.2.1 Materials

The tube material is the free-cutting steel 11SMn30K. This steel has a lot of S (sulphur) and P (phosphor), for good machinability. Because of these high concentrations of S and P, they are generally not recommended for welding. Table 3.1 lists some physical and mechanical properties of 11SMn30.

Physical properties			Mechanical properties			
Density	Electrical conductivity	Thermal conductivity	Elasticity modulus	Shear modulus	Tensile strength	Proof stress $R_{p0.2}$
$[g/cm^3]$	$[MS/m]$	$[W/(m.K)]$	$[GPa]$	$[GPa]$	$[MPa]$	$[MPa]$
7.85	5.56	47	207	79.6	360-570	245-440

Table 3.1: Properties of 11SMn30 at 20°C [32].

To enable shielding of the magnetic field, a certain thickness of the tube material is required. The efficiency of the shielding phenomenon is linked to the skin depth of the material. The skin depth can be calculated as follows:

$$\delta = \sqrt{\frac{1}{\pi f \sigma \mu}} \quad (3.1)$$

With: f : frequency of the current [Hz]
 σ : conductivity of conductor [S/m]
 μ : absolute magnetic permeability of the conductor [H/m]

For the free-cutting steel used in these experiments, a magnetic permeability (μ) of 8.75×10^{-4} H/m is expected. The frequency f of the current in the multi turn coil can be calculated using the measured curve of current versus time from Figure 3.2. The frequency of the first pulse (this is the pulse where the deformation occurs) is independent of the charging voltage level and is equal to 13.6 kHz for the multi-turn coil used in these experiments.

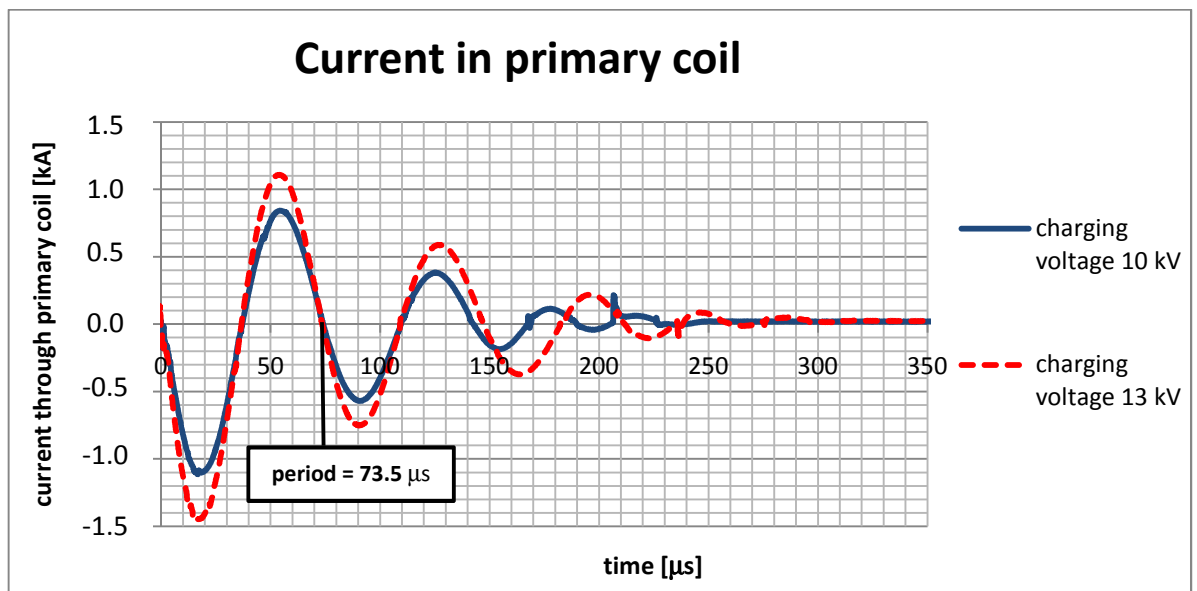


Figure 3.2: Current in the multiturn coil for a charging voltage of 13 kV.

The skin depth is:

$$\delta = \sqrt{\frac{1}{\pi \cdot (13.6 \cdot 10^3) \cdot (5.56 \cdot 10^6) \cdot (8.75 \cdot 10^{-4})}} = 6.9 \cdot 10^{-5} \quad (3.2)$$

This means that at a depth of 69 μm below the outer surface of the tube, the current density has decayed to 1/e of the current density at the surface. If the thickness of the tube equals two times the skin depth, already 98% of the magnetic field is shielded and there will be almost no loss of magnetic pressure [33]. In this case study, the tube wall thickness was 1.5 mm.

The material of the internal workpiece is a plain carbon steel.

3.2.2 Test setup

Figure 3.3 shows a scheme of the set up. An electric insulating Ertalon support part (4) is used to support and position the tube (2). Ertalon 6 SA is favourable for general applications where mechanical stiffness, wear resistance, electrical insulation and good chemical resistance is required. This material is used for insulation and positioning of the workpiece at the same time. Also the two insulating flanges (10) are made of Ertalon 6 SA. The tube to be deformed (2) is positioned around the inner workpiece (1) with a small press fit.

The internal workpiece (1), the tube to be deformed (2) and the support (4) are inserted from the right side into the machine.

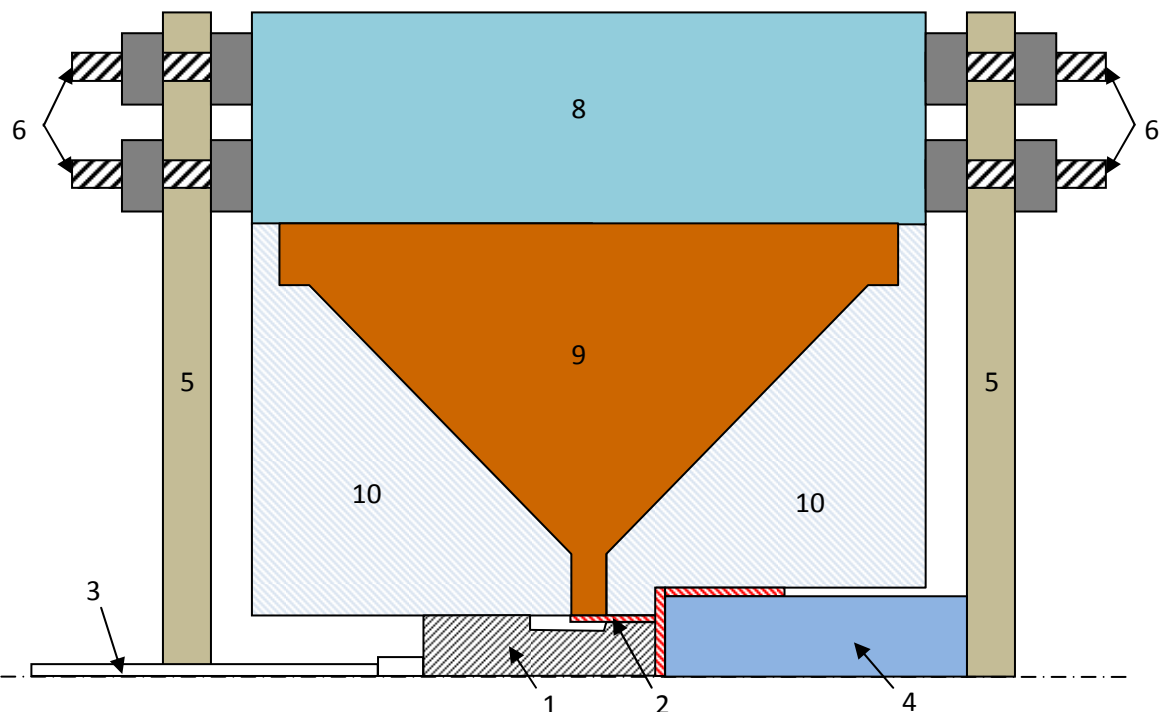


Figure 3.3: Schematic overview of the set-up.

A polymer side bar (5) on the right side is used to lock the workpieces axially. This polymer bar can be attached by using screws (6). Component (8) is the primary coil. The field shaper (9) is

isolated on both sides by two flanges, which also serve for positioning of the tubular workpieces. Note that the internal workpiece is still able to move axially to the left side after insertion. A round bar (3), supported by the left polymer side bar prevents movement of the internal workpiece and assures that the internal workpiece is correctly positioned.

3.2.3 Field shaper

A CuBe_2 field shaper with internal diameter of 18 mm and an internal axial length of 15 mm was used. The technical drawing of this field shaper can be found in Appendix B. Copper-Beryllium is a high performance alloy, used in applications requiring strength, fatigue resistance, non-magnetic properties, conductivity and corrosion resistance. Some properties of the alloy are listed in Table 3.2.

Physical properties			Mechanical properties			
Density	Electrical conductivity	Thermal conductivity	Elasticity modulus	Shear modulus	Tensile strength	Proof stress $R_{p0.2}$
$[\text{g}/\text{cm}^3]$	$[\text{MS}/\text{m}]$	$[\text{W}/(\text{m}\cdot\text{K})]$	$[\text{GPa}]$	$[\text{GPa}]$	$[\text{MPa}]$	$[\text{MPa}]$
8.36	25-32	92-125	131	51	1130-1520	890-1380

Table 3.2: Properties of CuBe_2 at 20°C [34].

3.3 Measurement methods

Four test series were performed. Every sample will either be subjected to a tensile test, either be measured for eccentricity evaluation, or will be cross sectioned to gain information about the deformation behaviour.



Figure 3.4: Amstler universal testing machine in Laboratory Soete [35].

All tensile tests were performed on the Amsler universal testing machine (Figure 3.4). The Amsler universal testing machine has a maximum force of 600 kN (\approx 60 tonnes) in both compression and tension. A spring with capacity 120 kN was used for these test series.

The downward movement of the lower part of the universal testing machine is measured using a linear variable differential transformer (LVDT). The tensile force is also recorded and force versus displacement curves are generated.

After cross sections were made, a microscopic image was taken of some samples. All microscopic pictures discussed in this work have been made with a binocular microscope Carl Zeiss Discovery.V12 with a minimal magnification of 5x and a maximal magnification of 100x (see Figure 3.5).



Figure 3.5: Carl Zeiss Discovery.V12 microscope.

The eccentricity will be measured by clamping the specimen on a lathe. During rotation, a dial test indicator will measure the eccentricity.

3.4 Results and discussion

The internal workpiece is a rod with an outer diameter equal to 15.8 mm. Figure 3.6 clarifies the setup and indicates the three parameters that will be varied during the experiments: overlap length of field shaper and tube, overlap length of tube and internal workpiece, and the length of the rod end. The blue part between the field shaper and the workpiece indicates a small isolation tube (wall thickness: 1 mm) to prevent direct contact of the field shaper and the workpiece.

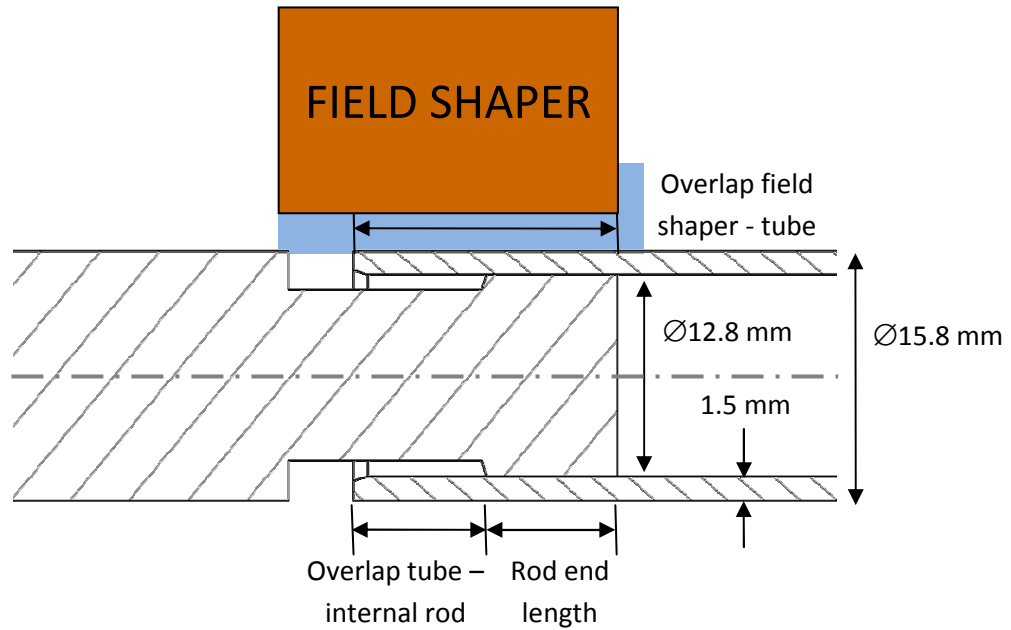


Figure 3.6: Nomenclature and general dimensions of the samples.

Four crimp test series were performed. For the first test series, the charging voltage of the machine was determined to create an axial crimp joint with a clear deformation of the tube into the groove. In the other test series, each sample was made three times, to investigate the repeatability of the process.

The charging voltage for the first sample was set at 10 kV. Visual inspection revealed that there was hardly any deformation, so the charging voltage was increased to 15 kV in a second sample. The tube was deformed but there was still a clearance between the internal workpiece's groove bottom and the deformed tube. Following, the maximum charging voltage of the Pulsar machine (19 kV) was used to obtain a satisfactory result. Additional experiments at three distinct charging voltages between 15 kV and 19 kV were performed. Table 3.3 gives an overview of all performed experiments and the corresponding parameters. The parameter values that have been changed in every test series are indicated in red. The table also lists the evaluation methods and the available results of the tensile tests.

The evaluation by the company is still in process and not all results are known at the time of writing this thesis, so it is not yet possible to formulate clear conclusions. However, some conclusions can be drawn. First, it should be mentioned that the maximum charging voltage was required to create sufficient deformation of the tube into the groove. The high energy input will result in a higher operating cost than for a workpiece with a higher electrical conductivity. It might be appropriate to choose a more conducting material for the tube, if that would be allowed by the application of course. Also, increasing the work pieces' diameter, allows the tube to deform more easily under a certain pressure.

Series	Sample number	Charging voltage [kV]	Overlap field shaper - tube [mm]	Overlap tube - internal rod [mm]	Rod end length [mm]	Investigation method	Axial tensile load [kN]
1	1	15	15	10	10	Eccentricity + tensile test	
	2	16	15	10	10	Eccentricity + tensile test	
	3	17	15	10	10	Eccentricity + tensile test	
	4	18	15	10	10	Eccentricity + tensile test	
	5	19	15	10	10	Eccentricity + tensile test	
	6	19	15	10	10	Tensile test	30.7
	7	19	10	10	10	Tensile test	33.3
2	8	19	10	5	10	Eccentricity + cross section	
	9	19	10	5	10	Eccentricity + tensile test	
	10	19	10	5	10	Eccentricity + tensile test	
3	11	19	8	3	10	Eccentricity + cross section	
	12	19	8	3	10	Eccentricity + tensile test	
	13	19	8	3	10	Eccentricity + tensile test	
4	14	19	8.5	5	5	Cross section	25.8
	15	19	8.5	5	5	Tensile test	
	16	19	8.5	5	5	Tensile test	

Table 3.3: Overview of test parameters and evaluation methods used for the industrial case study.

It can be observed that reducing the overlap length of the field shaper and the tube increased the strength of the joint from 30.7 kN (sample 6) to 33.3 kN (sample 7). The difference in joint strength is not very large (only 8.5%) and this can be attributed to scatter of the crimping process, clamping into the testing machine,... The decrease in overlap of the field shaper and the tube does have an influence on the area of the tube subjected to magnetic pressure. In this case, it does not matter if the field shaper covers 15 mm or only 5 mm of the tube, as long as it covers the whole area of the tube that can deform into the groove (this area is indicated by the overlap of the tube and the internal rod). The internal axial length of the field shaper is 20 mm, and in samples 6 and 7 the field shaper will cover the whole length of the tube to be deformed into the groove. This is also the case in test series 4, but now the overlap of the tube and the internal rod is smaller. A smaller volume of the tube was deformed into the groove and therefore, a lower tensile strength (25.8 kN) is measured in sample 15. Thus, it is believed that the larger the overlap of the tube and the internal rod will be, the more tube material will deform into the groove and the higher the tensile strength will be.

The minimum requirement of strength for this application was 35 kN. None of the 3 tested samples matched this requirement. It might be appropriate to use a double groove design in order to match the requirement. Also, the eccentricity was found to be insufficient for this application as well. To create a joint with better eccentricity, a larger tube and rod can be used to create more supporting surface.

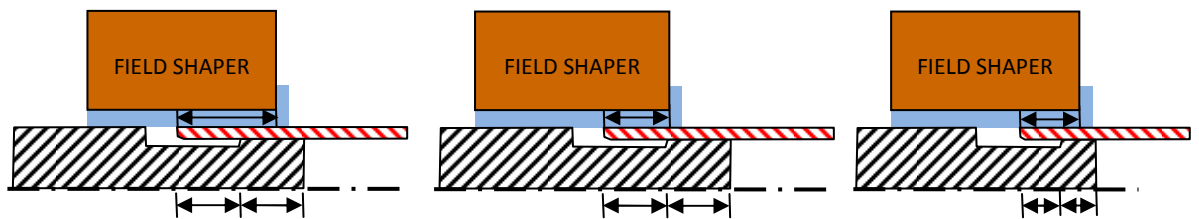


Figure 3.7: Schematic view of samples 6, 7 and 15.

The samples of test series 1 differ in failure mechanism from the sample in test series 4. Figure 3.8 and Figure 3.9 show the failed joint of sample 6 and sample 15 respectively. In the first tensile test series, the tube suddenly tore at the groove's edge, while in the fourth tensile test series the tube was pulled out of the internal rod. Because a smaller area of the tube could only be deformed during the crimping process of sample 15, compared to sample 6 and 7, it is more likely to pull the small volume of tube material out of the groove than to shear at the edge. As a natural consequence of the radial pressure working on the tube during its sliding, 4 cracks are formed in the tube, mutually spaced by an angle of 90 degrees.



Figure 3.8: Failed axial crimp joint (sample 6).



Figure 3.9: Failed axial crimp joint (sample 15).

When looking at the cross section of sample 15 in Figure 3.10, local shearing of the tube at the sharp groove edge is noticed. This results in a local decrease of the tube wall thickness. In the following text, tube wall reduction is denoted as “necking”. If a large amount of necking occurs, the crimp joint fails at the edge of the groove (like in sample 6 and 7). Extensive necking can finally lead to cutting the tube, and this concept is used for the electromagnetic punching process [10]. No cross section view is available from sample 6 or 7, but it is expected that the amount of tube wall reduction is larger than in sample 15.

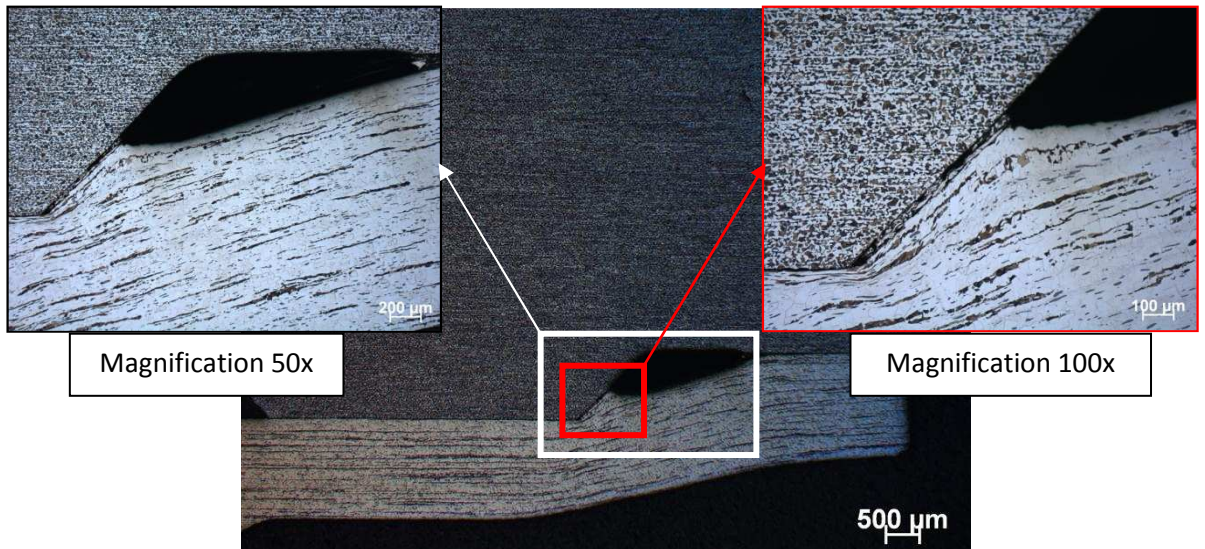


Figure 3.10: Cross section of the deformed tube of sample 15.

3.5 Conclusion

With a limited amount of experiments and results, some general conclusions can be drawn.

First, it is a challenge to determine the appropriate charging voltage that will ensure an optimal deformation of the tube into the groove. If the voltage level is set too low, the tube will almost not deform into the groove. If the voltage level is set too high, the amount of necking will increase, and the groove edge might cut the tube. In the next chapter, the relation between the applied charging voltage and the tube deformation will be investigated.

It is not beneficiary to always crimp a joint at the maximum charging voltage of the machine. In order to get equal deformation for a lower charging voltage and thus lower energy input, the tube material should be more electrically conducting. Another possibility is to increase the diameter of the workpieces, so the tube will deform more easily.

The overlap of the tube and the internal rod determines the amount of tube material to be deformed. When more tube material deforms into the groove, a larger tensile strength is expected.

During the crimping process, the tube material shears off at the groove edge. This shearing off will be greater for grooves with sharper edges. Also, this means that there is a locally decreased tube wall thickness. The phenomenon of tube wall reduction is called necking. It should be investigated to quantify in advance what the amount of necking will be for a certain groove design. This will be done in the next chapter.

When a tensile test is preformed on the axial crimp joint, the tube can fail by shearing in the groove edge zone or by pulling off.

Chapter 4: Free deformation experiments

4.1 Introduction

During the industrial case study, it was observed that it is a challenge to determine the appropriate capacity charging voltage to be used for a given groove design. If the voltage level is set too low, the tube will not deform into the groove and the connection will hardly have any strength. On the other hand, if the voltage level is set too high, the tube will deform too much into the groove, necking at the groove edges will become too severe and the internal workpiece will act as a cutting tool. Therefore it would be helpful to have graphs which, for a certain groove design, link the radial inward tube displacement and necking occurring at the groove edges with the applied voltage. This would provide a first estimate of the magnitude of the charging voltage level to be applied.

The same graphs can be used to make a decision about the optimal groove design when a certain voltage level is used. For economical reasons, it is beneficial to minimize the charging voltage. A lower applied voltage means less use of electricity, a less powerful and therefore cheaper machine, the capacitor bank can be charged to a lower energy level and the process will be shorter, etc.

Also, these graphs are a great source of information to build and verify finite element models. They provide the basic information (necking and radial inward displacement of the deformed tube) which need to be known to build up a finite element model to predict the tensile load capacity of a crimp joint. The information can also be used for model validation (comparison of experimental data with the modelled results).

In order to be able to generate these graphs with low material resources and with a low processing and evaluation time, a test setup inspired on [13] was designed and built. The system offers the flexibility to simulate a large amount of grooves, without manufacturing an internal workpiece for every test condition. More details about the test setup can be found below.

4.2 Material properties

The experiments discussed in this and following chapters were performed with aluminum tubes EN AW-6060 with a wall thickness of 1.5 mm and an outer diameter of 50 mm. The tubes are extruded material with a temper designation T6 (precipitation hardened). Some properties of the alloy are listed in Table 4.1.

The reason for this choice is that this aluminum alloy is nowadays used in a lot of industrial applications. Typical areas of application are railings and heating and cooling pipes. Also,

aluminum is more and more used in several other industrial sectors: transportation, manufacturing of machines and equipment, electronics, etc. [36]

Physical properties			Mechanical properties			
Density	Electrical conductivity	Thermal conductivity	Elasticity modulus	Shear modulus	Tensile strength	Proof stress $R_{p0,2}$
$[g/cm^3]$	$[MS/m]$	$[W/(m.K)]$	$[GPa]$	$[GPa]$	$[MPa]$	$[MPa]$
2.7	34-38	200-220	69.5	26.1	min. 190	min. 150

Table 4.1: Properties of EN AW-6060 T6 at 20°C [37].

The main problems in forming operations of aluminum which prevent even further application growth are tearing of the material, wrinkling and springback. A minimum amount of stretch is necessary to eliminate wrinkling and reduce springback to acceptable limits. But, stretching the material beyond a limit could cause tearing. A metal forming operation is limited by tearing (or necking) on the one hand and wrinkling and springback on the other hand. Especially for aluminum the parameter window is rather small.

By using a high speed forming process, the material behaviour is completely different than in conventional forming processes. Electromagnetic forming tends to increase formability [10,15].

The choice for aluminum also allows to perform experiments with larger diameter tubes and still use lower charging voltages than experiments performed with steel (see chapter 3). The reason is the better electrical conductivity of aluminum, which causes a more efficient process due to the smaller skin depth as compared to steels. The lower yield stress allows a lower charging voltage and consequently implies a decrease in the reaction forces on the field shaper, resulting in a longer lifetime.

The skin depth of the aluminum can be calculated with equation (3.1). A magnetic permeability of $1.26 \mu H/m$ is expected. The skin depth becomes:

$$\delta = \sqrt{\frac{1}{\pi \cdot (13.6 \cdot 10^3) \cdot (36 \cdot 10^6) \cdot (1.26 \cdot 10^{-6})}} = 7.18 \cdot 10^{-4} \quad (4.1)$$

This means that at a depth of $718 \mu m$ (or $0.7 mm$) the current density has decayed to $1/e$ of the current density at the surface. Because the tube wall thickness ($1.5 mm$) equals 2 times the skin depth, 98% of the magnetic field is shielded and thus there will be not much loss in magnetic pressure.

4.3 Experimental test setup

The individual components of the test setup are shown in Figure 4.1: two steel cylinders S235 with an internal screw thread, two steel threaded rods S235 and some metal rings without internal screw thread. It should be noted that the outer diameter of the metal rings should be small enough, in order not to interfere with the inward deformation of the tube (cfr. 'free deformation').



Figure 4.1: Components required for the test setup.



Figure 4.2: First (left) cylinder and positioning rings placed on the threaded rod.

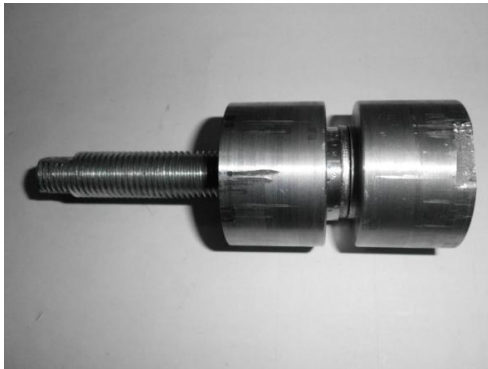


Figure 4.3: Second (right) cylinder screwed onto the threaded rod.



Figure 4.4: Aluminum tube is positioned over the cylinder system.

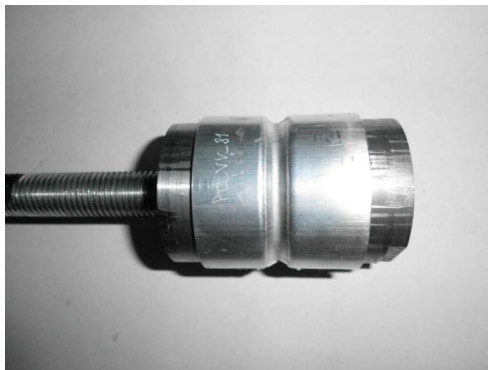


Figure 4.5: Crimping action is performed.

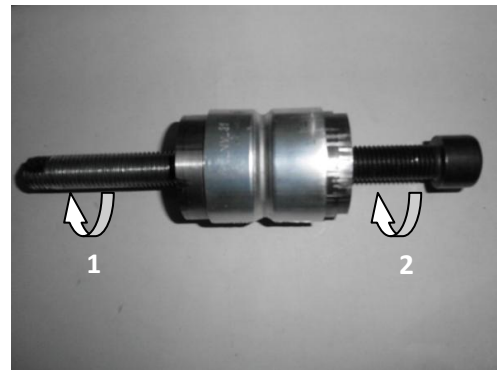


Figure 4.6: 1. The first (left) rod is screwed out until its end is in the middle between the two cylinders, 2. The second (right) rod is screwed into the second cylinder until its end touches the end of the first rod.

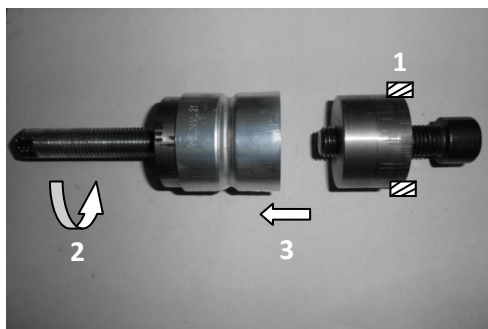


Figure 4.7: 1. The second cylinder is clamped in a bank screw, 2. The first rod is turned further into the first cylinder again, 3. The second cylinder is pushed out of the deformed tube.



Figure 4.8: The first cylinder can now be pushed out of the deformed tube.

The first cylinder is screwed onto the rod, the correct number of metal rings are placed over the rod in order to obtain the chosen axial length of the simulated groove. Then the second cylinder is screwed onto the rod (see Figure 4.2 and Figure 4.3).

Subsequently, an aluminum tube with an axial length of 50 mm is positioned over the two cylinders. This combination is then placed in the machine and the crimping operation is performed. A typical result can be seen in Figure 4.5. In order to be able to separate the deformed tube and the cylinder system, the second rod is required. The disassembly process is illustrated in Figures 6 to 8.

The isolated deformed tube shown in Figure 4.9, will be subjected to dimensional control measurements, as will be discussed in the next section.



Figure 4.9: The resulting deformed tube.

4.4 Positioning

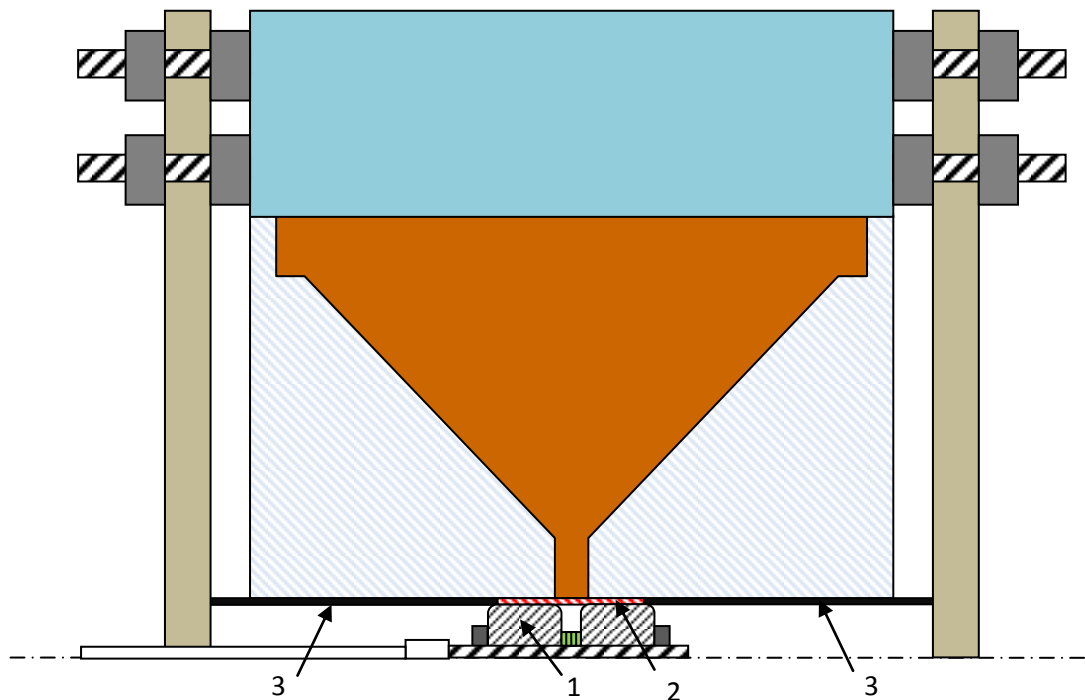


Figure 4.10: Positioning of the cylinder system inside the machine.

The set up for positioning is the same as explained in the previous chapter, see Figure 4.10. However, for this set of experiments, the tube to be deformed (2) is hold in place by using two extra positioning tubes (3). Positioning of the cylinder system (1) was performed by measurements with a micrometer gauge. An accuracy of 0.1 mm was obtained. The reason for measuring instead of using an insert is that experiments were done on different groove widths and this avoided the need to design several polymer inserts with different lengths.

4.5 Test matrix and measurement methods

The 3 parameters which were varied during the experiments are the groove edge radius, the groove width and the applied voltage. The groove edge radius was set at 0.5 mm, 1 mm and 1.5 mm. For each of these three groove radii, a pair of cylinders was manufactured to be used in the test setup. The groove width was varied between 6 and 14 mm, with a 2 mm interval. It was observed that 5 kN was the minimum charging voltage needed to deform the tube. Therefore this charging voltage was set as the lower value. The maximum voltage that could be applied without cutting the tube varied between 10 and 13 kV, depending on the combination of the previous 2 parameters.

Some of the experiments were repeated, in order to verify the scatter on the results. This resulted in a test matrix with 132 experiments. An overview can be found in Appendix C. The tensile strength and the leakproofness are very important evaluation parameters for axial crimp joint applications. For both of these, information can be extracted from the free deformation experiments by measuring the radial inward tube displacement and the wall thickness reduction at the edges of the deformed tube.

The radial inward displacement of the tube into the groove is measured by using an internal micrometer (see Figure 4.11).



Figure 4.11: Internal micrometer [38].

Analysing the relationship between the applied charging voltage and the radial inward tube displacement, allows to predict the minimal voltage required for the tube to touch the groove bottom. This is important for the leak tightness: when the tube touches the groove bottom, there are three areas of contact between the tube and the internal workpiece instead of two, making it more difficult for fluids to leak (see Figure 4.13). For further considerations concerning the leakproofness of the crimp joints, the reader is referred to chapter 8.



Figure 4.12: The leakproofness of the crimp joint is improved when the tube touches the bottom of the groove.

Besides the leakproofness, it is also beneficial for strength considerations to know the minimal required voltage for making the tube touch the bottom. Applying a voltage larger than this minimal voltage will cause the tube to deform as shown in Figure 4.14 on the right. The tube has a larger contact area with the bottom of the groove, which creates a stronger interference fit. Also, the angle θ is smaller, which means that a stronger mechanical interlock behind the corner of the groove is realised.

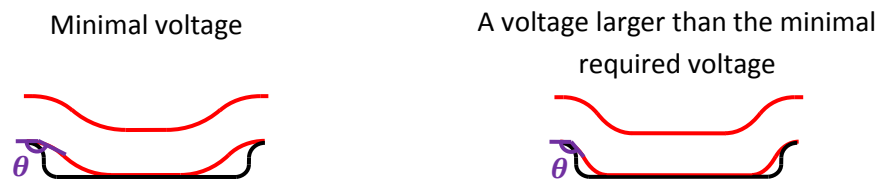


Figure 4.13: A larger voltage creates a stronger interference fit and a stronger mechanical interlock.

As will be demonstrated in chapters 5 and 6, mechanical interlock behind the groove edge is the most important strengthening mechanism for the crimp joint. It is therefore important to be able to estimate the thinning of the tube at the edge of the groove. Each of the deformed tubes was cross-sectioned and the tube wall thickness was measured at four locations: the 2 upper edges and the 2 lower edges. Figure 4.14 is referred to for an example of the measurements at the 2 upper edges. The average of these four values was determined in order to exclude measurement inaccuracies, possible local material impurities or influence of the radial cut of the field shaper on the deformation (see further).

To exclude the scatter on the tube wall thickness of the used aluminum tubes as much as possible, the tube wall thickness of the undeformed material was measured and the average was calculated. The ratio of the tube wall thickness at the edges (the tube thinning) relative to the average measured wall thickness was calculated and compared.

Also, the radial inward displacement of the inside tube wall was measured (as a verification for the measurements performed with the micrometer), as well as the thickness of the tube at the maximum inward displacement.

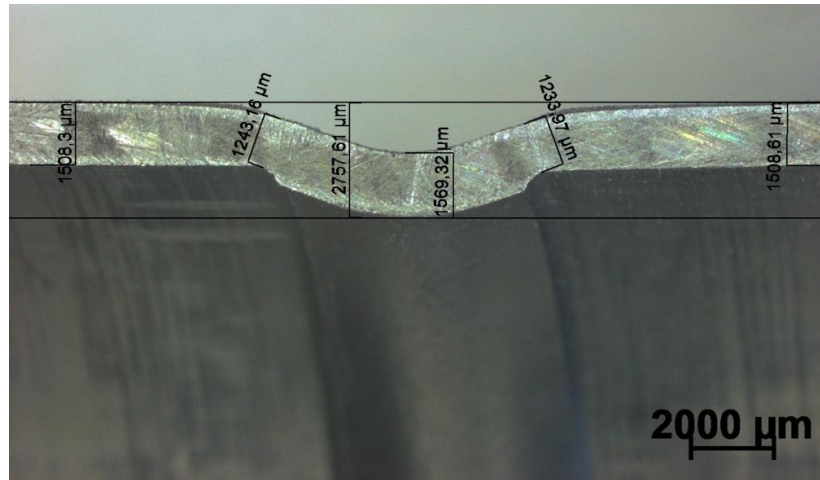


Figure 4.14: Microscopic measurement of the wall thickness reduction at the edges of the upper half of a cross sectioned deformed tube.

4.6 Results and discussion

There are three input parameters (the groove edge radius, the width of the groove and the charging voltage) and two evaluation parameters (the radial inward tube displacement and the necking at the groove edge). The groove edge radius was held constant in every graph. This resulted in six graphs in both 2D and 3D: three graphs that show the radial inward displacement as a function of the groove width and the voltage, and three graphs showing the necking as a function of the groove width and the voltage.

For each of the 3D-graphs, the equation of the surface was determined. These equations can be a very useful tools, because they link the input parameters with the evaluation parameter. They provide the opportunity to get a first estimate of an evaluation parameter for a certain input, or to get an estimate of which input parameter combinations can be used when a certain value for an evaluation parameter is premised.

However, the reader must keep in mind that this is the equation of a fitted surface determined by using a 4th degree-polynomial fit in both the x- and y-direction (with x-axis = groove width and y = voltage) through a discrete set of measured points (25 for every graph).

The general form of the equation of the fitted surface is:

$$f(x, y) = C1 + C2 * x + C3 * y + C4 * x^2 + C5 * x * y + C6 * y^2 + C7 * x^3 + C8 * x^2 * y + C9 * x * y^2 + C10 * y^3 + C11 * x^4 + C12 * x^3 * y + C13 * x^2 * y^2 + C14 * x * y^3 + C15 * y^4$$

With x : groove width [mm]

y : charging voltage [kV]

f : evaluation parameter (either the radial displacement [mm], or the necking [%])

C : fitting constants

The specific constants C1 up to C15 for each graph, can be found in Table 4.2 and Table 4.3. In the same tables, the statistical evaluation parameters for the goodness of the fit are provided. How these should be interpreted is explained below [39].

- **Sum of Squares due to Error (SSE)** measures the total deviation of the response values from the fit to the response values. A value closer to 0 indicates that the model has a smaller random error component, and that the fit will be more useful for prediction.
- **R-square** measures how successful the fit is in explaining the variation of the data. A value closer to 1 indicates that a greater proportion of variance is accounted for by the model.
- **Adjusted R-square** adjusts the R-square parameter based on the residual degrees of freedom. A value closer to 1 indicates a better fit.
- **Root Mean Squared Error (RMSE)** is an estimate of the standard deviation of a random component in the data. A value closer to 0 indicates a fit that is more useful for prediction.

A table with the measured numerical values of the evaluation parameters can be found in Appendix C.

4.6.1 Radial inward displacement as a function of the groove width and the charging voltage

4.6.1.1 Two-dimensional graphs

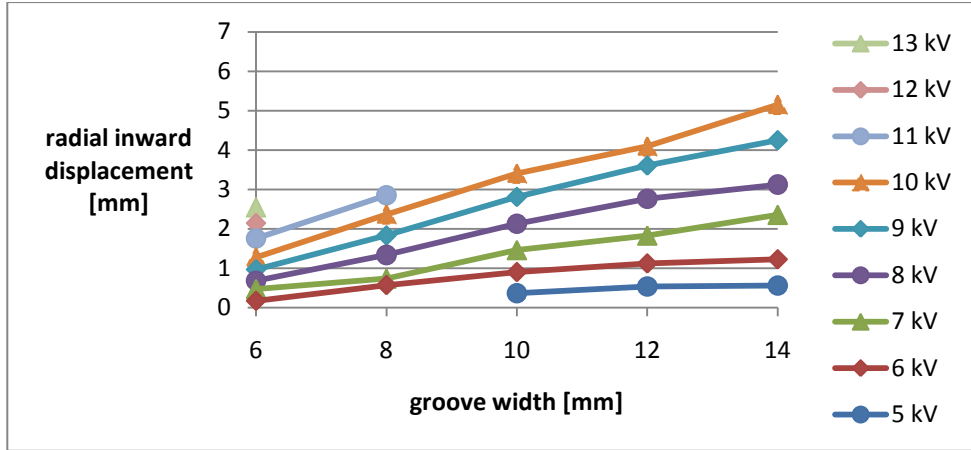


Figure 4.15: Radial inward displacement as function of the groove width and the charging voltage for a groove edge radius of 0.5 mm.

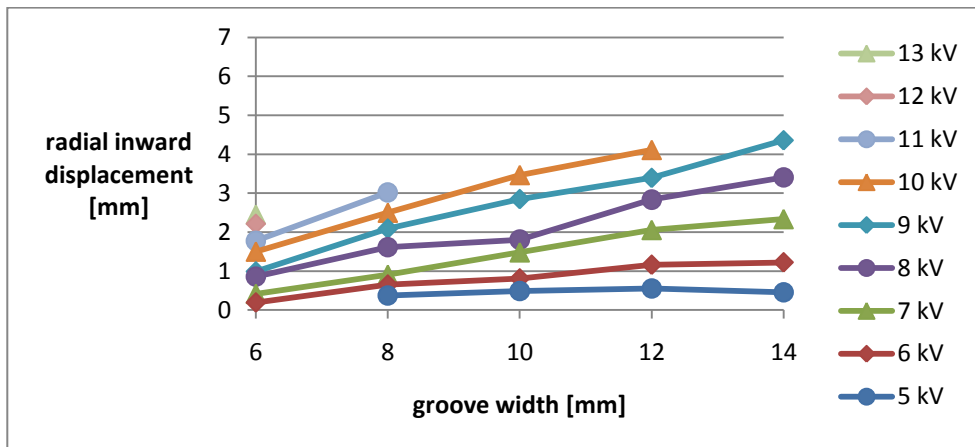


Figure 4.16: Radial inward displacement as a function of the groove width and the charging voltage for a groove edge radius of 1 mm.

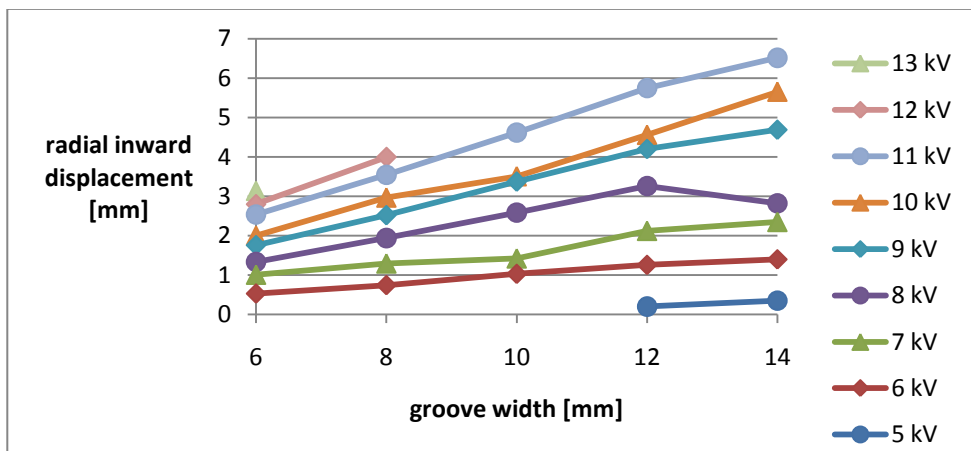


Figure 4.17: Radial inward displacement as a function of the groove width and the charging voltage for a groove edge radius of 1.5 mm.

4.6.1.2 Three-dimensional graphs and equations

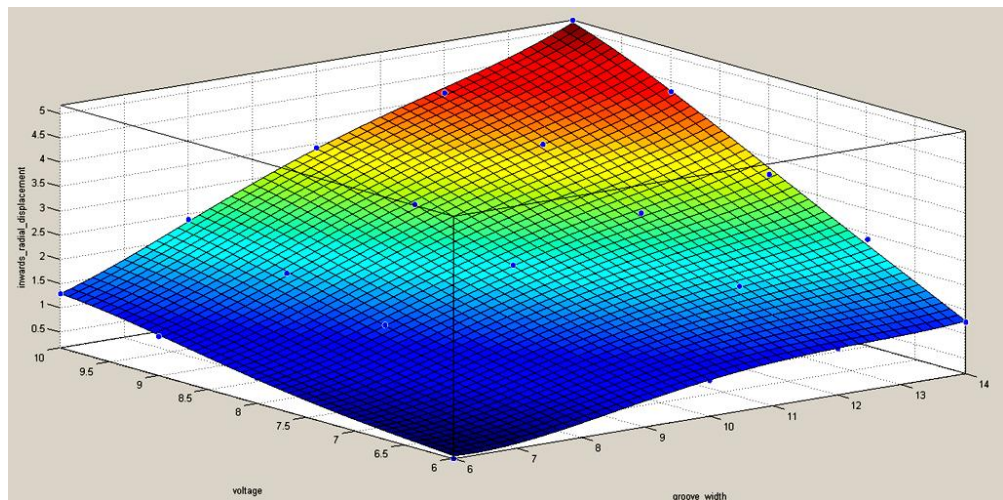


Figure 4.18: Fitted surface of the radial inward displacement as a function of the groove width and the charging voltage for a groove edge radius of 0.5 mm.

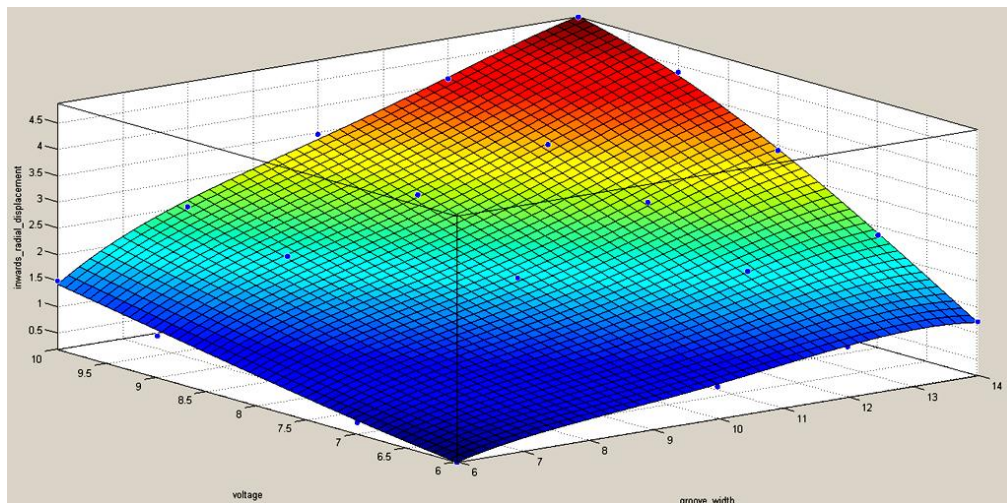


Figure 4.19: Fitted surface of the radial inward displacement as a function of the groove width and the charging voltage for a groove edge radius of 1 mm.

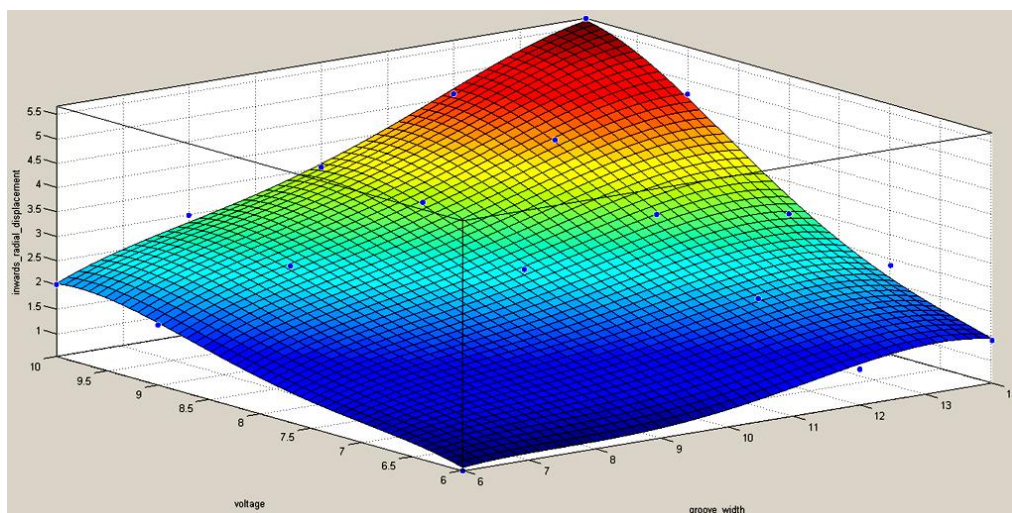


Figure 4.20: Fitted surface of the radial inward displacement as a function of the groove width and the charging voltage for a groove edge radius of 1.5 mm.

	Groove edge radius 0.5 mm	Groove edge radius 1 mm	Groove edge radius 1.5 mm
Coefficient			
C1	2.1200	2.0520	2.4670
C2	0.9945	0.8989	0.8389
C3	0.9810	0.9607	1.2550
C4	-0.2846	0.2080	0.1771
C5	0.3069	0.2413	0.3771
C6	0.0710	0.0269	0.1312
C7	-0.0303	0.0332	-0.0794
C8	-0.0041	-0.0097	0.0197
C9	-0.0331	-0.0823	0.0576
C10	-0.0463	-0.0290	-0.1479
C11	0.1041	-0.0955	-0.1594
C12	0.0349	0.0514	0.0412
C13	-0.0059	-0.0621	0.1185
C14	-0.0047	-0.0122	-0.0513
C15	-0.0286	0.0024	-0.1338
Goodness of fit			
SSE	0.1036	0.1970	0.4293
R-square	0.9976	0.9951	0.9902
Adjusted R-square	0.9942	0.9883	0.9764
RMSE	0.1018	0.1403	0.2072

Table 4.2: Constants for the general equation of the fitted surface and the goodness of the fit for the radial inward displacement.

4.6.1.3 Discussion

The graphs show that an increase of the charging voltage leads to a larger radial inward displacement. This is exactly what was expected: a higher applied voltage generates a higher transient current and this generates a stronger magnetic field and pressure. The repulsion force is therefore stronger, and the tube is repelled over a longer radial distance.

The graphs also show that the relationship between the groove width and the radial inward displacement is directly proportional. A larger radial inward displacement is measured when the groove width is larger. This can be explained by looking at the tube as if it is a beam imposed on two supports. If these support points are close together (cfr. a small groove width) the tube will be stiff and it will be difficult to deform the tube into the groove. If the contact points are more separated, the tube will be slender and less stiff and it will be easier to deform the tube into the groove.

It can be noted that for the combination of a groove width of 10 mm and a charging voltage of 8 kV in Figure 4.16, as well as for the combination of a groove width of 14 mm and a charging voltage of 8 kV in Figure 4.17, a lower radial inward displacement value is observed than expected. The explanation for this, is that the tube was cross-sectioned where the radial cut of the field shaper was during crimping. The radial inward displacement is smaller there (see 4.6.3).

By comparing the three 2D-graphs, it is concluded that the groove edge radius has a very limited influence on the radial inward displacement.

There are no measured values for the combinations of a large groove width and a high charging voltage. This is because the tube was cut for such combinations due to shearing (see 4.6.2).

It should be noted from the goodness of fit-values from Table 4.2 that a very good fit was obtained in all three cases and that it is reliable to use the equations of the fitted surfaces to make predictions within the given boundaries (groove width: [6 mm up to 14 mm] and voltage: [6 up to 10 kV]) because then no cutting will occur.

4.6.2 Necking at the groove edge as a function of the groove width and the charging voltage

4.6.2.1 Two-dimensional graphs

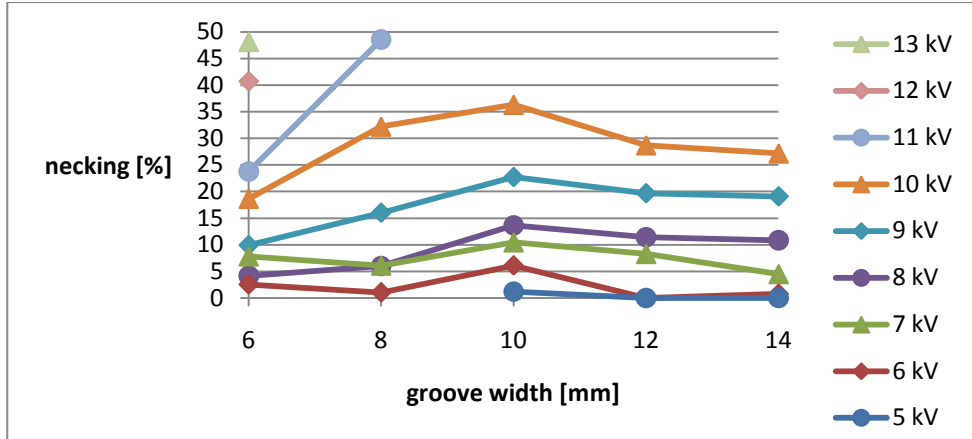


Figure 4.21: Necking as a function of the groove width and the charging voltage for a groove edge radius of 0.5 mm.

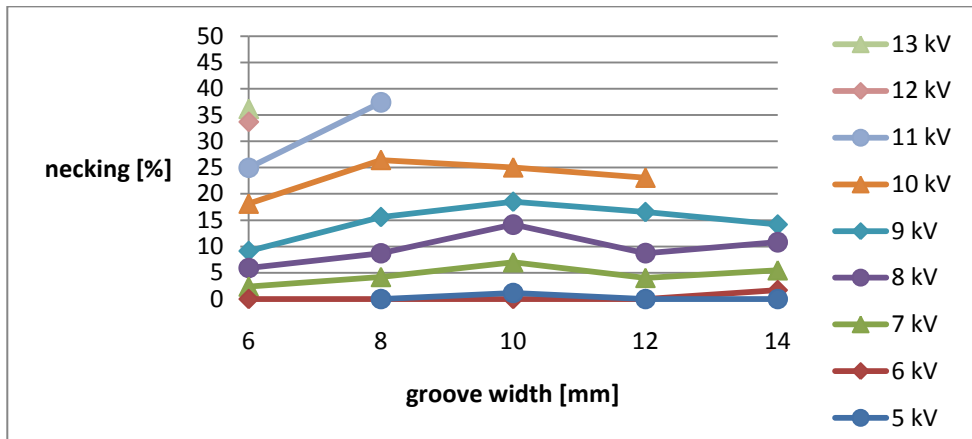


Figure 4.22: Necking as a function of the groove width and the charging voltage for a groove edge radius of 1 mm.

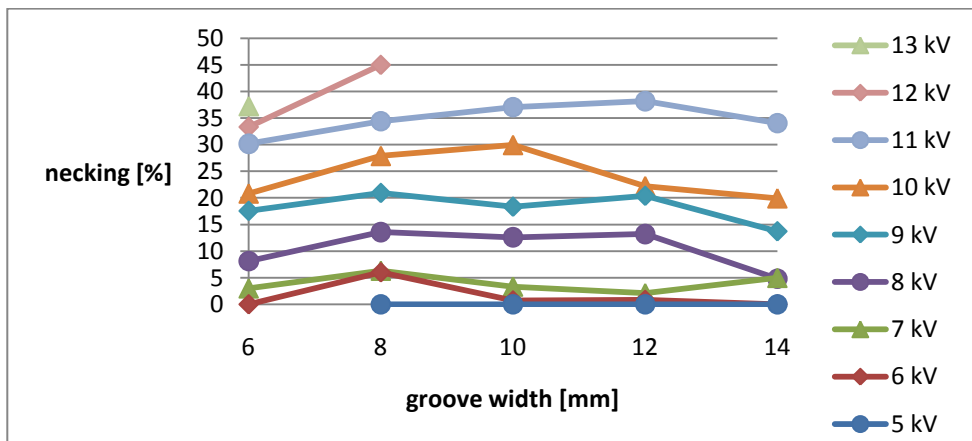


Figure 4.23: Necking as a function of the groove width and the charging voltage for a groove edge radius of 1.5 mm.

4.6.2.2 Three-dimensional graphs and equations

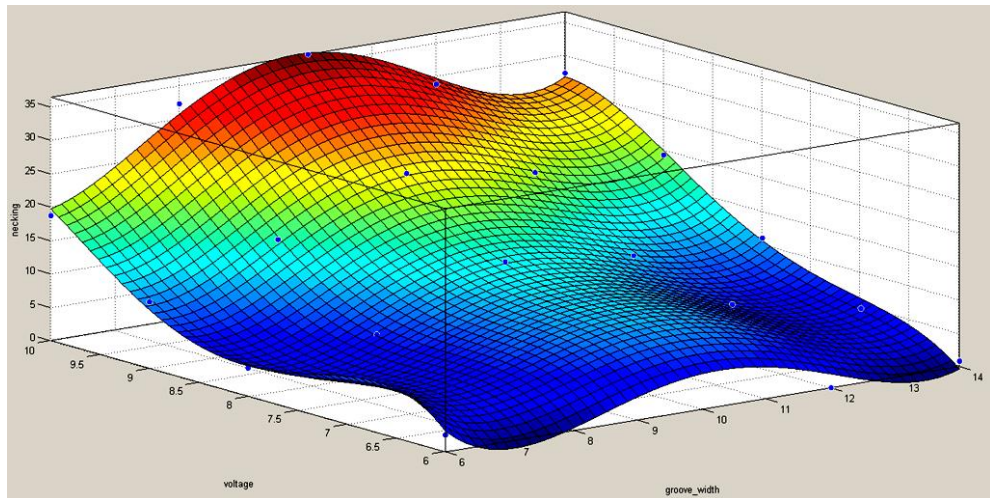


Figure 4.24: Fitted surface of the necking as a function of the groove width and the charging voltage for a groove edge radius of 0.5 mm.

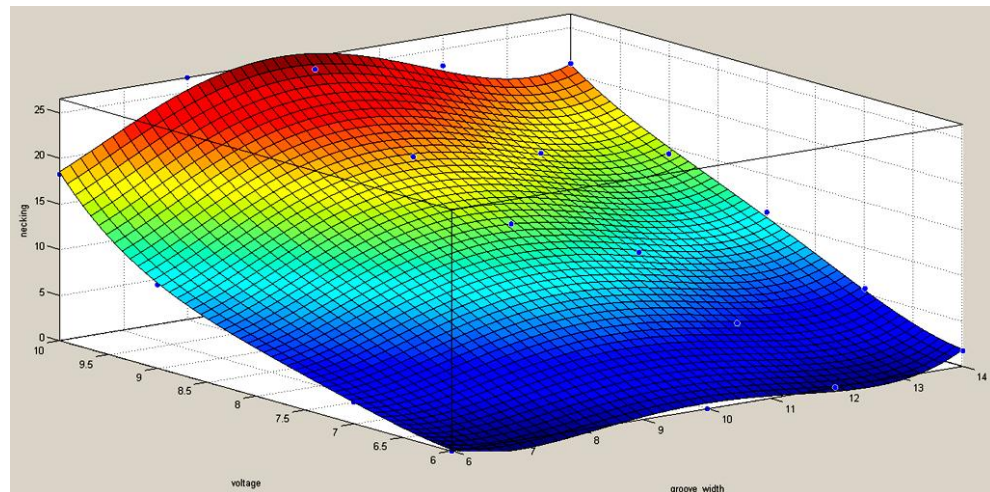


Figure 4.25: Fitted surface of the necking as a function of the groove width and the charging voltage for a groove edge radius of 1 mm.

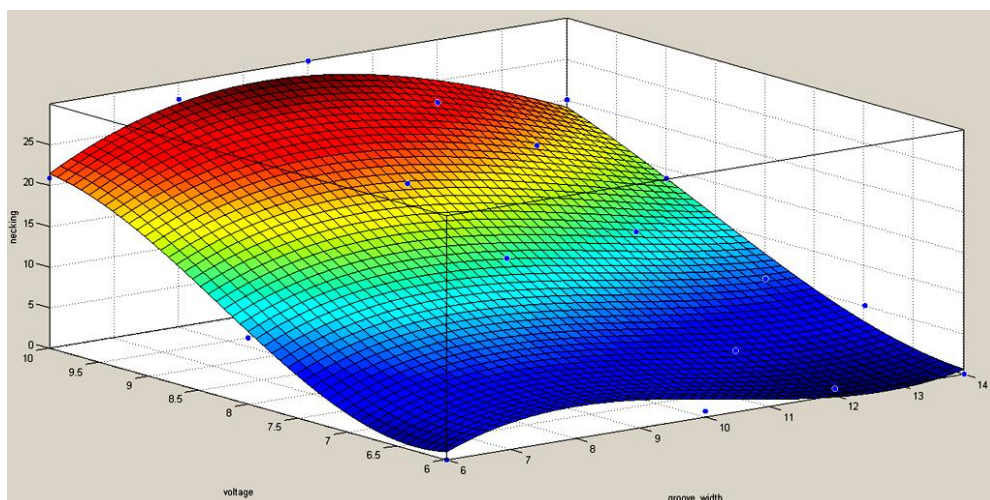


Figure 4.26: Fitted surface of the necking as a function of the groove width and the charging voltage for a groove edge radius of 1.5 mm.

	Groove edge radius 0.5 mm	Groove edge radius 1 mm	Groove edge radius 1.5 mm
Coefficient			
C1	13.4200	12.5400	11.6600
C2	1.5930	-0.3913	-2.8670
C3	8.1970	8.4360	12.1300
C4	-11.6600	-5.8080	1.7850
C5	1.0120	-0.1954	-0.2833
C6	8.6450	-0.6256	1.3800
C7	0.2910	1.1360	1.2990
C8	-1.7840	-1.4020	-1.2170
C9	-0.7934	-0.5438	-0.0646
C10	1.6040	0.5178	-1.4540
C11	4.4650	1.7220	-1.8580
C12	1.4370	0.5579	-0.4773
C13	-0.7488	0.3984	-0.1459
C14	-1.2560	-0.4013	0.4917
C15	-2.4670	0.6368	-0.0017
Goodness of fit			
SSE	22.8200	16.0800	58.4700
R-square	0.9909	0.9904	0.9711
Adjusted R-square	0.9782	0.9770	0.9306
RMSE	1.5110	1.2680	2.4180

Table 4.3: Constants for the general equation of the fitted surface and the goodness of the fit for the necking.

4.6.2.3 Discussion

The graphs show that a larger necking of the deformed tube occurs at the groove edge when the applied voltage is higher. The cause of this is the larger radial inward displacement when the voltage is higher, as discussed in the previous paragraph.

A remarkable trend is observed when relating the amount of necking to the groove width. At first necking increases when the groove width increases. Thereafter the necking reaches a maximum, and then declines when the groove width further increases. This is an interesting observation, especially when keeping in mind that the radial inward displacement linearly increases with the groove width (see 4.6.1.). The explanation for this trend can be found in the relationship between shearing and bending deformation of the tube wall at different groove widths. If the groove width is small, the bending of the tube into the groove is limited, and the radial inward displacement will for the most part be achieved by shearing at the groove edges. This causes fairly large necking for a relatively small radial inward displacement. As the groove width increases, the radial inward displacement is larger and the necking increases until a maximum is reached. This is because the part of the displacement due to bending is still small and the larger radial inward displacement requires more shearing at the edges.

If the groove width further increases, it becomes large enough for the bending moment to have a significant effect. A part of the radial inward displacement into the groove is realised by bending, which does not cause necking at the groove edges. The remaining energy after bending of the

tube is then used to realise the rest of the radial inward displacement by shearing at the groove edges (see also Figure 4.27). As the groove width increases, a greater part of the radial inward displacement is done by bending and a smaller part by shearing at the edges. This explains how a larger radial inward displacement is possible in combination with a declining percentage of necking.

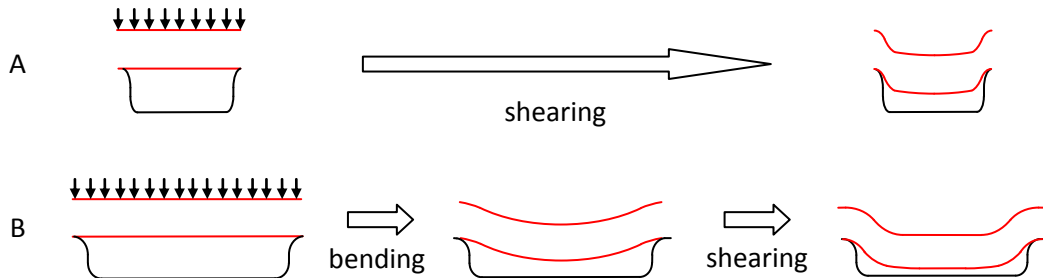


Figure 4.27: A. Only shearing occurs for a small groove width, B. A combination of bending and shearing occurs for a larger groove width.

Images from the remarkable trend are shown in Figure 4.28. The necking increases from Figure 4.28.A to Figure 4.28.B and then decreases again from Figure 4.28.B up to Figure 4.28.D. The radial inward displacement increases from Figure 4.28.A up to Figure 4.28.D.

Images Figure 4.28.A and Figure 4.28.C have the approximately same necking (about 30%, see Figure 4.21), but the radial inward displacement is 75% higher in the latter one. The only difference between both is the groove width. This is an experimental evidence that the bending moment has a significant influence as the groove width increases.

Groove edge radius = 0.5 mm and charging voltage = 10 kV

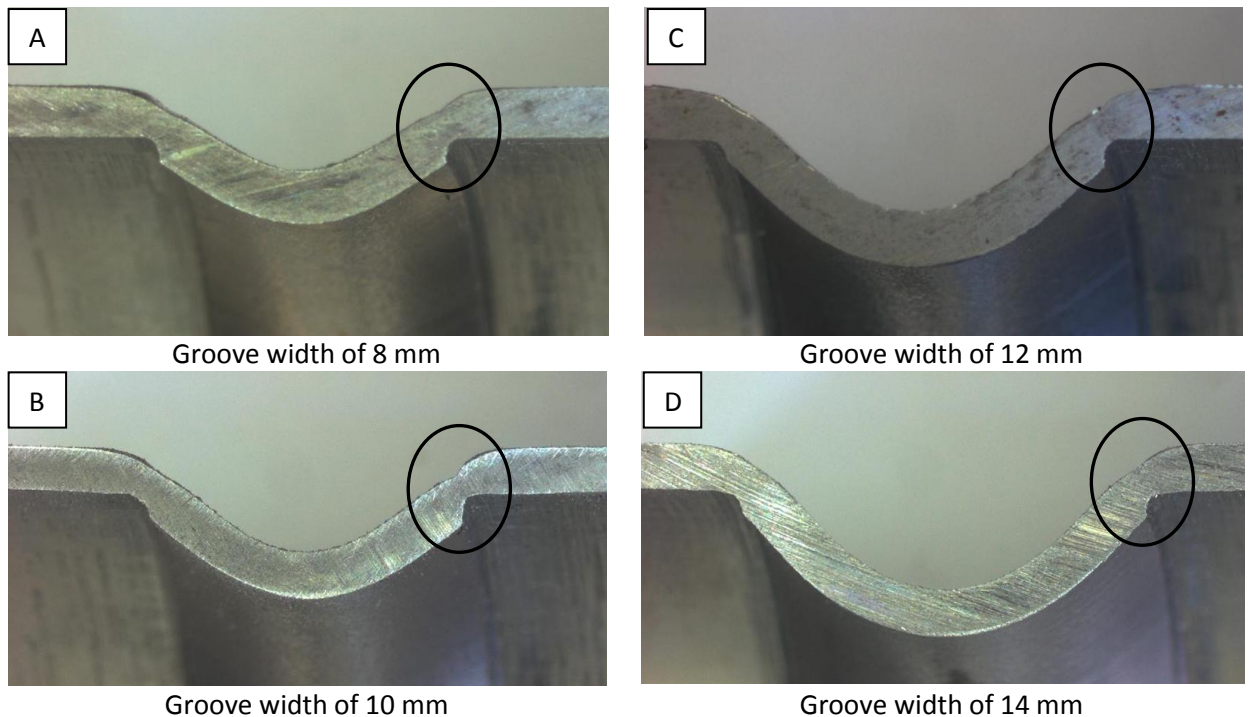


Figure 4.28: Increasing influence of the bending moment as the groove width increases.

To obtain experimental evidence of the shearing near the groove edges, some of the deformed tubes were embedded and studied under a microscope. An example of a test specimen is given in Figure 4.29. The orientation and the severe deformation of the grains clearly evidence that shearing occurred at the groove edge.



Figure 4.29: Shearing at the groove edge.

When comparing the three different graphs, it is noted that the groove edge radius has a significant influence on the necking. As expected, a smaller groove edge radius causes more necking. When the groove edge radius is smaller, the edges will act like a knife, cutting the material during the crimping operation and thus causing larger necking.

From Table 4.3 it can be observed that the goodness of fit-values are less than in the previous section, especially for the equation related to the groove edge radius of 1.5 mm. The reason is that there is still some scatter present in the measured necking values, even after the corrections which were described higher.

Nevertheless, the fittings for a groove edge radius equal to 0.5 and 1 mm are good and it should be possible to make reliable predictions with these equations. With the equation for a groove edge radius of 1.5 mm, one should be more careful, and verify the predicted values with some additional experimental tests.

4.6.3 Effect of the radial cut in the field shaper

The cylinder system also offered the opportunity to investigate the inside of the deformed tubes. In all the deformed tubes, a very localized zone could be observed where the radial inward displacement was less (see Figure 4.30.B).

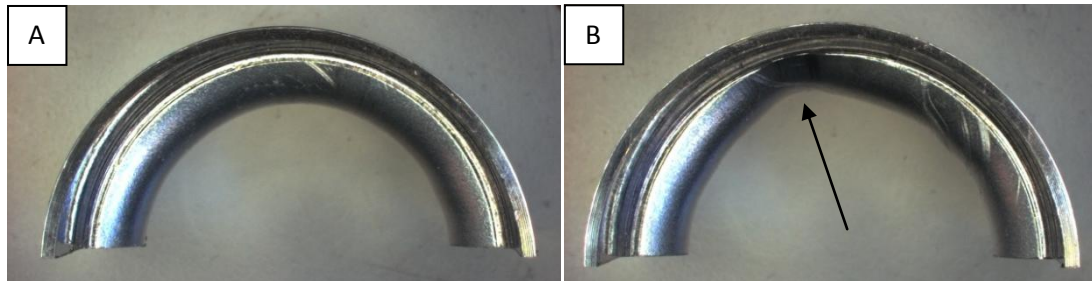


Figure 4.30: A. Upper half of the cut tube: uniform deformation, B. Lower half of the cut tube: a zone with less deformation.

The explanation for this zone with less radial inward displacement can be found by looking at the geometry of the field shaper. There is a radial cut machined in the field shaper in order to make the current flow at the inside of the field shaper (see Figure 4.31). This causes locally a less strong magnetic field, and thus the deformation will be less in this zone.

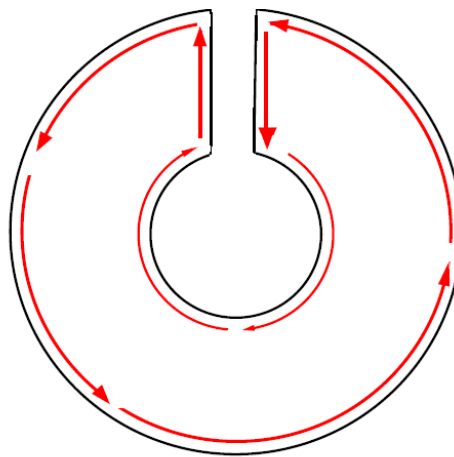


Figure 4.31: Radial cut in the field shaper to lead the current to the inside of the field shaper.

This effect needs to be kept in mind, especially for applications where roundness or leakproofness of the product are of importance (e.g. roller bearings and cooling pipes).

4.7 Conclusions

A cylinder system, which allows to simulate different types of single grooves with low material resources and with low processing and evaluation time, was designed and built. The groove edge radius, the groove width and the charging voltage were varied.

For each of the 132 samples made, the largest radial inward displacement and the necking at the groove edge were measured. It should be noted that the radial inward displacement was never restricted (cfr. 'free deformation').

It was observed that an increase of the charging voltage leads to a larger radial inward displacement. The relationship between the groove width and the radial inward displacement is directly proportional: a larger radial inward displacement is measured when the groove width is larger. It was also observed that the groove edge radius has a very limited influence on the radial inward displacement.

A larger necking of the deformed tube occurs at the groove edge when the charging voltage is higher. A remarkable trend was observed when relating the amount of necking to the groove width: at first necking increases when the groove width increases. It reaches a maximum and then the necking starts to decline as the groove width increases further (while the radial inward displacement linearly increases as the groove width increases further). This was clarified by looking at the ratio of shearing and bending. It was also observed that the groove edge radius has a significant influence on the necking: a smaller groove edge radius causes more necking.

The maximal radial inward displacement that was obtained causes a 27.8% decrease in diameter and a 34% tube wall thickness reduction.

Equations for fitted 3D-surfaces were generated. These link the groove width and the voltage to the radial inward displacement and the necking at the groove edge and they allow to make a first estimate for the parameters in a groove design.

It was observed that there is a localised zone in which the radial inward displacement is less. This is due to the presence of a radial cut in the field shaper.

The experiments were done on an aluminum tube with a wall thickness of 1.5 mm and an outer diameter of 50 mm. It is more than likely that the qualitative trends will be the same for other materials/wall thicknesses/diameters, but in order to obtain quantitative observations, experimental research on the specific combination is necessary.

Chapter 5: Preliminary experiments

5.1 Introduction

The joint strength is dependent on two main forces. The first force is the result of residual hoop stresses which exist after the joint is created. After the tube deformation, the surfaces of the mating parts (internal workpiece and tube) rebound elastically inducing stresses. These so-called hoop stresses induce frictional forces when the joint is loaded. The frictional force depends on the material properties (yield strength, Young's modulus), the friction coefficient and the geometrical stiffness of the joined parts [25].

The second acting force when loading the joint is a restraining force resulting from the geometrical configuration of the groove. Interlocking geometries are required to make a joint that maximises mechanical strength while minimising the electromechanical energy necessary to create it [40].

The joint strength, which is the ability to resist external loading, can be expressed as:

$$F_{joint} = F_{friction} + F_{groove} \quad (5.1)$$

With: F_{joint} : joint strength [N]
 $F_{friction}$: frictional force caused by the contact pressure [N]
 F_{groove} : restraining force caused by the groove geometry [N]

Because the frictional force will not be sufficient to resist heavy external loading, the restraining force must be maximised. This will be obtained by optimising the groove design.

There is a limit of the joint strength when a single groove is used, even though the groove configuration is optimised. In other words, a single groove is not able to provide the full strength of the material. This is because necking of the tube wall after electromagnetic crimping cannot be avoided. The necking zone will cause premature failure of the joint. Tensile strengths up to 75% (see § 5.4.1) of the base material were obtained. It is believed that a much higher percentage is possible with an increased number of grooves [10,25]. But, it is meaningless to increase the number of grooves without changing the groove design for the additional grooves because the joint strength does not increase arithmetically (see also [25]). This means that the joint strength of a double groove crimp joint, designed with two similar grooves, will not be twice as high as the joint strength of a single groove crimp joint designed with this particular groove.

When loaded axially with a tensile force $F_{applied}$ and restraining the internal workpiece, the tube will suffer deformation and is pressed against the groove's edges. The idea of a double groove design is that each groove should bear a part of the load. A stronger joint is expected when the two grooves in a double groove design bear an equal part of the force. In Figure 5.1 the two curves (a and b) represent the ratio of the adopted force to the applied force over the axial length

of the crimp joint. In situation a (curve a), the crimp joint adopts all the force in the first groove while the second groove is useless. In situation b (curve b), the crimp joint adopts an equal force on each groove. The crimp joint in situation a will fail in the first groove and it is expected that the maximum joint strength in situation b will be much larger than in situation a if an optimal groove design is used.

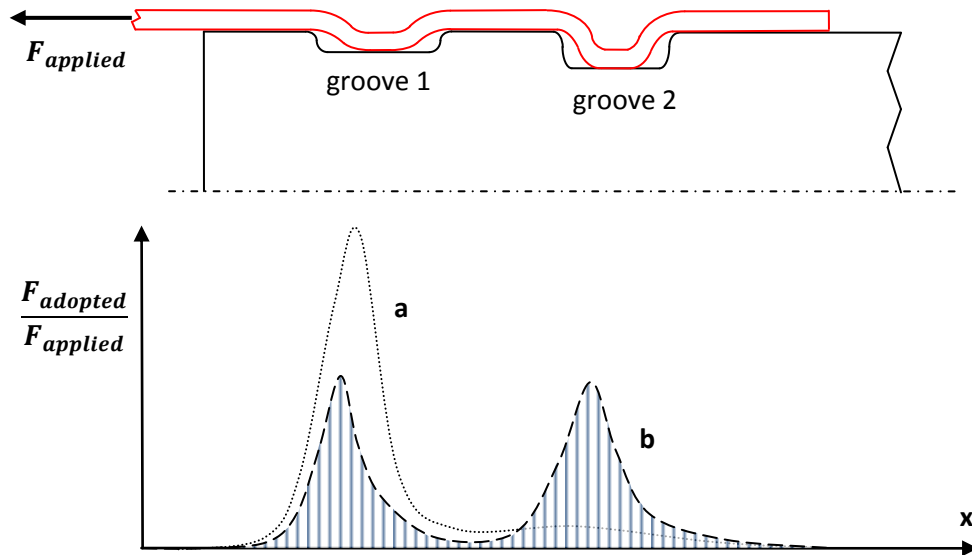


Figure 5.1: A double groove design distributes the applied force over the two grooves.

Optimising the groove design signifies decreasing the amount of stress taken by the first groove and homogenises the distribution of the load taken up by each groove. Tube wall thickness reduction at the first groove should be minimised or avoided because the wall thickness at this location governs the joint strength [25]. This can be obtained by reducing the groove's depth, increasing the radius of the edges of the first groove, increasing the groove's length or a combination of these three factors.

Some test series were designed to investigate the influence of the groove geometry on the deformation and on the tensile strength. Also, a finite element simulation will investigate the mechanism of a double groove crimp joint subjected to axial load.

5.2 Finite element simulations

Finite element simulations of a tensile loaded joint have been performed using the software ABAQUS (version 6.9). The main goal is to get confirmation that a second groove will increase the load bearing capacity of an axially loaded joint. Hereto the magnitude and distribution of the stresses and deformations in both components are studied in detail.

An axisymmetric model consisting of a steel internal workpiece with two grooves (with a groove width and depth of respectively 13 mm and 2 mm, separated 10 mm apart) and an aluminum tube (with a wall thickness of 1.5 mm and with its assumed deformed shape obtained after crimping) was built. Linear elastic material behaviour is assumed. A static friction coefficient μ_S of

0.61 [23] was used to define the interaction between both parts. The internal workpiece was clamped at the bottom and an upwards displacement was imposed at the tube end. The resulting stress distribution in the axial direction obtained for a representative simulation can be seen in Figure 5.2. In the unloaded condition, the aluminum tube makes contact with the internal workpiece at the bottom of both grooves.

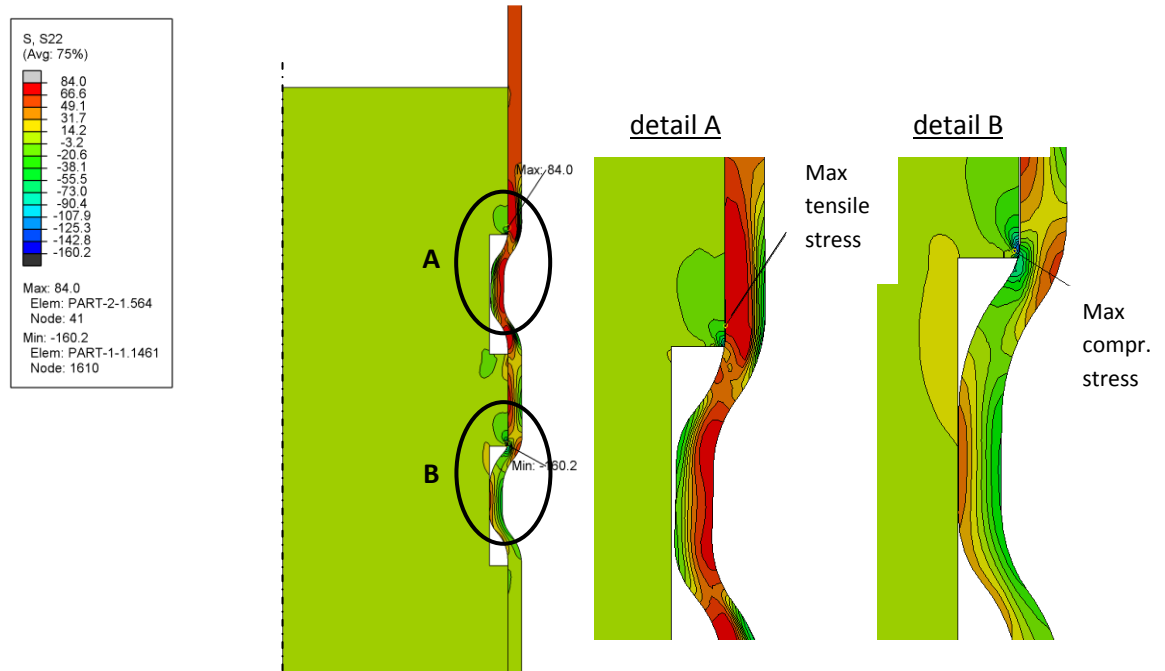


Figure 5.2: Stress distribution in a tensile loaded joint with a double groove internal workpiece.

The simulation results revealed that a clearance appeared at the bottom of the first groove during the tensile loading (Figure 5.2A). As a consequence, the tube is pulled out of the first groove and the mechanical interlock behind the upper corner of the second groove becomes the most important mechanism that prevents the tube from sliding off against the internal workpiece. The highest compression stress in the internal workpiece can therefore be found at this corner (Figure 5.2B). The highest tensile stress is found in the tube near the upper corner of the first groove (Figure 5.2A). This confirms that the tube wall thickness reduction at the first groove should be minimised or avoided. Without a first groove design which minimises this reduction, it is possible that the joint fails before the second groove can take up a part of the load (see § 7.4.1).

Based on these conclusions, the joint design can be further optimised. The edge radius of the upper corner of the first groove is made larger and this groove is made less deep, in order to prevent early localised shearing of the tube. Also, the first groove is made wider to obtain a larger contact area at the base of the first groove, thus creating a stronger interference fit that will longer withstand pull-out. The second groove is deeper than the first groove and the edge radius of the upper corner is made larger to optimise the form fit and joint strength. In order to verify these conclusions through experiments, tensile tests were done on both an internal workpiece with two equal grooves and an internal workpiece with the proposed optimised grooves, and the results were compared. More finite element simulations may be appropriate to get more insight on the failure mechanism during tensile testing.

5.3 Experimental data

5.3.1 Materials

In previous work, a few experiments were performed to get acquainted with the groove design of the internal workpiece [40]. Carbon steel (S235) was used as material for both the internal workpieces and the tubes. Cross sections of the joints were compared and an optimal design was proposed [10].

In a first stage, similar designs with those used in the previous work were studied. Instead of using carbon steel components and small diameter tubes, experiments were performed with aluminum components. The aluminum based alloy EN AW-6060 in the T6 condition (precipitation hardened) was used as the material for both the internal workpiece and the tube (see Table 4.1 for the properties).

Tubes with an outer diameter of 50 mm and a wall thickness of 1.5 mm were used. The outer diameter of the internal workpiece is equal to 46.8 mm over an axial length of 29 mm. A part of the internal workpiece had a smaller diameter, to allow clamping in the universal testing machine (see Figure 3.5).

Because of the limited internal axial length of the field shaper, the zone that can be deformed is restricted in length in the axial direction. The sum of both groove widths plus the length of the collar must be approximately equal to the field shaper width. In this case, the axial length of the work zone of the field shaper equals 15 mm (see § 5.3.3) and the total field concentration zone was assumed to be equal to 16 mm. Finite element calculations show that a small area outside the effective work zone also experiences sufficient magnetic pressure [20].

The specimens for cross sectioning had a total axial length of 59 mm and the specimens for tensile testing had a total axial length of 159 mm. This is because the tensile test specimen requires a longer length to be clamped in the tensile testing machine. An Amsler universal testing machine (maximum capacity 600 kN) was used (see the § 3.3). Figure 5.3 shows the general dimensions of the internal workpiece.

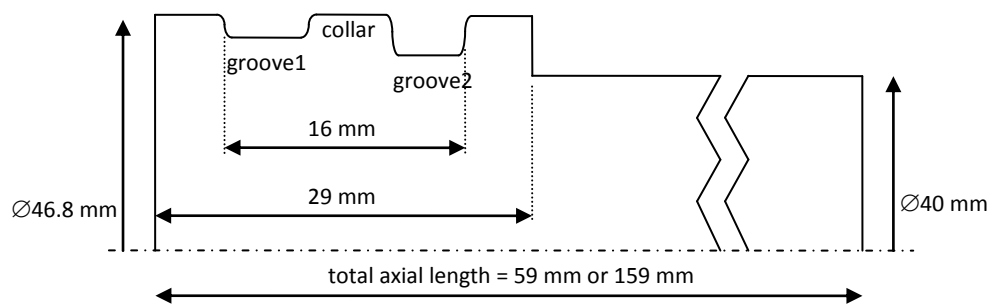


Figure 5.3: Nomenclature and dimensions of the double groove design.

5.3.2 Test setup

The setup for positioning the specimens in the electromagnetic pulse machine is the same as explained in chapter 3, see Figure 5.4. However, for this set of experiments, the tube to be deformed (2) is clamped between an extra positioning tube (3) and an electric insulating support part (4). The internal workpiece (1) is inserted in this support part. The axial movement of the internal workpiece to the right is prevented by the support, while the movement to the left is prevented by the round bar or 'ejector' (5).

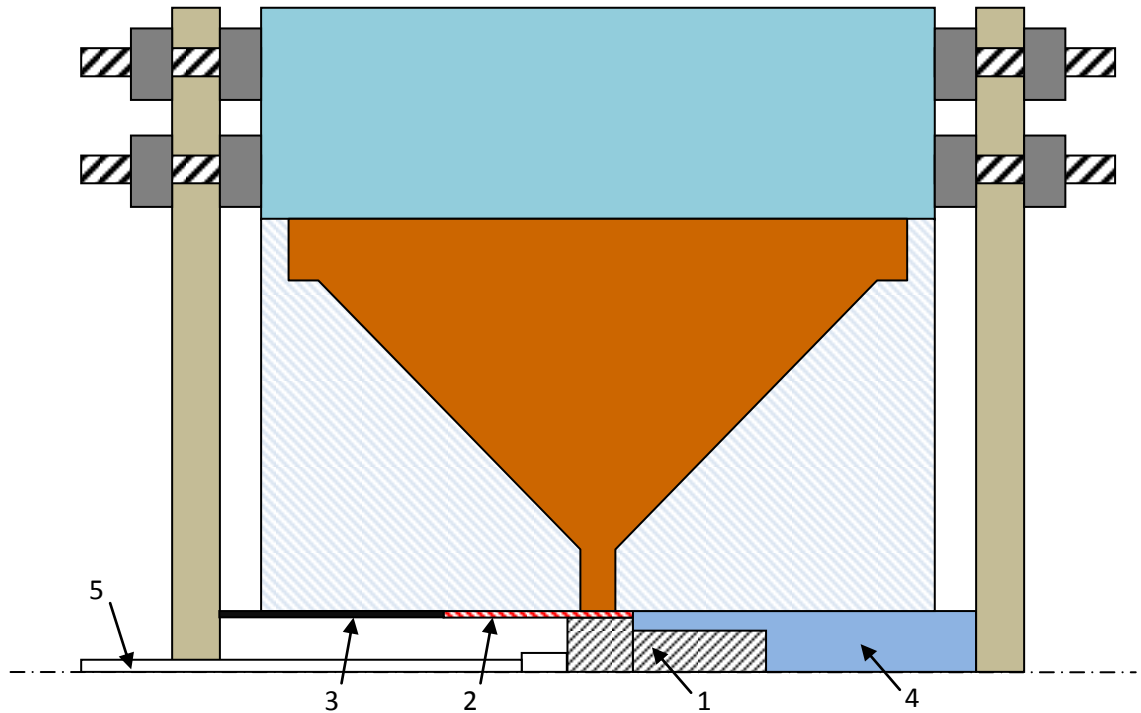


Figure 5.4: Schematic overview of the setup.

5.3.3 Field shaper

A CuCrZr field shaper with an internal diameter of 52 mm and an internal axial length of 15 mm was used. The technical drawing of this field shaper can be found in Appendix B. Copper-chrome-zirconium is a hardened copper alloy with excellent hardness and a high electrical and chemical conductivity. Some properties of the alloy are listed in Table 5.1.

Physical properties			Mechanical properties			
Density	Electrical conductivity	Thermal conductivity	Elasticity modulus	Shear modulus	Tensile strength	Proof stress $R_{p0.2}$
$[g/cm^3]$	$[MS/m]$	$[W/(m.K)]$	$[GPa]$	$[GPa]$	$[MPa]$	$[MPa]$
8.9	26-48	320	108	45	min. 370	min. 270

Table 5.1: Properties of CuCrZr at 20°C [41].

5.3.4 Process parameters

Eight test series were performed, denoted as test series A up to H. Figure 5.5 shows the geometric parameters. The first edge of the first groove (parameter a) is called edge 1₁, the second edge of the first groove (parameter d) is called 1₂, the first edge of the second groove (parameter g) is called 2₁ and the second edge of the second groove (parameter j) is called edge 2₂. This nomenclature is also used in subsequent chapters.

An overview of the geometric parameter settings is listed in Table 5.2. The unit of all geometric parameters listed in this chapter is mm. Test series A and B are performed to investigate the influence of the edge radius. Test series C is performed to determine the effect of the collar depth (parameter f) and test series D is performed to investigate the influence of two grooves with a different groove width. The internal workpieces used in test series E, F, G and H are improved designs of respectively test series A, B, C and D. The improvement is based on the knowledge acquired during the experiments.

Besides the geometric parameters, the applied charging voltage is also taken into account. In each set of test series, 4 samples are produced. Three tests were performed with three different charging voltages. These specimens were then cut through axially to gain knowledge about the deformation. Test series A, B and C consist each of three axial crimp joints performed at 10.0, 12.5 and 15.0 kV and a fourth axial crimp joint performed at 12.5 kV for tensile testing. Note that in all test series, the fourth workpiece with a longer axial length was performed at 12.5 kV. This was done to consistently compare the tensile strength of all test series. Based on the knowledge gained in test series A, B and C, other charging voltages were used in the succeeding test series. The lower voltage limit was set to 11.0 kV while the upper voltage limit was equal to 15.0 kV for test series D. For test series E, F, G and H, the lower voltage limit was equal to 11.0 kV while the upper voltage limit was reduced to 14.0 kV (compared to the previous test series). The middle setting of the applied voltage was calculated based on a linear interpolation of the minimum and maximum energy level. The energy provided by the pulse generator is proportional to the square of the voltage :

$$E = \frac{CV^2}{2} \quad (5.2)$$

With: C : capacity of the capacitor bank [F] (for Pulsar: $C = 160 \mu\text{F}$)

V : charging voltage [V]

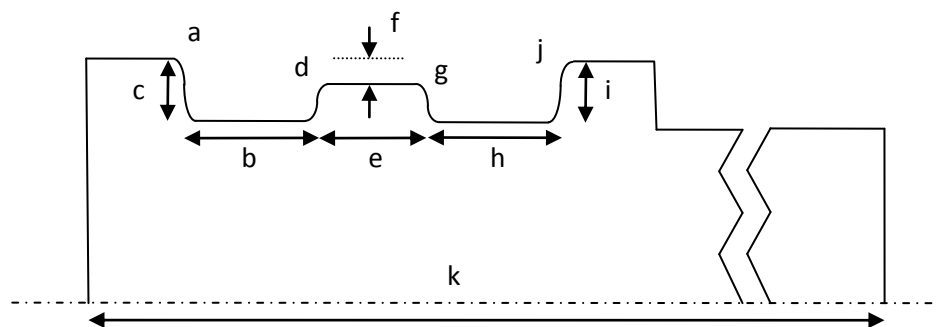


Figure 5.5: Nomenclature of parameter indication.

Design Name	groove 1			collar			groove 2				Total length k	applied voltage [kV]
	radius a	width b	depth c	radius d	width e	depth f	radius g	width h	depth i	radius j		
A1	1.0	6	3.5	1.0	4	1.0	1.0	6	3.5	1	59	10.0
A2	1.0	6	3.5	1.0	4	1.0	1.0	6	3.5	1	59	12.5
A3	1.0	6	3.5	1.0	4	1.0	1.0	6	3.5	1	59	15.0
A4	1.0	6	3.5	1.0	4	1.0	1.0	6	3.5	1	159	12.5
B1	0.0	6	3.5	0.0	4	1.0	0.0	6	3.5	0	59	10.0
B2	0.0	6	3.5	0.0	4	1.0	0.0	6	3.5	0	59	12.5
B3	0.0	6	3.5	0.0	4	1.0	0.0	6	3.5	0	59	15.0
B4	0.0	6	3.5	0.0	4	1.0	0.0	6	3.5	0	159	12.5
C1	1.0	6	2.0	1.0	4	0.0	1.0	6	3.0	1	59	10.0
C2	1.0	6	2.0	1.0	4	0.0	1.0	6	3.0	1	59	12.5
C3	1.0	6	2.0	1.0	4	0.0	1.0	6	3.0	1	59	15.0
C4	1.0	6	2.0	1.0	4	0.0	1.0	6	3.0	1	159	12.5
D1	1.0	8	1.5	1.0	4	0.0	1.0	4	2.5	1	59	11.0
D2	1.0	8	1.5	1.0	4	0.0	1.0	4	2.5	1	59	13.2
D3	1.0	8	1.5	1.0	4	0.0	1.0	4	2.5	1	59	15.0
D4	1.0	8	1.5	1.0	4	0.0	1.0	4	2.5	1	159	12.5
E1	1.0	6	2.0	0.5	4	1.0	0.5	6	2.0	1	59	11.0
E2	1.0	6	2.0	0.5	4	1.0	0.5	6	2.0	1	59	12.6
E3	1.0	6	2.0	0.5	4	1.0	0.5	6	2.0	1	59	14.0
E4	1.0	6	2.0	0.5	4	1.0	0.5	6	2.0	1	159	12.5
F1	0.0	6	2.0	0.0	4	1.0	0.0	6	2.0	0	59	11.0
F2	0.0	6	2.0	0.0	4	1.0	0.0	6	2.0	0	59	12.6
F3	0.0	6	2.0	0.0	4	1.0	0.0	6	2.0	0	59	14.0
F4	0.0	6	2.0	0.0	4	1.0	0.0	6	2.0	0	159	12.5
G1	0.5	6	1.0	0.0	4	0.5	1.0	6	2.0	1	59	11.0
G2	0.5	6	1.0	0.0	4	0.5	1.0	6	2.0	1	59	12.6
G3	0.5	6	1.0	0.0	4	0.5	1.0	6	2.0	1	59	14.0
G4	0.5	6	1.0	0.0	4	0.5	1.0	6	2.0	1	159	12.5
H1	0.0	8	0.5	0.0	2	0	1.0	6	1.5	1	59	11.0
H2	0.0	8	0.5	0.0	2	0	1.0	6	1.5	1	59	12.6
H3	0.0	8	0.5	0.0	2	0	1.0	6	1.5	1	59	14.0
H4	0.0	8	0.5	0.0	2	0	1.0	6	1.5	1	159	12.5

Table 5.2: Process parameters used in the preliminary experiments (geometrical parameters in mm).

5.4 Results and discussion

For the double groove design samples that were cut through axially, the points of interest are the tube wall thickness reduction after crimping, the deformed tube in the groove and zones of plastic deformation of the internal workpiece surface. These points of interest will be related to the tensile strength of the crimp joint.

5.4.1 Single groove strength

Before discussing results of the test series, the tensile strength of two single groove designs has been measured. The geometrical and process parameters of the crimp joints are listed in Table 5.3. The strength of the base material is determined by performing a tensile test on a tubular piece with sufficient axial length. This strength was equal to 56.1 kN.

Both single groove designs had a groove width of 6 mm. In sample X, sharp edges are present (radius = 0 mm) where in sample Y, a groove edge radius of 1 mm is used. The depth of the groove in sample X is chosen sufficiently small (1 mm) in order to not just cut the tube as if it was a free deformation experiment (see chapter 4). The depth of the groove in sample Y is taken 1.5 mm. Both crimp joints have been performed at 12.5 kV.

It is seen in Table 5.3 that a tensile strength of almost 75% of the tensile strength of the base material is reached in sample X. The design with sharp edges and lower groove depth (sample X) had a stronger crimp joint than the other design.

Design Name	groove				Total length k	applied voltage [kV]	Tensile strength [kN]	Relative tensile strength [%]
	radius a	width b	depth c	radius d				
X	0	6	1	0	159	12.5	41.8	74.5
Y	1	6	1.5	1	159	12.5	35.9	64.0

Table 5.3: Geometrical and process parameters of single groove design X and Y.

5.4.2 Test series A & B

5.4.2.1 Design and setup

The first crimping experiments on a double groove design were performed using internal workpieces with two similar grooves. Later, this design will be compared with a design with two dissimilar grooves in test series C, D, G and H. The dimensions of the internal workpiece of design A and B are shown in Figure 5.6 and Figure 5.7 respectively. Table 5.4 lists the process parameters of test series A and B. The difference between the two designs is the edge radius. In design A, an edge radius of 1 mm is used where in design B no edge rounding is applied. The aim is to determine the effect of the groove edge radius.

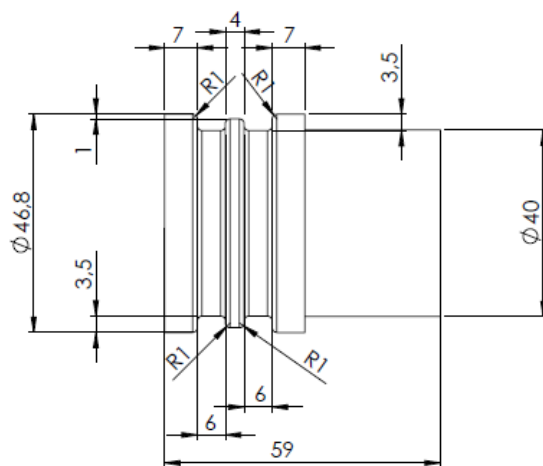


Figure 5.6: Axial crimp joint design A.

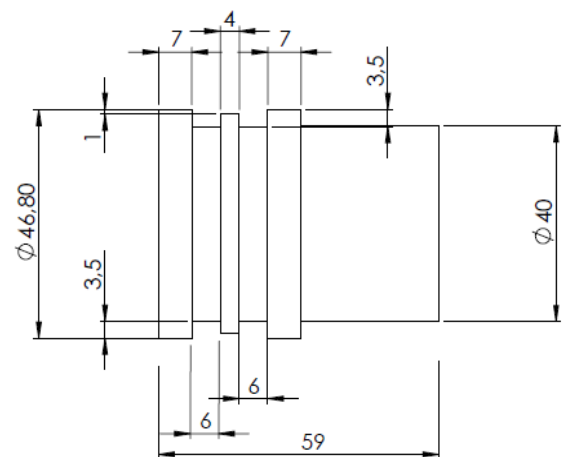


Figure 5.7: Axial crimp joint design B.

Design Name	groove 1				collar				groove 2			Total length k	applied voltage [kV]
	radius a	width b	depth c	radius d	width e	depth f	radius g	width h	depth i	radius j			
A1	1	6	3.5	1	4	1	1	6	3.5	1	59	10.0	
A2	1	6	3.5	1	4	1	1	6	3.5	1	59	12.5	
A3	1	6	3.5	1	4	1	1	6	3.5	1	59	15.0	
A4	1	6	3.5	1	4	1	1	6	3.5	1	159	12.5	
B1	0	6	3.5	0	4	1	0	6	3.5	0	59	10.0	
B2	0	6	3.5	0	4	1	0	6	3.5	0	59	12.5	
B3	0	6	3.5	0	4	1	0	6	3.5	0	59	15.0	
B4	0	6	3.5	0	4	1	0	6	3.5	0	159	12.5	

Table 5.4: Geometrical and process parameters of test series A and B.

5.4.2.2 Results

Before discussing the results, it is important to mention that after cutting the joints, the elastic residual stresses will disappear, resulting in a springback of the tube. Therefore, the accuracy of the measurements may be questioned. The preliminary experiments are developed to gain some basic knowledge about axial crimp joints with two grooves. General trends and observations are investigated, so the issue of the poor accuracy is not such a problem.

As can be seen in Figure 5.8, there is not too much difference between the deformation performed at 10.0 kV (sample A1) and at 12.5 kV (sample A2). Obviously, the test performed with 15.0 kV (sample A3) shows more deformation. A first remark can be made about the zone of the tube next to the grooves. It is observed that there is no feeding of the surrounding tube material into the groove (there has been no axial displacement of the tube towards the grooves). This can be attributed to the high deforming velocities and the fact that the friction between the contact areas of both pieces restrict the inward movement (REF also [10]). High speed forming occurs only at those zones where the radial deformation is allowed.

In sample A3, the collar of the internal workpiece has experienced plastic deformation. The flat top is now convex. Although the edge radii were large to prevent excessive wall thickness reduction in test series A, in sample A3 very small wall thicknesses were observed at all groove edges.

Figure 5.9 shows clearly that the tube wall was subjected to local shearing at the sharp outside edges, even for small charging voltages. As could be expected, in sample B3, the tube was cut at 15.0 kV. A deep groove without edge rounding will act as a knife and will cut the tube. Sample B2 was also cut at certain zones of the circumference (cannot be seen in this figure).

The difference in radial displacement between sample B1 and sample B2 is clear, but between sample B2 and sample B3, there is not so much difference. This may be explained by the decrease of the groove width caused by the large plastic deformation of the central collar. When the tube impacts with the central collar, this collar deforms plastically and both edges (edge 1₂ and edge 2₁) are pushed towards the centre of the groove. This decreases the groove width, making it more difficult for the tube to deform into the groove. Comparing sample B3 with sample A3, more

energy is used for the excessive deformation of the collar in sample B3, resulting in less deformation of the tube into the grooves.

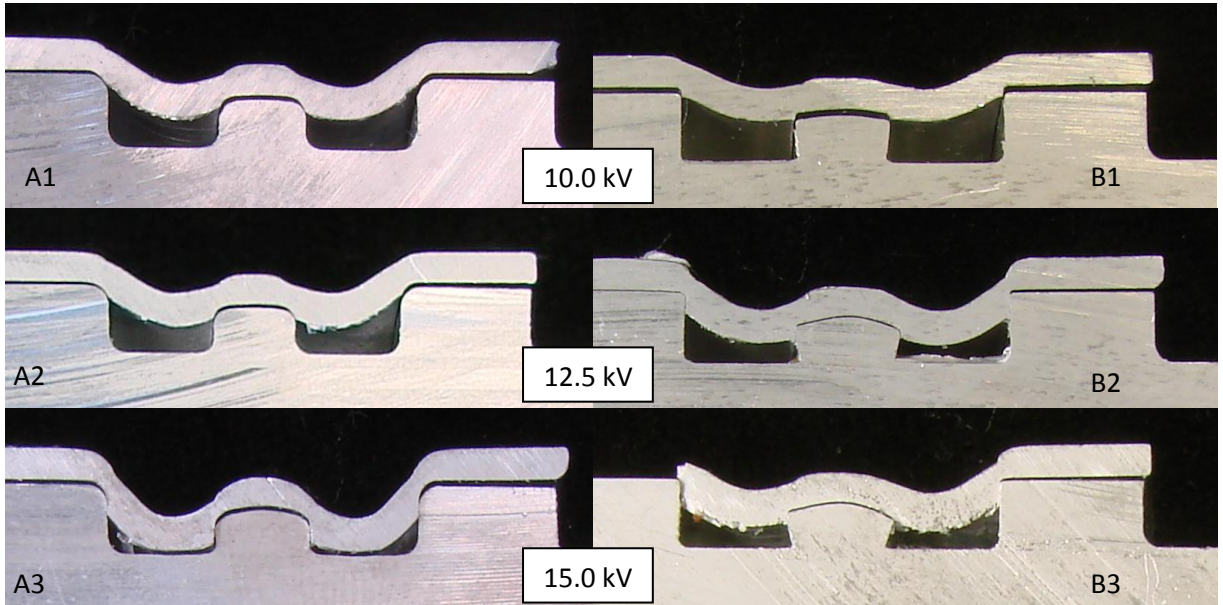


Figure 5.8: Cross sections of the samples of test series A.

Figure 5.9: Cross sections of the samples of test series B.

The tensile strength of the axial crimp joint design A was equal to 39.9 kN; a lower tensile strength of 23.2 kN was measured for design B. Both failed joints can be seen in Figure 5.10 and Figure 5.11. The lower maximum tensile strength of design B is attributed to the excessive thinning of the tube at edge 1_1 (the critical point) due to the sharp edges. Both designs failed at this critical point while the other zones of the crimp joint did not seem to experience deformation during tensile testing. More detailed investigation of the deformation during tensile testing can be found in chapter 7. Because the tube at the second groove did not deform during tensile loading, it might be probable that this second groove did not absorb much force and therefore, a relatively small joint strength (compared to the single groove joint strength) is found.



Figure 5.10: Tensile test sample of test series A (39.9 kN).



Figure 5.11: Tensile test sample of test series B (23.2 kN).

Important to mention is that in design B, even before submitting a tensile force, the tube was already cut at certain zones along the circumference. After crimping, the tube of sample B4 was almost cut at edge 2₂. By removing the crimp joint out of the test setup, small forces were applied on this zone. These forces had torn the tube apart at edge 2₂. Luckily, this zone is of the least importance for the tensile strength.

5.4.3 Test series C

5.4.3.1 Design and setup

In the third axial joint design (design C), two dissimilar grooves were used. As mentioned in the introduction, this is done because the joint strengths does not increase proportional. The tube wall thickness reduction at edge 1₁, the critical zone, needs to be minimised in order to create a strong crimp joint. Compared to designs A and B, the groove depths were changed. A groove depth of 2 mm was used for the first groove and a depth of 3 mm for the second groove. All groove radii were set to 1 mm (as in design A). No diameter reduction was used for the central collar. Figure 5.11 shows the internal workpiece of design C, while Table 5.5 lists all process parameters.

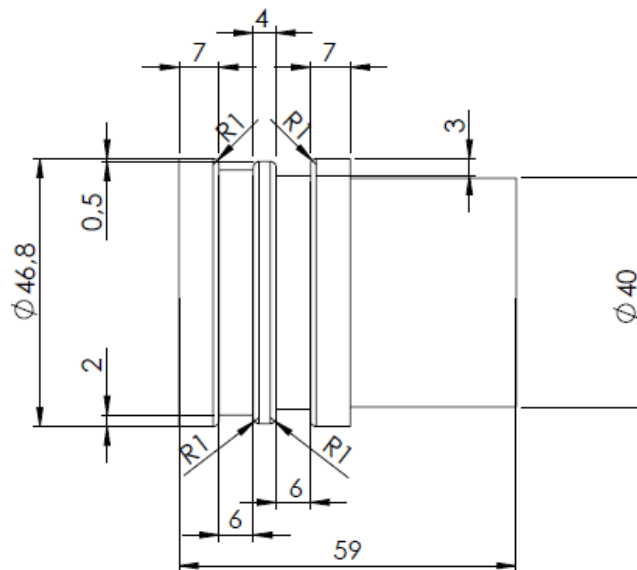


Figure 5.12: Axial crimp joint design C.

Design Name	groove 1				collar			groove 2			Total length k	applied voltage [kV]
	radius a	width b	depth c	radius d	width e	depth f	radius g	width h	depth i	radius j		
C1	1	6	2	1	4	0	1	6	3	1	59	10.0
C2	1	6	2	1	4	0	1	6	3	1	59	12.5
C3	1	6	2	1	4	0	1	6	3	1	59	15.0
C4	1	6	2	1	4	0	1	6	3	1	159	12.5

Table 5.5: Geometrical (in mm) and process parameters of test series C.

5.4.3.2 Results

In sample C1 (10.0 kV), the tube does not touch the first groove's bottom. Thus, to obtain an interference fit in the first (left) groove, a larger charging voltage has to be applied. In sample C2 (12.5 kV), a clear zone of interference fit can be observed. Increasing the voltage to 15.0 kV, will increase the length of this zone with a limited amount. More obvious is the increase in radial displacement of the tube in the second groove. Compared to designs A and B, this radial displacement is smaller because of the higher collar in between the grooves in design C.

Note that in the free deformation, the tube was cut, for a groove width equal to 6 mm and an edge radius equal to 1 mm, when a charging voltage of 15 kV was applied. This is not the case when a limited groove depth is present. A part of the energy during deformation of the tube goes to the plastic deformation of the internal part.

Although a shallow groove depth and relatively large edge radii were used for the first groove, tube wall thinning at both grooves' edges is significant in sample C3, leading to a decreased joint strength. Also, the first groove's bottom experienced little plastic deformation. Thinning of the tube wall at edge 2_2 is comparable to the thinning in sample A3.

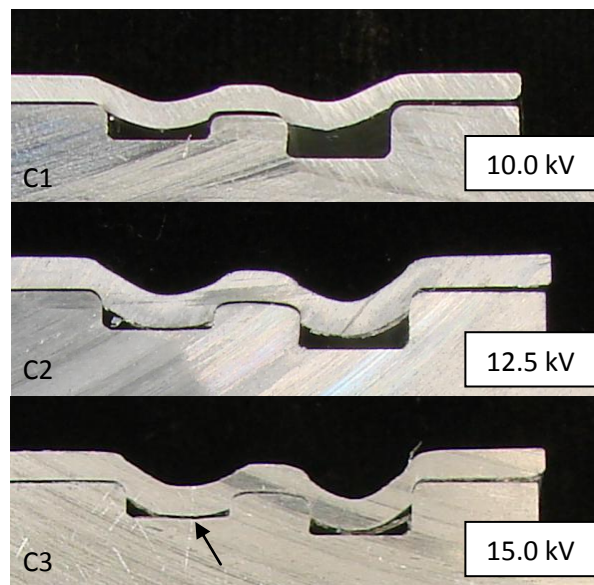


Figure 5.13: Cross sections of the samples of test series C.

The strength of axial crimp joint design C, formed at 12.5 kV was equal to 39.3 kN. The failed crimp joint is shown in Figure 5.14. The tensile strength is comparable to the tensile strength of the axial crimp joint design A, although better results were expected because dissimilar grooves were used. This unexpected result could be explained by the severity of local thinning at the critical zone. It can also be concluded that the distribution of the applied load over the two grooves is not equal and further groove optimization is needed.

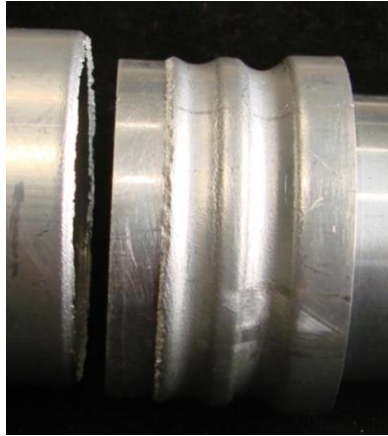


Figure 5.14: Tensile test sample of test series C (39.3 kN).

5.4.4 Test series D

5.4.4.1 Design and setup

The fourth axial joint design (design D) was also based on two dissimilar grooves. To further optimise the joint strength, some modifications were made. First, to further minimise thinning of the tube wall at the critical point, the groove depth was further decreased to 1.5 mm compared to the previous designs. Second, the groove width was increased to 8 mm, which will lead to a larger contact zone of the tube and the internal workpiece, increasing the frictional factor in equation 5.1. Third, the width of the second groove was reduced to 4 mm. This was done due to the limited axial space in the field shaper and to keep the central collar width equal to 4 mm.

In design C, the tube did not touch the bottom of the second groove, not even at high charging voltages. With the similar design of series D, but with a reduced groove width, the depth of the second groove could be reduced. The groove depth of the second groove was reduced to 2.5 mm. Figure 5.15 shows the drawing of design D, while Table 5.6 lists all process parameters used in test series D.

The lower limit of the charging voltage was increased to 11.0 kV. The upper limit was equal to 15.0 kV and the middle voltage was calculated (with equation 5.2) as 13.2 kV.

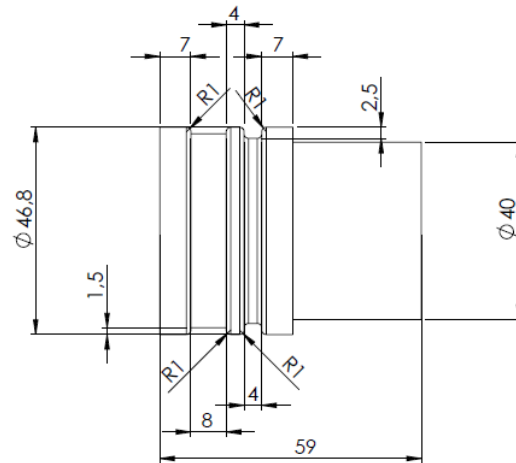


Figure 5.15: Axial crimp joint design D.

Design Name	groove 1				collar				groove 2			Total length k	applied voltage [kV]
	radius a	width b	depth c	radius d	width e	depth f	radius g	width h	depth i	radius j			
D1	1	8	1.5	1	4	0	1	4	2.5	1	59	11.0	
D2	1	8	1.5	1	4	0	1	4	2.5	1	59	13.2	
D3	1	8	1.5	1	4	0	1	4	2.5	1	59	15.0	
D4	1	8	1.5	1	4	0	1	4	2.5	1	159	12.5	

Table 5.6: Geometrical (in mm) and process parameters of test series D.

5.4.4.2 Results

For all applied voltages, the tube touched the bottom of the first groove. When increasing the charging voltage, the internal part is plastically deformed over a large zone in the first groove. The second groove is narrow and the tube deforms very little inside the groove. Compared to previous designs, thinning at the critical zone is reduced and a strong joint is expected.

The strength of the axial crimp joint design D, formed at 12.5 kV, was equal to 41.7 kN. The result of the failed crimp joint is shown in Figure 5.16. The crimp joint failed again at the critical zone, where tube wall thinning occurred. The tensile strength of joint design D is the highest so far and is approximately equal to the joint strength of single groove design X (which was 41.8 kN).

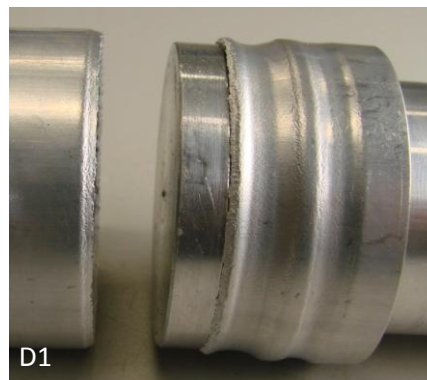


Figure 5.16: Tensile test sample of test series D (41.7 kN).

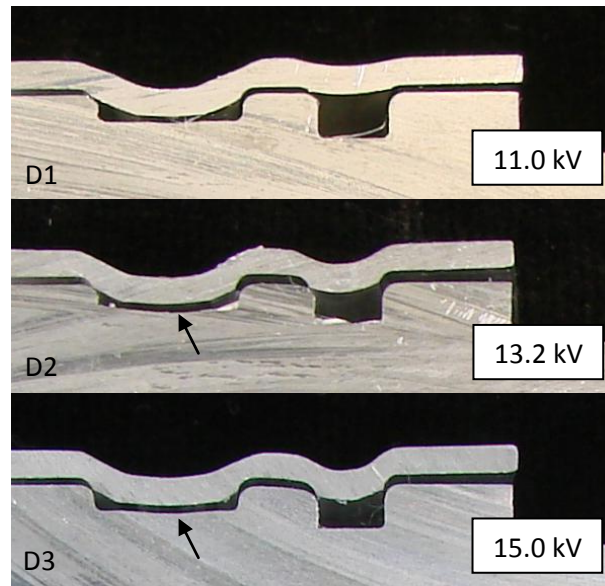


Figure 5.17: Cross sections of the samples of test series D.

5.4.5 Test series E & F

5.4.5.1 Design and setup

Because the strength of the axial crimp joint designs A to D is still lower than the strength of a single groove crimp joint design, further optimisation is required. The axial joint designs E and F are improved designs of type A and F respectively. As could be concluded in test series A and B, the tube did not make contact with the groove bottom, unless high voltages were applied. In that case, the tube thinning was excessive in test series A, and the tube was cut in test series B. So friction does not contribute to the joint strength. To create friction, shallower grooves are required. Grooves of 2 mm deep were chosen. Because of the reduced groove depth, the edge radius of the collar had to be changed in test series E (physical limitation). An edge radius of 0.5 mm was used. No edge rounding was used for test series F.

Because not too much useful information could be obtained for low voltages, the lower limit voltage was increased to 11.0 kV. The upper limit was equal to 14.0 kV and the middle voltage was calculated (with equation 5.2) as 12.6 kV. These charging voltages are also used in the succeeding test series.

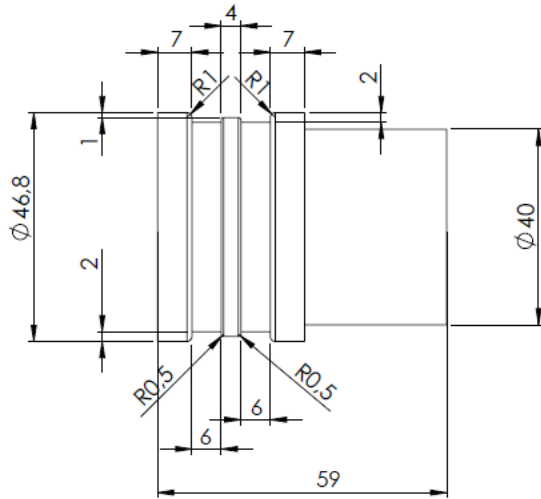


Figure 5.18: Axial crimp joint design E.

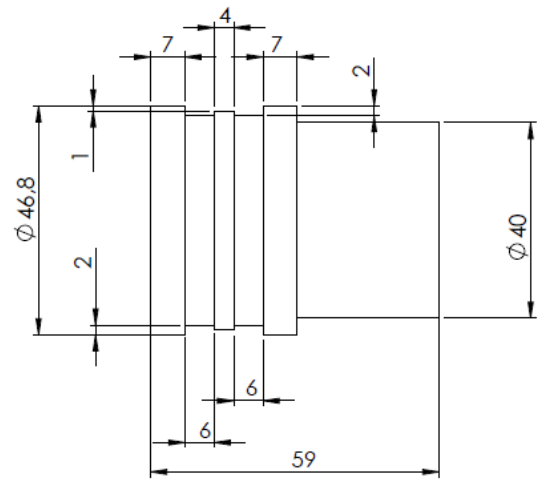


Figure 5.19: Axial crimp joint design F.

Design Name	groove 1				collar			groove 2			Total length k	applied voltage [kV]
	radius a	width b	depth c	radius d	width e	depth f	radius g	width h	depth i	radius j		
E1	1	6	2	0.5	4	1	0.5	6	2	1	59	11.0
E2	1	6	2	0.5	4	1	0.5	6	2	1	59	12.6
E3	1	6	2	0.5	4	1	0.5	6	2	1	59	14.0
E4	1	6	2	0.5	4	1	0.5	6	2	1	159	12.5
F1	0	6	2	0.0	4	1	0.0	6	2	0	59	11.0
F2	0	6	2	0.0	4	1	0.0	6	2	0	59	12.6
F3	0	6	2	0.0	4	1	0.0	6	2	0	59	14.0
F4	0	6	2	0.0	4	1	0.0	6	2	0	159	12.5

Table 5.7: Geometrical (in mm) and process parameters of test series E & F.

5.4.5.2 Results

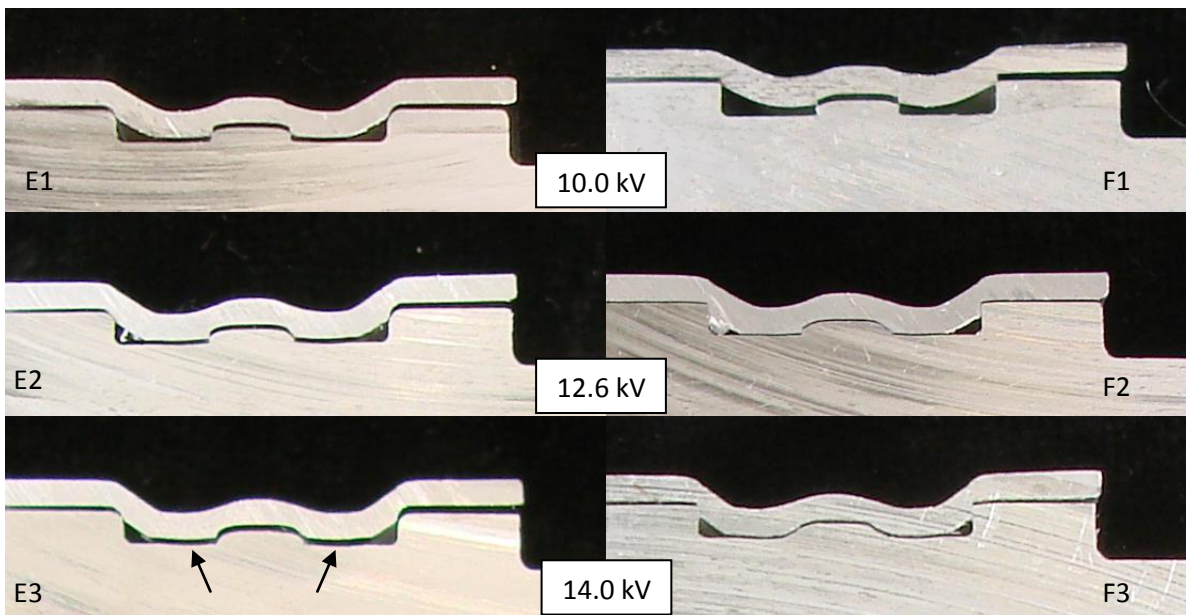


Figure 5.20: Cross sections of the samples of test series E. Figure 5.21: Cross sections of the samples of test series F.

The tube makes contact with the bottom of both grooves. This results in the desired frictional load transfer. Less wall thinning is observed at the groove edges which should result in a stronger joint. Little difference is observed, in samples E1, E2 and E3, in the axial length over which the tube touches the internal part for the different applied voltages. Little plastic deformation of the groove bottom is noticed for sample E3, performed at the highest energy level. The central collar is plastically deformed and the edges have been flattened due to the high forces exerted during the crimping process. This effect is more visible for the samples in test series F. The sharp edges of the central collar are plastically deformed due to the impact of the tube during the crimping process. The result is that for high voltages, no shearing of the tube is noticed at edges 1_2 and 2_1 .

The strength of the axial crimp joint type E, formed at 12.5 kV, was equal to 45.4 kN. The failed crimp joint is shown in Figure 5.22. The strength of the axial crimp joint type F, also formed at 12.5 kV, was equal to 48 kN. This failed crimp joint is shown in Figure 5.23. Unlike test series A and B, the design with sharp groove edges (design F) had the highest joint strength. Sharp edges combined with deep grooves are not beneficial because the tube will be cut, but sharp edges with shallow grooves is beneficial for the tensile strength. More investigation on this subject can be found in the next chapter.

When the axial crimp joint sample E4 was created, the tube only deformed inside the second groove. This could be the result of an incorrect positioning of the sample in the pulse machine. Instead of shearing at the first edge of the second groove, the whole tube was pulled off from the internal workpiece. Both samples have the highest tensile strength thus far and exceed the strength of a single groove crimp joint.



Figure 5.22: Tensile test sample of test series E (45.4 kN).

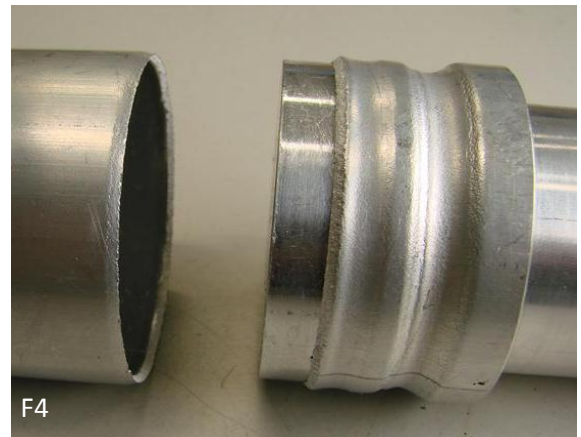


Figure 5.23: Tensile test sample of test series F (48 kN).

5.4.6 Test series G

5.4.6.1 Design and setup

The axial joint design G is an improved design of type C. The internal part is shown in Figure 5.24. Both groove depths have been reduced with 1 mm compared to design C in order to create a larger contact zone and thus more frictional load transfer. The first groove edge radii were reduced to 0.5 mm for edge 1_1 and no edge radius (0 mm) for edge 1_2 . From the previous test

series, it was noticed that a sharp edge on a sunk collar gives no clear problems for shearing the tube, but instead deforms the collar edge.

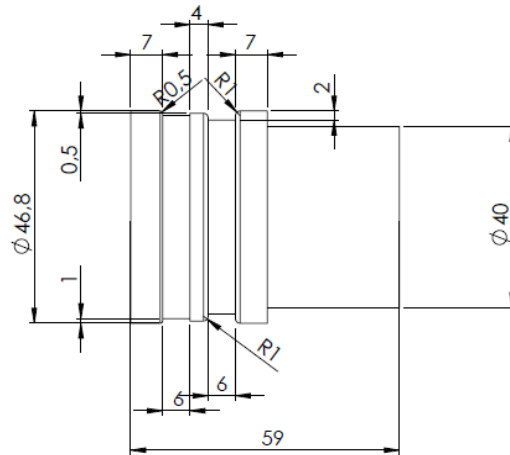


Figure 5.24: Axial crimp joint design G.

Design Name	groove 1				collar				groove 2			Total length k	applied voltage [kV]
	radius a	width b	depth c	radius d	width e	depth f	radius g	width h	depth i	radius j			
G1	0.5	6	1	0	4	0.5	1	6	2	1	59	11.0	
G2	0.5	6	1	0	4	0.5	1	6	2	1	59	12.6	
G3	0.5	6	1	0	4	0.5	1	6	2	1	59	14.0	
G4	0.5	6	1	0	4	0.5	1	6	2	1	159	12.5	

Table 5.8: Geometrical (in mm) and process parameters of test series G.

5.4.6.2 Results

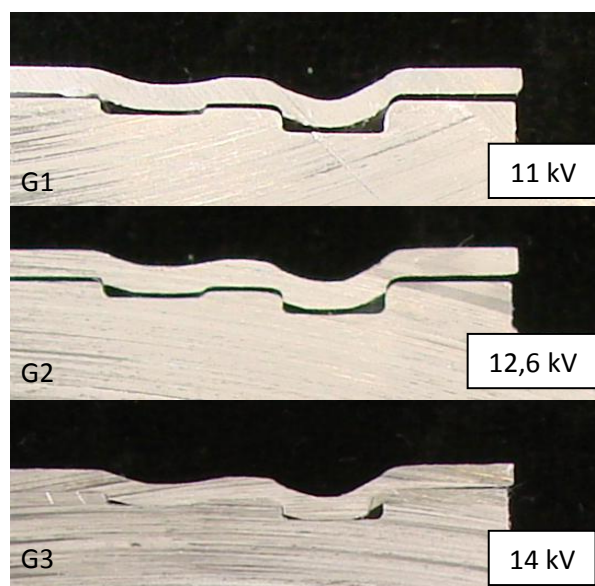


Figure 5.25: Cross sections of the samples of test series G.

Very little difference is seen between the deformation of the tube in samples G1 and G2 (see Figure 5.25). The sharp collar edge is plastically deformed, as was expected. In sample G3, the tube remained connected to the internal workpiece, even after being cross sectioned. This is the result of a good compression of the tube onto the internal workpiece.

The strength of the axial crimp joint type G, formed at 12.5 kV, was equal to 37.9 kN. This is a surprisingly low tensile strength (comparable to the tensile strength of single groove design Y). This crimp joint failed at the critical point, edge 1₁, due to shearing. The failed crimp joint is shown in Figure 5.26.



Figure 5.26: Tensile test sample of test series G (37.9 kN).

5.4.7 Test series H

5.4.7.1 Design and setup

The axial joint design H is an improved design of type D. Similar to design G, both groove depths have been reduced with 1 mm compared to design D to create a larger contact zone and thus more frictional load transfer. The first groove was then 0.5 mm and therefore, no edge radii at the first groove were used because not much necking was expected. Because the tube did almost not deform into the second groove in design D, the second groove width was increased to 6 mm. To meet the condition of the limited axial length of the field shaper, the collar width had to be decreased with 2 mm. The internal part is shown in Figure 5.27.

Design Name	groove 1				collar			groove 2			Total length k	applied voltage [kV]
	radius a	width b	depth c	radius d	width e	depth f	radius g	width h	depth i	radius j		
H1	0	8	0.5	0	2	0	1	6	1.5	1	59	11.0
H2	0	8	0.5	0	2	0	1	6	1.5	1	59	12.6
H3	0	8	0.5	0	2	0	1	6	1.5	1	59	14.0
H4	0	8	0.5	0	2	0	1	6	1.5	1	159	12.5

Table 5.9: Geometrical (in mm) and process parameters of test series H.

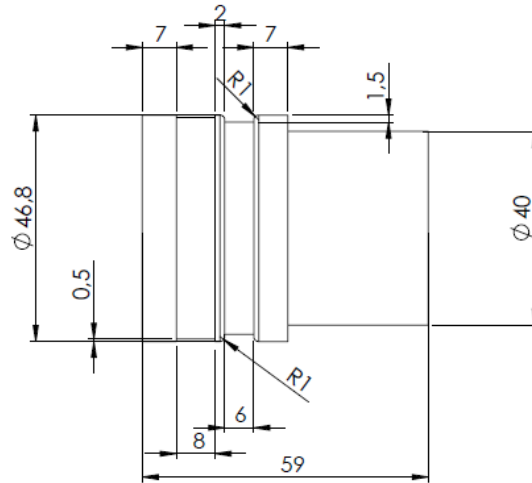


Figure 5.27: Axial crimp joint design H.

5.4.7.2 Results

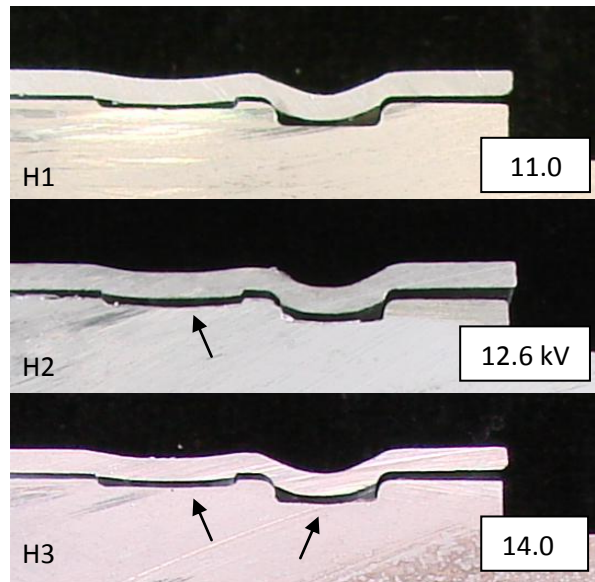


Figure 5.28: Cross sections of the samples of test series H.

In the three samples H1, H2 and H3, the tube experienced little shearing at the sharp edges of the first groove. Even for high a voltage, little shearing is visible. In design F and G, the sharp edges of the collar were flattened by the tube. The tube in design H was initially in contact with the collar and thus no large impact of the tube on these edges was possible. The tube in sample H3, performed at 14.0 kV, touched the bottom of the second groove and plastic deformation can be observed.

The strength of axial crimp joint design H, performed at 12.5 kV, was equal to 53.8 kN. This is the highest tensile strength obtained. Relative to the theoretical tensile strength of the tube this is 96%. It can be seen in Figure 5.29 that the tube sheared half at the critical point and half in the base material. This is a very promising result, because it proves that by optimising a double groove design, it is possible to create a strong joint which is (almost) as strong as the base

material. The design also indicates that the assumption put forward in the literature [25] of an optimised design with a shallow first groove and a deeper second groove might be correct. The parameter combinations for an optimal design will be further investigated in the next chapter.



Figure 5.29: Tensile test sample of test series H (53.8 kN).

5.5 CONCLUSION

It was assumed that the tensile strength of a single groove crimp joint can be increased by increasing the number of grooves. Some finite element simulations showed that, when axially loading a double groove crimp joint, the tube experiences severe local stress at the edge of both grooves.

To gain knowledge about the tube deformation into the grooves of a double groove design, eight test series of four samples were performed. In all test series, three joints were cross sectioned and one joint was subjected to tensile testing. The results of the tensile tests is shown in Table 5.10.

Sample name	groove 1				middle			groove 2			tensile strength [kN]	relative tensile strength [%]
	radius a	width b	depth c	radius d	width e	depth f	radius g	width h	depth i	radius j		
A4	1.0	6	3.5	1.0	4	1.0	1.0	6	3.5	1	29.9	53.4
B4	0.0	6	3.5	0.0	4	1.0	0.0	6	3.5	0	23.3	41.4
C4	1.0	6	2.0	1.0	4	0.0	1.0	6	3.0	1	39.3	70.0
D4	1.0	8	1.5	1.0	4	0.0	1.0	4	2.5	1	41.7	74.3
E4	1.0	6	2.0	0.5	4	1.0	0.5	6	2.0	1	45.4	80.9
F4	0.0	6	2.0	0.0	4	1.0	0.0	6	2.0	0	48.0	85.5
G4	0.5	6	1.0	0.0	4	0.5	1.0	6	2.0	1	37.9	67.5
H4	0.0	8	0.5	0.0	2	0.0	1.0	6	1.5	1	53.8	96.0
X	0.0	6	1.0	0.0							41.8	74.5
Y	1.0	6	1.5	1.0							35.9	64.0

Table 5.10: Results of tensile test of test series A to H, X and Y.

A first observation is that the tube did not feed any material into the groove during deformation. Further, it was seen that the use of sharp edges and deep grooves could cut the tube, and thus

create a weak crimp joint. On the other hand, if sharp edges were combined with a shallow groove depth, the crimp joint had a good tensile strength.

It is useless to combine deep grooves with a small groove width because the tube will almost not deform into the groove, not to mention touch the groove bottom. It is beneficiary to have a tube that touches the groove bottom, because this induces frictional load transfer and the joint will become stronger.

The amount of tube wall reduction was less in those designs where a sunk collar was present. In those designs, the tube impacts on the collar and plastically deforms the collar. If the collar has sharp edges, the tube will plastically deform the edges and the edge radius will increase.

Also the bottom of the groove might be plastically deformed if the charging voltage level is high.

Sample H4 had a tensile strength which was very close to the tensile strength of the base material. This promising result indicates that it might be possible to create a crimp joint with a strength (almost) as strong as the base. The optimisation of the design parameters of a double groove axial crimp joint is further investigated in the next chapter.

Chapter 6: Design of Experiments

6.1 Introduction

In the previous chapter, it was demonstrated that a double groove design for axial crimp joints can lead to a higher tensile strength than with a single groove design. In a double groove design, there are many parameters which affect the joint integrity and furthermore, these parameters can possibly have a combined effect as well.

In order to obtain the optimal setting for each process parameter in a structured way, a statistical approach is often used [42-44]. In this thesis, the choice was made to use Design of Experiments (DoE). Experimental design or DoE is a powerful technique to investigate the influence of a certain amount of parameters and also the mutual interaction. The concept is to gain as much information as possible with a minimal amount of experiments. In general, to investigate the influence of n parameters at two levels, 2^n experiments are required. DoE takes out a subset, reducing the number of experiments. This causes a certain loss of information, but it is still possible to draw statistically sound conclusions if the subset is well chosen. This reduction of experiments is of great importance because costs can be reduced and time demanding analysis can be performed only on relevant specimens.

It should be noted that the preliminary experiments and the free deformation experiments which are described in the previous chapters were required in order to use DoE in an effective way. The results of those experiments offer the possibility to make well-founded choices when selecting the most important parameters and when determining realistic values for these parameters.

6.2 Test setup

6.2.1 Choosing the parameters for DoE

The parameters which might have an influence on the tensile strength are indicated in Figure 6.1.

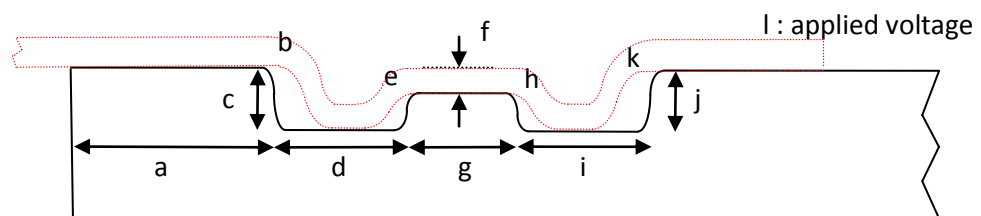


Figure 6.1: Parameters for a double groove internal workpiece (a: axial length in front of the first groove – b: first edge radius of the first groove – c: first groove depth – d: first groove width – e: second edge radius of the first groove – f: collar depth – g: collar width – h: first edge radius of the second groove – i: second groove width – j: second groove depth – k: second edge radius of the second groove – l: voltage applied).

Parameter a is the axial length of the part left of the first groove. This length provides a frictional factor in equation 5.1. It does not change the deformation of the tube inside the groove because the tube material in that zone does not feed material into the groove (see chapter 5). The effect of this parameter is known: increasing the axial length increases the frictional factor (depending on how tight the fitting is between the tube and the internal part in this zone) and thus increases the joint strength. In general, a loose fitting between the parts is used and the effect of this parameter will be negligible. Also, economically seen, it is unbeneficial to increase this length because extra material is needed and the material cost will be higher. This parameter will not be considered in the DoE.

The groove depth and length of both grooves (parameters c , d , i and j) are important parameters because they determine the groove geometry for a major part and they must be taken into account in the DoE.

Only one of the two edge radii from each groove is of importance. Using finite-element simulations with Abaqus (see chapter 5), it was noted that the tube tends to get pulled out of the grooves when performing a tensile test, imposing a force on the first edge of the first groove and on the first edge of the second groove. Thus, the second edge of each groove (parameters e and k) will be of less importance when loading an axial crimp joint. They will not be taken into account in the DoE.

The collar length between the grooves (parameter g) will be determined by the limited axial length of the field concentration zone of the field shaper. The sum of the first groove's width, the width of the collar in between the grooves and the second groove's width must be approximately equal to the total axial length of the work zone of the field shaper.

The charging voltage (parameter l) will also be of importance, because it determines the strength of the repelling magnetic fields, and as a consequence the tube deformation.

The preliminary experiments, as well as experiments performed in a previous thesis [10] showed that the depth of the collar between the two grooves is important for the joint strength.

Summarising, the influence of eight parameters (b , c , d , f , h , i , j , l) will be investigated on level 2 (meaning that every parameter can have two different values). Each experiment will be repeated in order to get an idea on the scatter on the results.

6.2.2 Parameter values

Because the DoE uses a 2-level design, each parameter will be varied at two values. These values must be chosen wisely and they must meet two conditions. First, the difference between the two values should be maximal. Second, the values of the different parameters must be combinable and realistic.

Grooves with a sufficient depth to allow a complete edge radius have been assumed here, see Figure 6.2 on the right. For example, the combination of an edge radius of 2 mm with a groove depth of 0.5 mm is not allowed, as shown in Figure 6.2 on the left.

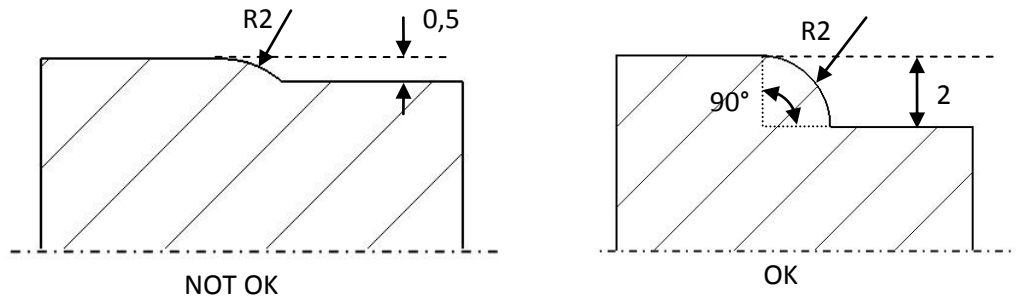


Figure 6.2: A smaller edge radius than the groove depth is not allowed.

The nomenclature and the dimensions that all samples have in common can be found in Figure 6.3. The same nomenclature and dimensions as in the preliminary experiments are used. The first edge of the first groove is called edge 1_1 , the second edge of the first groove is called edge 1_2 , the first edge of the second groove is edge 2_1 and the second edge of the second groove is called edge 2_2 . All specimens have a total axial length of 159 mm, required for tensile testing. The part with a diameter 40 mm and an axial length 130 mm is required to clamp the workpiece into the tensile testing machine.

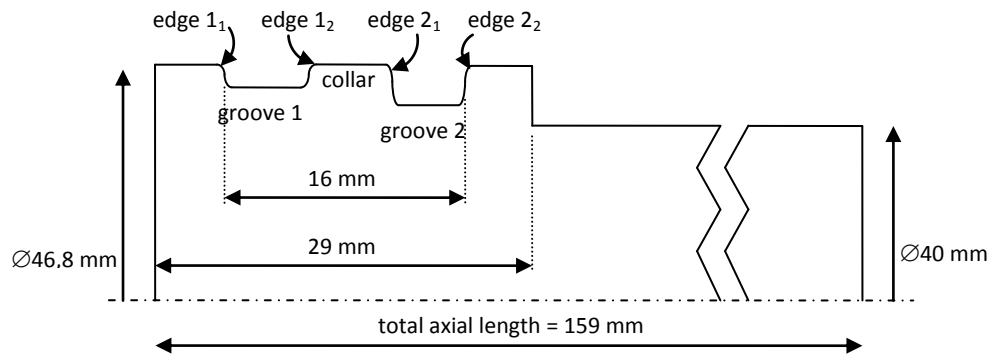


Figure 6.3: Nomenclature and common dimensions for the DoE samples.

Based on previous experiments (chapter 4 & 5), the following values have been chosen:

Parameter	Lower value	Upper value
b = edge 1_2	0.5 mm	1.5 mm
c = depth groove 1	1.5 mm	3.0 mm
d = width groove 1	6.0 mm	8.0 mm
f = collar depth	0 mm	1.0 mm
h = edge 2_1	0.5 mm	1.5 mm
i = width groove 2	4.0 mm	6.0 mm
j = depth groove 2	2.5 mm	4.0 mm
l = charging voltage	10.5 kV	12.0 kV

Table 6.1: Overview of the parameters' upper and lower values.

The first step is to choose two values for the collar depth (parameter f). The collar depth will be varied between 0 (no depression) and 1 mm. With these values, the lower limit of the groove's depth must be at least 1 mm.

A sharp edge (edge radius = 0 mm) would cut the tube during deformation (see § 5.4.2), so 0.5 mm was taken as the lower limit value for all edge radii. The values of edge 1_2 and edge 2_1 have been set to 0.5 mm. The upper limit value of edge 1_1 and edge 2_1 have been chosen to be equal to 1.5 mm.

The depth of the first groove must be minimal 1.5 mm (the maximal edge radius of edge 1_1 is equal to 1.5 mm and the collar depth of 1 mm combined with edge 1_2 also demands a minimal depth of 1.5 mm). The upper limit value is chosen to be 3 mm.

Because the preliminary experiments proved that a design with a long shallow first groove generated the highest tensile strength, the upper value of the first groove's width is chosen to be slightly larger than that of the second groove. The sum of both groove widths and the length of the central collar must be approximately equal to the field shaper length. Finite-element calculations [20] show that a small area outside the effective work zone also experiences sufficient magnetic forces. In this case, the axial length of the work zone of the field shaper is 15 mm and the total field concentration zone was assumed to be equal to 16 mm. Equalising the lower limit value for the width of the first groove and the upper limit value for the width of the second groove, creates the opportunity for the DoE to disprove the assumption that a slightly larger width of the first groove would generate a higher tensile strength. The width of the first groove cannot be too small because the tube must be able to deform into the groove. Neither must this width be too large because it must stay combinable with the chosen second groove width. The lower limit is chosen to be equal to 6 mm, and equal to the upper limit of the second groove's width.

Because of strength considerations, a minimal collar length of 2 mm has been assumed, resulting in an upper value for the first groove's width of 8 mm (8 mm + 2 mm + 6 mm = axial field concentration length). The lower limit of the second groove's width must not be too small because deformation must be possible into the groove. This value is chosen to be 4 mm.

The depth of the second groove must be at least 2.5 mm. This is because the most extreme combination of the collar's depth of 1 mm and the edge radius of 1.5 mm imposes this lower value. The upper value was chosen to be equal to 3.5 mm, so that the difference between both values is large enough to draw conclusions.

It is useless to choose a value which is larger than 3.5 mm, because experiments performed with a single groove show that the combination of a groove width of 6 mm with an edge radius of 0.5 mm or 1.5 mm leads to a radial inward displacement which does not exceed 3 mm when 12 kV is applied. A lower voltage (10.5 kV) or a smaller groove width (4 mm) will cause an even smaller inward displacement (see chapter 4). A larger groove depth than 3.5 mm would also increase the machining cost, without any other benefits.

Also based on the free deformation experiments, the values for the applied charging voltage were chosen. The lower limit is chosen to be 10.5 kV and the upper limit is 12 kV. These values can deform the tube in every groove combination possible and yet do not cut the tube in any location.

6.2.3 Test-matrix

The number of experiments to perform is determined by the DoE design, the number of parameters and the level of assessment. The level indicates the number of values for each parameter. In this case, a fractional factorial design is performed with n parameters, each varied at two levels. The number of experiments required in a fractional factorial design is a fraction of the 2^n experiments needed in the case of a full factorial design. In this study, only a fourth of the experiments required for a full factorial design were performed, resulting in a so-called 'resolution IV' test setup. This means that it is possible to distinguish the influence of a single parameter from the combined interaction effect of two parameters (also called a 2-level interaction). The resolution describes the degree to which estimated main effects are confounded (or aliased) with estimated 2-level interaction, 3-level interactions,... In general, the resolution of a design is one more than the smallest order interaction that some main effect is confounded (aliased) with. Resolution III cannot distinguish the influence of a single parameter because some effects are confounded with a double effect.

In this study, resolution IV is desired because all single parameter effects are important to investigate. To reach a resolution IV with 8 parameters and at two levels, at least 16 experiments have to be conducted. The more experiments are performed, the more double effects can also be investigated. There are 28 double effects for 8 parameters (combination of 2 out of 8 = $\binom{8}{2}$). Performing 64 (2^{8-2}) experiments allows to investigate 22 of 28 double effects. Six double effects are confounded with each other. Each experiment will be performed twice to reduce the scatter and to increase the statistical reliability. The statistical reliability is also dependent on α (see below). With Matlab, a test matrix was designed, which is shown in Table 6.2. The '-1' indicates the lower limit value of the parameter and the '+1' is the upper limit value.

Trial number	X1	X2	X3	X4	X5	X6	X7	X8
1	-1	-1	-1	-1	-1	-1	1	1
2	-1	-1	-1	-1	-1	1	-1	-1
3	-1	-1	-1	-1	1	-1	-1	-1
4	-1	-1	-1	-1	1	1	1	1
5	-1	-1	-1	1	-1	-1	-1	-1
6	-1	-1	-1	1	-1	1	1	1
7	-1	-1	-1	1	1	-1	1	1
8	-1	-1	-1	1	1	1	-1	1
9	-1	-1	1	-1	-1	-1	-1	-1
10	-1	-1	1	-1	-1	1	1	1
11	-1	-1	1	-1	1	-1	1	-1
12	-1	-1	1	-1	1	1	-1	-1
13	-1	-1	1	1	-1	-1	1	1
14	-1	-1	1	1	-1	1	-1	-1
15	-1	-1	1	1	1	-1	-1	-1
16	-1	-1	1	1	1	1	1	1
17	-1	1	-1	-1	-1	-1	-1	1
18	-1	1	-1	-1	-1	1	1	-1
19	-1	1	-1	-1	1	-1	1	-1
20	-1	1	-1	-1	1	1	-1	1
21	-1	1	-1	1	-1	-1	1	-1
22	-1	1	-1	1	-1	1	-1	1
23	-1	1	-1	1	1	-1	-1	1
24	-1	1	-1	1	1	1	1	-1
25	-1	1	1	-1	-1	-1	1	-1
26	-1	1	1	-1	-1	1	-1	1
27	-1	1	1	-1	1	-1	-1	1
28	-1	1	1	-1	1	1	1	-1
29	-1	1	1	1	-1	-1	-1	1
30	-1	1	1	1	-1	1	1	-1
31	-1	1	1	1	1	-1	1	-1
32	-1	1	1	1	1	1	-1	1
33	1	-1	-1	-1	-1	-1	-1	1
34	1	-1	-1	-1	-1	1	1	-1
35	1	-1	-1	-1	1	-1	1	-1
36	1	-1	-1	-1	1	1	-1	1
37	1	-1	-1	1	-1	-1	1	-1
38	1	-1	-1	1	-1	1	-1	1
39	1	-1	-1	1	1	-1	-1	1
40	1	-1	-1	1	1	1	1	-1
41	1	-1	1	-1	-1	-1	1	-1
42	1	-1	1	-1	-1	1	-1	1
43	1	-1	1	-1	1	-1	-1	1
44	1	-1	1	-1	1	1	1	-1
45	1	-1	1	1	-1	-1	-1	1
46	1	-1	1	1	-1	1	1	-1
47	1	-1	1	1	1	-1	1	-1
48	1	-1	1	1	1	1	-1	1
49	1	1	-1	-1	-1	-1	1	1
50	1	1	-1	-1	-1	1	-1	-1
51	1	1	-1	-1	1	-1	-1	-1
52	1	1	-1	-1	1	1	1	1
53	1	1	-1	1	-1	-1	-1	-1
54	1	1	-1	1	-1	1	1	1
55	1	1	-1	1	1	-1	1	1
56	1	1	-1	1	1	1	-1	-1
57	1	1	1	-1	-1	-1	-1	-1
58	1	1	1	-1	-1	1	1	1
59	1	1	1	-1	1	-1	1	1
60	1	1	1	-1	1	1	-1	-1
61	1	1	1	1	-1	-1	1	1
62	1	1	1	1	-1	1	-1	-1
63	1	1	1	1	1	-1	-1	-1
64	1	1	1	1	1	1	1	1

Table 6.2: DoE test matrix where '-1' denotes the lower value and '1' the upper value.

Table 6.3 indicates the possibilities of distinguishing the single and the double effects of the 8 parameters.

'Factor'	'Confounding'	'Factor'	'Confounding'
'X1'	NO	'X2*X6'	NO
'X2'	NO	'X2*X7'	'X1*X8 + X2*X7'
'X3'	NO	'X2*X8'	'X1*X7 + X2*X8'
'X4'	NO	'X3*X4'	NO
'X5'	NO	'X3*X5'	NO
'X6'	NO	'X3*X6'	NO
'X7'	NO	'X3*X7'	NO
'X8'	NO	'X3*X8'	NO
'X1*X2'	'X1*X2 + X7*X8'	'X4*X5'	NO
'X1*X3'	NO	'X4*X6'	NO
'X1*X4'	NO	'X4*X7'	NO
'X1*X5'	NO	'X4*X8'	NO
'X1*X6'	NO	'X5*X6'	NO
'X1*X7'	'X1*X7 + X2*X8'	'X5*X7'	NO
'X1*X8'	'X1*X8 + X2*X7'	'X5*X8'	NO
'X2*X3'	NO	'X6*X7'	NO
'X2*X4'	NO	'X6*X8'	NO
'X2*X5'	NO	'X7*X8'	'X1*X2 + X7*X8'

Table 6.3: Overview of the parameter setup and confounding possibilities.

The 8 selected parameters b, c, d, f, h, i, j and l in Table 6.1 should be assigned to the eight parameters X1 to X8 in Table 6.3. The double effect of parameters X1 and X2 for example cannot be distinguished from the double effect of parameters X7 and X8. Both couples are confounded (or aliased). Assigning the parameters b up to l to X1 up to X8 must be done wisely. Figure 6.4 shows the assignment of the statistical parameters to the physical parameters.

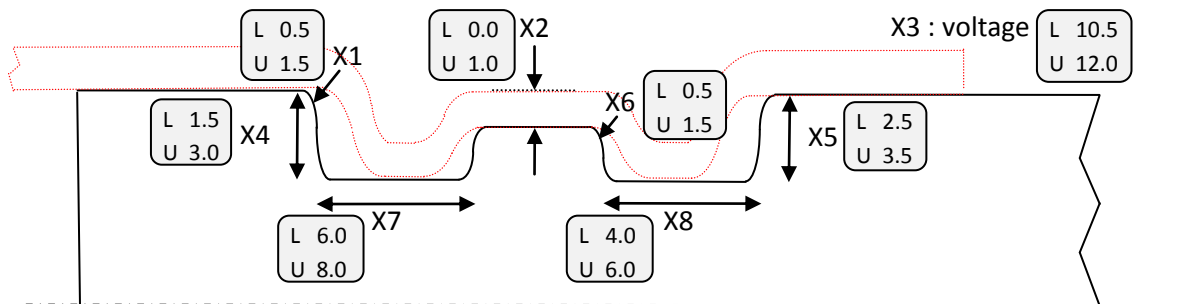


Figure 6.4: Parameters (in mm) according to the test matrix and with the lower- (L) and the upper- (U) values expressed in mm and in kV (only for the charging voltage X3).

As is discussed in the results below, the aliasing which occurs with the choice of the parameters does not cause any difficulties for a proper evaluation.

6.3 Discussion of the experiments

6.3.1 Analytical background of the evaluation method

To determine the important parameters in the crimp joint design, a statistical approach of the DoE is used. The Analysis of Variance (ANOVA) will help to determine whether or not a parameter induces a significant change in the output value. A brief explanation of ANOVA for DoE is given below [45].

In this case, 64 specimens are designed with proper parameter settings. Every experiment has been done twice, providing two values y_1 and y_2 for the output value y (= relative tensile strength). For every experiment, an average value of the maximum tensile strength can be calculated as:

$$\bar{y}_r = \frac{\sum_{i=1}^{n_r} y_i}{n_r} = \frac{y_1 + y_2}{2} \quad (6.1)$$

where y_i is an individual measured test value and n_r is the number of response values for run r (in this case, $n_r = 2$). For a specific parameter, the average measured output values for the '-1' and '+1' settings are noted as $\bar{y}_{par,-}$ and $\bar{y}_{par,+}$ respectively.

The difference is defined as:

$$\Delta = \bar{y}_{par,+} - \bar{y}_{par,-} \quad (6.2)$$

If this difference Δ is large, it means that the choice of the input parameter value has a significant influence on the output value. Is this difference large enough to conclude that the true means $\mu_{par,+}$ and $\mu_{par,-}$ (both estimated by the experimental means) are different? To judge whether or not Δ is large enough to result in a significant effect, Δ is compared with the variation S_r^2 :

$$S_r^2 = \frac{\sum_{i=1}^{n_r} (y_i - \bar{y}_r)^2}{(n_r - 1)} \quad (6.3)$$

For this comparison, a statistical framework consisting of two complementary statements or hypotheses about the true state of nature:

H_0 : $\mu_{par,+} = \mu_{par,-}$, meaning the parameter has no influence on the output value.

H_1 : $\mu_{par,+} \neq \mu_{par,-}$, meaning the parameter does have an influence on the output value.

H_0 is called the "null hypothesis" and H_1 the "alternative hypothesis". Since statistical conclusions are obtained with less than 100% certainty, either conclusion has a probability of error. Table 6.4 shows the two types of error that can occur.

Decision resulting from data analysis	True condition	
	H ₀ false ("Change has occurred")	H ₀ true ("No change")
Reject H ₀ ("Change has occurred")	Correct decision (1-β: Power of the test)	Error (Type I) (α)
Fail to reject H ₀ ("No change")	Error (Type II) (β)	Correct decision

Table 6.4: Type I and Type II error if the conclusion is not correct [46].

Statistical hypothesis tests are commonly designed in such a way that the most critical decision error is a Type I error (α). So α needs to be set to a minimum level. In this case, the commonly used value 0.01 is chosen. This means that there exists a 1% chance that a parameter is concluded to be important when it is actually not. A Type II error (β) indicates the missed detection rate. Holding α constant and minimising β requires an increased number of experiments to perform. For this case (sample size 2), β is 0.30 [47]. This means that there exists a 30% chance of missing a significant term if one really exists. The power of the test, $1 - \beta$, is 70% and this means that there exists 70% chance of finding a significant term if one really exists.

Variation exists within each run of replicated response values and also between high and low average output values. It is possible to estimate the true variability σ^2 in two independent ways. The variance of each run (S_r^2) could be used to estimate σ^2 but a better estimate will be obtained by pooling all the S_r^2 -values. This pooled estimate of run variances is referred to as mean square error (MSE) and can be calculated as follows:

$$MSE = \frac{\sum(df_r)(S_r^2)}{\sum(df_r)} = \frac{\sum(n_r - 1)(S_r^2)}{\sum(n_r - 1)} \quad (6.4)$$

where the sum is taken over all design matrix runs. This MSE is a weighted average of the S_r^2 -values.

Assuming H_0 is true implies that $\bar{y}_{par,-}$ and $\bar{y}_{par,+}$ are both estimates of μ and they both vary about μ with variance $\sigma_y^2 = \sigma^2/n'$ where n' is the number of data values used to determine each \bar{y} . A second estimation of σ^2 called 'mean square between' can be made with the following equation:

$$MSB = n' \cdot S_{\bar{y}}^2 \quad (6.5)$$

Which in a 2-level design results in a simpler form of

$$MSB = \frac{N}{4} (\Delta_{par}^2) \quad (6.6)$$

where N is the total number of output values obtained in the entire experimental matrix. Since MSE and MSB are independent estimates of σ^2 , their ratio

$$F_0 = \frac{MSB}{MSE} \quad (6.7)$$

behaves according to an F-distribution. If the null hypothesis (H_0) is true, the F_0 -value is usually close to unity, where in the other case MSB will increase, causing an F_0 -value larger than one. In the latter case, a comparison with the theoretical F-distribution must be made.

First the F_C -value must be looked up in an F table, where $F_C = F(1 - \alpha, df_B, df_E)$. df_B is the degree of freedom for MSB, equal to the number of levels minus one (for this 2-level design $df_B = 1$). The degrees of freedom for MSE, df_E , is equal to the following sum:

$$df_E = \sum (n_r - 1) \quad (6.8)$$

In this case $df_E = 64 \cdot (2 - 1) = 64$. Now the F_0 -value is compared to the F_C -value and if $F_0 \leq F_C$, the null hypothesis is true meaning that this parameter has no significant effect on the response or output value. On the other hand, if $F_0 > F_C$, the null hypothesis is rejected and the parameter is concluded to have a significant effect on the response. This latter verdict has 99% chance (with $\alpha = 0,01$) of being correct. All of the above is integrated in the statistical software package MINITAB [48], and this package was used to analyse the results.

An equation predicting the relative tensile strength of an optimal design, can also be generated with the calculated results of the ANOVA. The predicted value of the output parameter is:

$$\hat{y} = \bar{y} + \left(\frac{\Delta_A}{2}\right) \cdot A + \left(\frac{\Delta_B}{2}\right) \cdot B + \dots \quad (6.9)$$

where A is a coded value of -1 through +1 for the significant parameter A. If no significant parameters are found, then the prediction equation simply becomes $\hat{y} = \bar{y}$ [45].

6.3.2 Scatter on the DoE

The relative tensile strength of the crimp joint was chosen as output value y for the evaluation of the DoE. The relative tensile strength is equal to the ratio of the tensile strength of the specimen to the experimental tube's tensile strength. This ratio was defined to eliminate the effect of the

differences in tensile strength of the used tube materials. It is therefore possible to do extra verification tests later on without requiring the original base material.

Aluminum EN AW-6060 T6 tubes coming from three different batches (see § 4.2) were used. . Two specimens (based on ASTM B221) of every batch of base material were subjected to a tensile test on the Instron 4505 universal testing machine and the maximum tensile strength was recorded. The testing machine has a load cell of 10 kN. Figure 6.5 shows the tensile testing machine, a sample according to ASTM B221 and four specimens after failure. The stress-displacement curves of base material 1 and 2 are represented in respectively Figure 6.6 and Figure 6.7. Due to technical difficulties, the stress-displacement curves of base material 3 were not captured, but only the ultimate tensile strength (UTS) was recorded. The results of the tensile tests can be found in Table 6.5. These values are used to calculate the relative tensile strength of the crimp joints. When comparing the ratio of the yield strength (YS) over the ultimate tensile strength (UTS) of base material 1 and 2, an equal ratio is noticed. This means that an equal strain hardening behaviour is observed in the different batches.

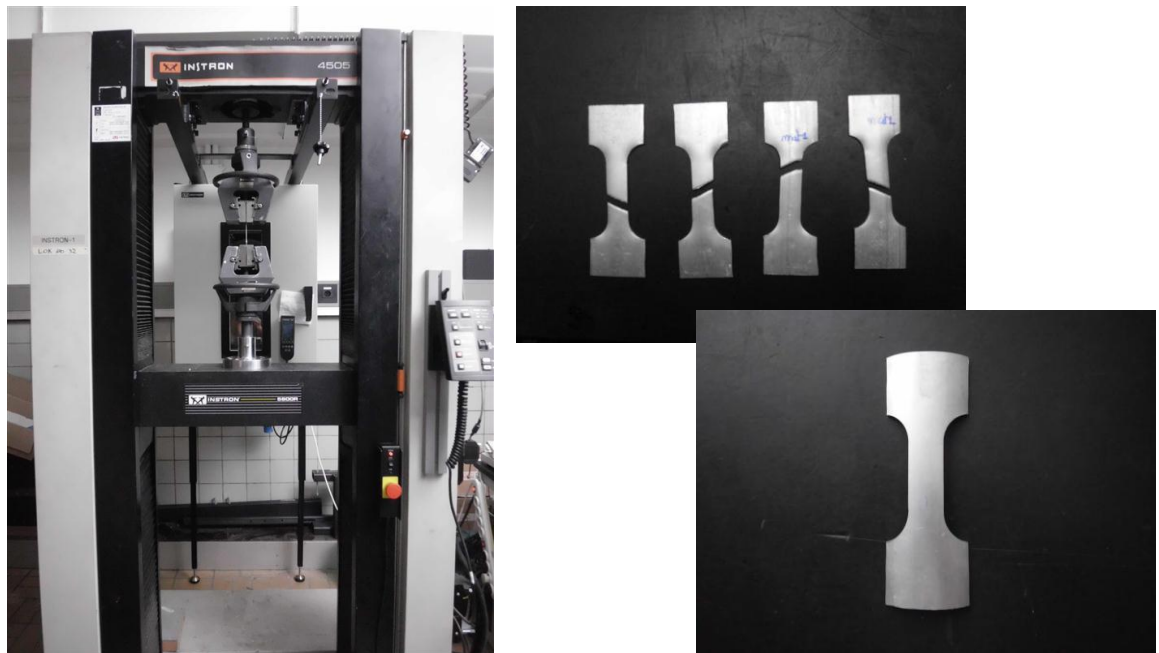


Figure 6.5: Instron 4505 tensile testing machine and specimens according to ASTM B221.

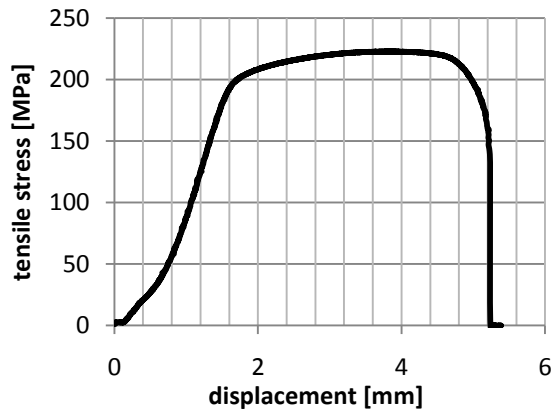


Figure 6.6: Stress versus displacement curve of base material 1.

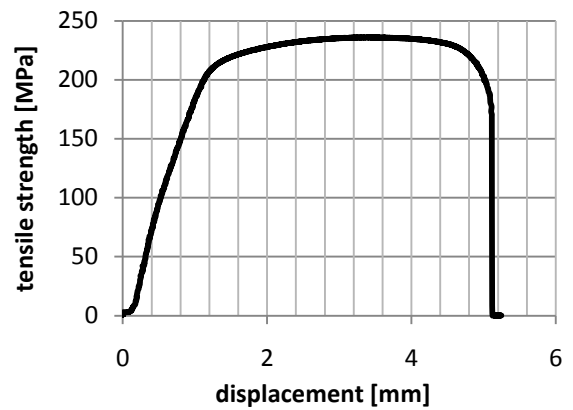


Figure 6.7: Stress versus displacement curve of base material 2.

Tube base material	Avg. YS [MPa]	Avg. UTS [MPa]	Ratio YS/UTS
1	196.7	219.5	0,896
2	211.9	235.4	0,900
3	X	221.9	X

Table 6.5: Strength properties of the tube materials.

As mentioned before, each experiment was repeated once in order to evaluate the scatter on the results. As a criterion, it was set that a scatter of less than 10% on the relative tensile strength between the two test series is acceptable. Thirteen couples of samples did not meet this criterion. This can be due to scatter on the base material, scatter in the crimping process, an imperfect alignment in the tensile testing machine, scatter in strength-measuring sensors and LVDT, etc. Thirteen verification samples were produced and tensile tests were performed. For each condition it was determined which of the two tensile strengths was out of range, and this value was replaced by the tensile strength obtained with the verification specimen.

In Figure 6.8, the scatter is shown in 4 different types of graphs generated by Minitab. Each of them shows that the scatter is within the 10% criterion (the two right graphs) and it can be seen that a normal distribution is found (the two left graphs). It can therefore be concluded that the results of the executed DoE will be valid.

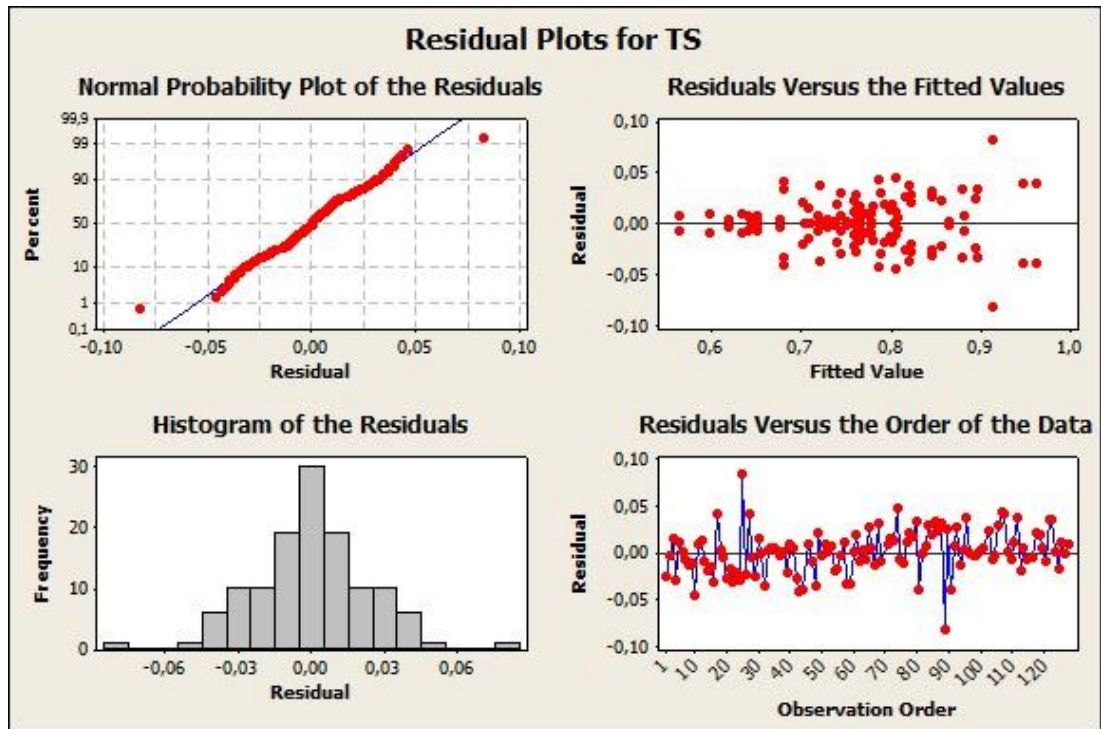


Figure 6.8: Residual plots (generated by Minitab) for the output value TS (= tensile strength) for evaluation of the scatter.

6.3.3 Results

The absolute tensile strength of the crimp joints was determined using the Amsler universal testing machine (at testing capacity 120 kN). The relative tensile strength was determined as explained before, by using the base material tensile strength (see Table 6.5).

Also, the load versus displacement curves were recorded for each tensile test, since these provide important information about the failure behaviour, which needs to be taken into account in the interpretation of the results (see chapter 7).

The results of the tensile tests are represented in Table 6.6. The samples with an average relative joint tensile strength between 95% and 100% are marked in dark blue. The samples with an average relative tensile strength between 90% and 95% are marked in a lighter blue, and the ones with an average relative tensile strength between 85% and 90% are marked in a light blue colour. The overall average of the relative tensile strength is equal to 76.362 % ($= \bar{y}$). All the relative tensile strength versus displacement curves of the samples are included in Appendix D.

design number	relative tensile strength 1st series [%]	relative tensile strength 2nd series [%]	average tensile strength [%]	design number	relative tensile strength 1 [%]	relative tensile strength 2 [%]	average tensile strength [%]
1	79.0	84.4	81.7	33	86.7	86.5	86.6
2	75.9	76.6	76.3	34	62.2	61.5	61.9
3	81.3	78.6	80.0	35	73.4	72.5	73.0
4	75.9	82.0	79.0	36	71.0	71.0	71.0
5	81.7	79.6	80.6	37	67.3	68.0	67.6
6	70.3		70.3	38	72.1		72.1
7	71.1	72.7	71.9	39	73.7	78.2	76.0
8	69.4	72.3	70.9	40	64.7	63.1	63.9
9	74.7	76.9	75.8	41	77.0	76.2	76.6
10	75.9	85.1	80.5	42	73.3	79.1	76.2
11	89.1	87.4	88.3	43	74.5	83.0	78.8
12	77.8	75.4	76.6	44	64.0	72.2	68.1
13	76.9	78.9	77.9	45	59.0	64.6	61.8
14	68.1	72.3	70.2	46	57.1	55.6	56.4
15	74.9	78.2	76.6	47	58.7	60.7	59.7
16	64.7	71.2	68.0	48	68.3	75.6	72.0
17	100.3	92.4	96.4	49	84.3	80.4	82.4
18	74.1	73.6	73.9	50	64.8	62.7	63.8
19	73.7	75.1	74.4	51	64.3	62.6	63.4
20	79.5	85.1	82.3	52	80.4		80.4
21	72.0	75.9	73.9	53	65.7	64.3	65.0
22	81.3	87.9	84.6	54	77.4	81.3	79.4
23	83.4	88.0	85.7	55	76.3	79.7	78.0
24	71.3	77.4	74.3	56	63.9	64.8	64.3
25	99.8	83.3	91.5	57	78.4	76.5	77.5
26	87.1	92.1	89.6	58	84.7	91.5	88.1
27	98.7	90.8	94.7	59	86.4	93.1	89.8
28	80.2	81.4	80.8	60	75.6	75.5	75.6
29	82.0	87.2	84.6	61	81.9	78.2	80.0
30	77.4	74.8	76.1	62	76.0	78.0	77.0
31	74.9	75.1	75.0	63	78.0	77.7	77.8
32	78.5	85.8	82.2	64	76.7	78.3	77.5

Table 6.6: Tensile testing results.

Each sample is named according to the design and the series number. For example: sample X_i is referring to crimp joint-design X of the series i . Due to an error in the material delivery, the results of samples 6_2 , 38_2 and 52_2 are not included in Table 6.6.

The observations during and after tensile testing of the three designs with the highest relative tensile strength (designs 17,25 and 27), are discussed in detail below.

Sample 17₁ did not fail in the joint connection during tensile testing. A relative tensile strength of 100% was measured. The tube sheared in the base material. This is a very promising result for future designs. Figure 6.9 shows the failed crimp joint and Figure 6.10 shows the load-displacement curves corresponding with this design (samples 17₁ and 17₂). These curves represent what is called a 'normal' failure behaviour, meaning a sudden failure of the crimp joint by shearing of the tube in a certain zone (mostly at edge 1₁, for sample 17₁ exceptionally in the base material). A detailed discussion of the different failure behaviours can be found in the next chapter.

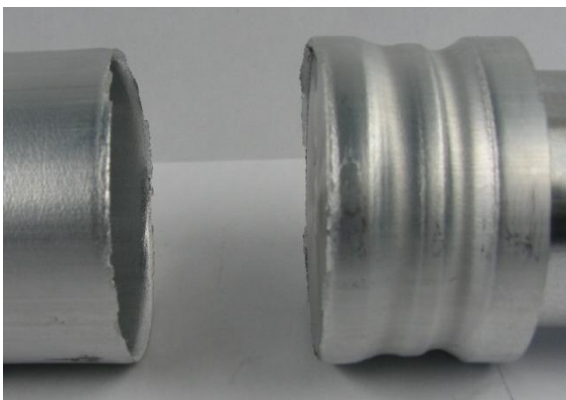


Figure 6.9: Failed crimp joint-sample 17₁.

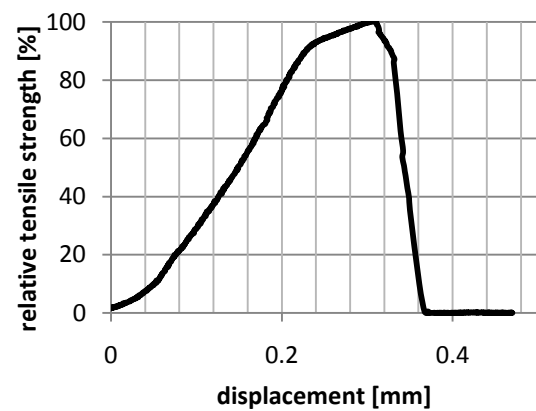


Figure 6.10: relative tensile strength versus displacement curve corresponding to sample 17₁.

In sample 17₁, the tube failed in the zone at the left side of the internal workpiece. The explanation is that the diameter of a tube tends to decrease during a tensile test as it absorbs the applied strain. At the point where the tube first makes contact with the internal workpiece, the internal workpiece constrains the diameter decrease of the tube. Thus, high stresses will be built up in this zone and the tube will fail there. Figure 6.11 shows the forces acting on the tube. The resultant force (F_{res}) is the vectorial sum of two perpendicular forces ($F_{tensile}$ and $F_{restrain}$).

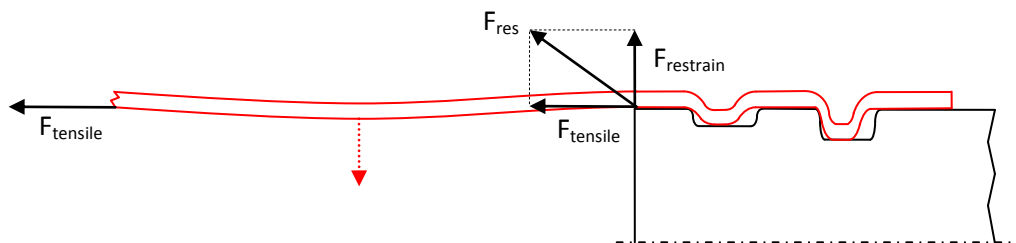


Figure 6.11: Explanation of failing at the internal workpiece's left edge.

Sample 17₂ failed at the critical zone (edge 1₁), and the tensile strength was equal to 92,4% of the base material tensile strength. This is within the acceptable limit of 10% difference between equal samples.

Design 27 is also close to the optimal design because the relative tensile strength in both series has a value of more than 90%.

It should be mentioned that in the first test series, for specimen of crimp joint-design 27 a relative tensile strength of 75.1% was recorded. Due to excessive scatter compared to the second test series (90.7%), a third sample was produced. The relative tensile strength of this sample was equal to 98.7%, and the value of 27_1 was replaced by this value. On one hand because the values then show the least amount of scatter, but on the other hand also because the specimens are taken from the same material batch, which is undeniably more reliable.

The value of 90.7% must be interpreted carefully: it lies within the acceptable limit of 10%, but sample 27_2 failed at the clamps of the tensile testing machine. The tube failed in the base material but no relative tensile strength of 100%, which is expected if the tube material fails before the crimp joint does, was observed. This is because localised stress concentrations were present in the tube at the clamping zone and possibly the clamping was not performed optimal for this specimen. Figure 6.12 shows the failed sample and indicates the different parts. When clamping, the tube is supported by an internal workpiece to create a good grip of the left- and right clamping chucks on the tube. The relative tensile strength versus displacement curves are similar to those of design 17.

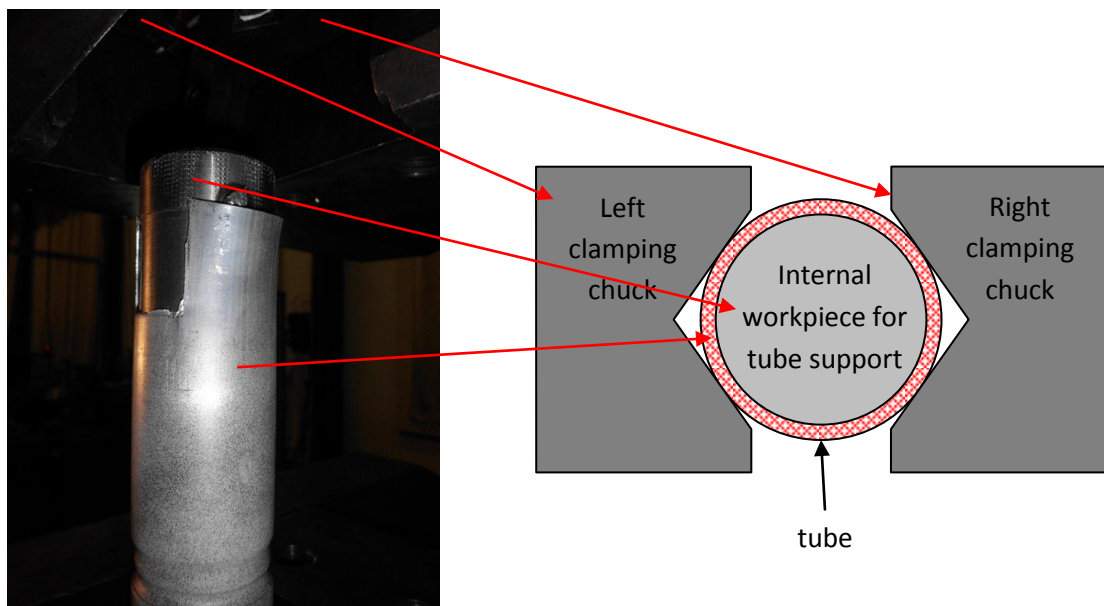


Figure 6.12: Failed crimp-joint sample 27_2 .

Design 25 initially showed more than 10% difference in the relative tensile strength (72.6% and 83.3%) between the two series and thus a third workpiece was made to reduce the scatter. Unfortunately, this introduced an even bigger difference in values. The two highest values have been taken into account (99.8% and 83.3%) and the third (low) value has been rejected, mainly because the same tube material was used for the two highest values, which is more reliable. Figure 6.13 shows the failed crimp joint, Figure 6.14 shows the relative tensile strength versus displacement curves corresponding to this design. The failure behaviour of sample 25_1 shows a sheared tube at the first groove edge over about $3/4^{\text{th}}$ of the perimeter and over approximately $1/4^{\text{th}}$ of the perimeter in the base material. The fact that the tube partially failed in the base material indicates that this is a strong crimp joint. Note that the zone where the base material

failed, is again at the left end of the internal workpiece (see Figure 6.11). This '1/4th-3/4th' failure behaviour can be attributed to non-concentric positioning into the universal testing machine.

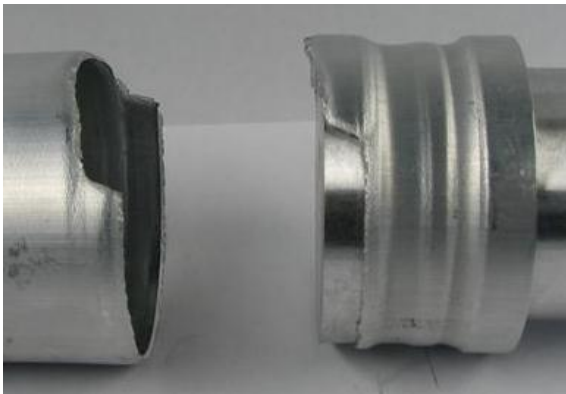


Figure 6.13: failed crimp joint-sample 25₁.

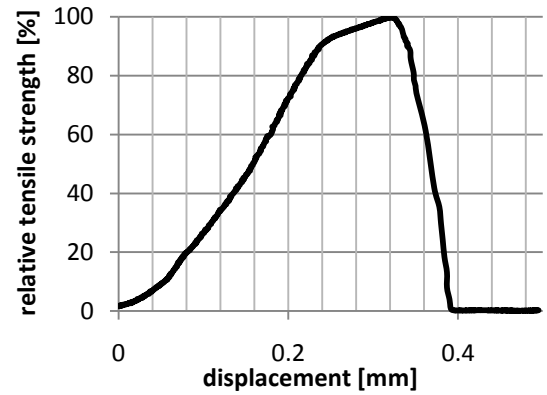


Figure 6.14: relative tensile strength-displacement curve corresponding to design 25₁.

The 3 best performing designs of the internal workpiece are shown in Figure 6.15. These designs have a small edge radius for the edges 1₁ and 2₁, the first groove is shallow and a collar diameter reduction is used. Design 17 and 27 also have a small first groove and a large second groove width in common.

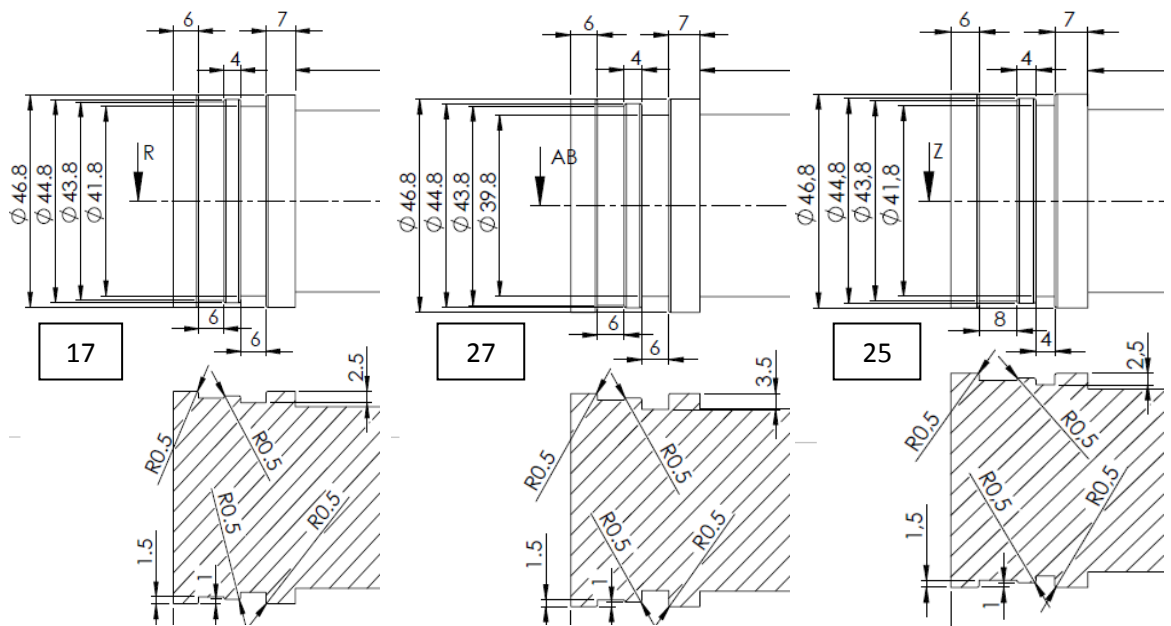


Figure 6.15: Technical drawings of designs 17, 25 and 27.

Trial number	X1	X2	X3	X4	X5	X6	X7	X8
17	-1	1	-1	-1	-1	-1	-1	1
27	-1	1	1	-1	1	-1	-1	1
25	-1	1	1	-1	-1	-1	1	-1

Table 6.7: Comparison of designs 17, 27 and 25.

Very promising results have been noticed, however no design was able to assure a minimal relative tensile strength of 100% in both specimens.

A Pareto-analysis was performed to extract the significant effects of the different parameters and parameter combinations on the relative tensile strength. A graphical presentation of this result is shown in Figure 6.16. The red line on the figure represents the accuracy (with $\alpha = 0.01$) criterion that is used for the reliability of the result. All bars on this Pareto-chart at the right of the red line are significant parameters. Their effect on the tensile strength and the uncertainty are listed in Table 6.8.

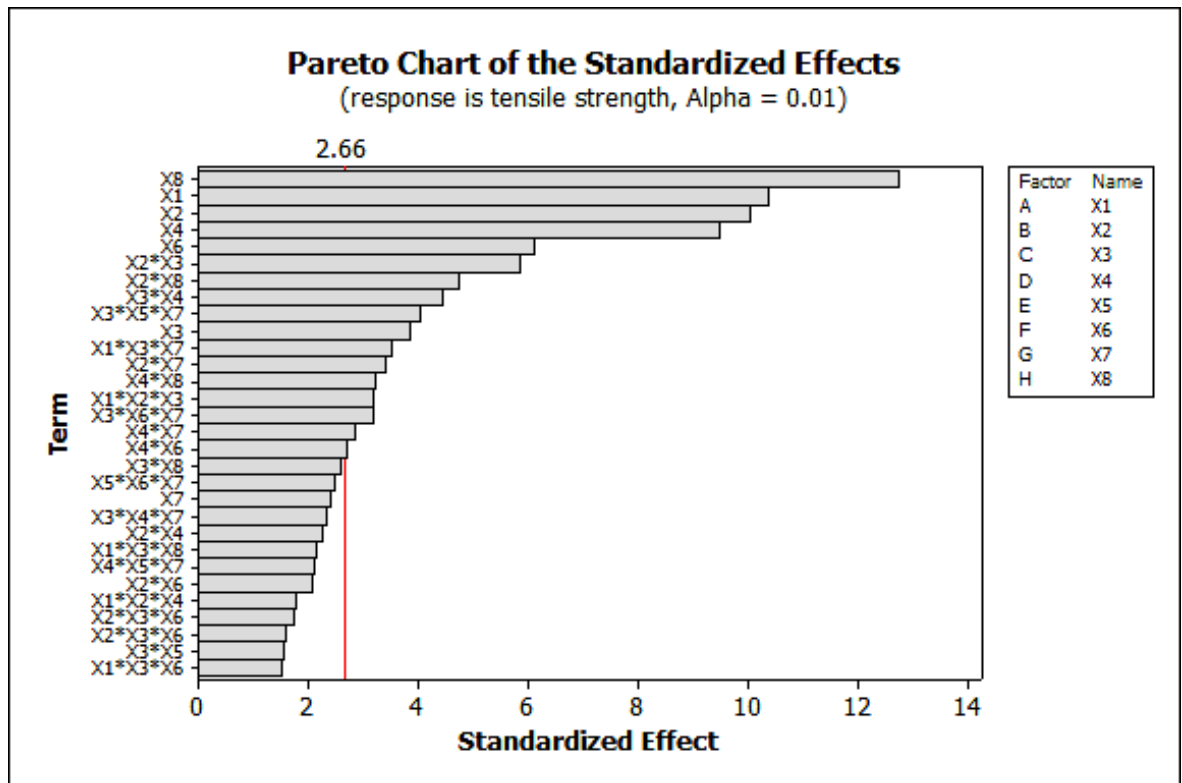


Figure 6.16: Pareto chart.

Parameter	Physical interpretation	Sign	Increase of relative Tensile Strength [%]	Uncertainty [%]
X8	Second groove width	+	7.7	0.0
X1	Edge 1 ₁	-	6.3	0.0
X2	Collar depth	+	6.1	0.0
X4	Depth first groove	-	5.8	0.0
X6	Edge 2 ₁	-	3.7	0.0
X2*X3	Collar depth and applied voltage	+	3.6	0.0
X2*X8	Edge 1 ₁ vs. first groove width	+	2.9	0.0
X3*X4	Applied voltage and first groove width	-	2.7	0.0
X3*X5*X7	-	-	2.5	0.0
X3	Applied voltage	+	2.3	0.0
X1*X3*X7	-	-	2.1	0.1
X2*X7	Edge 1 ₁ and second groove width	+	2.1	0.1
X4*X8	First groove depth and second groove width	-	1.9	0.2
X1*X2*X3	-	+	1.9	0.2
X3*X6*X7	-	-	1.9	0.2
X4*X7	First groove depth vs. first groove width	-	1.7	0.6
X4*X6	First groove depth vs. edge 2 ₁	+	1.6	0.9

Table 6.8: Significant effects of DoE for a confidence level of 1%.

6.4 Discussion of the results

Sixteen significant effects are appointed with a certainty level of 99%. Every important main effect and double effect is discussed below. The triple effects are of very little importance to the model and will not be discussed. An important remark is that the results of the DoE are only applicable for the parameter value variations used in the experiments. When it is stated that a sharp edge is profitable for the joint strength, it is not possible to assign an exact value to this.

6.4.1 Second groove width (X8)

The second groove width should be 6 mm instead of 4 mm when creating an axial crimp joint with these dimensions. A large groove width is needed to create a better 'filling' of the groove.

Figure 6.17 explains the effect of the groove width on the mechanical interlock in the groove (when an equal voltage is applied). When a pressure is applied on the outer diameter of the tube, the deformation process of the tube into the groove will be similar to a beam imposed onto two supports and will be subjected to an equally divided load. When the distance between the two supports increases, the tube will more easily deform between the supports. The angle θ on Figure 6.17 gives an indication for the mechanical interlock. The smaller the angle θ , the more mechanical interlock is possible.

The fact that the width of the second groove is so important based on the Pareto-analysis, is because the DoE was unintentionally influenced: the minimal width of the second groove had to be 4 mm due to the choice of the maximal length of the first groove, the minimal required length for the collar and the restriction on the axial length of the field concentration zone. In combination with the applied voltages, this width is too small to allow a decent deformation of the tube into the second groove. As a consequence, the mechanical interlock behind the edge 2_1 will be a lot smaller and this has a significant influence on the tensile strength of the crimp joint.

The width of the second groove should therefore always be chosen large enough to allow a sufficient deformation of the tube into the second groove. Also, as was concluded in chapter 4, a short groove will cause more shearing which results in more necking than in a long groove.

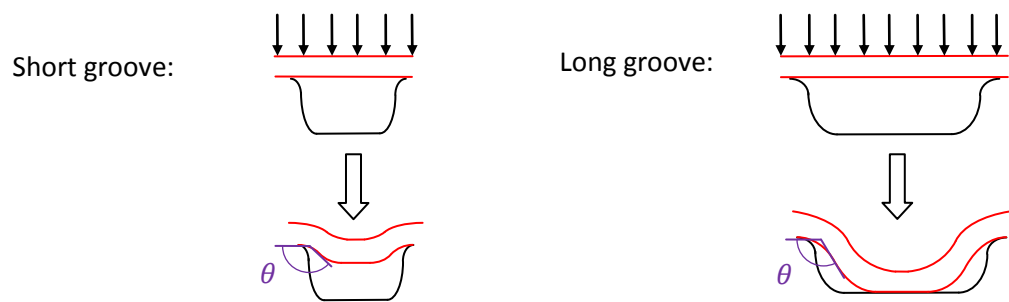


Figure 6.17: A difference of the groove width leads to a different mechanical interlock.

6.4.2 Edge 1_1 (X1)

In contrast to what initially was thought, a small edge radius is desired for the edge 1_2 . The first edge bears the major part of the axial load (see chapter 7) and thus there is a need for a good mechanical interlock. A sharp edge cannot be defined in values, but it can be said that for this design, it is better to use an edge radius of 0.5 mm than an edge radius of 1.5 mm.



Figure 6.18: A sharp edge will create better mechanical interlock.

6.4.3 Collar depth (X2)

For the optimal design, the collar depth must be chosen equal to 1 mm. During the tensile tests, it became clear that all designs with a sunk collar had a higher tensile strength than those without a sunk collar. This can be attributed to the fact that with a sunk collar, the tube first deforms into the gap covering the two grooves and later, when making contact with the collar, starts deforming in each groove separately (see Figure 6.19). When the tube deforms into a large gap, it acts like a beam imposed onto two supports with a large distance between the supports, under a

vertical evenly distributed load (the magnetic repulsive force from the coil). In Figure 6.19.A, the tube is divided into two beams imposed onto two supports, each with a small gap length. The tube experiences more shearing stress and less bending moment than in Figure 6.19.B. For an equal applied voltage and similar groove geometries in A and B, thinning in edge 1_1 and edge 2_2 will be less excessive in case B. A similar approach has been used in chapter 4.

It should be noted that in case A, the area of largest radial displacement of the deformed tube is approximately in the middle of the groove, while in case B the lowest area of the tube is found closer to the collar. The dotted vertical lines below the right part of Figure 6.19 indicate the position of these zones of maximal radial displacement. When these lines are positioned closer to the collar, a stronger mechanical interlock is obtained in the second groove. On the other hand, less mechanical interlock is obtained in the first groove, but this negative effect is compensated with less thinning at edge 1_1 .

In case of a sunk collar, some energy will be used for the deformation of the collar. In Figure 6.20, the cross sections of sample A2 and sample B2 from the preliminary experiments are shown. On sample A2 the red vertical lines indicate the zone of largest radial displacement, and on sample B2, a significant plastic deformation of the collar is marked in red.

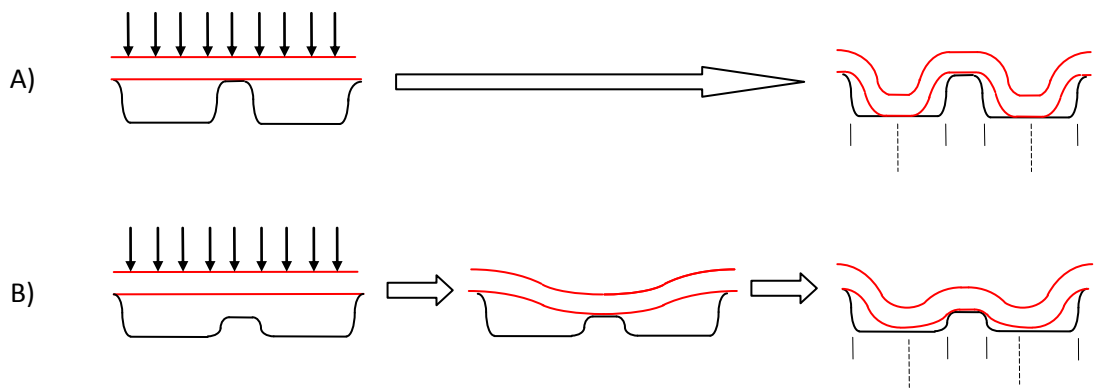


Figure 6.19: A sunk collar leads to less thinning and better interlock at the second groove.

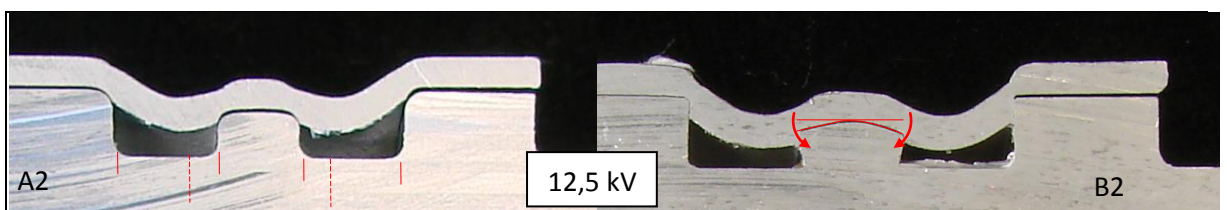


Figure 6.20: Influence of the collar depth on the radial displacement and on the deformation of the collar.

6.4.4 Depth of the first groove (X4)

The negative sign for this parameter indicates that it is beneficial to have a small depth of the first groove. This can be explained by the fact that the thinning at edge 1_1 will be less and so a sharper edge radius 1_1 can be allowed. This is beneficial because it creates a stronger mechanical interlock. Figure 6.21 indicates the influence of the groove depth on the thinning of the tube.

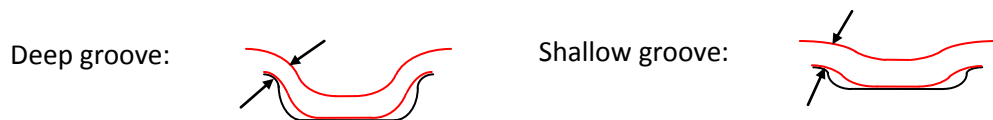


Figure 6.21: Influence of the groove depth on thinning.

6.4.5 Edge 2₁ (X6)

Again, a sharp edge 2₁ is desirable to create mechanical interlock in the second groove. In an optimal design, both grooves absorb tensile forces at the first groove edge. A sharp edge creates a mechanical interlock, so the tube is locked behind the corner.

6.4.6 Collar depth and applied voltage (X2*X3)

This second order effect contains the collar depth (parameter X2) and the applied voltage (parameter X3). As can be seen in Figure 6.19, when using a sunk collar, a high voltage is required to first bend the tube into the large gap covering the two grooves and to subsequently sufficiently deform the tube in each groove separately, while consuming some of the energy by deformation of the collar.

The fact that a sunk collar is desired to create a strong joint is already explained. The parameter X2 is thus positive (+ sign). The combined effect with X3 needs a positive sign to increase the joint strength. This implies a positive sign for parameter X3; the applied voltage.

6.4.7 Collar depth and width of second groove (X2*X8)

As already described above, with a sunk collar the zone of maximal radial displacement will be closer to the collar. This induces an increase of mechanical interlock at the second groove. Furthermore, when a larger second groove is present, the tube will more easily deform in this second groove, increasing the mechanical interlock even more. The increase of mechanical interlock due to a larger second groove in combination with a sunk collar also involves minimisation of the tube thinning at the edges.

It should be noted that X2*X8 is aliased with another 2-parameter effect: X1*X7 (edge 1₁ vs. width of first groove). It is more likely that the collar depth and the width of the first groove affect the joint strength than edge 1₁ together with the width of the first groove. Also, the main parameters X2 and X8 have significant effects, while parameter X7 almost does not appear in the list of significant effects on the joint strength (see Table 6.8).

6.4.8 Voltage and depth of first groove (X3*X4)

Increasing the joint strength by combining a shallow first groove (parameter X4, already discussed above) and a large charging voltage (parameter X3) is explained in Figure 6.22. A larger charging voltage increases the energy level. More energy induces more magnetic pressure, which in its turn results in more deformation of the tube. For a certain groove geometry, more deformation results in a better filling of the tube into the groove. A larger zone where the tube touches the

bottom of the groove can be noticed. This results in a better interference fit. Also, a better filling means that the angle θ decreases. This results in a better mechanical interlock. A shallow first groove in combination with a large charging voltage is preferred over a deep first groove in combination with the same large charging voltage, because there will be more contact and thus more interference fit when the groove is shallow.



Figure 6.22: A larger voltage creates a stronger interference fit and a stronger mechanical interlock.

6.4.9 Voltage (X3)

The positive sign of this main effect, was already noticed in previous effects. It is clear that a larger voltage causes more deformation and more filling into the grooves as already discussed above. More filling into both grooves means more mechanical interlock and some possible interference fit on the bottom of the grooves.

6.4.10 Collar depth and width of first groove (X2*X7)

The combination of a sunk collar and a large first groove is also beneficial for the crimp joint strength. A 2.1% increase is noticed (Table 6.8). When a large first groove is used, the tube can more easily deform into the groove. Moreover, when a sunk collar is present, the tube deforms even more into the groove while the tube wall reduction is minimised (see Figure 6.19).

It should be noted that this 2-parameter effect X2*X7 is aliased with X1*X8. It seems logical that the collar depth and the width of the first groove (effect X2*X7) are more related than edge 1₁ and the width of the second groove (effect X1*X8).

6.4.11 Depth of first groove and width of second groove (X4*X8)

The negative sign of this 2-parameter effect indicates that a large second groove width should be combined with a shallow first groove. A shallow first groove creates a good interference fit and minimises tube thinning at the first groove, while a large second groove width creates good filling and thus a good mechanical interlock into the second groove. When the tube is pulled out of the first groove, it still experiences sufficient restraining forces in the second groove, allowing the two-groove design to obtain a maximal strength. This combination however only leads to a 2% increase in crimp joint strength. This combination comes out so strongly because both parameters X4 and X8 have an individual strong effect on the joint strength.

6.4.12 Depth of first groove and width of first groove (X4*X7)

The combination of a shallow and wide first groove is good, but only leads to an increase of 1.7% of the joint strength. It was initially expected that this effect should be more pronounced.

A large groove width allows good filling of the tube into the groove, while a shallow groove minimises thinning. The combination of both parameters is profitable.

6.4.13 Depth of first groove and edge 2_1 (X4*X6)

This is the combination of a shallow first groove and a large edge radius 2_1 . There is 0.9% uncertainty for this effect. We can neglect the outcome of this effect in the DoE, because it was already observed that parameter X4 should be negative (shallow first groove) and that parameter X6 should be negative as well (sharp edge 2_1). Combining these two parameters will create a positive sign, thus opposite to what is stated in the analysis.

6.4.14 Estimating the maximal relative tensile strength

The maximal relative tensile strength of the optimal design can be calculated with the prediction equation from equation 6.9:

$$\begin{cases} = \hat{y} & \text{if } \hat{y} \leq 1 \\ = 1 & \text{if } \hat{y} > 1 \end{cases} \quad \text{maximal relative tensile} \quad (6.10)$$

Where \hat{y} is the predicted value of the tensile strength of the double groove design with a maximum uncertainty of 1%:

$$\begin{aligned} \hat{y} &= \bar{y} + \left(\frac{\Delta_{X8}}{2}\right) \cdot X8 + \left(\frac{\Delta_{X1}}{2}\right) \cdot X1 + \left(\frac{\Delta_{X2}}{2}\right) \cdot X2 + \left(\frac{\Delta_{X4}}{2}\right) \cdot X4 + \left(\frac{\Delta_{X6}}{2}\right) \cdot X6 + \left(\frac{\Delta_{X2 \cdot X3}}{2}\right) \cdot (X2 * X3) \\ &\quad + \left(\frac{\Delta_{X1 \cdot X7}}{2}\right) \cdot (X1 * X7) + \left(\frac{\Delta_{X3 \cdot X4}}{2}\right) \cdot (X3 * X4) + \dots \\ \hat{y} &= 76.362 \% + \left(\frac{7.7}{2}\right) \cdot (1) + \left(\frac{-6.3}{2}\right) \cdot (-1) + \left(\frac{6.1}{2}\right) \cdot (1) + \left(\frac{-5.8}{2}\right) \cdot (-1) + \left(\frac{-3.7}{2}\right) \cdot (-1) \\ &\quad + \dots > 100 \% \end{aligned}$$

Thus the optimal design should theoretically have a higher joint tensile strength than the strength of the base material. If the actual joint (the part where the tube and the internal part overlap) is stronger than the base material, the tensile strength of the whole crimp joint will be limited to the tensile strength of the base material.

It is seen that it is indeed possible to create such joints, because the samples 17_1 and 27_2 , which have most of the parameters according to the optimal design but still not all of them, failed in the base material instead of at the joint.

6.5 Optimal design according to DoE

The parameters and 2-parameter interactions which resulted from the analysis with 0.1% uncertainty or less, determine the optimal settings of the parameter values. In Table 6.8, the parameters are listed in order of significance, with parameter X8 mentioned first, meaning that this parameter leads to the most significant increase in crimp joint strength. As already mentioned, the main effects play the most important role for optimising a design. In Table 6.8, it is observed that the sign of 6 main effects (X8, X1, X2, X4, X6 and X3) directly determine the value

of the six corresponding parameters. Next, the sign of parameter X7 can be determined by the sign of the 2-parameter interaction X2*X7. Parameter X5 is only present in the 3-way interaction X3*X5*X7. Table 6.9 summarises the interpretation of the assignment of an upper or a lower value to the parameters.

Effect	Sign	Deriving sign	Physical interpretation
X8	+	$X8^+$	Large second groove width
X1	-	$X1^-$	Small groove edge 1 ₁ radius
X2	+	$X2^+$	Large central collar depth
X4	-	$X4^-$	Shallow first groove
X6	-	$X6^-$	Small groove edge 2 ₁ radius
X3	+	$X3^+$	High charging voltage
X2*X7	+	$X2^+ \Rightarrow X7^+$	Large first groove width
X3*X5*X7	-	$X3^+ \wedge X7^+ \Rightarrow X5^-$	Shallow second groove
X2*X3	+	$X2^+ \wedge X3^+ \quad OK$	
X2*X8	+	$X2^+ \wedge X8^+ \quad OK$	
X3*X4	-	$X4^- \wedge X3^+ \quad OK$	

Table 6.9: Signs of parameters for a possible optimal design (1).

Parameter	From main effect	From 2-way effect	From 3-way effect
X1	-		
X2	+		
X3	+		
X4	-		
X5			-
X6	-		
X7		+	
X8	+		

Table 6.10: Signs of parameters for a possible optimal design (2).

For an axial crimp joint design with the general dimensions shown in Figure 5.3 and with the two assumed values of Figure 6.4, an optimal design is proposed in Figure 6.23.

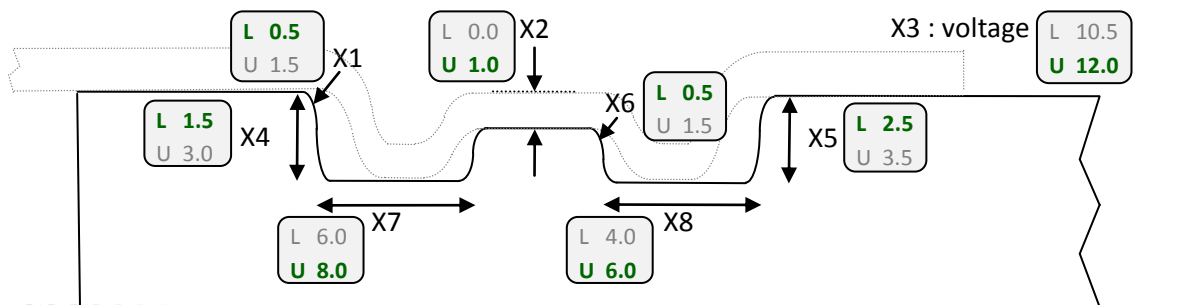


Figure 6.23: Optimal design with the proposed values.

Note that the DoE performed on a double groove design of an axial crimp joint only includes geometric parameters related to the grooves and the charging voltage. The evaluation parameter of the analysis was the relative tensile strength. It does not depend on the used materials nor the tube diameter and wall thickness. Therefore, the results of the DoE-analysis are applicable for different materials with the same geometric dimensions.

To propose a good design for a double groove axial crimp joint with a sufficient tensile strength, the following points of attention should be kept in mind: the critical zone where most crimp joints fail is at edge 1_1 . The finite element simulations discussed in chapter 4 also indicated the highest stress concentration in that zone. Therefore, tube wall thinning should be minimised in this zone, but keep in mind that some thinning is inevitable when deforming a tube into a groove. A wide shallow first groove with a sharp edge 1_1 is proposed. The sharp edge is required to create interlock, while the groove width and shallow depth create a good filling and minimise thinning of the tube.

It is important to have a central collar which is sunk below the specimen surface to further minimise the tube thinning at edge 1_1 and edge 2_2 and to better distribute the tensile strength over the two grooves (see chapter 7). For a certain collar depth, the mechanical interlock in the second groove is increased. It is also preferred that the second groove is wide and shallow, with a sharp first edge 2_1 . No statements are made about the exact groove width, but it is assumed that the groove width suffices as long as the tube can easily deform into the groove and realise a good filling into the groove.

6.6 Remarks and evaluation of the methodology

6.6.1 A design with other diameters

When a smaller diameter of the workpieces is used and the tube wall thickness is the same, a larger charging voltage will be required to deform the tube. The ratio of the wall thickness over the diameter should be taken into account when choosing a voltage level.

The values for the groove depth, groove width and edge radius of the optimal design can be extrapolated according to the change in diameter. A possible way to extrapolate is to use equal relative dimensions (ratio of geometrical parameter to tube outer diameter). For example, when a diameter of 30 mm is used and the optimal parameter for a groove's depth is 3 mm, then the optimal groove depth for a piece with diameter of 20 mm is 2 mm. More research is needed to investigate this hypothesis.

6.6.2 Evaluation of the methodology

The choice of the eight parameters was done carefully and no remarks can be made about this choice. Assigning an upper and lower value to each parameter was more delicate. It is not obvious to choose values which satisfy all conditions. Finally, it was observed that the width of the second groove should have had larger values because the tube almost did not deform into the groove when a groove width of 4 mm was used. A better value for the groove widths might be 6 mm as the lower limit value and 8 mm as the upper limit value for both grooves. However, in that case the sum of both grooves' width and the collar will be larger than the internal axial length of the

field shaper. By applying a sufficiently high charging voltage, the part of the tube that is covered by the field shaper and that experiences most of the magnetic pressure will pull the other part of the tube into the grooves as well due to the inertia.

No remarks need to be made about the choice of the values for the collar depth, edge radii 1_1 and edge radius 2_1 . On the other hand, the value 0.5 mm for the edge radii for the edges 1_2 and 2_2 (not the important edges 1_1 and 1_2) might have been too small, because some crimp joints failed in this area. In chapter 4, it was seen that the edge radius has very limited influence on the inwards radial displacement, but has a significant influence on the tube wall reduction. By increasing the value of edge radius 1_2 and 2_2 , less thinning, but equal deformation will occur, resulting in a stronger joint and likely a reduced failure in this area.

The depth of the first groove appeared to be an important parameter, while the depth of the second groove appeared to be of almost no importance. This also was due to unintentionally influencing of the DoE by choosing both values of the second groove's width too small. The tube had almost no contact with the groove's bottom. Making extra specimens to investigate the deformation of the tube into the grooves by making cross sections would be appropriate in this case.

Overall, DoE is a good statistical method that allows to optimise a design. The results depend a lot on the choice of the parameters, so drawing a conclusion must be done carefully. DoE is more useful to qualitatively investigate a design rather than to quantify values for an optimal design. Anyway, it is better to use DoE than to design some tests to investigate the influence of 1 single parameter at a time. Less experiments are needed with DoE and it is more likely to come to useful conclusions.

Note: with 128 runs (2 times 64) and 8 parameters, resolution V could have been applied. This allows to investigate all main effects and all 2-parameter interactions without confounding them with other effects. In this work, resolution IV was used, resulting in 6 confounded 2-parameter interactions. It was seen that these aliases had no impact on the understanding of the results and it was clear every time which 2-parameter interaction had the biggest effect. So, equal conclusions would most probably have been drawn based on a DoE with resolution V.

Chapter 7: Digital Image Correlation

7.1 Introduction

In the finite element simulation of a double groove design (see § 5.2) it was observed that the tube was pulled out of the first groove when the joint was axially loaded. In order to get experimental validation of this phenomenon, tensile tests were performed during which the three-dimensional displacement was recorded using Digital Image Correlation (DIC).

DIC also allows to determine the three-dimensional deformation of the loaded test specimen as a function of time. This deformation is denoted in the form of the Lagrange strain value. Since the Lagrange strain is linked to the displacement (see further), DIC is therefore a useful tool to study the relationship between the relative tensile strength and the displacement behaviour.

After tensile tests were performed on the first series of 64 experiments of the DoE, the relative tensile strength versus displacement curves were analysed and 32 interesting crimped joints were selected to be analysed with the DIC technique during the second series of tensile tests.

The DIC technique provides results concerning displacement and strains, but these results can nevertheless be used to have an idea about the load distribution over the 2 grooves during a tensile test. If strain is present in the tube at the groove edge, this implies that the groove edge must take up some part of the axial load. On the other hand, if no strain is noticed in the tube at the groove edge, it can be concluded that the groove edge does not bear a part of the axial load.

7.2 The Digital Image Correlation technique

The idea behind the DIC method is to infer the material displacement during testing by tracking the deformation of a random speckle pattern in digital images acquired during the testing [49]. The image analysis process can be understood as a pattern recognition technique, which searches locally the random speckle pattern by comparing the images of the deformed with the reference state (see Figure 7.1).

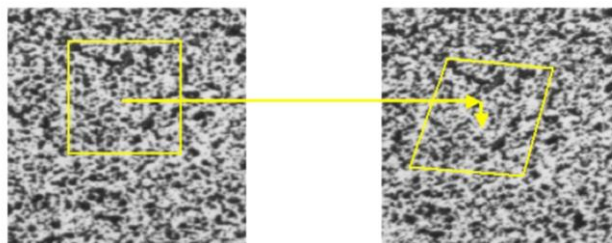


Figure 7.1: The speckle pattern of a deformed state (right hand side) is compared to the undeformed speckle pattern of the reference state (left hand side) [49].

By using two synchronised cameras which acquire images of the loaded specimen from different viewing angles (see Figure 7.2 for a schematic setup and Figure 7.3 for the used setup in this

thesis), it is possible to determine both the three-dimensional displacement and three-dimensional deformation based on a simple camera calibration. Also, rigid body movement is taken into account.

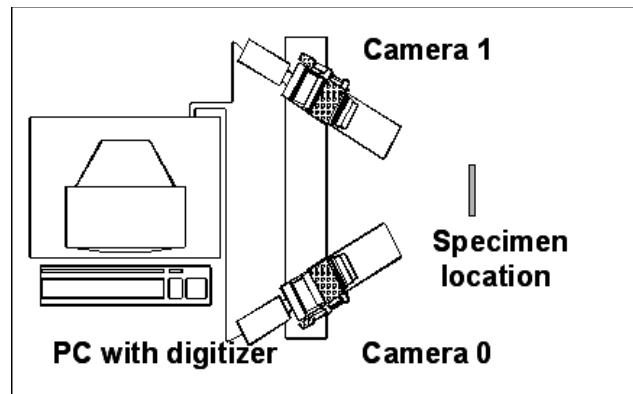


Figure 7.2: Schematic setup for three-dimensional measurements with two cameras [49].

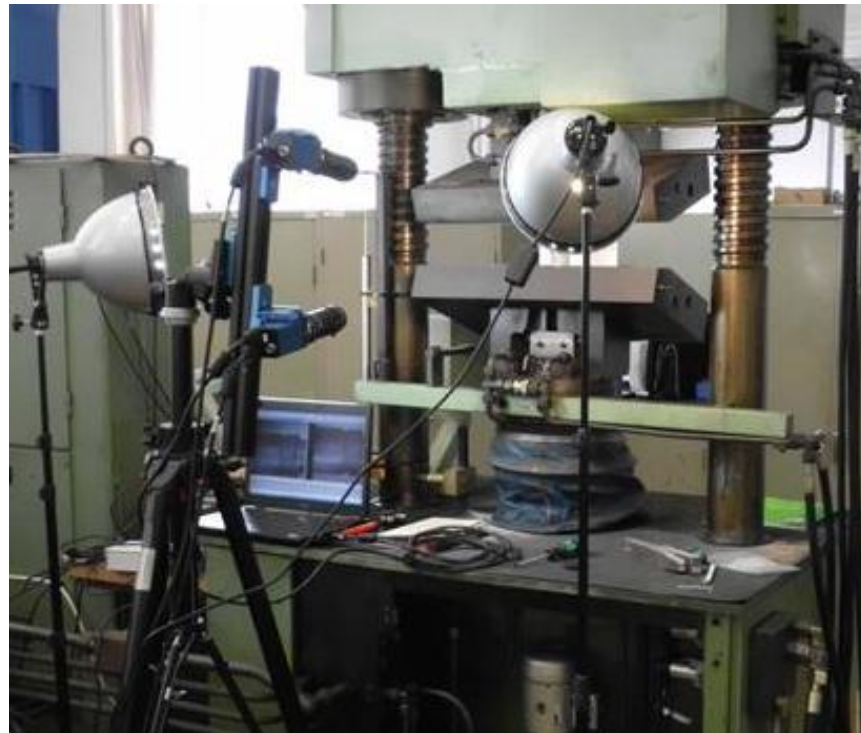


Figure 7.3: The test setup used in this thesis.

The specimen is illuminated by means of two white-light sources (see Figure 7.3), in order to assure that there is enough light to get good results, independent of the light of the surroundings.



Figure 7.4: Close up of the cameras.

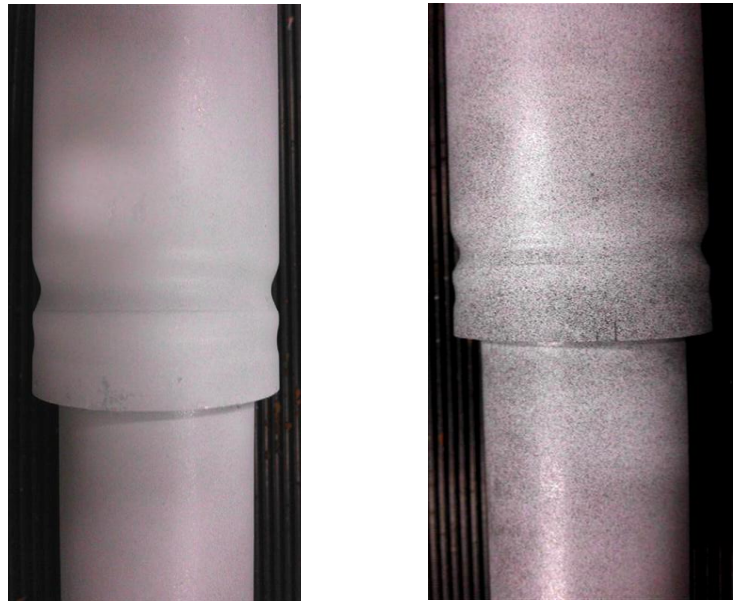


Figure 7.5: Detail of the test specimen with white layer (left) and with the black speckle pattern (right).

The specimen surface must have a random speckle pattern (see Figure 7.5 and Figure 7.6), which is applied to the specimen prior to testing. Some examples of the different methods to apply a pattern are self-adhesive, pre-printed patterns, stamps and application of paint speckles with brushes or spray cans. The latter one is used in this thesis: a white base layer was sprayed onto the crimp joint and consequently a black speckle pattern was created by spraying from a larger distance and allowing the paint drops to atomize onto the white base layer (see Figure 7.5).

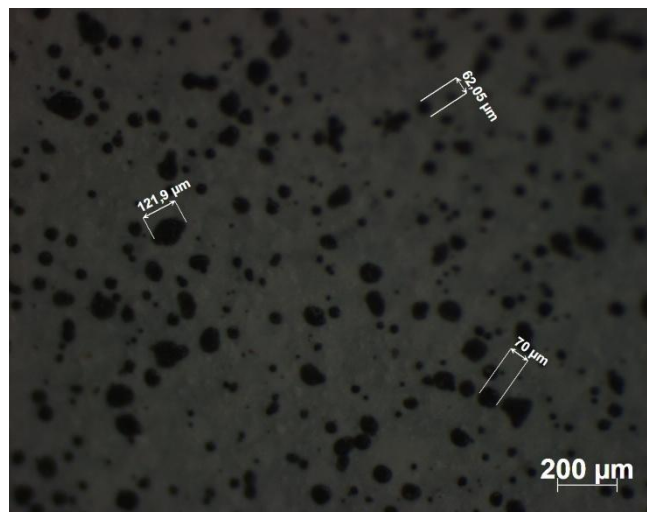


Figure 7.6: Microscopic measurement of the speckle pattern.

As a rule of thumb, a good speckle size is about 3 pixels per speckle. The resolution of the cameras used here is 2452x2054 pixels. The size of the area which is studied is approximately 90x70 mm. This results in an ideal speckle diameter of 69 μm.

A microscopic measurement was performed on the speckle pattern, see Figure 7.6. It can be seen that most of the speckles have a diameter which is very close to the ideal diameter. It should be noted that 121.9 μm is the largest diameter measured and this results in 9 pixels per speckle, which is still acceptable to obtain good results.

The automatic calibration process involves the acquisition of a series of images of a calibration grid in different orientations (rotations around all three axes). Two example images are shown in Figure 7.7. Based on the images of the calibration grid, the relative orientation of the cameras is automatically determined by the processing software package.

In this thesis the VIC 3D software was used [50].

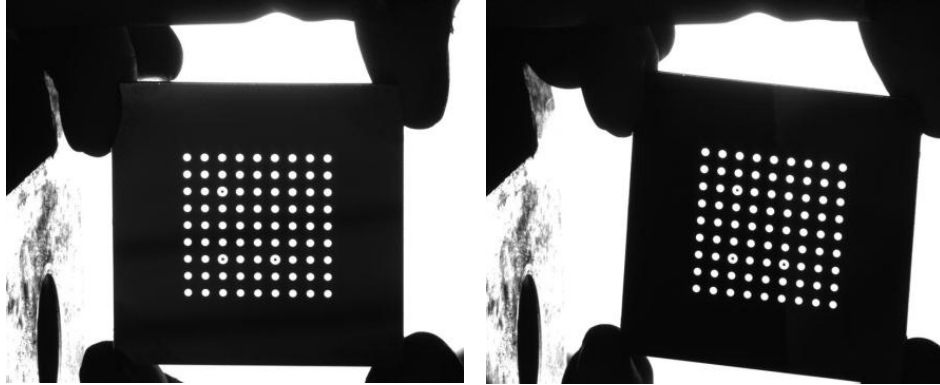


Figure 7.7: Calibration images.

7.3 Lagrange strain

In the VIC 3D software, the Lagrange strain is used to evaluate the strain occurring in the test specimen. The Lagrange strain is defined as

$$\varepsilon = \frac{l^2 - l_0^2}{2l_0^2} = \frac{\delta l}{l_0} + \frac{(\delta l)^2}{2l_0^2} \quad (7.1)$$

With: l : length of workpiece after deformation ($l = l_0 + \delta l$) [mm]

l_0 : length of workpiece before deformation [mm]

δl : length increase [mm]

This definition of strain is similar to the standard true strain definition $\varepsilon = \frac{\delta l}{l_0}$, but it contains an additional second order term. This additional term is negligible for small δl . In other words, the Lagrange strain is the equivalent of true strain for large δl .

A more detailed description of the Lagrange strain can be found in Appendix E.

7.4 Analysing the different failure modes

After studying the 125 curves (there were 2*64 experiments and 3 samples were not delivered) of the relative tensile strength (see Appendix D) versus displacement from the DoE together with the observations, it was concluded that there are three main failure modes (see § 5.3.4 for the nomenclature of the edges):

- ✓ **Failure mode 1:** The tube tears at edge 1₁ at the complete circumference (360°). The curve shows a maximum and drops immediately to zero after failure has occurred (Figure 7.9).
- ✓ **Failure mode 2:** The tube tears at edge 2₁ at the complete circumference (360°). The curve goes to a maximum and drops to a value in between the maximum value and zero. The applied force then increases again to a second (lower) maximum after which it drops to zero.
- ✓ **Failure mode 3:** The tube gets pulled of the internal workpiece, no tearing occurs. The curve goes to a maximum and then goes to zero stepwise.

From these three main failure modes, failure mode 1 occurred most frequently (see Figure 7.8). The different failure modes will be discussed more in detail in what follows and explanations will be evidenced by using DIC images. It should be noted that there are no fixed scales of the legend used in the different DIC images. This was done because otherwise, no clear observations on the occurring effects could be made.

It was observed that there is about 11% of the failed crimp joints which did not fail according to one of the three main failure modes. These joints failed differently due to bad positioning in the EMP machine, bad clamping in the testing machine, etc. These will not be discussed in what follows.

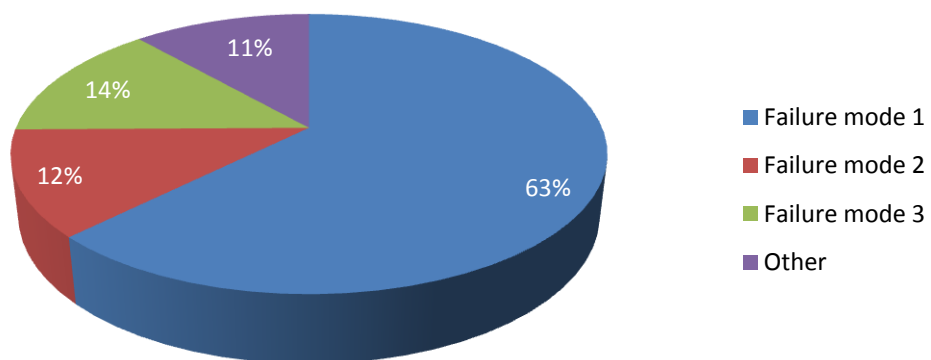


Figure 7.8: Percentages of occurrence for the different failure modes.

7.4.1 Failure mode 1

In Figure 7.9, a typical curve of the relative tensile strength versus the displacement corresponding with failure mode 1 is shown. In failure mode 1, the tube tears at edge 1_1 over the whole circumference.

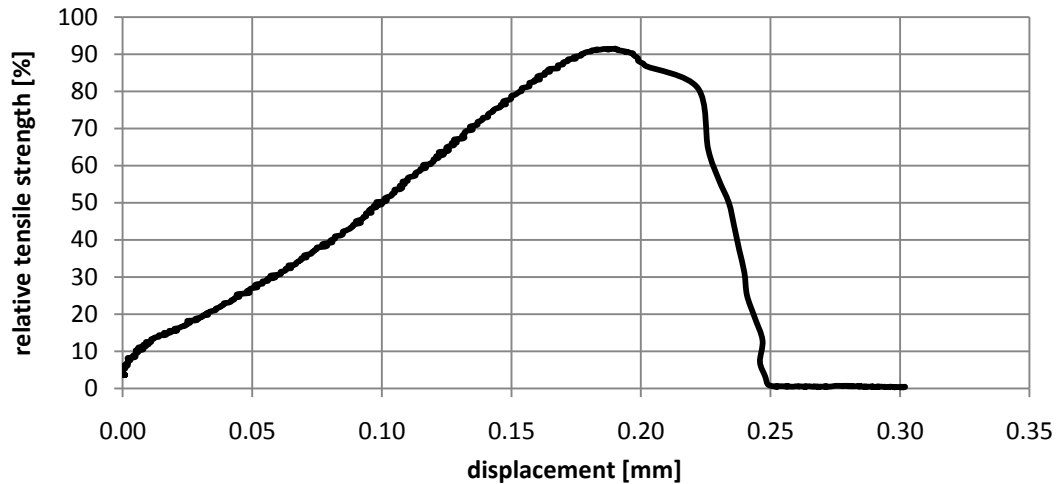


Figure 7.9: Relative tensile strength versus displacement curve for crimp joint 58.

Fifteen of the 32 specimens investigated with DIC failed according to this failure mode. It is interesting to see that the maximum relative tensile strength varied over a wide range for these 15 selected crimp joints: from 70.3% to 93.1% (see Table 7.1).

Crimp joint	Relative tensile strength [%]	Second groove bears a part of the load	Collar depth of 1 mm
1	84.4	✓	
4	82.0	✓	
5	79.6	✓	
6	70.3		
11	87.4	✓	
15	78.2	✓	
16	71.2		
26	92.1	✓	✓
29	87.2	✓	✓
30	74.8		✓
35	72.5	✓	
41	76.2	✓	
55	79.7		✓
58	91.5	✓	✓
59	93.1	✓	✓

Table 7.1: Comparison between the crimp joints which fail according to failure mode 1.

An explanation for this wide range can be found by looking at the distribution of the load over the 2 grooves. The Lagrange strain which is provided by the VIC 3D evaluation software can be used for this, as was explained in the introduction.

In crimp joints 6, 16, 30 and 55, the second groove did not bear any load. Because these crimp joints behaved in a similar way, which results in the same DIC images, only the DIC images for crimp joint 16 (see Figure 7.10) will be used to evidence the explanations.

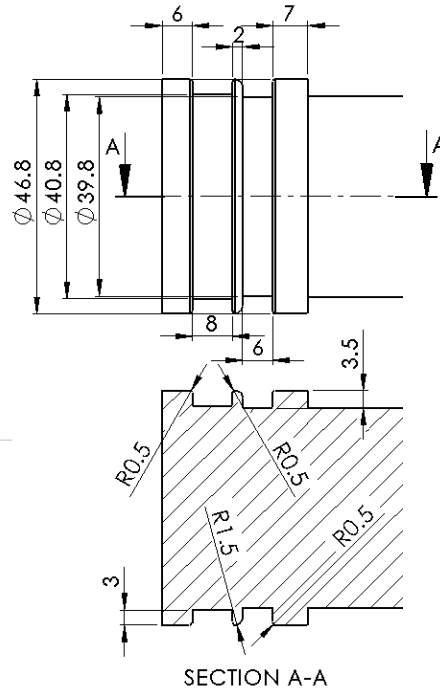


Figure 7.10: Groove design for crimp joint 16.

The average relative tensile strength of the 4 connections in which the second groove does not bear a part of the axial load is 74.0%, which is significantly lower than the average relative tensile strength for the eleven other connections (84.0%). The fact that the second groove does not bear a part of the load in those 4 connections is due to a bad design of the first groove (see Figure 7.11).

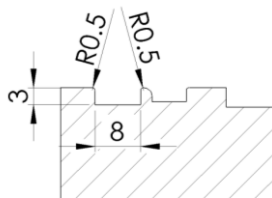


Figure 7.11: Bad design of the first groove.

Because the groove is 3 mm deep, free deformation will occur (the tube will not touch the bottom of the groove). Also, as was concluded in chapter 4, a groove edge radius of 0.5 mm combined with a groove width of 8 mm results in severe tube thinning at the groove edges. When a tensile load is exerted on the joint, the first groove will bear the load and the accompanied strain will cause further thinning in the already necked zone of the tube near the edge 1_1 . A critical value of

tube thinning will be exceeded and the tube tears at edge 1_1 , making the second groove useless. This is confirmed by Figure 7.12: there is no Lagrange strain visible in the second groove, meaning that the second groove does not bear any load.

It can be noted that the relative tensile strength of crimp joint 6 and 16 are lower than the ones of crimp joint 30 and 55 (see Table 7.1). This can be explained by the fact that in the latter samples, a collar depth of 1 mm was present: this will cause less thinning of the tube at the edge 1_1 during the crimping operation (see chapter 6). Thus, a larger strain is allowed before tearing will occur and a somewhat higher load can be taken.

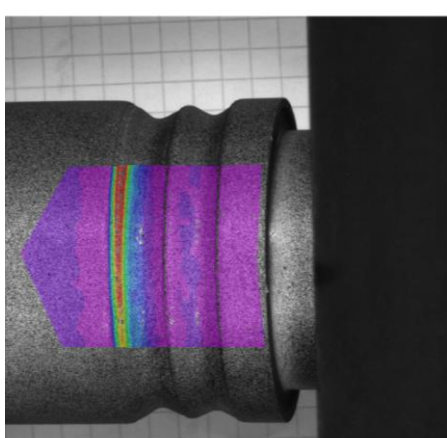


Figure 7.12: The Lagrange strain for crimp joint 16 before failure occurs. At edge 1_1 a strain of about 4.5% can be seen (red zone).

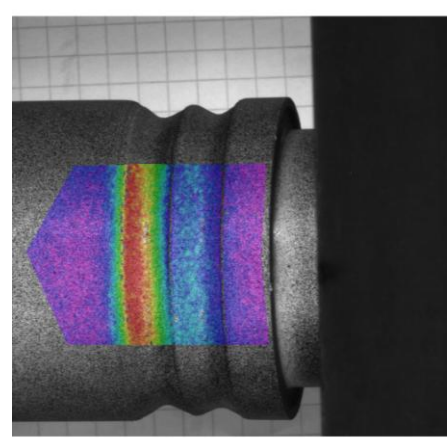


Figure 7.13: The z-displacement for crimp joint 16 before failure occurs. In the first groove there is a displacement of about 0.1 mm (red zone).

When looking at the DIC images, it has to be kept in mind that a right-handed coordinate system is used (see Figure 7.14) and that the Lagrange strain shown is the principal strain according to the x-axis.

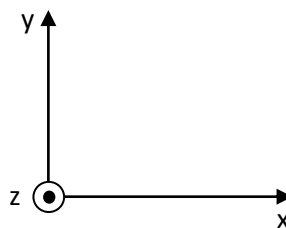


Figure 7.14: Right-handed coordinate system.

When looking at the z-displacement at the moment before failure occurs (see Figure 7.13), it is observed that the tube is pulled out of the first groove. This is an experimental confirmation of what was seen in the finite element simulation in Abaqus (see chapter 4). It can also be observed that no z-displacement took place at the second groove

All of the eleven remaining joints for failure mode 1 have a better design of the first groove. The second groove will in this case also bear a part of the axial load, resulting in a higher relative

tensile strength. When only considering these connections, the relative tensile strength still varies over a wide range, from 72.5 to 93.1%. The explanation for this can be found by looking at the collar depth: when the collar is at the same height of the outer surface of the internal specimen, the average relative tensile strength is 80.0%. If on the other hand the collar depth is 1 mm, the average relative tensile strength increases to 91.0%.

The 7 crimp joints for which the second groove bears a part of the load, with a collar depth equal to zero, have a similar deformation behaviour. The same can be stated about the other 4 crimp joints in which the second groove bears a part of the applied load and a collar depth of 1 mm is used. The DIC images for respectively crimp joint 41 (see Figure 7.15) and crimp joint 58 (see Figure 7.16) will be used below to evidence these explanations.

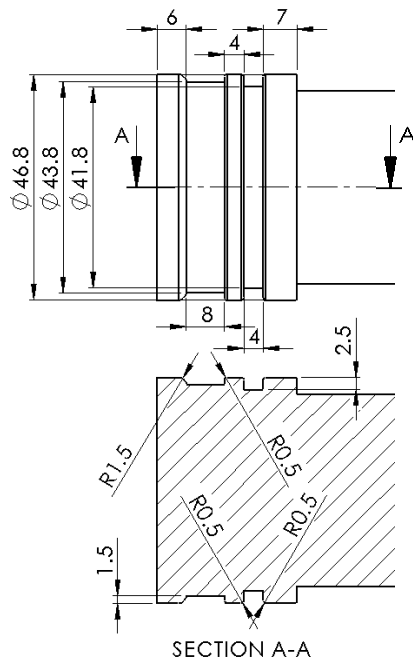


Figure 7.15: Groove design for crimp joint 41.

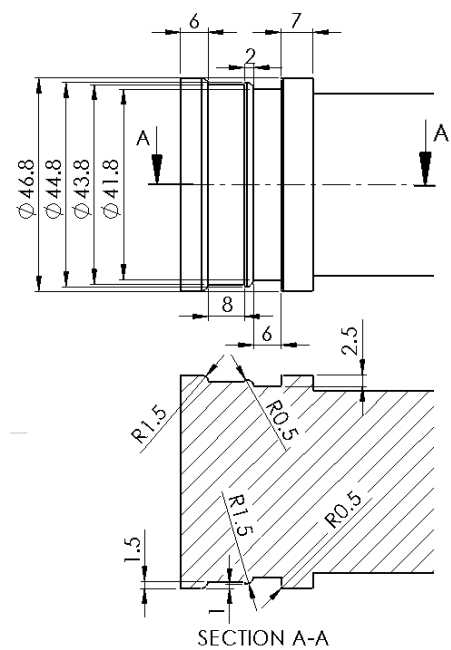


Figure 7.16: Groove design for crimp joint 58.

As mentioned before, in both types, the second groove bears a part of the load (see Figure 7.17.A and Figure 7.17.B). Because the load is linked to the strain, it can be stated that a larger observed strain implies a larger absorbed load. In crimp joint 41 the strain observed at the second groove is approximately half the strain observed at the first groove. In crimp joint 58 this ratio increases to $\frac{3}{4}$. As a consequence, the second groove will bear a larger part of the load when a collar diameter reduction is used.

A part of the explanation has been given before: the presence of a sunken collar will cause less thinning of the tube near edge 1_1 , thus ensuring that tearing at edge 1_1 is postponed. This allows the second groove to bear part of the load. The second part of the explanation is that the presence of a sunken collar creates a stronger interlock behind edge 2_1 (see chapter 6), and the second groove can therefore absorb a larger part of the load.

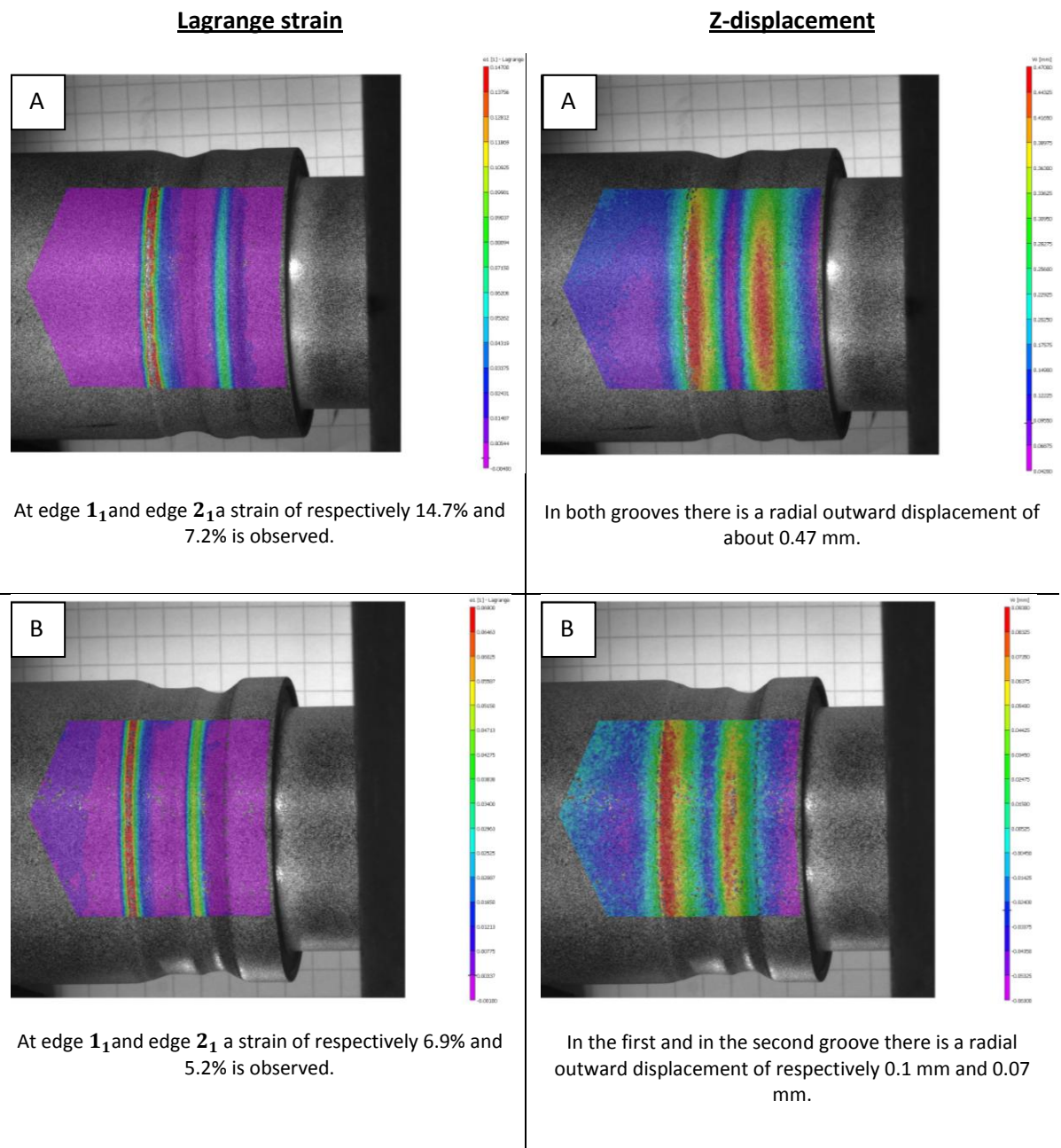


Figure 7.17: A. Crimp joint 41 right before failure occurs, B. Crimp joint 58 right before failure occurs.

Figure 7.18: A. Crimp joint 41 before failure occurs, B. Crimp joint 58 before failure occurs.

When looking at the z-displacement for both crimp joints, it is seen that pull out occurs at both grooves (see Figure 7.18A and Figure 7.18B).

To summarise: the crimped joints investigated with DIC which failed according to failure mode 1 can be divided into 3 subgroups. The distribution of the load over the two grooves as well as the deformation behaviour at the grooves (amount of pull-out) is the same within each of these subgroups. Therefore only one crimp joint per subgroup was looked at in detail using DIC:

- ✓ **Subgroup 1:** These crimp joints have a bad design for the first groove in common (see Figure 7.11). As a consequence, thinning at edge 1_1 is too excessive and the second groove will not bear any part of the load. The average relative tensile strength is 74%. Crimp joint 16 was looked at in detail.
- ✓ **Subgroup 2:** These crimp joints have a better design for the first groove, allowing the second groove to bear part of the load, but they do not have a sunken collar. The average relative tensile strength is 80%. Crimp joint 41 was looked at in detail.
- ✓ **Subgroup 3:** These crimp joints have a better design for the first groove, as well as a sunken collar with a depth of 1 mm, which causes less thinning at the edge 1_1 and which allows the second groove to bear a larger part of the load. The average relative tensile strength is 91%. Crimp joint 58 was looked at in detail.

7.4.2 Failure mode 2

In Figure 7.19, a typical curve of the relative tensile strength versus displacement corresponding to failure mode 2 is shown. In failure mode 2, the tube tears at edge 2_1 at the whole circumference. From the selected crimp joints investigated by DIC 3 failed according to this failure mode. The average relative tensile strength of these joints is 75.3%.

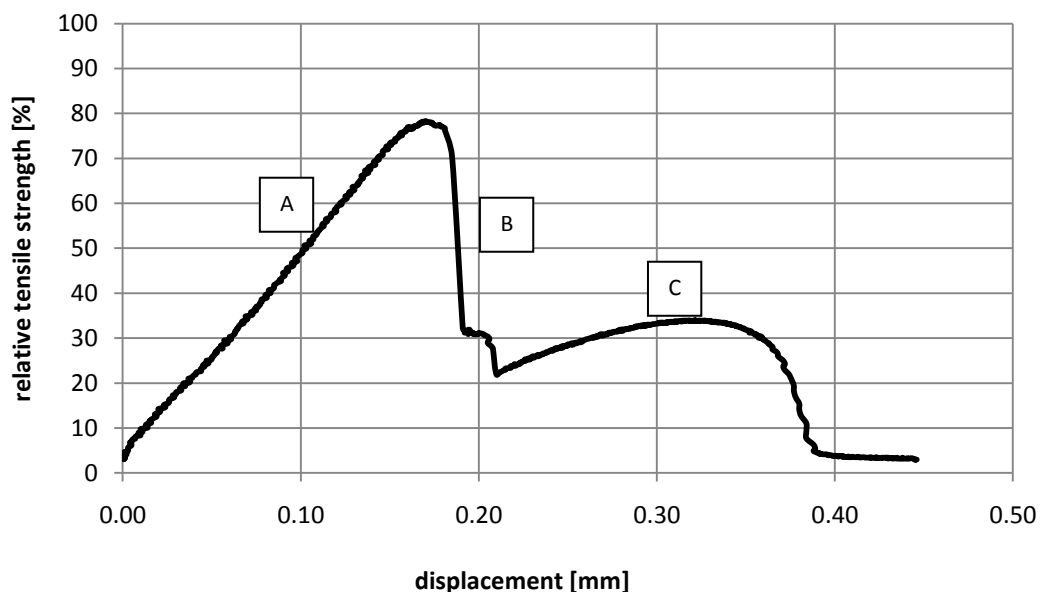


Figure 7.19: Relative tensile strength versus displacement curve of crimp joint 39.

All three of the crimp joints show the same failure behaviour because part of their groove design is the same (see Figure 7.20).

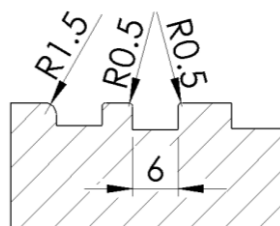


Figure 7.20: The groove design parameters which the crimp joints from failure mode 2 have in common.

Because the failure behaviour and thus the DIC images for all three crimp joints are the same, only crimp joint 39 (see Figure 7.21) will be discussed in detail.

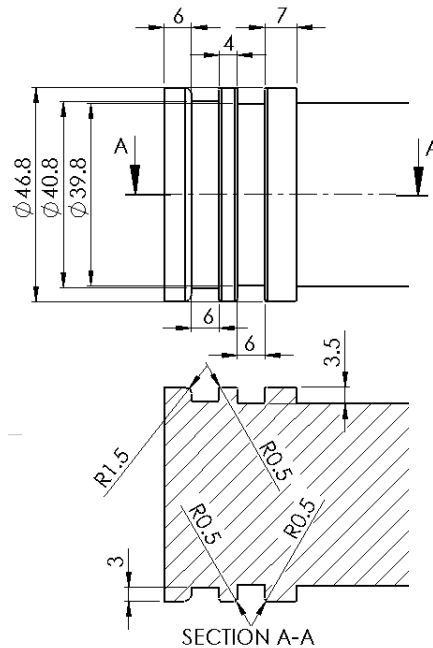


Figure 7.21: Groove design of crimp joint 39.

As can be seen in Figure 7.19, the relative tensile strength versus displacement curve can be subdivided into three main parts, denoted by “zone A”, “zone B” and “zone C”. These will be clarified below by making use of the DIC images.

Zone A:

Both edges (edge 1_1 and edge 2_1) bear a part of the load (see Figure 7.24.A) and the tube gets pulled out of both grooves (see Figure 7.25.A). The tensile load increases to a maximum.

Zone B:

Once the maximum is reached, the curve suddenly drops to a value in between the maximum value and zero. This corresponds with the tube tearing at edge 2_1 over the complete circumference (see Figure 7.24.B). This seems strange at first, especially since there is only a relatively small Lagrange strain near that edge, but can be clarified by looking at the groove geometry (see Figure 7.20). The second groove is wide, deep and has a sharp edge radius. The first groove is also wide and deep, but it does not have a sharp edge radius. As was concluded in chapter 4, for the same width and depth, thinning of the tube near a sharp groove edge is a lot larger than when the groove edge is not sharp. Because of this, a large wall thinning will be located in the tube near edge 2_1 and this will be the weakest point. The limited additional wall thinning caused by the small strain is sufficient to cause the tube to fail at edge 2_1 .

Zone C:

The fact that the curve drops to a value in between the maximum and zero (and not to zero, as was the case in failure mode 1), is because the part of the tube which is deformed into the first groove still ensures a certain interlock behind edge 1_1 .

The failure mechanism now changes: The tube no longer tears, but it gets pulled out of the internal workpiece. Thinning of the tube wall near the edge in combination with the strain is no longer of importance, because thinning near edge 1_1 is limited and the material at that location is strong enough to absorb additional strain without tearing. It is the radial inward tube displacement into the first groove in combination with the axial displacement at the edge 1_1 of the internal workpiece relative to the tube which is of importance (see Figure 7.22).

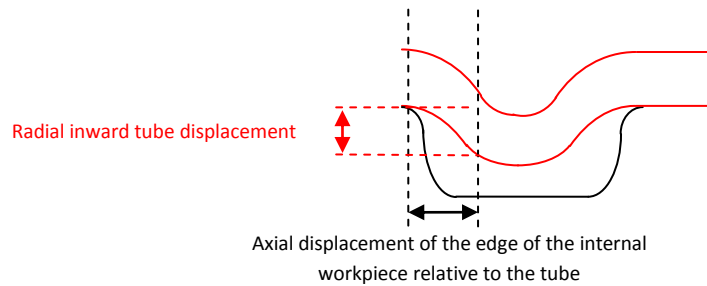


Figure 7.22: Combination which determines the load necessary to push the tube out of the groove.

When the internal workpiece is considered as a fixed entity and the displacement of the tube increases, the tube is “pulled” out of the first groove, see Figure 7.23. Experimental evidence can be seen by comparing the deformation into the first groove between Figure 7.24.B and Figure 7.24.C.

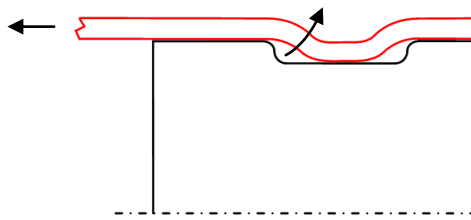


Figure 7.23: The tube is “pulled” out of the groove.

It should be noted that it is equally valid to consider the tube as a fixed entity and the internal workpiece as a moving body: the tube will get “pushed” out of the groove. More specific, the edge 1_1 will push the deformed tube out of the first groove.

The larger the radial inward displacement is for a certain axial displacement, the more the tube will need to get pushed out of the groove and the higher the load which is required to pull the tube out of the internal workpiece.

This explains why the curve of the relative tensile strength versus displacement increases to a second (lower) maximum. This corresponds with the point of greatest radial inward tube displacement. Once the edge 1_1 is past this point, the tube which was originally deformed into the first groove is almost completely pushed back to its original position before crimping was done. As a consequence, the internal workpiece will find little resistance when the displacement increases further, and this is why the load finally drops to zero.

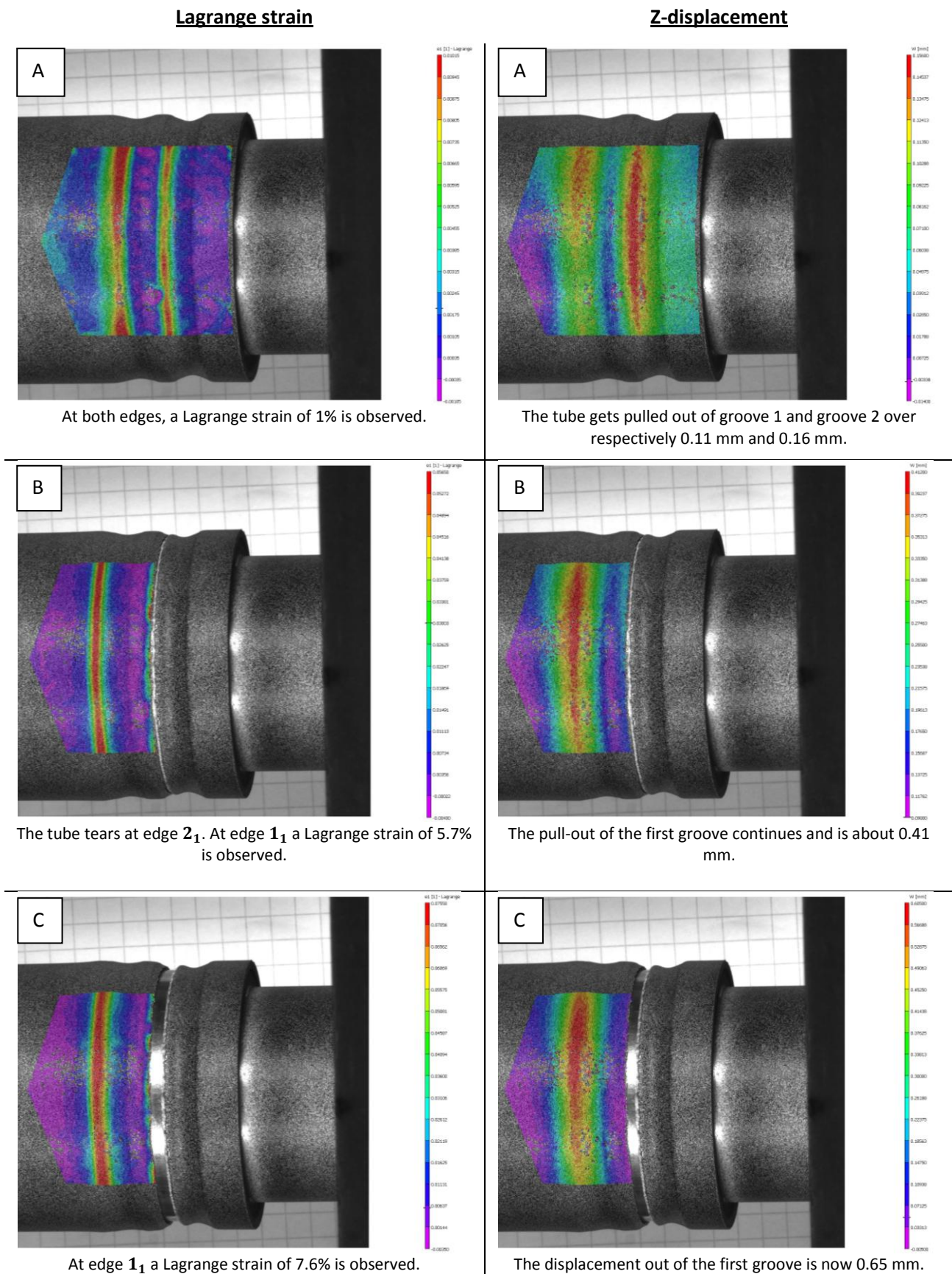


Figure 7.24: Lagrange strain for crimp joint 39.

Figure 7.25: Z-displacement for crimp joint 39.

7.4.3 Failure mode 3

In failure mode 3, the tube gets pulled out of the internal workpiece, and no tearing occurs. Six from the selected crimp joints examined with DIC failed according to this failure mode. The average relative tensile strength of these joints is 66.4%, but the relative tensile strengths vary over a fairly wide range: from 61.9 to 71.0% (see Table 7.2).

As mentioned before, because no tearing of the tube occurs, this difference in relative tensile strength cannot be explained by wall thinning at the edges. As soon as the tube is pulled out of the internal workpiece, it is the radial inward displacement of the tube into the grooves in combination with the axial displacement of the edges of the internal workpiece relative to the tube which is of importance, see Figure 7.22. The higher the radial inward displacement is for a certain axial displacement, the more the tube will need to get pushed out of the groove and the higher the force which is required.

The parameters which determine these phenomena can be found in Table 7.2.

It should also be noted that all 6 crimp joints were executed with a charging voltage of 10.5 kV. Because of this, wall thinning at the edges 1_1 and 2_1 will be less. It is more than likely that the applied voltage has a major effect on the type of failure mode occurring.

Crimp joint	Groove edge radius for edge 1_1 [mm]	Groove width first groove [mm]	Groove width second groove [mm]	Collar depth [mm]	Relative tensile strength [%]
8	0.5	6	4	0	70.9
34	1.5	8	4	0	61.9
36	1.5	6	6	0	71.0
50	1.5	6	4	1	62.7
53	1.5	6	4	1	64.3
56	1.5	6	4	1	64.8

Table 7.2: Overview of the crimp joints which failed according to failure mode 3.

Typically, the curve of the relative tensile strength versus displacement will go to a maximum and will then go to zero stepwise. Every “step” represents a part of the deformed tube which needs to be expanded in order for the internal workpiece to be able to be pulled out of the tube. An example is shown in Figure 7.26.

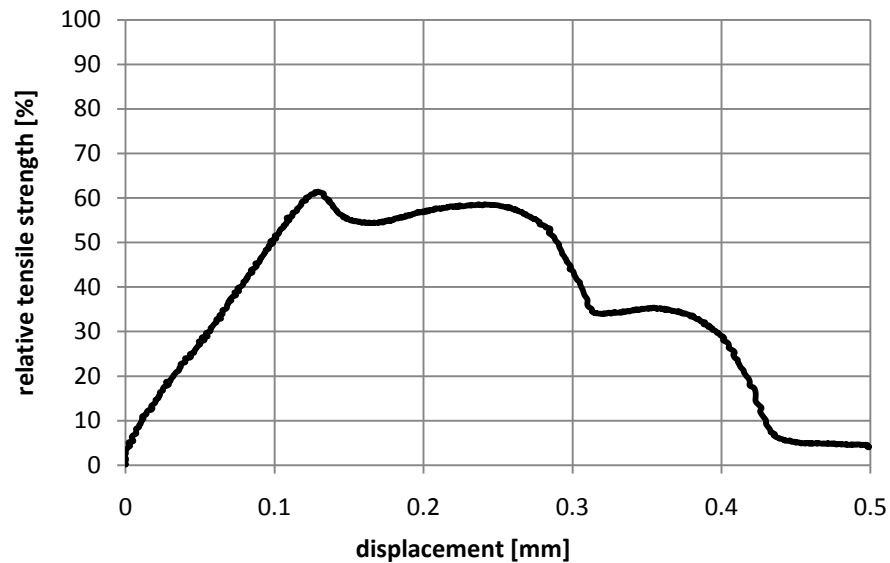


Figure 7.26: Relative tensile strength versus displacement curve for crimp joint 34.

7.4.3.1 Discussion on crimp joint 8

The reason that crimp joint 8 has a higher relative tensile strength than the average for the six joints, is due to the small edge groove radius at edge 1_1 . As a result, there is a stronger interlock behind edge 1_1 , the pull out is postponed and a higher applied force will be required for pulling out the tube at the first groove.

7.4.3.2 Discussion on crimp joints 34 and 36

Both crimp joints have about the same groove design (see Figure 7.27 and Figure 7.28). Nevertheless, there is a difference of the relative tensile strength of approximately 10%. It can be seen that the only difference between the two designs is the groove width of both grooves and the depth of the second groove. As was concluded in chapter 6, the groove depth of the second groove has very limited influence on the tensile strength due to the choices for the -1 and +1 value in the DoE. The explanation for the difference of the tensile strength will therefore be found in the difference of the groove widths.

The groove width of the first groove is larger in crimp joint 34. As a consequence, there will be a radial inward displacement of the tube over a larger axial length. The tube will have to get “pushed” out over this larger axial length and therefore the first groove of crimp joint 34 will absorb a larger amount of axial load than the first groove of crimp joint 36. This can be seen in Figure 7.29 and Figure 7.30. For the same axial displacement of the internal workpiece relative to the tube, in the first groove of crimp joint 34 a strain value of 20.6% is observed, where the strain value is 15.7% in crimp joint 36. Consequently, the load beared by the first groove is higher for crimp joint 34. This however does not explain why crimp joint 36 has a relative tensile strength which is 10% higher than crimp joint 34, on the contrary. Therefore, there must be another effect caused by the design of crimp joint 36 and this effect must be stronger than the effect mentioned above.

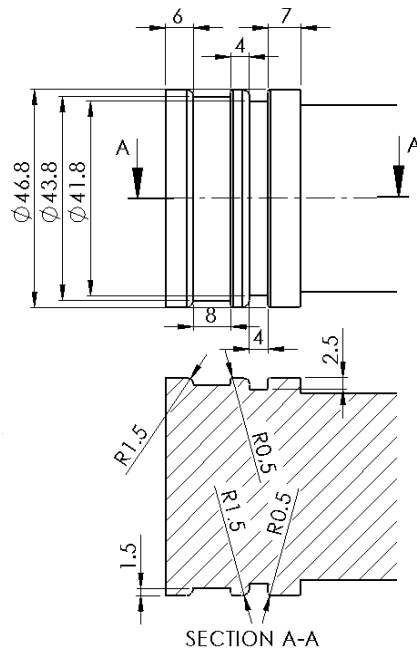


Figure 7.27: Groove design of crimp joint 34

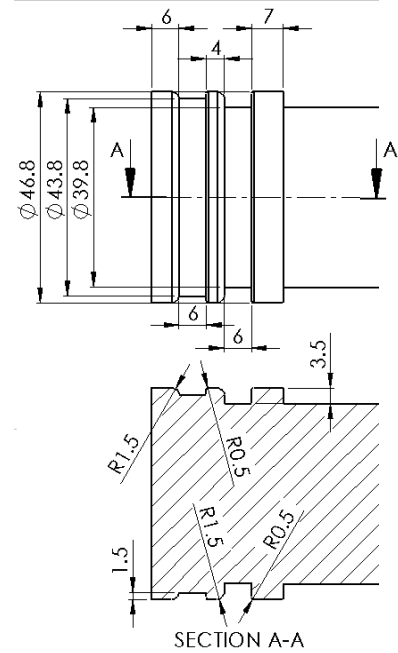


Figure 7.28: Groove design of crimp joint 36.

When comparing the width of the second groove, it is observed that this width is equal to 6 mm for crimp joint 36, while it is only 4 mm for crimp joint 34. This has a major effect on the deformation of the tube into the second groove. As was concluded from the DoE, a groove width of 4 mm is too small to get a complete deformation in such a groove, especially when fairly low voltages are used (which is the case here, since all joints were executed with 10.5 kV). A groove width of 6 mm will on the contrary allow for a complete deformation into the groove. As a consequence, the radial inward displacement into the second groove is more pronounced for crimp joint 36. The tube will have to get pushed out over a larger distance (in the radial direction, because there is a larger inward displacement, and in the axial direction, because the groove is wider) and thus more force is required.

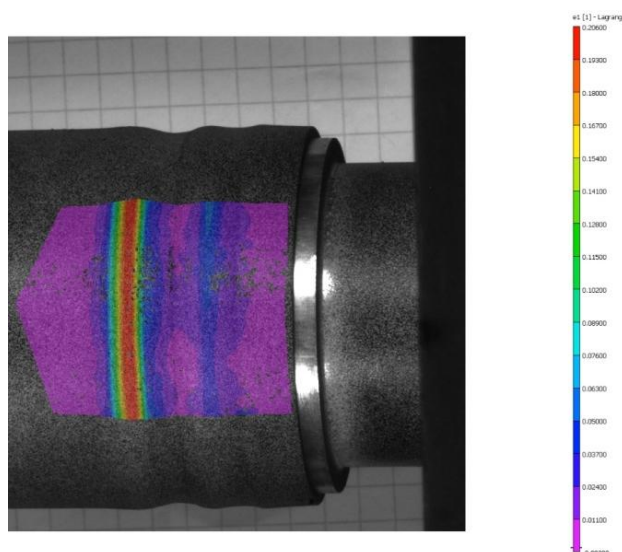


Figure 7.29: The Lagrange strain for crimp joint 34 during the pull-out. At edge 1_1 a strain of 20.6% is observed. At edge 2_1 hardly any strain is observed.

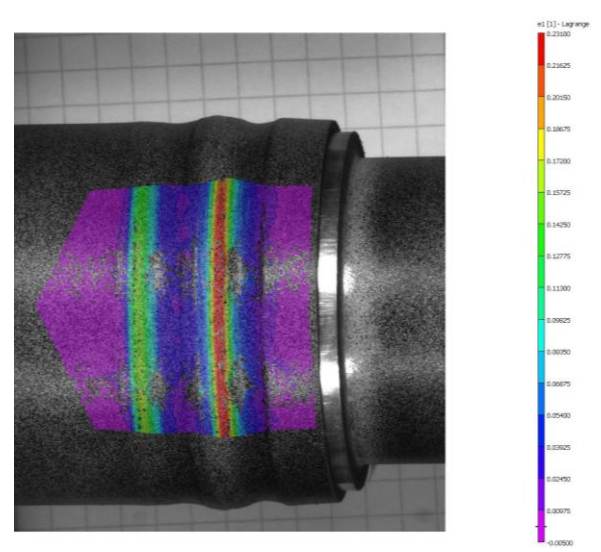


Figure 7.30: The Lagrange strain for crimp joint 36 during the pull-out. At edge 1_1 and edge 2_1 a strain of respectively 15.7% and 23.1% is observed.

This can be observed by looking at the second groove in Figure 7.29 and Figure 7.30: after the internal workpiece has reached a certain displacement, the tube of crimp joint 34 will already be pushed straight, while it still has a significantly inward displacement into the second groove for crimp joint 36. Because of this, there is hardly any strain visible near edge 2_1 in crimp joint 34. In crimp joint 36 however, a strain of 21.3% is observed edge 2_1 . This explains the large difference in relative tensile strength between the two connections.

7.4.3.3 Discussion on crimp joint 50, 53 and 56

Crimp joints 50, 53 and 56 all show the same failure behaviour (see Figure 7.32 for a typical diagram of the relative tensile strength versus the displacement). These joints also have about the same relative tensile strength (see Table 7.2). This is because the parameters which determine the radial inward displacement of the tube into the grooves, are the same for all three crimp joints (see Table 7.2). Only crimp joint 50 (see Figure 7.31) will be studied. The relative tensile strength versus displacement curve will be discussed in detail because it differs significantly from the curves of the other joints (compare Figure 7.32 with Figure 7.26).

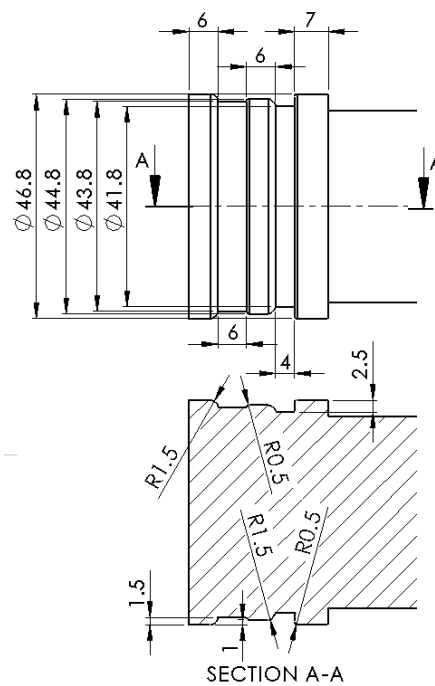


Figure 7.31: Groove design of crimp joint 50.

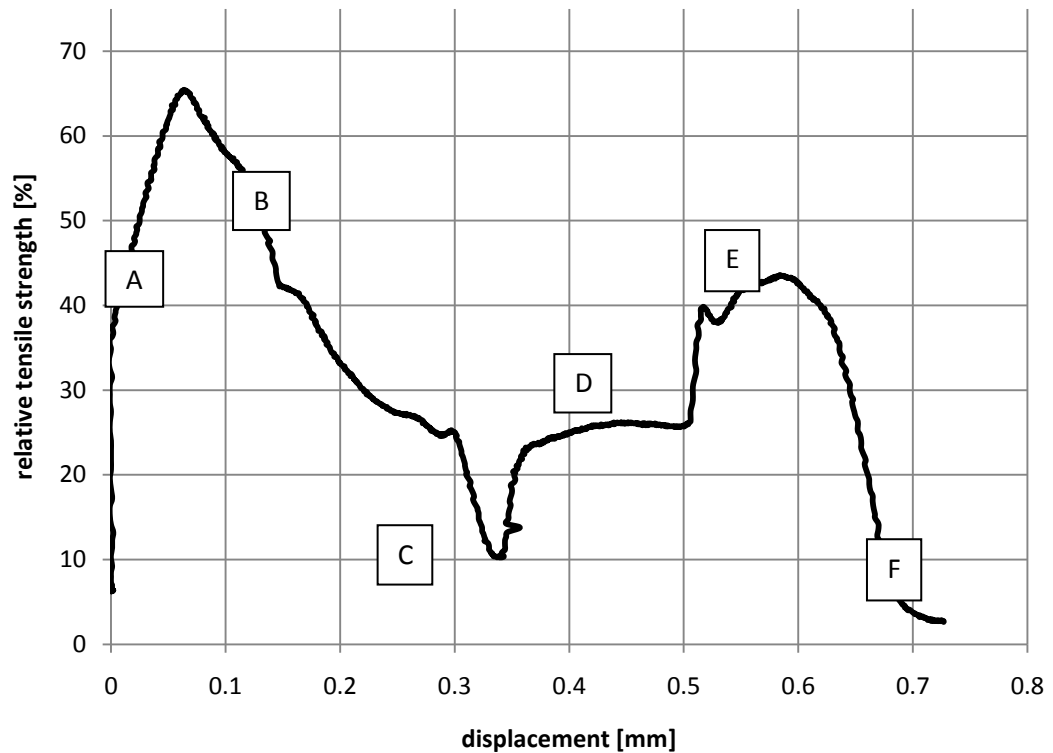


Figure 7.32: Relative tensile strength versus displacement curve for crimp joint 50.

As can be seen in Figure 7.32, the relative tensile strength versus displacement curve can be subdivided into six main parts, denoted by “zone A” up to “zone F”. These will be analysed below by making use of the DIC images.

Zone A

Initially, there is an interlock behind both edges (edge 1_1 and edge 2_1) and they both bear a part of the load (see Figure 7.35.A). The relative tensile strength versus displacement curve increases to a maximum. This maximum is only about 65% of the tensile strength of the tube material. This can be explained by looking at the parameters which were used to create this joint. Due to the combination of a large edge radius, a small width of the second groove and a low charging voltage, the interlock is limited.

Zone B

The tube is pulled off the internal workpiece. The tube was hardly deformed into the second groove and is pushed out straight away (the point of most radial inward displacement will be close to the collar, see chapter 6).

The load taken up in zone B in Figure 7.32 is generated by pushing out the tube of the first groove. Based on what was said before about the push-out mechanism, one would expect to observe an increase to a second (lower) maximum (which corresponds to the point of maximal radial inward displacement into the first groove) and then a decline once the edge is past this maximum. However, it is seen that the curve declines in the whole zone B. This unexpected trend is due to the sunken collar (see Figure 7.33). Because the slope of the deformed tube near the edge 1_1 will become less negative (the tube straightens out and becomes more horizontal) the needed radial

tube displacement is becoming smaller every time for the same axial displacement, and the required force declines in zone B.

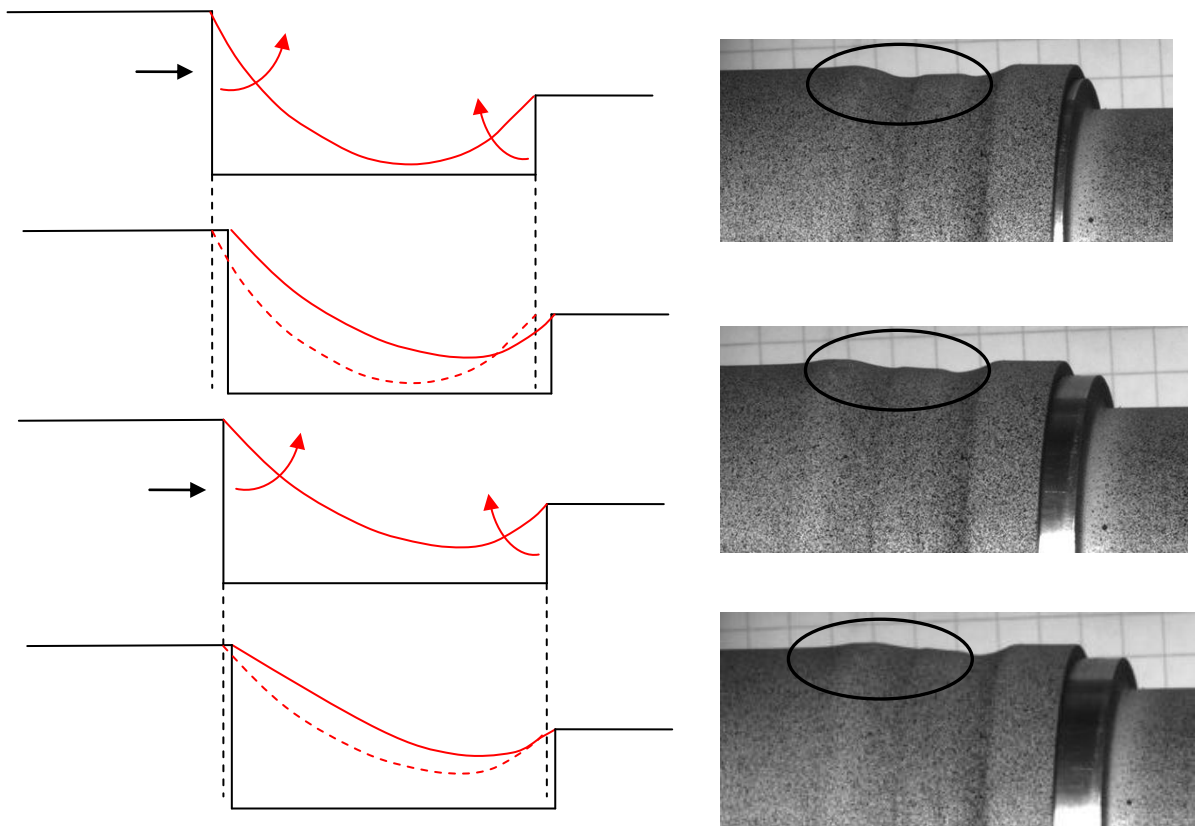


Figure 7.33: Effect of the collar depth on the deformation of the tube in the first groove during push-out.

Zone C

The part of the tube in front of edge 1_1 is straight and almost horizontal, see Figure 7.34. Because of this, there is some “space” in front of edge 1_1 and the internal workpiece can move to the right without having to deform the tube. As a consequence, there is a drop in the absorbed load. When the displacement increases further, the piece of the tube which was originally above the collar needs to be pushed out and the absorbed load increases again.

Zone D

The edge 1_1 pushes the piece of the tube which was originally above the collar up. Because this piece of the tube is in fact a zone with the same inwards radial displacement over a certain axial length, the force which is needed is a constant, thus explaining the horizontal part in the curve of the relative tensile strength versus displacement.

Zone E

The edge 1_1 then reaches the part of the tube which was originally deformed into the second groove. This part of the tube already got pushed out over a small radial distance by the edge 2_1 (in order to allow the sunken collar to pass underneath it). In other words, that part of the tube only needs to be pushed out over the same radial distance as the part of the tube that was originally above the collar. One would therefore expect that the relative tensile strength versus displacement would continue to be horizontal in zone E. However, this is not the case. The curve

increases to a second (lower) maximum. This can be explained by the fact that this part of the tube is strain hardened due to the earlier push-out. Therefore more energy will be required to achieve the same radial displacement.

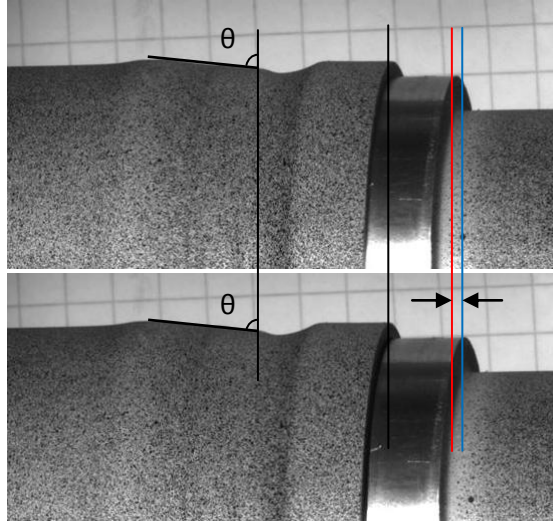


Figure 7.34: Explanation for the drop in the relative tensile strength versus displacement curve.

Zone F

Once the strain hardened part of the tube is pushed out, the curve declines again. It does however not just drop to zero, it rather gradually goes to zero. The explanation for this can be found by looking at the deformation of the end of the tube during the push-out process. A bending moment will be exerted on the end of the tube during the push-out by edge 1_1 , and it undergoes a small radial inward displacement. This can be seen by comparing the end of the tube in Figure 7.35.C and Figure 7.35.D. The edge 1_1 will have to push this deformed end of the tube out again before it can slide out.

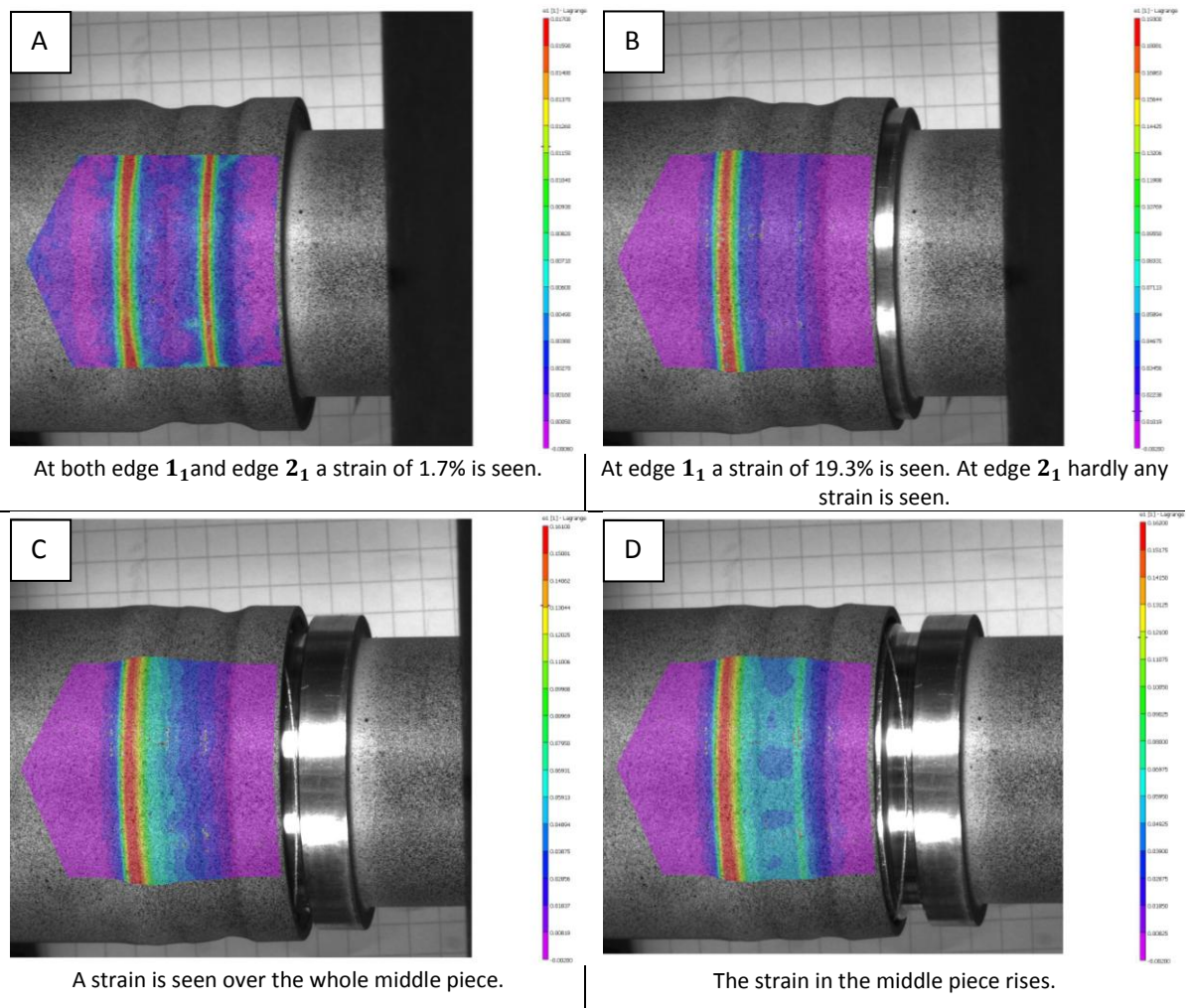


Figure 7.35: Lagrange strain for crimp joint 50.

7.5 Conclusions

The Digital Image Correlation (DIC) technique was explained and this technique was used to study the failure behaviour of a double groove design subjected to an axial load.

It was stated that this failure behaviour can be divided into 3 main failure modes:

- ✓ **Failure mode 1:** The tube tears at edge 1_1 at the complete circumference.
- ✓ **Failure mode 2:** The tube tears at edge 2_1 at the complete circumference.
- ✓ **Failure mode 3:** The tube gets pulled off the internal workpiece, no tearing occurs.

In failure mode 1, it is the thinning of the tube wall near the groove edge 1_1 and the amount of load taken up by the second groove which determine the tensile strength of the joint. After the tube tears at edge 1_1 , the joint can no longer bear a load.

It was observed that failure mode 1 could be divided into 3 subgroups:

- ✓ **Subgroup 1:** These crimp joints have a bad design for the first groove. As a consequence, thinning at edge 1_1 is too excessive and the second groove will not bear any part of the load. The average relative tensile strength is equal to 74%.

- ✓ **Subgroup 2:** These crimp joints have a better design for the first groove, allowing the second groove to bear part of the load, but they do not have a sunken collar. The average relative tensile strength is 80%.
- ✓ **Subgroup 3:** These crimp joints have a better design for the first groove, as well as a sunken collar with a depth of 1 mm, which causes less thinning at the edge 1₁ and which allows the second groove to bear a larger part of the load. The average relative tensile strength is 91%.

In failure mode 2, it is the thinning of the tube wall near the groove edge 2₁ which determines the tensile strength until the tube tears at that edge. It was observed that the connection still has some strength after tearing occurred. This is because the failure mechanism changes: the tube needs to be pushed out of the first groove, and thus the load absorbed is determined by the radial inward tube displacement into the first groove in combination with the axial displacement at the edge 1₁ of the internal workpiece relative to the tube which is of importance. The average relative tensile strength is 75.3%.

In failure mode 3 no tearing occurs, and thus it is the radial inward tube displacement into both grooves in combination with the axial displacement of the internal workpiece relative to the tube which is of importance. The average relative tensile strength is 66.4%.

An axial crimp joint with failure mode 1 resulted in the highest tensile strength (see Table 7.3). But for some applications it is more appropriate to have partial or full pull out (failure mode 2 and 3) before the joining parts are separated. In the case of pull out, a warning can signalise the user that the joint is failing.

Failure behaviour	Average relative tensile strength [%]	Percentage of occurrence [%]
Failure mode 1	81.7	63.0
<i>Subgroup 1</i>	74.0	16.8
<i>Subgroup 2</i>	80.0	29.4
<i>Subgroup 3</i>	91.0	16.8
Failure mode 2	75.3	12.0
Failure mode 3	66.4	14.0

Table 7.3: Comparison of relative tensile strength and the occurrence of the 3 failure modes.

Chapter 8: Conclusions and recommendations

8.1 Single groove crimp joints

When a tube is crimped into a groove, the tube wall thickness reduces at the edges of the groove. Necking will have a significant influence on the crimp joint strength. It is a challenge to determine an appropriate charging voltage which will result in sufficient deformation of the tube into the groove, while the amount of necking at the groove edge is limited. The amount of necking and the radial inward displacement of a tube, which can freely deform into a groove (no restriction on the inwards movement by a groove bottom), were investigated for several groove geometries and charging voltages.

It was observed that an increase of the charging voltage leads to a larger radial inward displacement. The relationship between the groove width and the radial inward displacement is directly proportional: a larger radial inward displacement is measured when the groove width is larger. It was also observed that the groove edge radius has a very limited influence on the radial inward displacement. In this work, the largest radial inward displacement (decrease in diameter of 27.8%) was found for a groove edge radius equal to 1.5 mm, a groove width equal to 14 mm and a charging voltage of 11 kV. The tube wall thickness of this specimen was reduced to 34% of its original value due to necking.

It should be noted that at a localised zone of the tube experiences less deformation due to the presence of the radial slit in the field shaper

The groove edge radius does have an important influence on the amount of necking: a smaller groove edge radius causes more necking. A remarkable trend was observed when relating the amount of necking to the groove width. First, the amount of necking increases when the groove width increases. It reaches a maximum and then the amount of necking starts to decline as the groove width increases further (while the radial inward displacement linearly increases as the groove width increases further). This was clarified by looking at the ratio of shearing and bending: if the groove width is small, the bending of the tube into the groove is limited and the radial inward displacement will be achieved mostly due to shearing at the groove edges. On the other hand, if the groove width is large, the bending moment will become more significant. Bending does not increase necking and so, less necking is noticed for large groove widths (see Figure 8.1).

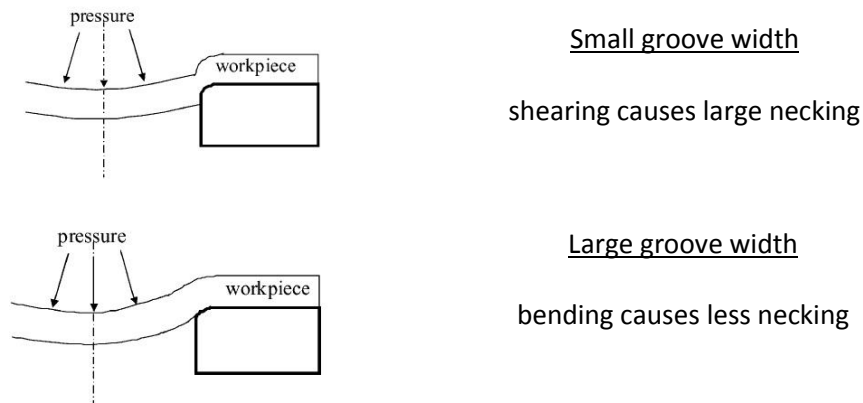


Figure 8.1: Shearing causes more necking than bending does [25].

Equations for fitted 3D-surfaces were generated. These link the groove width and the charging voltage to the radial inward displacement and the necking at the groove edge. They allow to make a first estimate for the parameters in a groove design.

The experiments of free deformation were performed on aluminium EN AW-6060 tubes with a wall thickness of 1.5 mm and an outer diameter of 50 mm. It is more than likely that the qualitative trends will be the same for other materials and dimensions, but in order to obtain quantitative observations, experimental research on the specific combination is necessary.

The tensile strength of two single groove crimp joints was determined. A tensile strength, relative to the base material of the tube, of about 75% was measured. It was assumed that creating a stronger joint must be possible by using a double groove design. To acquire basic knowledge about the deformation of the tube, the amount of necking, plastic deformation of the internal workpiece and the tensile strength of double groove crimp joints, some preliminary experiments were performed.

8.2 Double groove crimp joints

In the preliminary experiments, 8 test series with different groove dimensions were designed. It was noted that the tube does not feed material into the groove. As a consequence, the qualitative observations from the free deformation experiments are applicable on a double groove design. Plastic deformation is noticed at the bottom of the groove when a high charging voltage is applied and when the groove has a shallow depth. By increasing the charging voltage, the plastic deformation becomes more obvious and the tube makes more contact with the groove bottom. Once the tube has reached the bottom, it was observed that the necking decreases very little when applying higher charging voltages.

The amount of necking was less in the designs where a sunk collar was present. When the tube deforms into two grooves with a sunk collar in between, the zone of largest radial inward displacement moves closer towards the collar. A sunk collar also experiences plastic deformation due to the tube impact, especially when high charging voltages are applied. If the collar has sharp edges, the tube will plastically deform the edges and the edge radius will increase significantly.

The combination of a deep groove and a sharp edge will cut the tube, but a sharp edge is beneficial if it is combined with a shallow groove. The combination of a deep groove with a small groove width will not allow the tube to sufficiently deform into the groove.

Finite element simulations of a tensile test performed on a double groove crimp joint were executed to get more insight in the stress distribution throughout the joint. It was seen that the tube experienced the highest tensile stress at edge 1_1 (see Figure 8.2). This was confirmed by the preliminary experiments (and also all further experiments) because in 60% of the experiments, the joint failed in this critical zone. The highest compressive stress during tensile testing was found at edge 2_1 (see Figure 8.2). An experimental research is performed to create an optimal double groove crimp joint with a strength as strong as the base material.

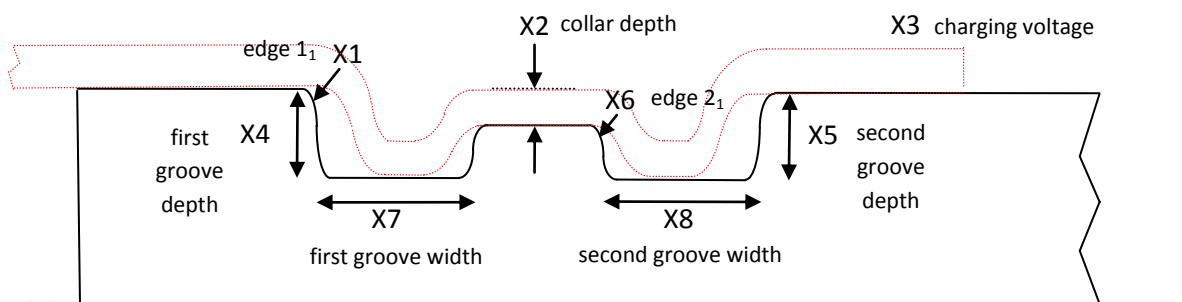


Figure 8.2: Nomenclature and parameter numbering for the DoE.

The design of experiments (DoE) method was used to investigate the importance and the influence of several parameters on the strength of a double groove design. Eight parameters (X1 to X8), shown in Figure 8.2 were investigated on 2 levels in the DoE. The choice for the parameters was based on the knowledge obtained during the free deformation and the preliminary experiments.

The results led to an optimal design which should provide a joint strength as strong as the base material. In the optimal design, each parameter has been given a value, either its low value or high value. The actual optimal design was not included in the test matrix, but designs which have seven out of eight optimal parameters in common with the optimal design were tested. These designs had a relative tensile strength more than 90%, which is very promising.

The optimal design should include a sharp edge radii for edges 1_1 and 2_1 to create sufficient mechanical interlock behind these corners. Because these edges need to be sharp, the other parameters must be designed in such way, that the necking is minimised at these sharp edges. A shallow first groove depth and a collar depth will minimise the necking, while a large first groove width insures friction between the tube and the groove's bottom. The second groove width should be large as well to allow deformation of the tube into the groove. For an aluminium tube EN AW-6060 with a wall thickness of 1.5 mm and an outer diameter of 50 mm the optimal design is shown in Figure 8.3.

The DoE method is very efficient to draw conclusion about an optimal design with a minimum number of experiments. Before designing the test matrix, one should have good knowledge of the parameters and possible values which are combinable with one another. In this case, the free deformation and the preliminary experiments provided sufficient knowledge to successfully design an optimal double groove crimp joint.

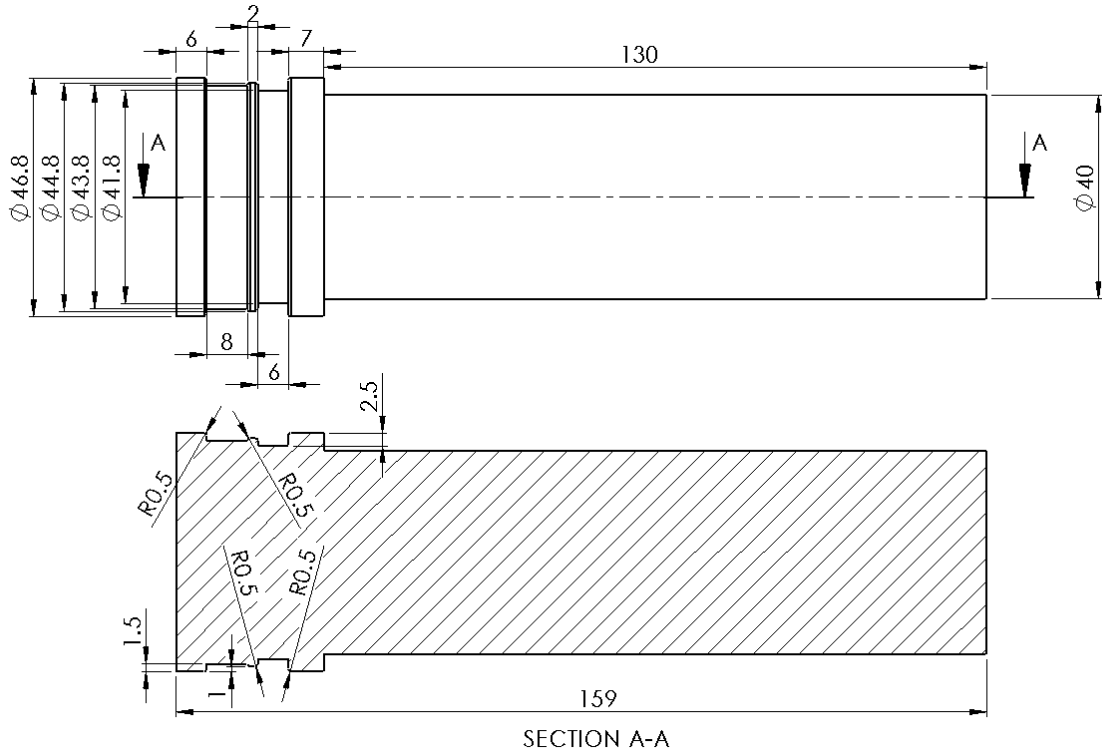


Figure 8.3: Technical drawing of the optimal design obtained by DoE.

It should be noted that the optimisation with the DoE only included geometric parameters, independent of the materials used. Therefore, the optimal design should be applicable for all materials, if the appropriate charging voltage (which will be different for all materials) is chosen.

For several applications, it is important to know how the crimp joint will fail when a certain load is applied. Therefore, an in depth study was performed on the failure behaviour of the crimp joints from the DoE. The digital image correlation technique was used to determine the distribution, the location and the magnitude of strains during tensile testing of the crimp joint.

Three main failure modes could be distinguished:

- ✓ **Failure mode 1:** The tube tears at edge 1_1 at the complete circumference.
- ✓ **Failure mode 2:** The tube tears at edge 2_1 at the complete circumference .
- ✓ **Failure mode 3:** The tube gets pulled of the internal workpiece, no tearing occurs.

In failure mode 1, the necking of the tube wall near the groove edge 1_1 and the amount of load taken up by the second groove determine the tensile strength of the joint. After the tube suddenly tears at edge 1_1 , the joint can no longer bear a load.

It was observed that failure mode 1 could be divided into 3 subgroups:

- ✓ **Subgroup 1:** These crimp joints have a bad design for the first groove. As a consequence, thinning at edge 1_1 is too excessive and the second groove will not bear any part of the load.
- ✓ **Subgroup 2:** These crimp joints have a better design for the first groove, allowing the second groove to bear part of the load, but they do not have a sunk collar.
- ✓ **Subgroup 3:** These crimp joints have a better design for the first groove, as well as a sunk collar with a depth of 1 mm, which causes less thinning at the edge 1_1 and which allows the second groove to bear a larger part of the load.

In failure mode 2, the thinning of the tube wall near the groove edge 2_1 determines the tensile strength until the tube tears at that edge. It was observed that the connection still has some strength after tearing occurred. This is because the remaining part of the tube needs to be pushed out of the first groove, and thus the load absorbed is determined by the radial inward tube displacement into the first groove in combination with the axial displacement at the edge 1_1 of the internal workpiece relative to the tube which is of importance.

In failure mode 3 no tearing occurs, and thus it is the radial inward tube displacement into both grooves in combination with the axial displacement of the internal workpiece relative to the tube which is of importance.

An axial crimp joint with failure mode 1 resulted in the highest tensile strength (see Table 8.1). Failure mode 1 also covers the vast majority of failures during crimping experiments. In Appendix D, the curves of relative tensile strength versus displacement as well as the failure mode can be found for all samples performed in the DoE.

Failure behaviour	Average relative tensile strength [%]	Percentage of occurrence [%]
Failure mode 1	81.7	63.0
<i>Subgroup 1</i>	74.0	16.8
<i>Subgroup 2</i>	80.0	29.4
<i>Subgroup 3</i>	91.0	16.8
Failure mode 2	75.3	12.0
Failure mode 3	66.4	14.0

Table 8.1: Comparison of relative tensile strength and the occurrence of the 3 failure modes.

8.3 Recommendation for future work

8.3.1 Further work on DoE

One of the main objectives of this master thesis was to determine an optimal double groove design for an axial load in order to demonstrate that magnetic pulse crimping is a valuable alternative for magnetic pulse welding. An optimal double groove design was proposed (see § 8.2) and it is more than likely that a joint with this design is able to bear an applied tensile force which is equal to the tensile force of the base material of the tube (see chapter 6).

However, this optimal design still needs to be experimentally tested. A discrete amount of joints with this design (for example 5, in order to limit the costs but still be able to get relevant information on the scatter) should be fabricated and tensile tests should be performed.

Good results are expected, but if the observed tensile strength would happen to be lower than the expected value, this will most likely be due to the fact that the DoE performed in this work was influenced by choices made for the value of the second groove width and depth. This may be resolved by performing a limited number of experiments with better values for the width and the depth of the second groove. By selecting 3 new values for both the second groove's width and depth (resulting in $3^2=9$ experiments), the expected tensile strength (equal to the tensile strength of the base material) should be achieved.

Based on the trends from the DoE and the knowledge acquired during the other experiments, the following values are proposed:

- ✓ Second groove width: 6 mm, 7 mm and 8 mm
- ✓ Second groove depth: 2 mm, 2.5 mm and 3 mm

It should be noted that a second groove width of 7 or 8 mm does not fulfil the restriction on the axial length of the field shaper (see § 6.2.2). However, it was seen that small area outside the effective work zone also experiences sufficient magnetic forces. This in combination with the inertia effect which will pull the tube near edge 2_2 (outside the field shaper zone) radial inward, should be sufficient to achieve a good deformation in the wider second groove.

8.3.2 Leakproofness

Besides being able to produce a strong crimp joint, it is also very important towards industrial applications to create leakproof crimp joints. Research on this subject should definitely be done in the future. In order to achieve leakproof crimp joints, rubber rings, solder or glues can be used. A proposition with a rubber ring is stated below.

To create leakproof joints, a rubber ring can be used and the ring should be placed at the bottom of the groove, close to the second edge of the groove (see Figure 8.4 and Figure 8.5). By placing the rubber ring at that position, the mechanism which provides the strength to a crimp joint (interlock behind the first edge of the groove) is completely separated from the mechanism which assures leakproofness, and hence both mechanisms can be optimised separately without influencing each other. For a double groove axial crimp joint, the rubber ring may be placed at the zone of edge 1_2 or at the zone of edge 2_2 , or both, because these zones are of least importance for the tensile strength of the crimp joint.

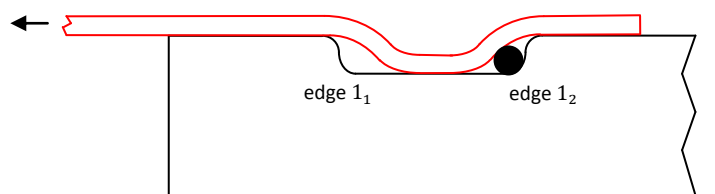


Figure 8.4: Position of the rubber ring for a single groove design.

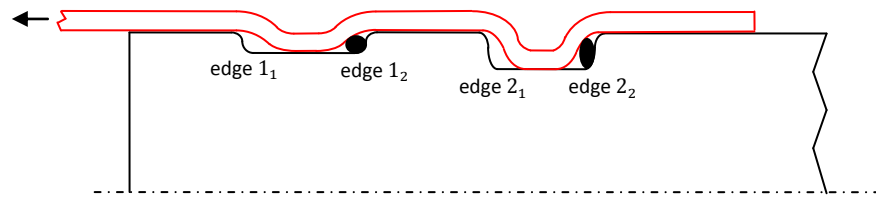


Figure 8.5: Position of the rubber ring for a double groove design.

When the tube is crimped into the grooves, it clamps the rubber ring in place. Because high speed forming is related with changing material behaviour during deformation, it is unknown how the rubber ring will react on the impact of the tube. Also heat generation might influence the ring's integrity. This needs to be investigated experimentally.

It should be noted that most of the internal workpieces used for the DoE-experiments are still intact after crimping and performing the tensile tests. Therefore, these might be re-used to perform leakproofness experiments.

To test the leakproofness, it is possible to apply pneumatic pressure on the inside of the tube and detect and measure leakage of the used gas. The workpiece is immersed in a water bad, and when the gas escapes, bubbles will be observed in the water. The amount and frequency of bubbles can be an indication of the leak flow rate.

Another way to measure the leak flow is by applying pneumatic pressure to a certain level. Then the pressure supply is shut off and the decrease of pressure inside the workpiece is recorded. The latter method can be used to measure the leak flow during tensile testing. This is of importance for industrial applications: for the transport of dangerous or environmentally harmful fluids, it is of importance that it can be assured that the connection will still be leakproof when the connection is subjected to a certain load.

Figure 8.6 shows a possible set up of a crimp joint in a tensile testing machine. The tube was crimped on the internal workpiece with the rubber rings in place. The internal workpiece is clamped by two lower clamping chucks (see also Figure 6.12). The hollow tube needs a support when clamped. The support in this set up is also a sealing component which prevents leaking in this area. The leak flow which needs to be measured is the leak along the grooves. The sealing/tube support features a connection to a manometer which will allow to measure the pressure drop during tensile testing.

The tensile test should be performed with great care, because when the crimp joint suddenly fails, the pressure inside the tube will drop. This will make a noise, high reaction forces will suddenly act on the workpiece and machine, specimens could become fragmented,

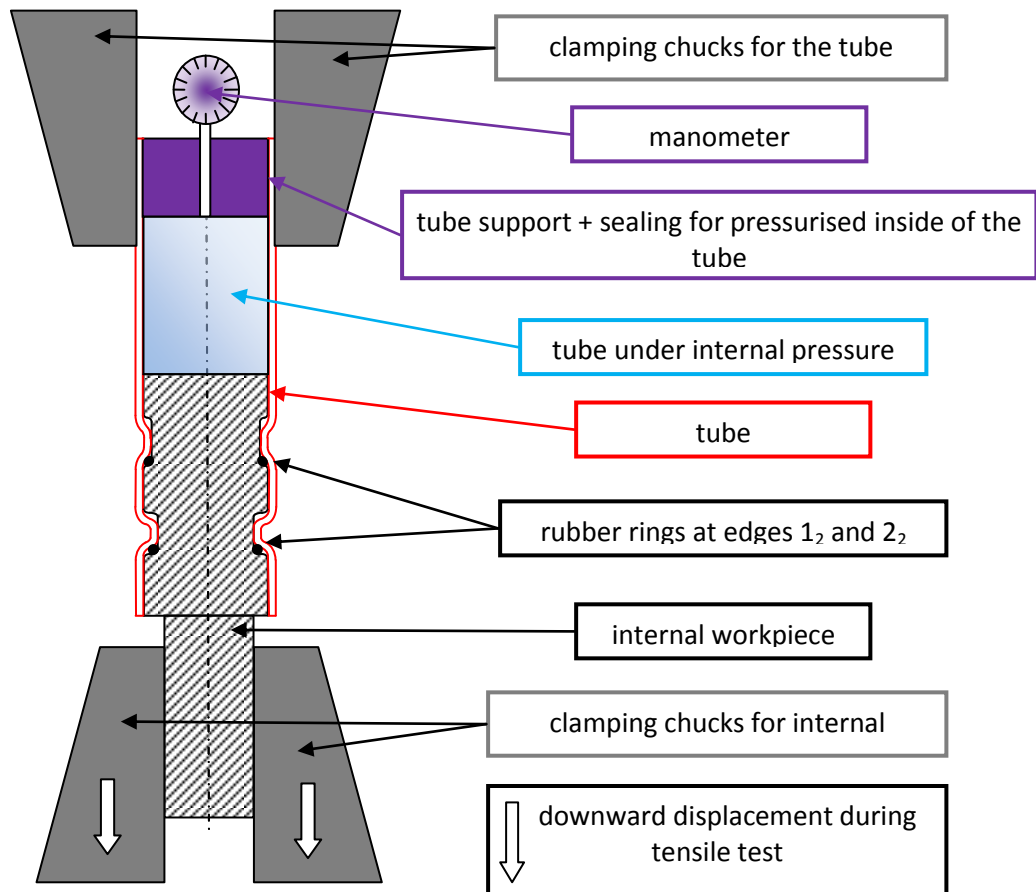


Figure 8.6: Set up for a tensile test with measurement of the leakflow.

8.3.3 Further work on free deformation

8.3.3.1 Validating the conclusions of the free deformation experiments

In this master thesis, conclusions and hypotheses were based on a limited amount of experiments.

Experiments should be performed using the cylinder system which was used in this master thesis with the same range of voltages and groove edge radii, but on a groove width which varies between 7 and 15 mm, with a 2 mm interval. The inward radial displacement as well as the necking at the groove edges should be measured. This will result in measurement points which are in between the measurement points determined in this thesis, and will allow to validate the correctness of the fitted surfaces, as well as conform or falsify hypotheses and conclusions which were made on the trends in the graphs in this thesis.

Since there was a fairly large amount of scatter for the necking for a groove edge radius of 1.5 mm, it might also be useful to repeat the measurements which were done in this thesis and replace the extreme values by the new measured values in order to obtain a better result.

8.3.3.2 Influence of the groove depth

No values are known for the tube wall thinning when a certain groove depth is present (limiting the deformation). To simulate such a groove without having to produce new internal workpieces for every groove, the design shown in Figure 8.7 can be used. The basic principle remains the same from the cylinder system which was used in this master thesis (see chapter 4), only now a full metal body (other materials can also be used) is used to separate the cylinders with a larger diameter than the metal rings. After deformation, the cylinder system can be separated again, and the metal body can be recovered and re-used together with the rest of the cylinder system.

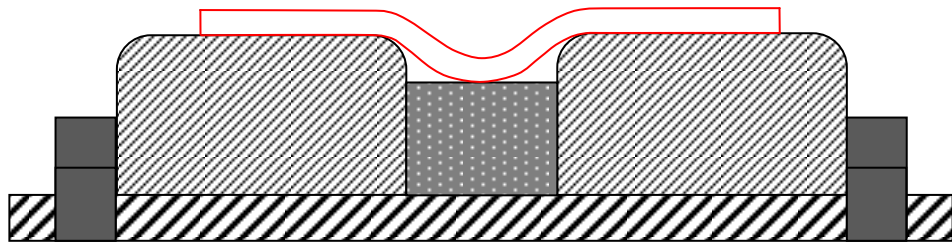


Figure 8.7: Cylinder system with a certain groove depth.

8.3.3.3 Evaluating a double groove design

The cylinder system can also be modified to investigate the free deformation of the tube into two grooves. Figure 8.8 shows a cross section of a modified cylinder system. It should be noted that the middle cylinder, which can be small, should be sufficiently supported over a large area, so that it does not collapse under the large pressures during the crimping process. Also, it should be noticed that the middle cylinder will be clamped after deforming the tube and that it will be impossible to remove this piece afterwards. After measuring, the tube can be cut and the middle cylinder might be re-used.

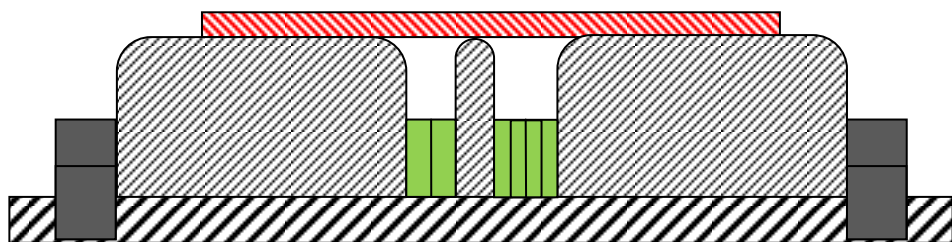


Figure 8.8: Cylinder system for a double groove design.

Of course, the principle of a cylinder system set up with a limited groove depth, which is discussed in the previous paragraph, can also be applied for the double groove design. Two metal bodies (or bodies made of any other material) can be placed in between the cylinders.

8.3.4 Finite element simulations of joint strength

With the information gathered in this thesis (the necking at the groove edge and the radial inward displacement of the tube for several single groove designs, the tensile strengths for the double groove designs from the DoE, the analysis of the failure behaviour with DIC, the axial strain-distribution in the tube from DIC, the z-displacement of the tube from the DIC, etc.), it should be possible to create fairly accurate finite element models.

Nevertheless, it should be possible to develop a program that is able to “read” the geometry of a cross-sectioned deformed tube and that copies the exact geometry into the finite element program. This would save a lot of time (creating models in finite element programs is very time consuming) and it would result in even more accurate finite element models.

8.3.5 Torque joints

A similar approach as the one followed in this thesis can be used to investigate torque crimp joints. First, clear objectives have to define the area of interest. An objective could be to create a torque crimp joint which fails in the base material, instead of in the joint. Also a combination of a torque and axial crimp joint is possible. The question in this case is: is it possible to design a crimp joint which resists high tensile forces, high torque loading and/or a combination of these two? One can also investigate the possibility to make the (torque) crimp joint leakproof. It is important to keep the industrial demands in mind..

After defining the objectives, some preliminary experiments can be set up. To create an optimal torque crimp joint, various designs can be proposed. Cross sections perpendicular to the axial length of possible torque joint designs are shown in Figure 8.9.

Joint design a is a regular hexagon, while design b has multiple grooves with a certain depth, width and edge radii. Design c has 2 types of grooves along the circumference: a big and a small groove. Design d has sharp edges and only 4 grooves along the circumference.

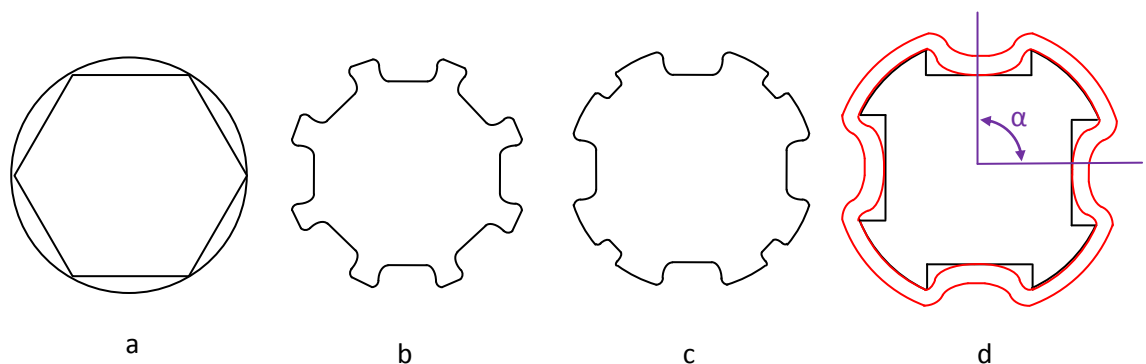


Figure 8.9: Some possible torque joint-designs.

The parameters which characterise a torque joint-design are shown in Figure 8.9.d and in Figure 8.10. The angle α determines the number of grooves along the circumference. Each groove has a

width, length, depth and has 4 edges. Alternative design proposals are a screw thread profile on the internal workpiece, designs as shown in Figure 8.11 ,...

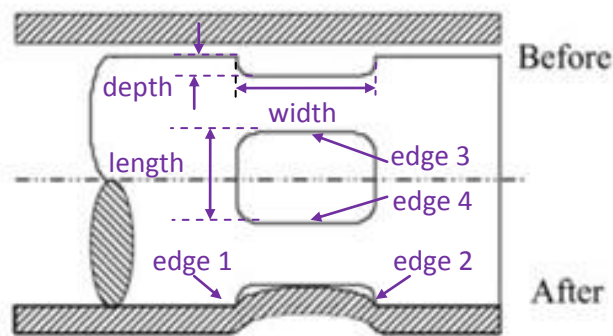


Figure 8.10: Nomenclature of groove design [25].

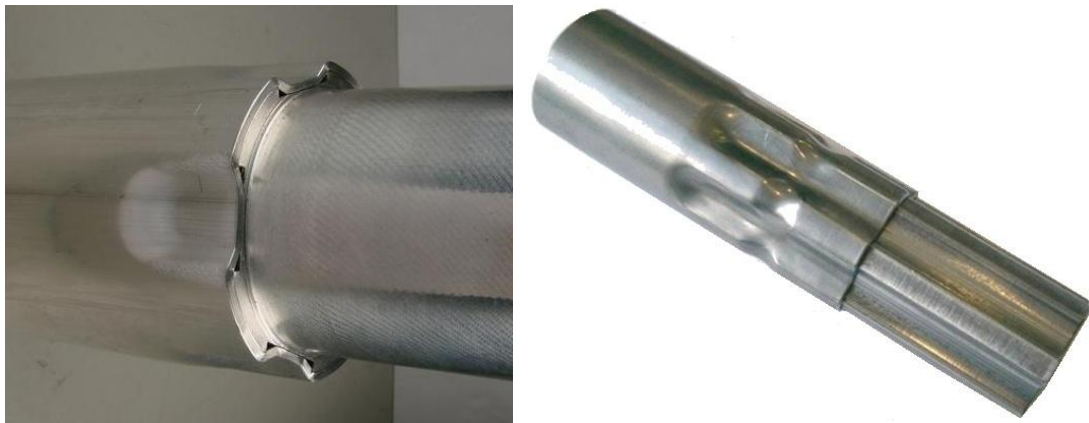


Figure 8.11: Pictures of a torque joint according to joint-design d and a torque joint combined with an axial joint [3].

Once a design to investigate is selected, the parameters should be determined. It is advised to use DoE to optimise the groove design. It is very likely to obtain good results if the values of the DoE are well chosen. It should be noted that more parameters (e.g. the groove length and the angle α) are present in a torque joint design than in the axial crimp joint discussed in this work. Thus, the amount of experiments will increase if good results have to be obtained.

8.3.6 Hollow internal workpiece

Up till now, experiments have been performed with a rigid internal workpiece. However, a lot of industrial applications demand a hollow internal workpiece. The electromagnetic pulse crimping technique might be used to connect water and pressure pipes, etc.

The reason that rigid internal workpieces were used in this thesis is that the groove design methodology was investigated. The grooves are located on the outer surface of the internal workpiece and thus it does not matter for the groove design if the internal part is rigid or not. By using a rigid internal workpiece, many problems could be avoided (concerning strength, etc..).

During the electromagnetic pulse crimping process, the high forces acting on the tube will create a compression and will even cause an impact onto the internal workpiece. If the internal

workpiece is hollow, there is a possibility that this workpiece is deformed if no support is applied. Furthermore, if the hollow internal workpiece is also electrically conductive, the magnetic repulsive forces are acting on it as well.

During crimping, it is desirable that a hollow internal workpiece cannot deform radially inwards. An internal support is required. However, there are two problems regarding this support. First, it will not be easy to remove the temporary support after the tube has been crimped onto the internal workpiece and as a consequence, the internal workpiece is crimped onto the support. Second, for some applications, the tubes used have a large axial length. So it will be hard to reach the crimping area to remove the support after crimping.

To remove the support after crimping, one can use a support that acts as a rigid body during the crimping process and that can relax or decrease its diameter after crimping. A possible support system could contain bevel gears (gears where the axis of the gears intersect) [51].

Figure 8.12 shows a set up of the bevel gear hollow internal workpiece support system. By turning the main rod (the black arrow in Figure 8.12), a bevel gear system opens or closes the internal workpiece supports.

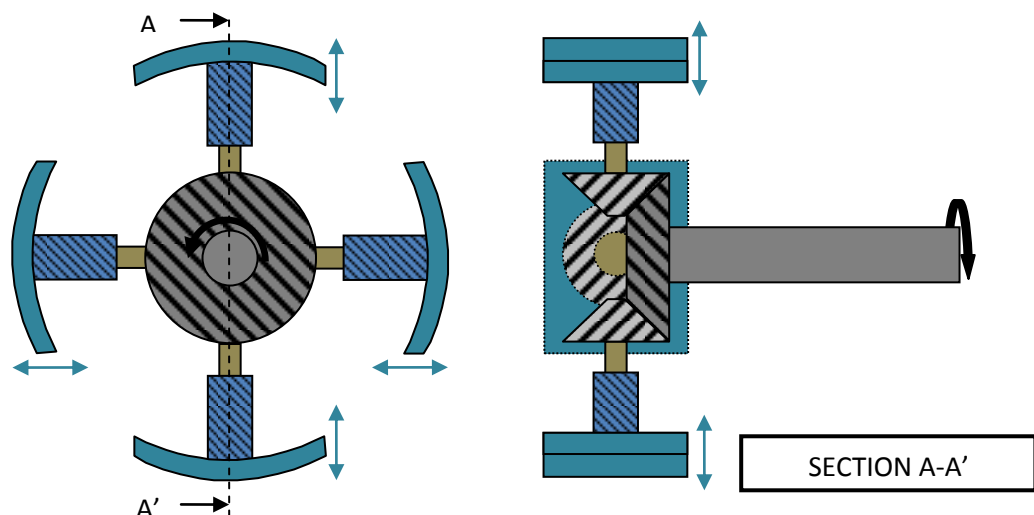


Figure 8.12: 'bevel gear'- hollow internal workpiece support system.

The disadvantage of this system is that all bodies are rigid bodies and the system cannot be used when crimping pipes which are not straight. Another disadvantage is that the hollow internal workpiece is only supported in discrete zones and not over the entire circumference.

A better support system is probably possible by using hydraulics. When a high pressure is applied inside a 'bag', which can be made of some kind of metal or plastic which is able to stretch sufficiently and has sufficient strength, the bag is inflated and fills the hollow internal workpiece. When the desired pressure is reached, the bag supports the internal workpiece in the zone where crimping will occur. In this support system, the whole circumference will be supported.

8.3.1 Field shaper design

The radial cut in the field shaper causes irregular deformation of the tube (see Figure 4.30). However, some applications (eg. roller bearings) demand a perfect regular deformation. Because less deformation is noticed in the zone near the radial cut, it was concluded that the magnetic pressure is lower than in the other areas of the circumference. To homogenise the magnetic pressure, the following option is proposed.

To locally increase the magnetic pressure, it might be useful to locally decrease the axial length of the field shaper (see chapter 2). Figure 8.13 shows a cross section of a field shaper with a decreased axial length in the radial cut zone. It should be noted that this operation brings along a higher manufacturing cost: the field shaper cannot be simply turned on the lathe, but needs extra milling operations.

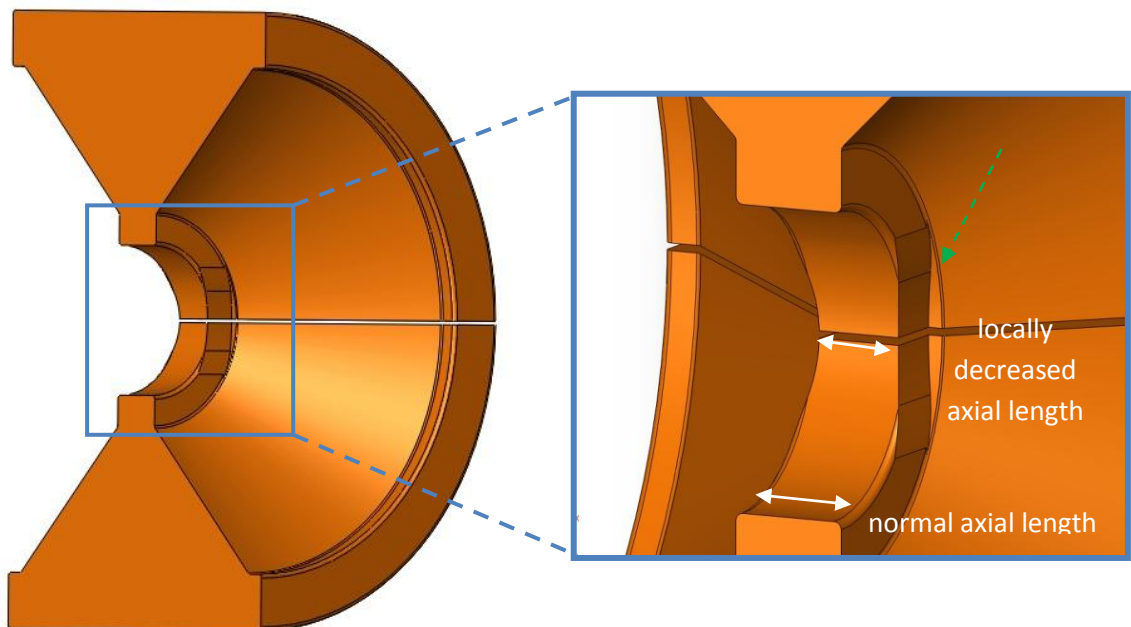


Figure 8.13: A local decrease of the axial length in the radial cut zone. The discontinuity seen in this picture (see dotted arrow) should be removed by a milling operation. A gradually decrease in axial length will lead to a better performance of the field shaper.

APPENDIX A SPECIFICATIONS

This Appendix provides the main specifications for the MPW 50 25 Magnetic Pulse System.

Detail	Description
Operating environment	(-15) °C to 30 °C (5 °F to 86 °F) 0 % to 70 % relative humidity
Power supply /phase	600 V x 3 phase 13 A
Power consumption for model MPW 50 25	13 kW maximum 6 kW RMS 0.47 kW idle
Maximal storage energy	50 kJ
Maximal pulse energy	40 kJ
Maximal voltage	25 kV (22.36 kV @ 40 kJ)
Maximal pulse current	500,000 A, 28 kHz
Maximum productivity for model MPW 50 25	15 PPM @ 5 kJ 6 PPM @ 25 kJ 4 PPM @ 40 kJ
Voltage-energy ratio	$V = \sqrt{\frac{E}{80}}$ E (J); V (kV)
COIL replacement	Each 50,000 pulses

The following table provides the system's dimensions:

System Layout	Dimensions (WxDxH ⁽³⁾)	
HIGH VOLTAGE CABINET ⁽¹⁾ ⁽²⁾	840x800x2660 mm	(33.1x31.5x104.7 inch)
ENERGY STORAGE CABINET	1000x1250x2030 mm	(39.4x49.2x79.9 inch)
WORK TABLE (for PREP system)	1000x840x2090 mm	(39.4x33.1x82.3 inch)
TRANSFORMER (for PREP system)	1000x840x1030 mm	(39.4x33.1x40.6 inch)
OPERATING PANEL	400x400x1170 mm	(15.8x15.8x46.1 inch)

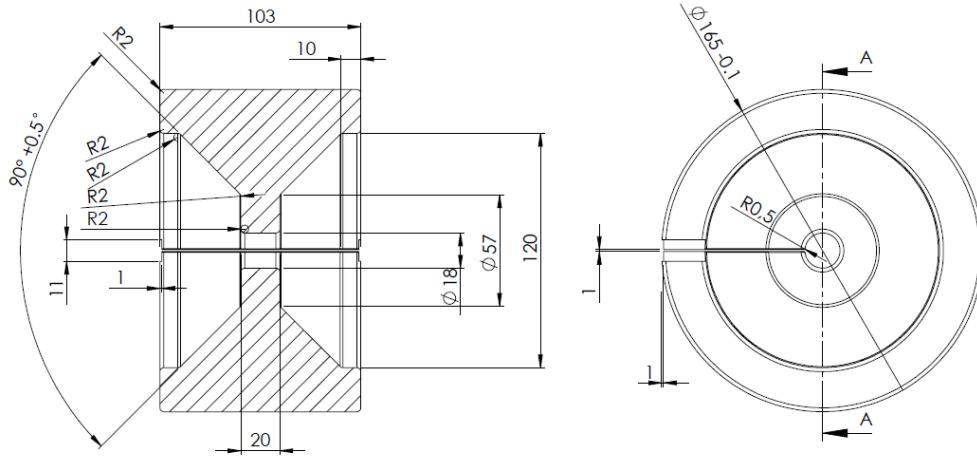
⁽¹⁾ Including feet (Cabinet's width without feet is 720 mm).

⁽²⁾ Including the STATUS-INDICATING LIGHT (460 mm), installed on top.


⁽³⁾ W=Width; D=Depth; H=Height

APPENDIX B

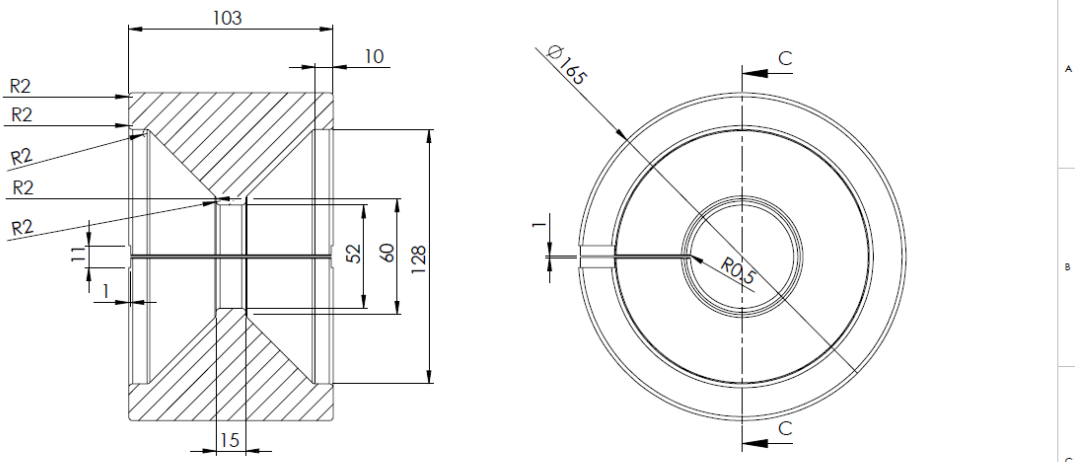
Field shaper for outer diameter 18 mm




SECTION A-A
SCALE 1 : 2

MODEL NAME	FIELD SHAPER 18mm	
DATE	27/10/2010	
DESIGNER(S)	KOEN FAES PIETER VANHULSEL MATTHIAS VAN WONTERGHEM	

Field shaper for outer diameter 52 mm



SECTION C-C
SCALE 1 : 2

MODEL NAME	FIELD SHAPER 52 mm	
DATE	27/10/2010	
DESIGNER(S)	KOEN FAES PIETER VANHULSEL MATTHIAS VAN WONTERGHEM	

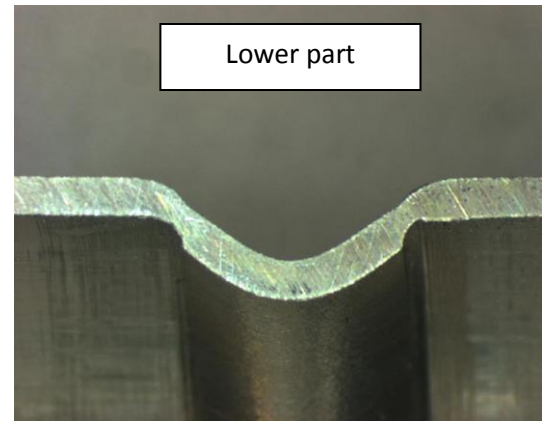
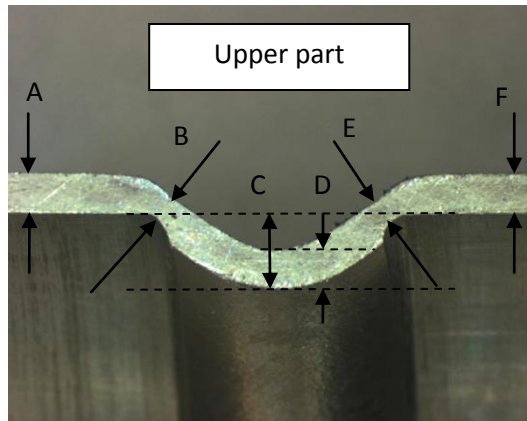
Appendix C

Test matrix and measured values from free deformation experiments

name	groove edge radius [mm]	groove width [mm]	charging voltage [kV]	name	groove edge radius [mm]	groove width [mm]	charging voltage [kV]
PC_VV_1	1.5	6.0	13.0	PC_VV_61	0.5	10.0	8.0
PC_VV_2	1.5	6.0	12.0	PC_VV_62	0.5	10.0	7.0
PC_VV_3	1.5	6.0	11.0	PC_VV_63	0.5	10.0	6.0
PC_VV_4	1.5	6.0	10.0	PC_VV_64	0.5	10.0	5.0
PC_VV_5	1.5	6.0	9.0	PC_VV_65	0.5	12.0	11.0
PC_VV_6	1.5	6.0	8.0	PC_VV_66	0.5	12.0	10.0
PC_VV_7	1.5	6.0	7.0	PC_VV_67	0.5	12.0	9.0
PC_VV_8	1.5	6.0	6.0	PC_VV_68	0.5	12.0	8.0
PC_VV_9	1.5	8.0	12.0	PC_VV_69	0.5	12.0	7.0
PC_VV_10	1.5	8.0	12.0	PC_VV_70	0.5	12.0	6.0
PC_VV_11	1.5	8.0	10.0	PC_VV_71	0.5	12.0	5.0
PC_VV_12	1.5	8.0	10.0	PC_VV_72	0.5	12.0	4.0
PC_VV_13	1.5	8.0	8.0	PC_VV_73	0.5	14.0	11.0
PC_VV_14	1.5	8.0	8.0	PC_VV_74	0.5	14.0	10.0
PC_VV_15	1.5	8.0	6.0	PC_VV_75	0.5	14.0	9.0
PC_VV_16	1.5	8.0	6.0	PC_VV_76	0.5	14.0	8.0
PC_VV_E1	1.5	8.0	13.0	PC_VV_77	0.5	14.0	7.0
PC_VV_E2	1.5	8.0	11.0	PC_VV_78	0.5	14.0	6.0
PC_VV_E3	1.5	8.0	9.0	PC_VV_79	0.5	14.0	4.0
PC_VV_E4	1.5	8.0	7.0	PC_VV_80	0.5	14.0	5.0
PC_VV_E5	1.5	8.0	5.0	PC_VV_81	1.0	6.0	13.0
PC_VV_17	1.5	10.0	13.0	PC_VV_82	1.0	6.0	12.0
PC_VV_18	1.5	10.0	12.0	PC_VV_83	1.0	6.0	11.0
PC_VV_19	1.5	10.0	11.0	PC_VV_84	1.0	6.0	10.0
PC_VV_20	1.5	10.0	10.0	PC_VV_E9	1.0	6.0	10.0
PC_VV_21	1.5	10.0	9.0	PC_VV_85	1.0	6.0	9.0
PC_VV_22	1.5	10.0	8.0	PC_VV_E10	1.0	6.0	9.0
PC_VV_23	1.5	10.0	7.0	PC_VV_86	1.0	6.0	8.0
PC_VV_24	1.5	10.0	6.0	PC_VV_E11	1.0	6.0	8.0
PC_VV_25	1.5	12.0	10.0	PC_VV_87	1.0	6.0	7.0
PC_VV_26	1.5	12.0	10.0	PC_VV_E12	1.0	6.0	7.0
PC_VV_27	1.5	12.0	8.0	PC_VV_88	1.0	6.0	6.0
PC_VV_28	1.5	12.0	8.0	PC_VV_E13	1.0	6.0	6.0
PC_VV_29	1.5	12.0	6.0	PC_VV_89	1.0	8.0	12.0
PC_VV_30	1.5	12.0	6.0	PC_VV_90	1.0	8.0	11.0
PC_VV_31	1.5	12.0	11.0	PC_VV_91	1.0	8.0	10.0
PC_VV_32	1.5	12.0	9.0	PC_VV_92	1.0	8.0	9.0
PC_VV_E6	1.5	12.0	7.0	PC_VV_93	1.0	8.0	8.0
PC_VV_E7	1.5	12.0	5.0	PC_VV_94	1.0	8.0	7.0
PC_VV_E8	1.5	12.0	4.0	PC_VV_95	1.0	8.0	6.0
PC_VV_33	1.5	14.0	11.0	PC_VV_96	1.0	8.0	5.0
PC_VV_34	1.5	14.0	10.0	PC_VV_97	1.0	10.0	11.0
PC_VV_35	1.5	14.0	9.0	PC_VV_98	1.0	10.0	10.0
PC_VV_36	1.5	14.0	8.0	PC_VV_99	1.0	10.0	9.0

PC_VV_37	1.5	14.0	7.0	PC_VV_100	1.0	10.0	8.0
PC_VV_38	1.5	14.0	6.0	PC_VV_101	1.0	10.0	7.0
PC_VV_39	1.5	14.0	5.0	PC_VV_102	1.0	10.0	6.0
PC_VV_40	1.5	14.0	4.0	PC_VV_103	1.0	10.0	5.0
PC_VV_41	0.5	6.0	13.0	PC_VV_104	1.0	10.0	4.0
PC_VV_42	0.5	6.0	12.0	PC_VV_105	1.0	12.0	12.0
PC_VV_43	0.5	6.0	11.0	PC_VV_106	1.0	12.0	11.0
PC_VV_44	0.5	6.0	10.0	PC_VV_107	1.0	12.0	10.0
PC_VV_45	0.5	6.0	9.0	PC_VV_108	1.0	12.0	9.0
PC_VV_46	0.5	6.0	8.0	PC_VV_109	1.0	12.0	8.0
PC_VV_47	0.5	6.0	7.0	PC_VV_110	1.0	12.0	7.0
PC_VV_48	0.5	6.0	6.0	PC_VV_111	1.0	12.0	6.0
PC_VV_49	0.5	8.0	13.0	PC_VV_112	1.0	12.0	5.0
PC_VV_50	0.5	8.0	12.0	PC_VV_113	1.0	14.0	11.0
PC_VV_51	0.5	8.0	11.0	PC_VV_114	1.0	14.0	10.0
PC_VV_52	0.5	8.0	10.0	PC_VV_115	1.0	14.0	9.0
PC_VV_53	0.5	8.0	9.0	PC_VV_116	1.0	14.0	8.0
PC_VV_54	0.5	8.0	8.0	PC_VV_117	1.0	14.0	7.0
PC_VV_55	0.5	8.0	7.0	PC_VV_118	1.0	14.0	6.0
PC_VV_56	0.5	8.0	6.0	PC_VV_119	1.0	14.0	5.0
PC_VV_57	0.5	10.0	12.0	PC_VV_119	1.0	14.0	5.0
PC_VV_58	0.5	10.0	11.0	PC_VV_116	1.0	14.0	8.0
PC_VV_59	0.5	10.0	10.0	PC_VV_117	1.0	14.0	7.0
PC_VV_60	0.5	10.0	9.0	PC_VV_118	1.0	14.0	6.0
PC_VV_61	0.5	10.0	8.0	PC_VV_119	1.0	14.0	5.0

The measured values in the table below are listed in μm . The parameters (A to F) that are measured are measured can be seen in the figure below:



	part	A	B	C	D	E	F
PC_VV_1	upper	1596.15	1068.54	4484.42	1626.62	1010.41	1596.22
	lower	1489.82	709.44	4879.66	1565.82	1085.39	1489.82
PC_VV_2	upper	1596.15	1021.55	4347.61	1626.62	1064.21	1550.62
	lower	1489.74	942.61	4302.00	1611.42	1037.49	1459.34
PC_VV_3	upper	1474.54	942.61	4271.71	1520.22	1078.34	1489.74
	lower	1520.14	1142.64	3876.39	1626.55	1125.32	1657.23
PC_VV_4	upper	1626.55	1191.64	3633.14	1504.94	1214.31	1505.25
	lower	1489.74	1142.13	3435.52	1565.75	1314.20	1520.22
PC_VV_5	upper	1428.93	1129.52	3222.70	1489.82	1217.06	1444.14
	lower	1444.14	1121.72	3161.90	1459.65	1258.14	1414.06
PC_VV_6	upper	1429.02	1199.76	2933.88	1459.34	1301.48	1444.46
	lower	1474.85	1424.07	2645.05	1611.42	1425.53	1474.54
PC_VV_7	upper	1459.34	1412.10	2386.67	1489.82	1409.15	1474.54
	lower	1444.46	1418.30	2584.24	1535.42	1482.59	1520.22
PC_VV_8	upper	1541.87	1458.63	2082.60	1504.94	1591.28	1512.57
	lower	1530.90	1432.12	1976.19	1459.42	1547.23	1482.31
PC_VV_9	upper	1433.32	733.14	5732.95	1494.23	743.99	1494.23
	lower	1570.46	873.36	5306.02	1616.27	991.89	1601.03
PC_VV_10	upper	1448.80	443.22	6007.40	1494.23	704.84	1494.30
	lower	1616.27	970.33	5473.74	1585.78	857.24	1555.29
PC_VV_11	upper	1525.02	1150.73	4482.68	1539.97	1103.92	1540.04
	lower	1482.88	1111.62	4509.59	1574.60	1074.53	1574.52
PC_VV_12	upper	1483.46	938.59	4601.50	1422.91	987.13	1437.97
	lower	1589.41	1196.93	4450.14	1604.47	1220.06	1544.22
PC_VV_13	upper	1604.54	1276.14	3330.03	1604.47	1364.39	1544.22
	lower	1439.24	1297.60	3572.22	1498.52	1234.25	1453.18
PC_VV_14	upper	1570.92	1318.92	3156.83	1601.12	1513.14	1540.64
	lower	1481.48	1217.38	3658.35	1541.95	1224.40	1451.33
PC_VV_15	upper	1587.37	1393.49	2449.03	1572.18	1377.07	1572.18
	lower	1662.96	1609.53	2282.74	1662.89	1611.02	1662.89
PC_VV_16	upper	1529.32	1487.93	2370.50	1559.91	1496.63	1559.91
	lower	1437.89	1377.84	2355.16	1422.35	1367.87	1468.23
PC_VV_17	upper	C	C	C	C	C	C
	lower	C	C	C	C	C	C
PC_VV_18	upper	C	C	C	C	C	C
	lower	C	C	C	C	C	C
PC_VV_19	upper	1553.21	1134.73	6014.90	1629.42	1017.86	1598.89
	lower	1507.53	818.33	6273.75	1553.21	882.94	1461.84
PC_VV_20	upper	1507.60	1127.76	4933.73	1553.28	1179.62	1583.67
	lower	1507.60	1099.13	5116.46	1446.70	850.70	1477.07
PC_VV_21	upper	1420.43	1304.97	5024.97	1496.88	1143.78	1451.70
	lower	1573.24	1388.63	4734.78	1649.61	1347.62	1588.44
PC_VV_22	upper	1512.07	1374.02	4139.22	1450.98	1341.72	1466.57
	lower	1573.24	1355.82	4093.32	1603.71	1415.83	1573.17
PC_VV_23	upper	1557.89	1502.48	2917.27	1603.79	1514.23	1527.35
	lower	1466.33	1493.76	2993.64	1496.88	1493.76	1573.17
PC_VV_24	upper	1527.35	1557.59	2428.53	1527.42	1497.74	1512.07
	lower	1496.80	1497.74	2657.76	1527.42	1508.44	1512.07
PC_VV_25	upper	1452.86	920.90	6178.47	1514.03	1231.56	1514.11
	lower	1544.62	1286.09	5933.80	1575.28	1224.32	1483.44
PC_VV_26	upper	1487.90	1142.99	6740.76	1487.90	1205.41	1472.96
	lower	1572.79	1285.51	5923.56	1603.10	1264.94	1557.22
PC_VV_27	upper	1605.86	1398.06	4786.78	1667.03	1416.34	1605.86
	lower	1453.18	1327.70	4786.78	1514.03	1371.71	1452.86
PC_VV_28	upper	1511.50	1215.61	5007.54	1496.16	1229.44	1450.44
	lower	1557.30	1352.65	4625.87	1618.36	1324.09	1618.29
PC_VV_29	upper	1633.63	1525.54	2671.71	1633.63	1466.02	1618.58
	lower	1496.23	1437.36	2946.51	1557.52	1484.98	1450.44
PC_VV_30	upper	1496.90	1432.55	2675.74	1481.79	1408.49	1511.72

	lower	1602.42	1518.50	2766.44	1587.30	1536.01	1526.83
PC_VV_31	upper	1444.22	453.50	7448.76	1504.94	952.00	1444.22
	lower	1611.42	1193.19	7068.68	1596.15	1142.64	1550.55
PC_VV_32	upper	1474.54	1179.95	5715.74	1505.02	1260.62	1565.75
	lower	1535.65	1230.56	5731.02	1550.55	1185.81	1520.14
PC_VV_33	upper	1496.88	831.67	8079.67	1512.38	907.20	1466.25
	lower	1573.46	1047.65	7988.03	1618.99	1123.41	1542.70
PC_VV_34	upper	1550.55	1310.59	7023.06	1611.35	1308.12	1718.03
	lower	1474.62	1185.52	7403.10	1489.74	1198.99	1504.94
PC_VV_35	upper	1444.22	1164.57	6506.23	1474.62	1177.60	1413.81
	lower	1549.29	1373.44	5817.16	1625.16	1372.35	1488.46
PC_VV_36	upper	1564.48	1426.82	4389.45	1518.92	1498.81	1488.54
	lower	1610.04	1517.70	4359.07	1579.89	1469.83	1549.52
PC_VV_37	upper	1458.40	1316.58	4161.73	1518.92	1340.46	1458.17
	lower	1594.85	1553.16	3569.31	1625.44	1548.92	1549.22
PC_VV_38	upper	1526.23	1546.68	2840.27	1564.70	1538.16	1544.46
	lower	1487.18	1503.58	2992.12	1549.29	1514.66	1524.23
PC_VV_39	upper	1503.65	1532.85	1868.17	1488.54	1565.18	1488.54
	lower	1543.41	1542.98	1837.86	1473.28	1592.16	1613.00
PC_VV_40	upper	LD	LD	LD	LD	LD	LD
	lower	LD	LD	LD	LD	LD	LD
PC_VV_41	upper	1526.03	982.84	3799.82	1587.07	887.20	1541.37
	lower	1434.47	550.43	4257.63	1495.51	651.92	1419.21
PC_VV_42	upper	1478.34	786.63	3779.68	1554.55	812.91	1493.58
	lower	1554.55	1030.29	3551.07	1691.71	975.52	1554.62
PC_VV_43	upper	1432.45	1036.01	3214.67	1462.68	954.50	1432.13
	lower	1493.38	1295.01	3214.67	1600.01	1151.56	1462.92
PC_VV_44	upper	1508.30	1243.16	2757.61	1569.32	1233.97	1508.61
	lower	1447.36	1144.68	2742.41	1325.57	1162.79	1416.97
PC_VV_45	upper	1524.06	1388.32	2529.95	1645.99	1371.49	1569.86
	lower	1478.34	1365.70	2438.50	1447.86	1327.34	1478.42
PC_VV_46	upper	1515.41	1499.88	2151.99	1530.49	1462.91	1530.56
	lower	1439.65	1420.54	2197.24	1515.33	1323.21	1469.95
PC_VV_47	upper	1493.58	1375.80	1950.80	1600.27	1370.81	1508.82
	lower	1493.58	1386.98	1981.28	1478.42	1373.10	1478.42
PC_VV_48	upper	1404.03	1372.58	1755.00	1388.69	1342.39	1388.77
	lower	1510.85	1500.49	1510.77	1739.68	1480.57	1541.37
PC_VV_49	upper	C	C	C	C	C	C
	lower	C	C	C	C	C	C
PC_VV_50	upper	C	C	C	C	C	C
	lower	C	C	C	C	C	C
PC_VV_51	upper	1414.34	835.19	4410.73	1566.49	574.89	1475.17
	lower	1495.59	863.93	4258.31	1480.33	774.83	1541.37
PC_VV_52	upper	1523.54	972.20	4006.94	1554.01	914.63	1508.61
	lower	1477.91	1079.14	3763.14	1538.85	1144.68	1554.31
PC_VV_53	upper	1495.51	1300.71	3174.29	1403.95	1399.46	1495.51
	lower	1434.55	1092.47	3448.83	1480.25	1167.09	1480.57
PC_VV_54	upper	1556.55	1333.16	2731.64	1434.55	1373.85	1449.81
	lower	1449.73	1385.67	2914.76	1464.99	1486.61	1480.33
PC_VV_55	upper	1493.58	1342.04	2453.74	1554.55	1352.90	1463.18
	lower	1493.58	1450.75	1996.52	1524.14	1435.70	1493.66
PC_VV_56	upper	1403.95	1366.72	2075.46	1480.25	1463.24	1449.81
	lower	1556.55	1498.31	2044.94	1571.81	1560.51	1541.29
PC_VV_57	upper	C	C	C	C	C	C
	lower	C	C	C	C	C	C
PC_VV_58	upper	C	C	C	C	C	C
	lower	C	C	C	C	C	C
PC_VV_59	upper	1386.51	1078.71	4921.06	1569.32	774.01	1493.07
	lower	1462.68	857.80	4814.41	1569.25	1014.27	1508.30
PC_VV_60	upper	1585.03	1220.20	4282.65	1645.99	1242.00	1585.03

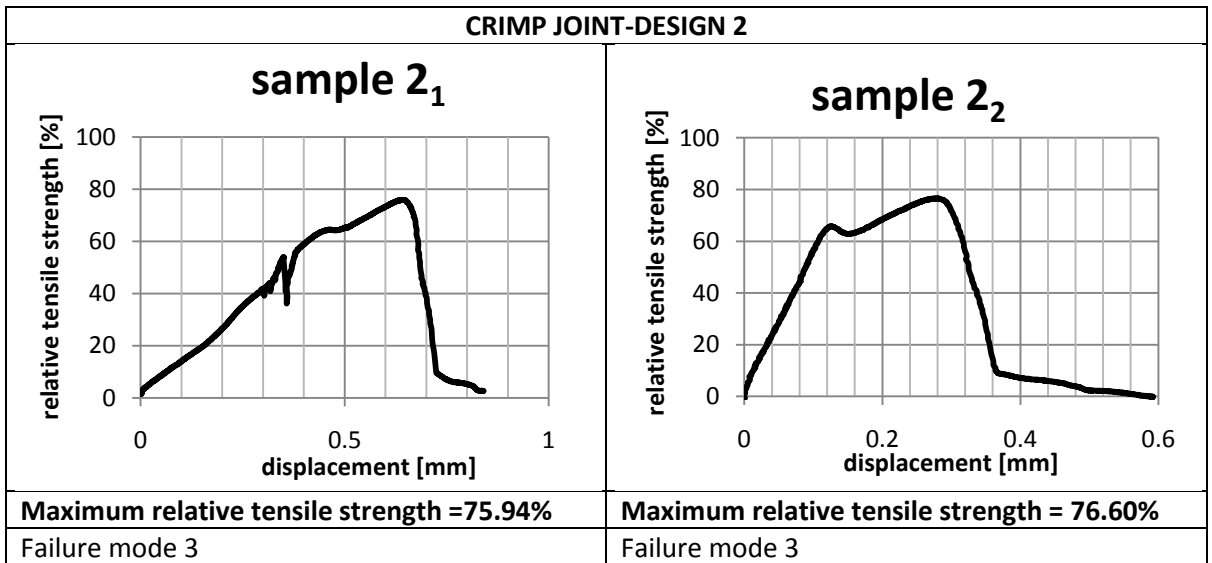
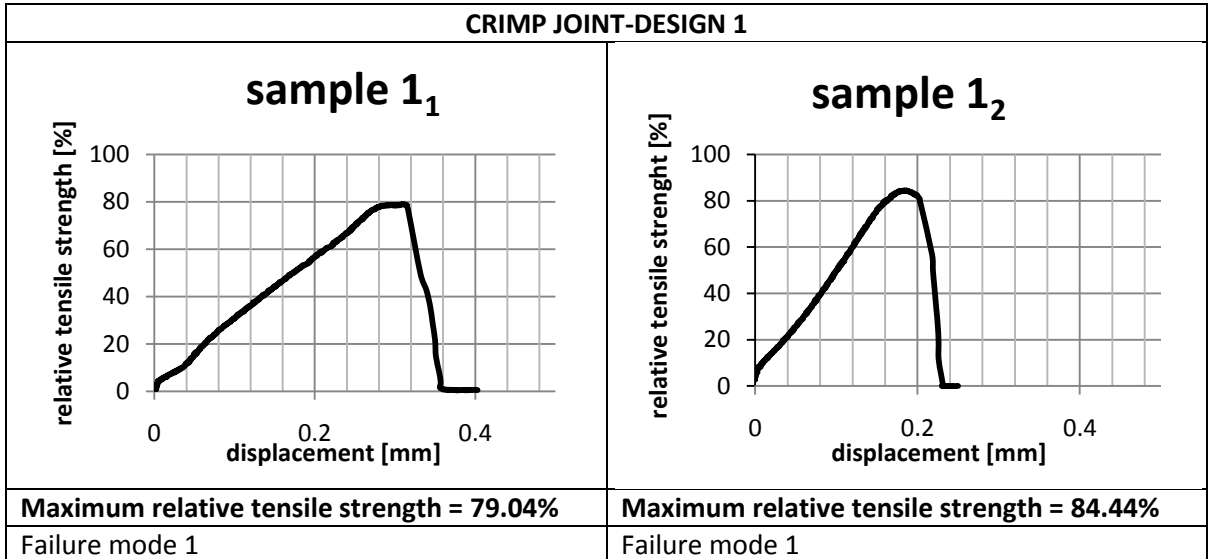
	lower	1463.18	1151.95	4389.31	1554.55	1097.54	1463.10
PC_VV_61	upper	1464.99	1332.55	3494.75	1480.96	1310.97	1480.25
	lower	1480.25	1201.70	3708.29	1510.85	1227.10	1449.81
PC_VV_62	upper	1447.86	1301.16	3032.89	1554.55	1287.54	1478.34
	lower	1524.06	1294.34	2880.48	1585.03	1386.98	1524.14
PC_VV_63	upper	1478.42	1383.88	2453.79	1508.82	1388.15	1493.66
	lower	1539.30	1463.50	2377.54	1630.75	1446.26	1539.30
PC_VV_64	upper	1447.86	1420.33	1783.22	1493.66	1410.40	1447.94
	lower	1432.62	1459.37	1874.60	1493.58	1491.56	1524.06
PC_VV_65	upper	C	C	C	C	C	C
	lower	C	C	C	C	C	C
PC_VV_66	upper	1671.44	1243.52	5682.65	1762.53	1108.35	1686.63
	lower	1519.50	1109.29	5743.51	1534.70	773.86	1595.47
PC_VV_67	upper	1572.11	1242.76	5219.03	1556.63	1092.47	1495.59
	lower	1465.07	1298.47	5005.39	1449.81	1196.26	1480.33
PC_VV_68	upper	1508.82	1234.59	4419.79	1493.66	1322.43	1478.34
	lower	1493.58	1356.42	4099.73	1600.27	1378.84	1493.66
PC_VV_69	upper	1462.92	1316.34	3412.87	1371.27	1373.30	1432.13
	lower	1523.84	1371.61	3214.71	1569.54	1374.91	1508.30
PC_VV_70	upper	1449.81	1496.45	2411.18	1495.82	1463.48	1480.25
	lower	1449.81	1476.39	2731.60	1556.55	1430.57	1419.21
PC_VV_71	upper	1368.35	1357.93	1919.41	1439.42	1377.55	1350.58
	lower	1332.82	1391.57	1901.65	1421.99	1430.51	1439.75
PC_VV_72	upper	LD	LD	LD	LD	LD	LD
	lower	LD	LD	LD	LD	LD	LD
PC_VV_73	upper	C	C	C	C	C	C
	lower	C	C	C	C	C	C
PC_VV_74	upper	1462.60	818.75	6932.13	1447.68	1032.98	1462.60
	lower	1508.30	1154.88	6368.40	1554.09	1082.68	1554.01
PC_VV_75	upper	1447.86	1194.71	6141.98	1478.34	1129.25	1539.30
	lower	1554.55	1315.47	5425.67	1585.10	1317.59	1585.10
PC_VV_76	upper	1463.10	1315.47	4892.25	1447.86	1322.34	1478.34
	lower	1585.03	1397.66	4374.09	1554.55	1327.34	1585.10
PC_VV_77	upper	1401.74	1404.39	3808.88	1477.83	1412.63	1432.21
	lower	1462.92	1352.44	3778.41	1493.15	1316.34	1447.36
PC_VV_78	upper	1508.38	1517.59	2498.65	1615.02	1512.84	1477.91
	lower	1432.13	1407.69	2894.73	1447.44	1396.76	1462.68
PC_VV_79	upper	LD	LD	LD	LD	LD	LD
	lower	LD	LD	LD	LD	LD	LD
PC_VV_80	upper	1485.72	1560.13	2091.38	1545.64	1528.09	1530.56
	lower	1409.59	1417.38	1985.15	1409.26	1466.04	1485.34
PC_VV_81	upper	1417.63	905.07	3991.70	1386.42	1110.93	1538.78
	lower	1538.85	929.86	3915.62	1599.72	895.78	1523.62
PC_VV_82	upper	1474.85	926.73	3571.80	1563.70	941.94	1492.73
	lower	1297.28	778.81	3678.24	1545.93	941.94	1386.12
PC_VV_83	upper	1449.73	1041.73	3265.71	1342.91	990.16	1403.95
	lower	1464.99	1236.46	3219.93	1556.55	1140.45	1556.55
PC_VV_84	upper	1480.25	1255.90	2868.94	1510.77	1307.86	1541.60
	lower	1373.43	1105.61	3067.36	1480.25	1126.06	1480.25
PC_VV_85	upper	1591.10	1370.94	2621.57	1560.79	1459.29	1439.65
	lower	1394.11	1346.26	2288.36	1621.41	1356.20	1439.57
PC_VV_86	upper	1432.13	1401.41	2254.89	1447.44	1375.07	1432.13
	lower	1584.77	1437.79	2483.37	1554.09	1430.02	1569.25
PC_VV_87	upper	1538.78	1482.85	1797.84	1508.61	1502.45	1554.09
	lower	1432.21	1422.70	2011.13	1401.74	1425.39	1432.21
PC_VV_88	upper	1469.87	1535.28	1848.77	1545.72	1429.56	1500.18
	lower	1439.57	1491.28	1469.95	1666.94	1479.30	1454.72
PC_VV_89	upper	C	C	C	C	C	C
	lower	C	C	C	C	C	C
PC_VV_90	upper	1477.79	968.89	4646.40	1508.18	917.34	1523.41

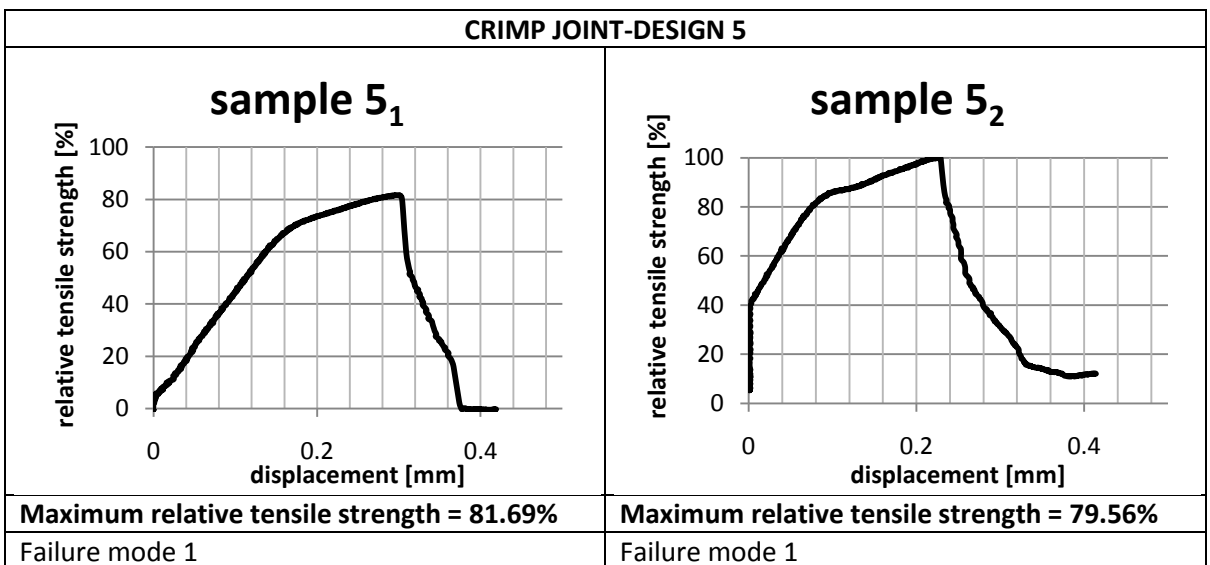
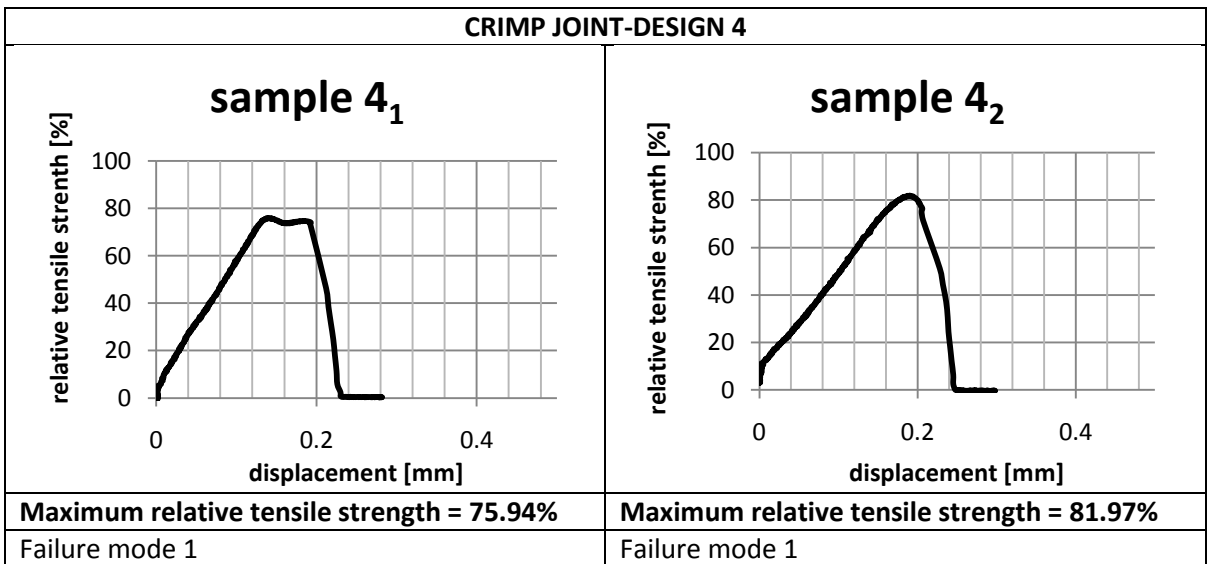
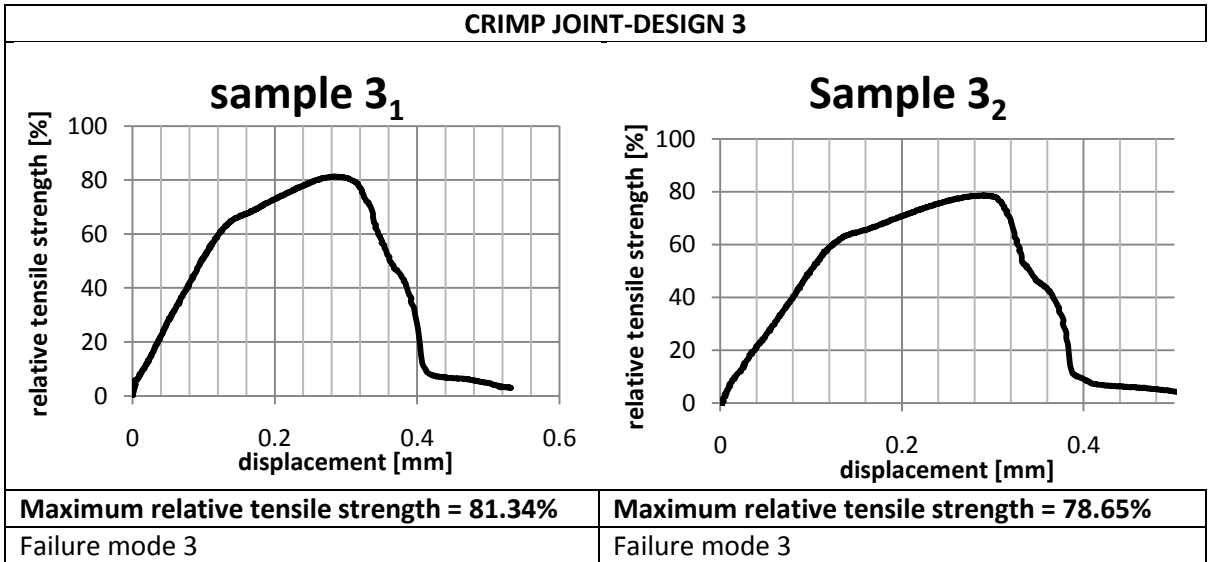
	lower	1505.59	888.33	4410.33	1475.17	961.96	1505.59
PC_VV_91	upper	1449.81	1039.16	4028.73	1312.39	1054.73	1464.99
	lower	1495.51	1147.27	3891.38	1541.29	1058.37	1434.47
PC_VV_92	upper	1495.51	1264.40	3479.39	1480.25	1255.90	1464.99
	lower	1373.51	1148.18	3586.18	1434.47	1201.31	1434.55
PC_VV_93	upper	1493.15	1341.58	3001.41	1569.32	1329.76	1477.91
	lower	1401.66	1304.39	3108.06	1477.91	1296.08	1401.66
PC_VV_94	upper	1539.30	1487.82	2164.17	1646.06	1491.56	1508.90
	lower	1493.58	1383.88	2651.87	1539.30	1390.24	1463.18
PC_VV_95	upper	1470.58	1452.98	1909.86	1545.64	1470.11	1439.65
	lower	1348.99	1361.10	2212.44	1379.70	1370.27	1379.04
PC_VV_96	upper	1434.47	1438.44	1724.42	1419.21	1435.77	1526.11
	lower	1449.73	1438.44	1953.38	1495.59	1508.61	1449.73
PC_VV_97	upper	C	C	C	C	C	C
	lower	C	C	C	C	C	C
PC_VV_98	upper	1421.54	1041.29	4922.13	1528.16	969.53	1421.65
	lower	1457.19	1163.18	4851.31	1545.93	1089.16	1386.12
PC_VV_99	upper	1432.21	1288.63	4342.12	1462.60	1262.33	1508.30
	lower	1554.09	1152.47	4372.56	1660.73	1214.44	1538.78
PC_VV_100	upper	1493.15	1282.13	3641.26	1645.49	1281.59	1493.15
	lower	1432.21	1404.63	2955.71	1493.38	1480.03	1386.51
PC_VV_101	upper	1484.16	1426.68	2564.91	1536.28	1467.26	1489.62
	lower	1438.49	1431.70	2456.50	1489.03	1453.24	1457.22
PC_VV_102	upper	1510.81	1460.65	1972.47	1457.08	1482.54	1403.89
	lower	1403.77	1364.54	2487.76	1457.19	1524.54	1368.24
PC_VV_103	upper	1386.46	1375.60	1777.28	1386.00	1408.15	1368.35
	lower	1421.54	1373.88	2008.01	1492.73	1393.28	1439.42
PC_VV_104	upper	LD	LD	LD	LD	LD	LD
	lower	LD	LD	LD	LD	LD	LD
PC_VV_105	upper	C	C	C	C	C	C
	lower	C	C	C	C	C	C
PC_VV_106	upper	C	C	C	C	C	C
	lower	C	C	C	C	C	C
PC_VV_107	upper	1474.96	1280.62	5401.86	1528.26	1064.53	1421.65
	lower	1421.99	1164.13	5686.62	1545.93	906.06	1421.54
PC_VV_108	upper	1538.85	1310.60	5088.65	1584.48	1230.68	1645.42
	lower	1508.38	1306.52	4829.72	1584.56	1379.12	1569.54
PC_VV_109	upper	1500.18	1323.12	4121.74	1606.25	1378.95	1485.72
	lower	1409.26	1281.69	4440.58	1651.99	1300.10	1394.19
PC_VV_110	upper	1439.57	1451.96	3379.23	1515.33	1435.09	1424.41
	lower	1439.65	1346.94	3651.99	1530.79	1380.37	1545.64
PC_VV_111	upper	1454.80	1499.49	2621.53	1506.98	1510.63	1439.57
	lower	1454.72	1468.08	2572.09	1515.41	1530.49	1500.18
PC_VV_112	upper	1530.49	1594.49	1985.32	1591.17	1455.12	1469.95
	lower	1454.72	1390.89	2060.85	1500.26	1457.40	1424.41
PC_VV_113	upper	C	C	C	C	C	C
	lower	C	C	C	C	C	C
PC_VV_114	upper	1579.24	1236.46	5932.46	1585.23	1321.23	1601.20
	lower	1621.30	1354.26	6213.12	1632.51	1482.65	1546.75
PC_VV_115	upper	1545.72	1573.40	5667.43	1636.63	1365.90	1500.26
	lower	1378.95	1220.29	5985.59	1545.64	1189.42	1439.65
PC_VV_116	upper	1514.36	1302.57	5106.77	1560.79	1377.70	1485.11
	lower	1560.87	1418.92	4788.46	1591.10	1401.34	1606.33
PC_VV_117	upper	1368.70	1303.83	3713.78	1439.42	1339.67	1404.22
	lower	1439.10	1271.72	3767.09	1581.47	1410.51	1421.54
PC_VV_118	upper	1368.35	1349.65	2665.39	1439.31	1362.11	1386.00
	lower	1492.73	1408.15	2665.45	1546.34	1557.73	1528.26
PC_VV_119	upper	1500.26	1479.30	1924.53	1500.18	1504.69	1469.87
	lower	1470.19	1458.58	1865.46	1485.03	1449.19	1439.57
PC_VV_E1	upper	C	C	C	C	C	C

	lower	C	C	C	C	C	C
PC_VV_E2	upper	1520.22	1065.51	4986.07	1596.15	992.64	1565.75
	lower	1474.85	866.61	5138.11	1550.55	1064.64	1520.22
PC_VV_E3	upper	1520.14	1121.61	4256.43	1520.22	1193.19	1489.82
	lower	1505.02	1218.11	3815.56	1611.35	1264.55	1550.62
PC_VV_E4	upper	1474.54	1346.34	3055.49	1504.94	1335.39	1459.34
	lower	1550.62	1387.50	2569.04	1565.75	1379.81	1581.02
PC_VV_E5	upper	1452.92	1411.26	1839.37	1565.75	1375.98	1576.28
	lower	1448.91	1377.65	1884.98	1411.99	1406.95	1535.20
PC_VV_E6	upper	1504.94	1467.94	3633.17	1520.14	1485.78	1550.55
	lower	1550.55	1487.64	3648.34	1565.75	1497.24	1459.42
PC_VV_E7	upper	1536.23	1458.65	1702.63	1556.49	1500.62	1503.22
	lower	1576.20	1498.36	1620.84	1597.34	1458.14	1497.13
PC_VV_E8	upper	LD	LD	LD	LD	LD	LD
	lower	LD	LD	LD	LD	LD	LD
PC_VV_E9	upper	1434.55	1078.64	3143.78	1541.29	1156.27	1449.73
	lower	1449.73	1242.38	2899.46	1434.47	1218.53	1388.69
PC_VV_E10	upper	1463.18	1263.04	2865.24	1691.71	1243.77	1524.14
	lower	1539.30	1403.88	2590.95	1539.38	1393.25	1539.30
PC_VV_E11	upper	1462.68	1326.97	2483.42	1508.38	1316.34	1447.44
	lower	1416.89	1385.75	2285.36	1447.36	1421.47	1447.36
PC_VV_E12	upper	1434.47	1418.64	2182.28	1526.03	1406.68	1480.25
	lower	1511.08	1412.71	2075.46	1556.55	1467.69	1434.47
PC_VV_E13	upper	1617.01	1642.58	1848.01	1652.64	1638.83	1617.10
	lower	1528.16	1481.69	1830.32	1457.19	1443.15	1439.42

APPENDIX D

Relative tensile strength versus displacement curves for DoE





CRIMP JOINT-DESIGN 6	
<p>sample 6₁</p>	<p>sample 6₂</p>
<p>Maximum relative tensile strength = 70.30%</p> <p>Failure mode 1</p>	<p>Maximum relative tensile strength = 52.36%</p> <p>Failure mode 1</p>

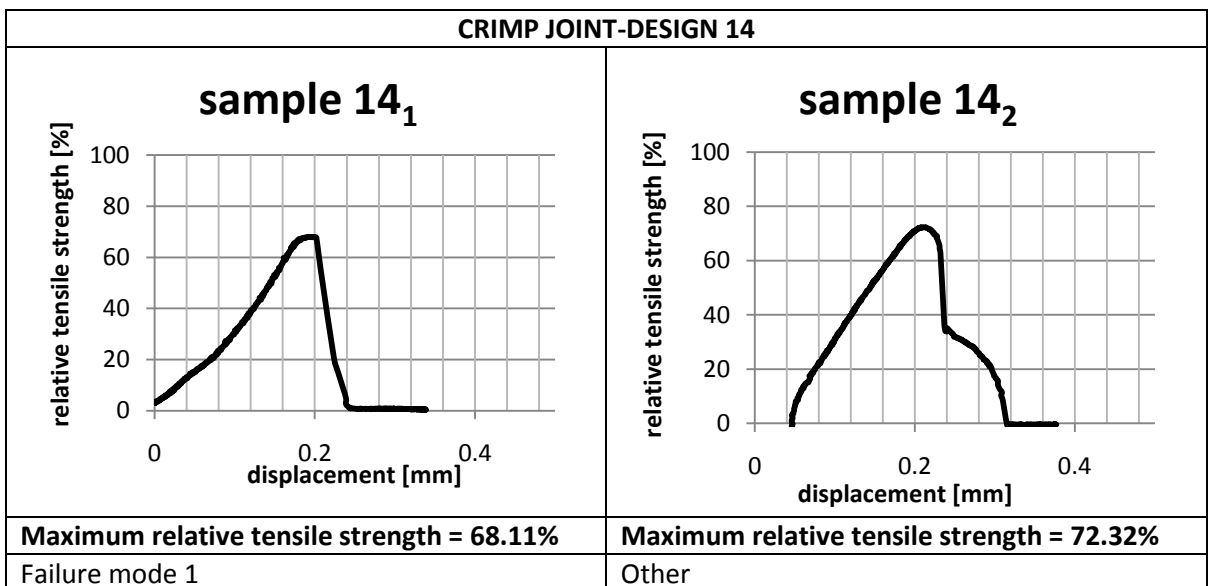
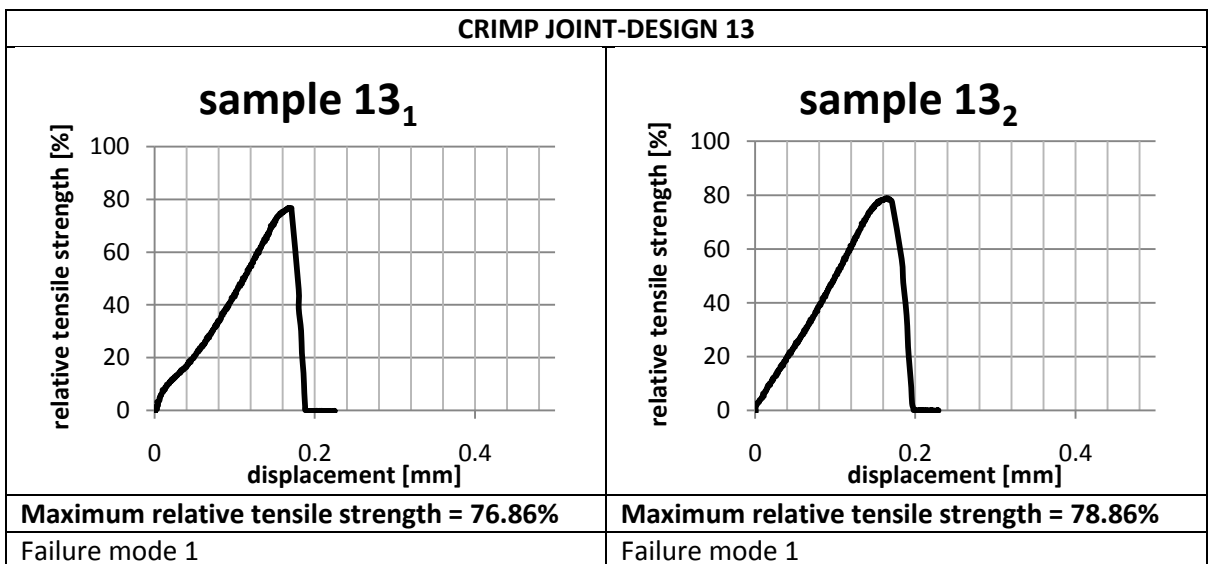
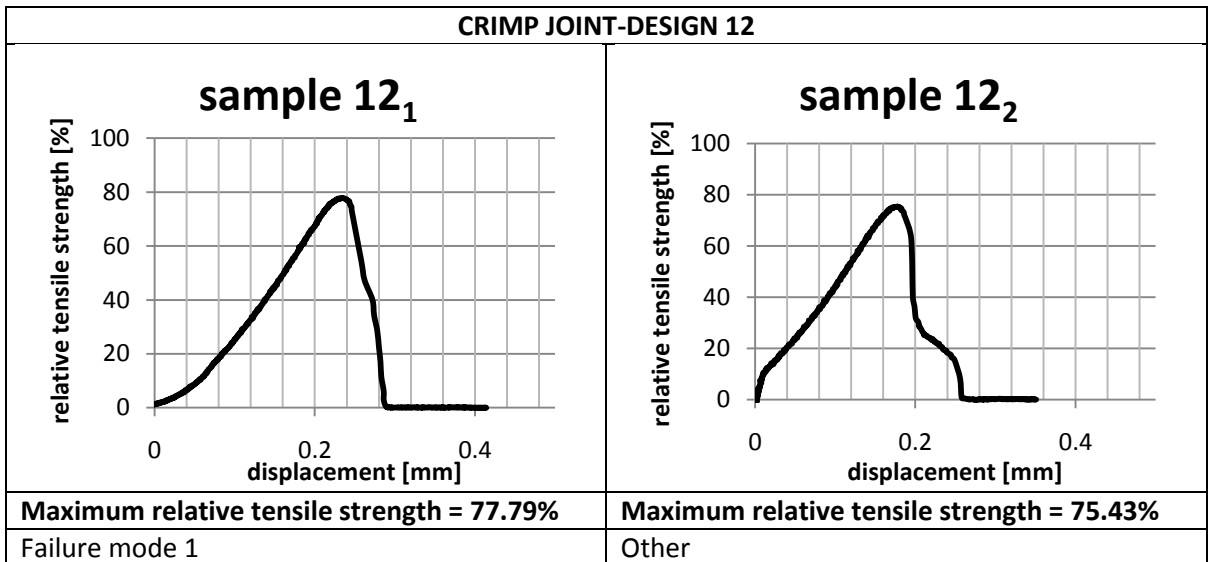
CRIMP JOINT-DESIGN 7	
<p>sample 7₁</p>	<p>sample 7₂</p>
<p>Maximum relative tensile strength = 71.10%</p> <p>Failure mode 1</p>	<p>Maximum relative tensile strength = 72.73%</p> <p>Failure mode 1</p>

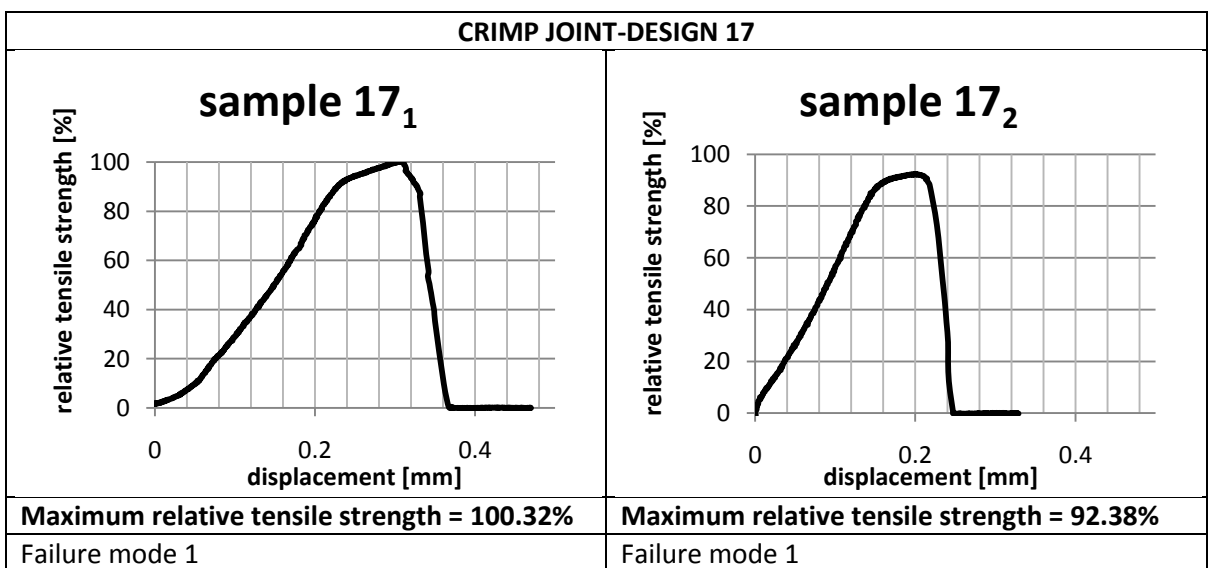
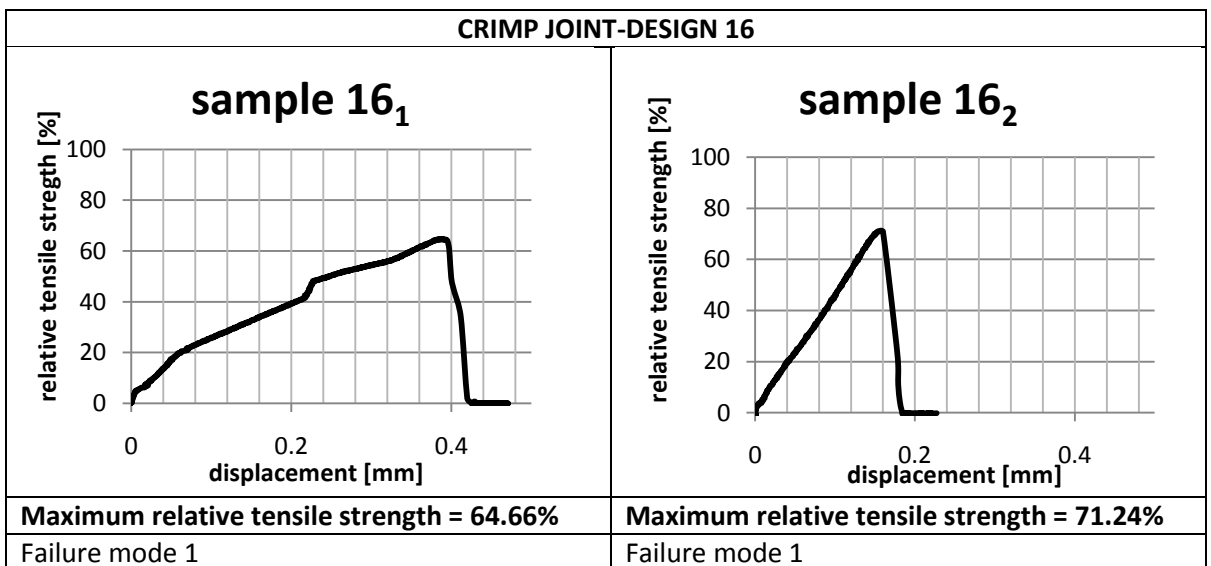
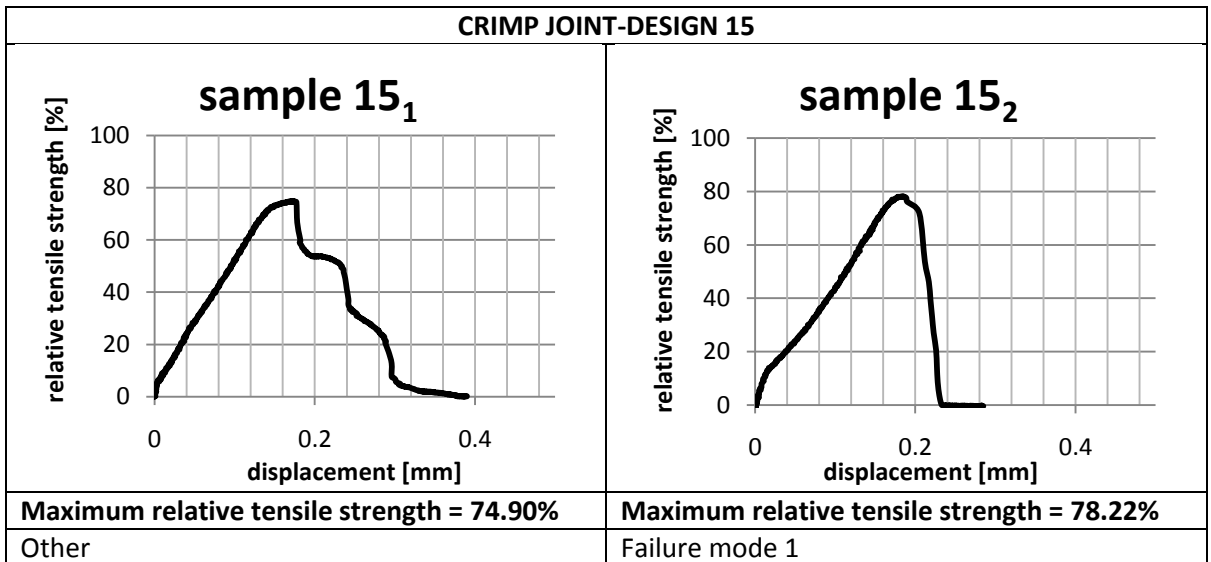
CRIMP JOINT-DESIGN 8	
<p>Not available</p>	<p>sample 8₂</p>
	<p>Maximum relative tensile strength = 72.32%</p> <p>Failure mode 1</p>

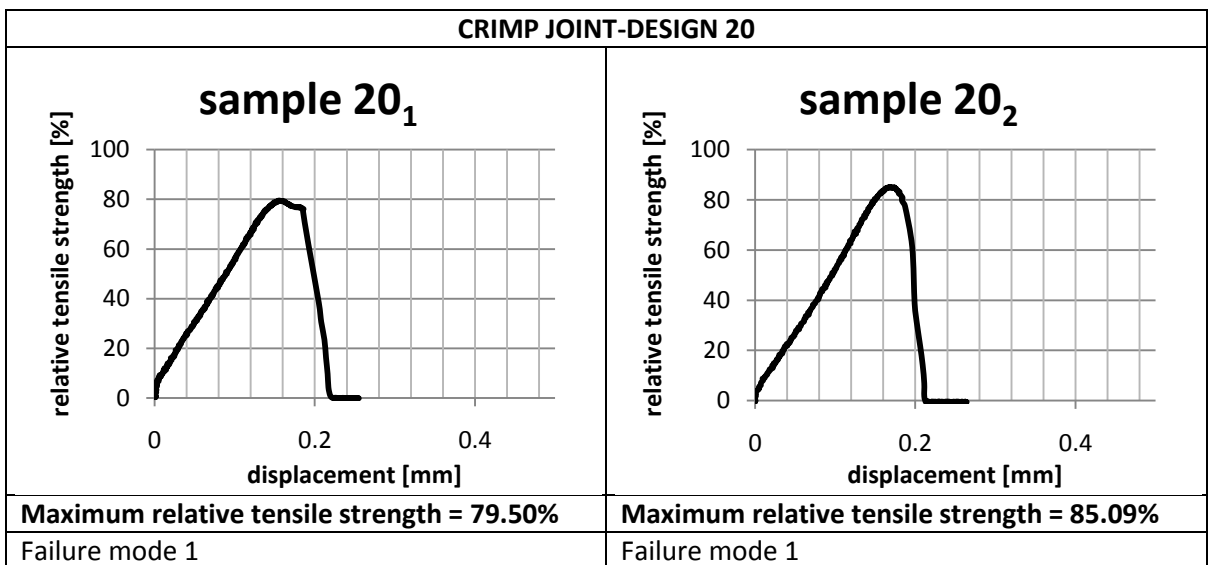
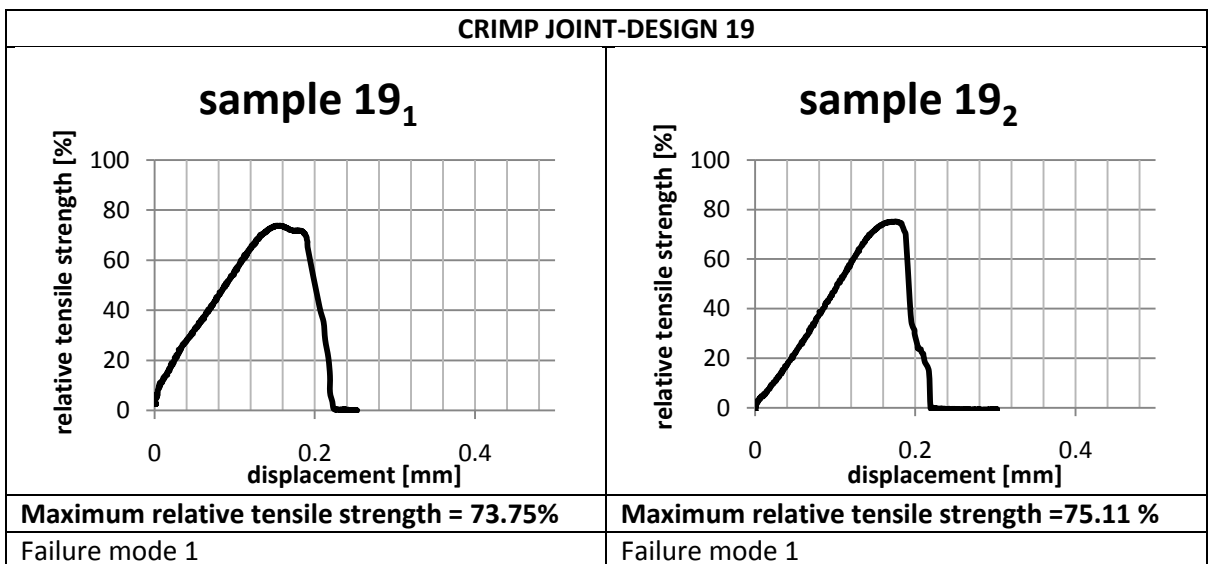
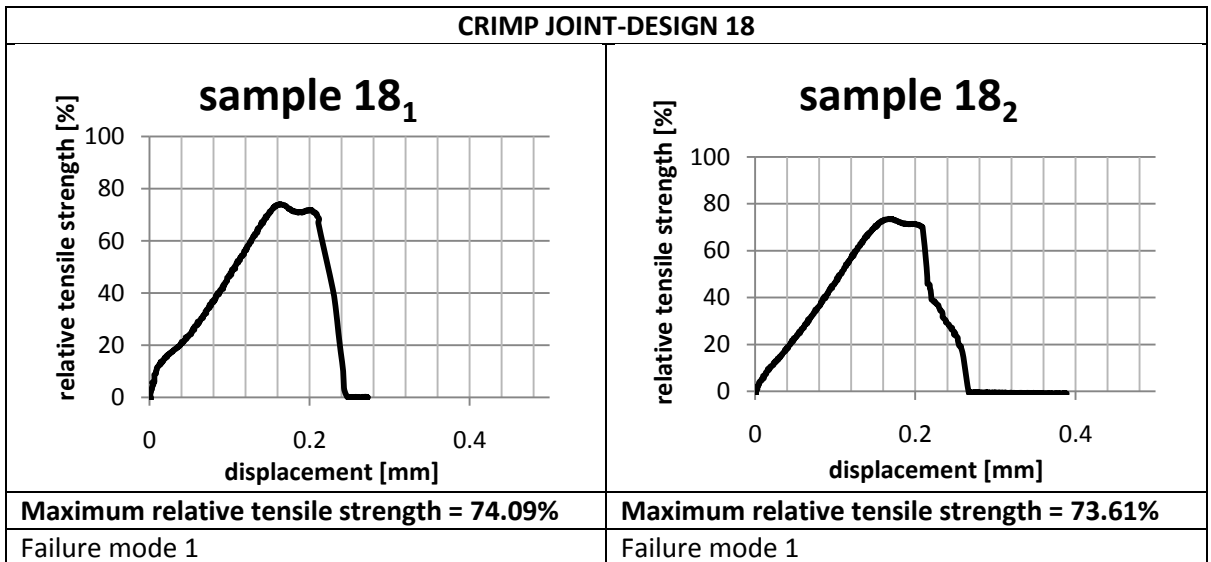
CRIMP JOINT-DESIGN 9	
<p>sample 9₁</p>	<p>sample 9₂</p>
Maximum relative tensile strength = 74.67%	Maximum relative tensile strength = 76.93%
Other	Failure mode 1

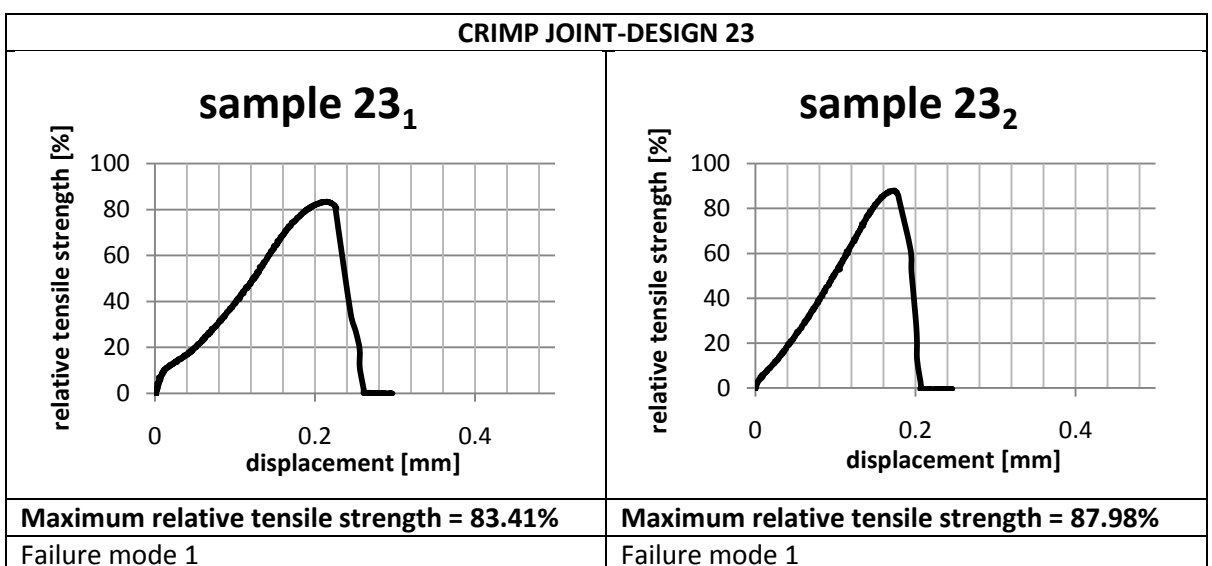
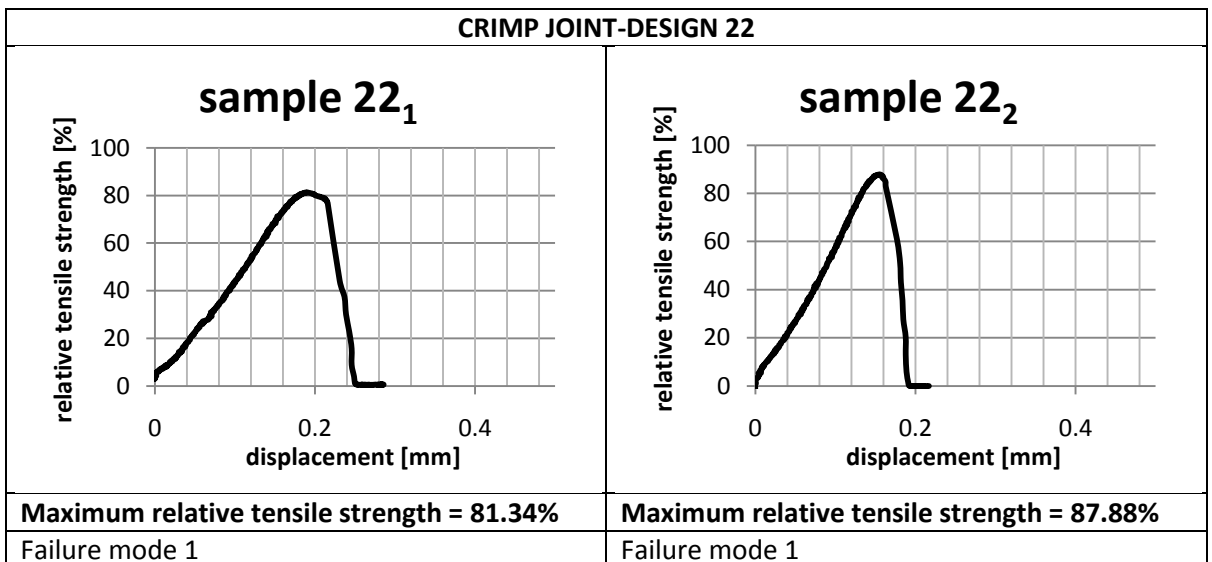
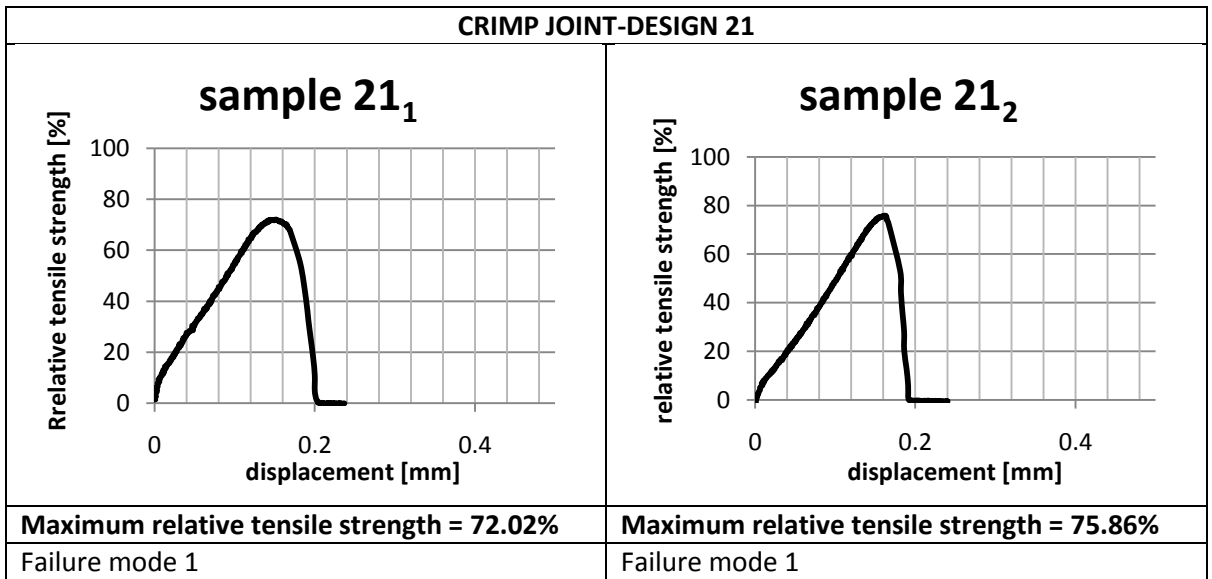
CRIMP JOINT-DESIGN 10	
<p>sample 10₁</p>	<p>sample 10₂</p>
Maximum relative tensile strength = 75.94%	Maximum relative tensile strength = 85.09%
Failure mode 1	Failure mode 1

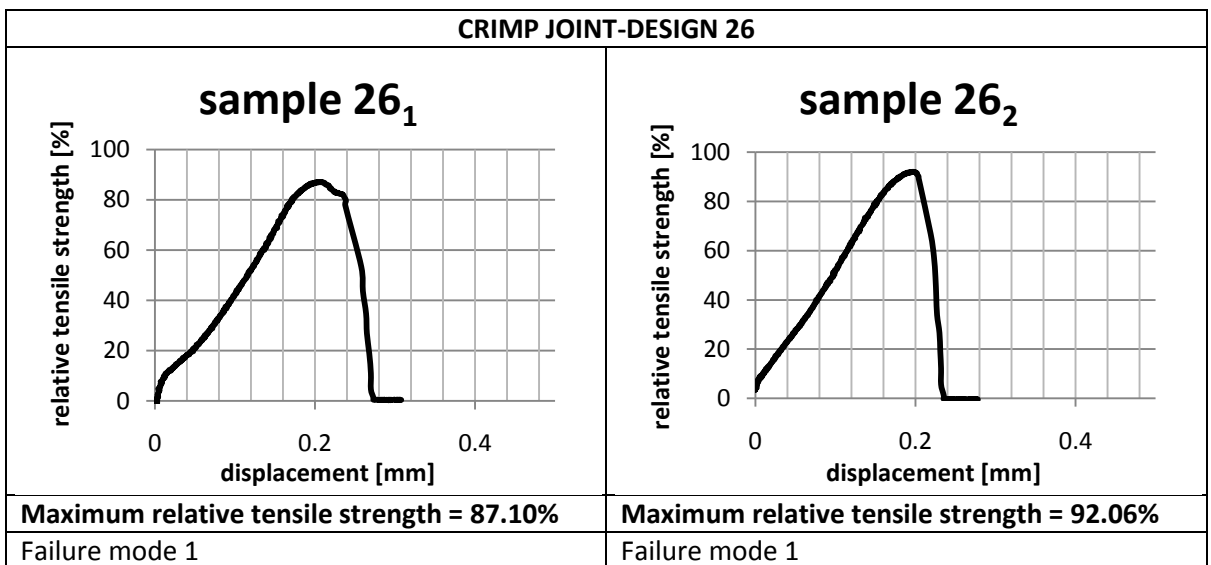
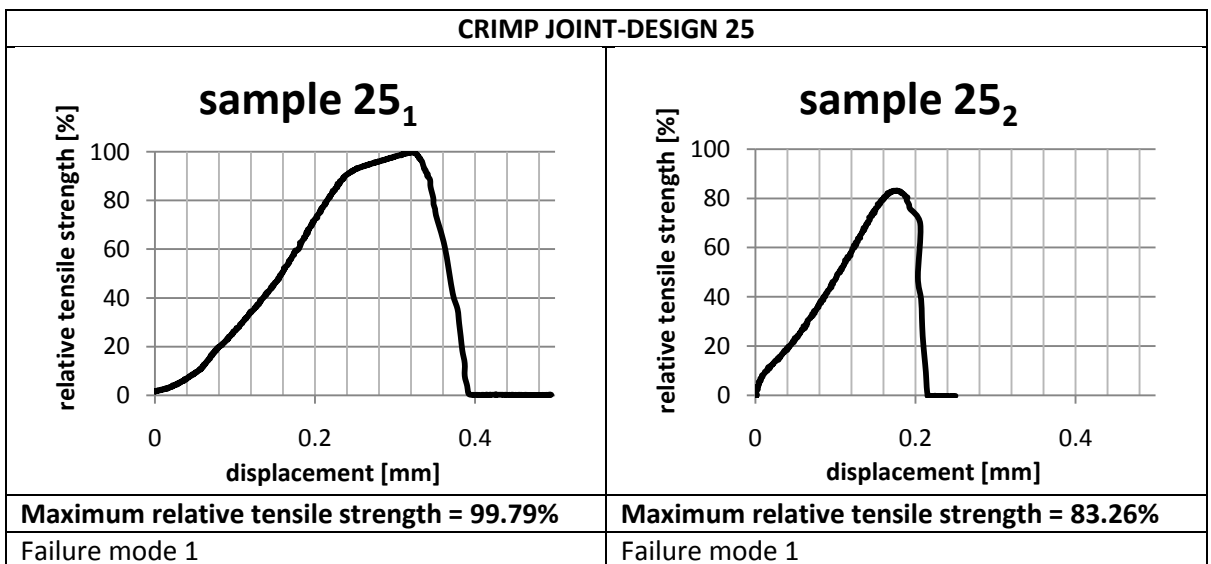
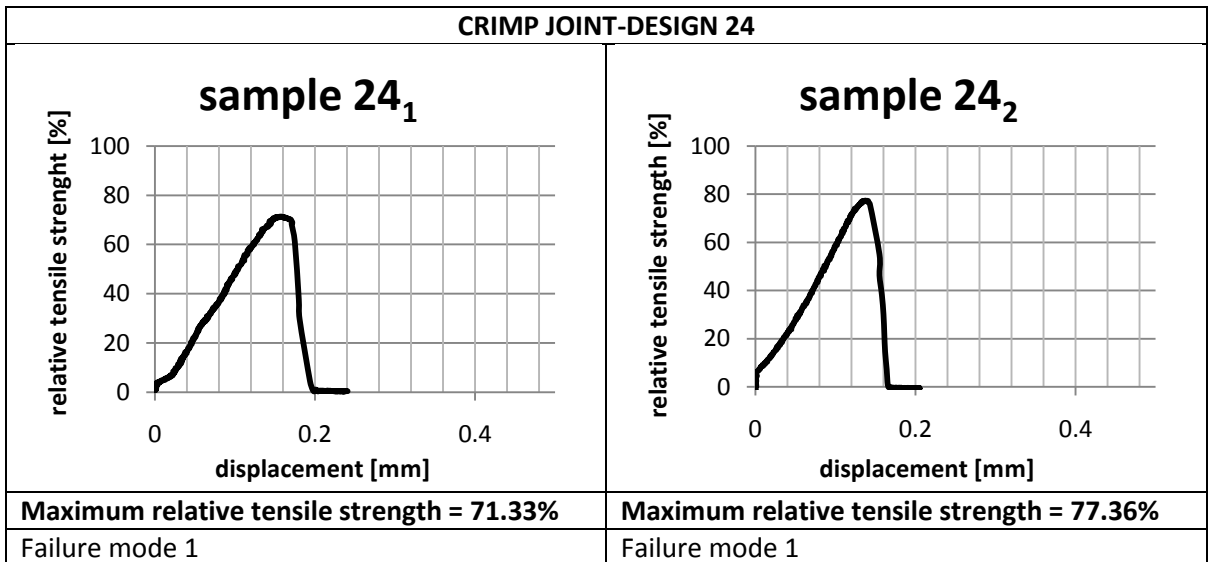
CRIMP JOINT-DESIGN 11	
<p>sample 11₁</p>	<p>sample 11₂</p>
Maximum relative tensile strength = 89.06%	Maximum relative tensile strength = 87.45%
Failure mode 1	Failure mode 1

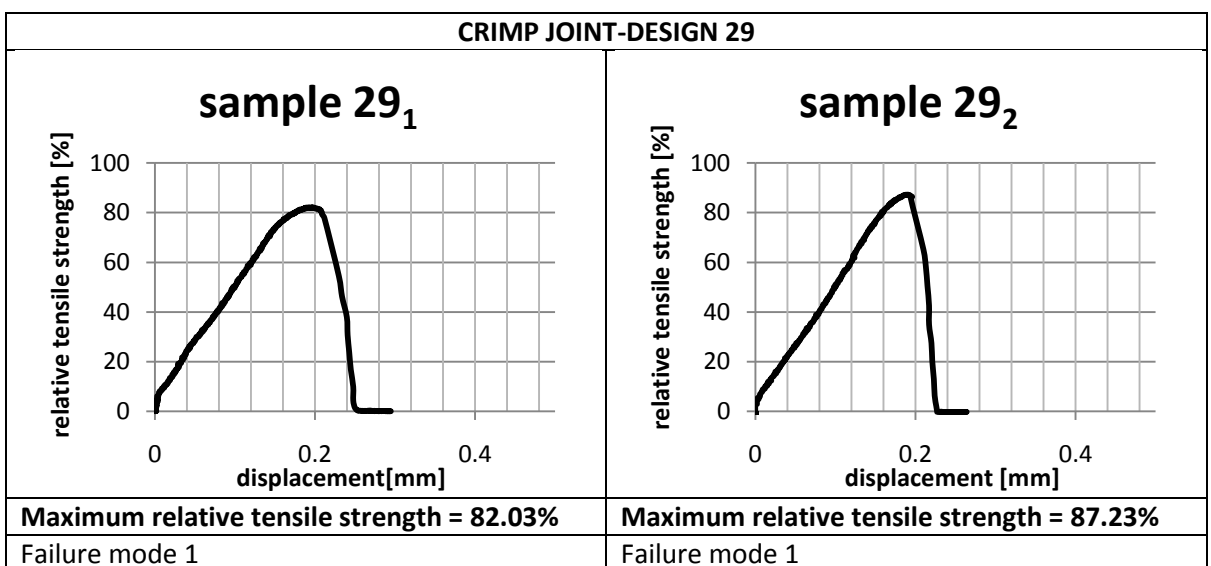
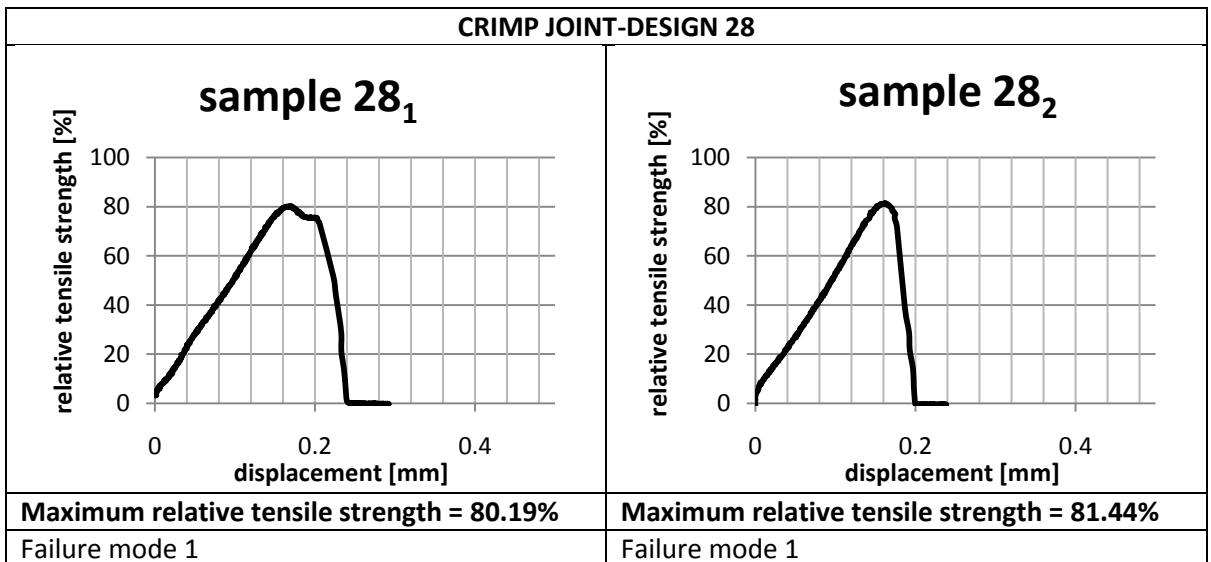
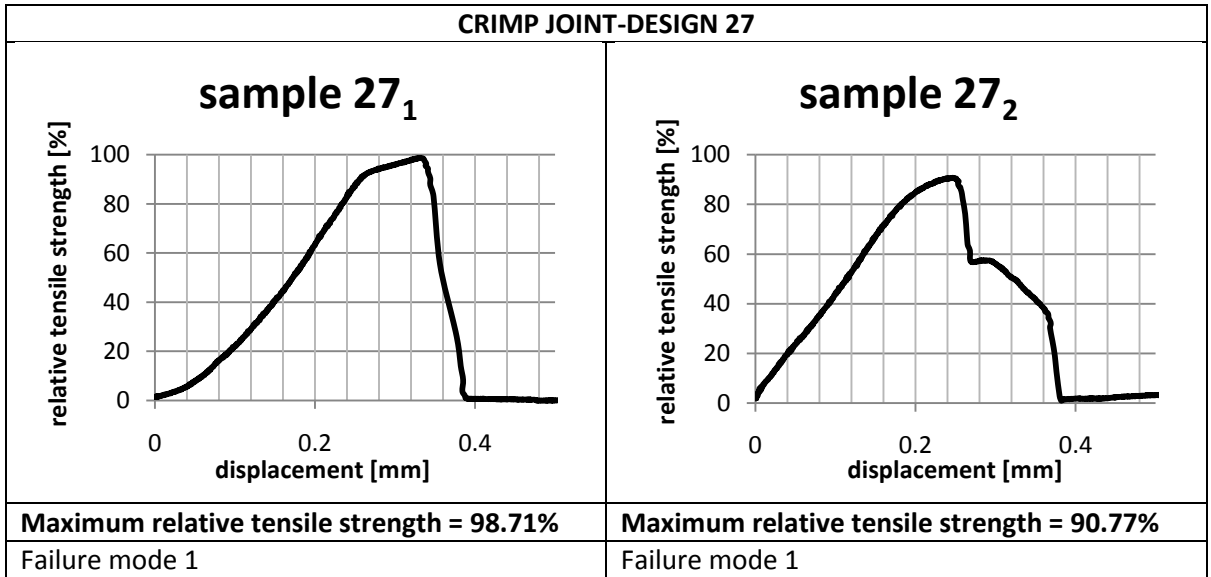


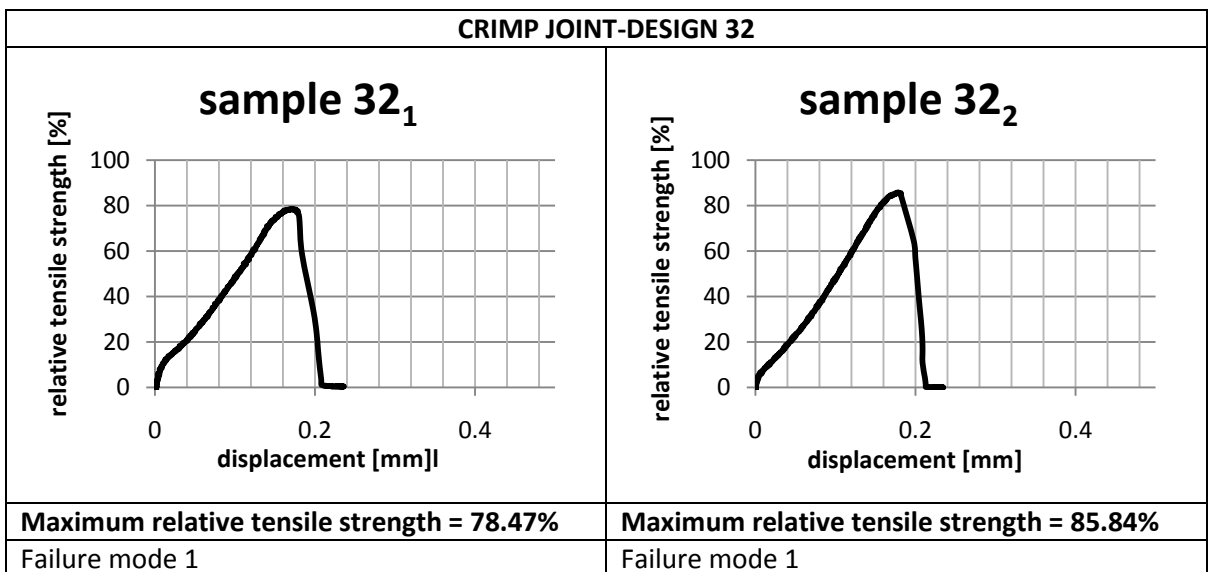
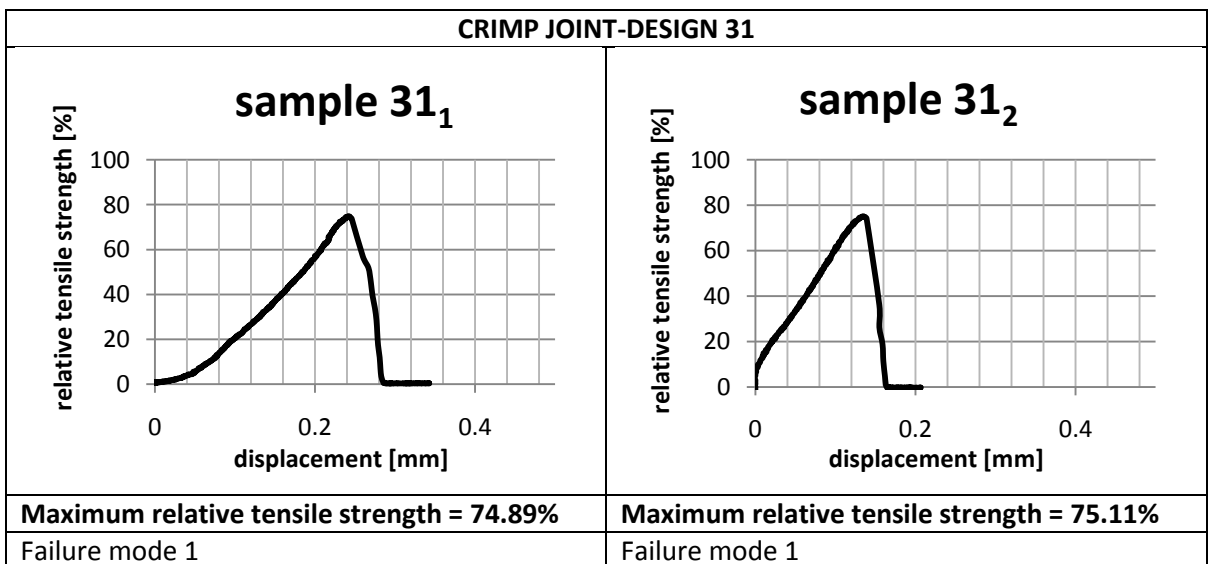
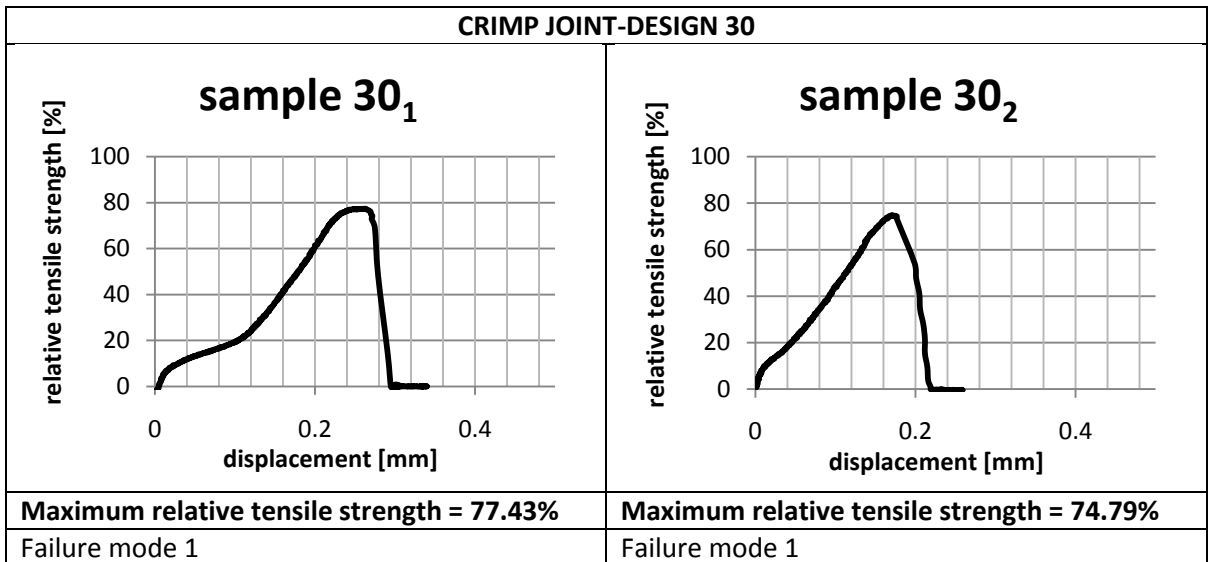


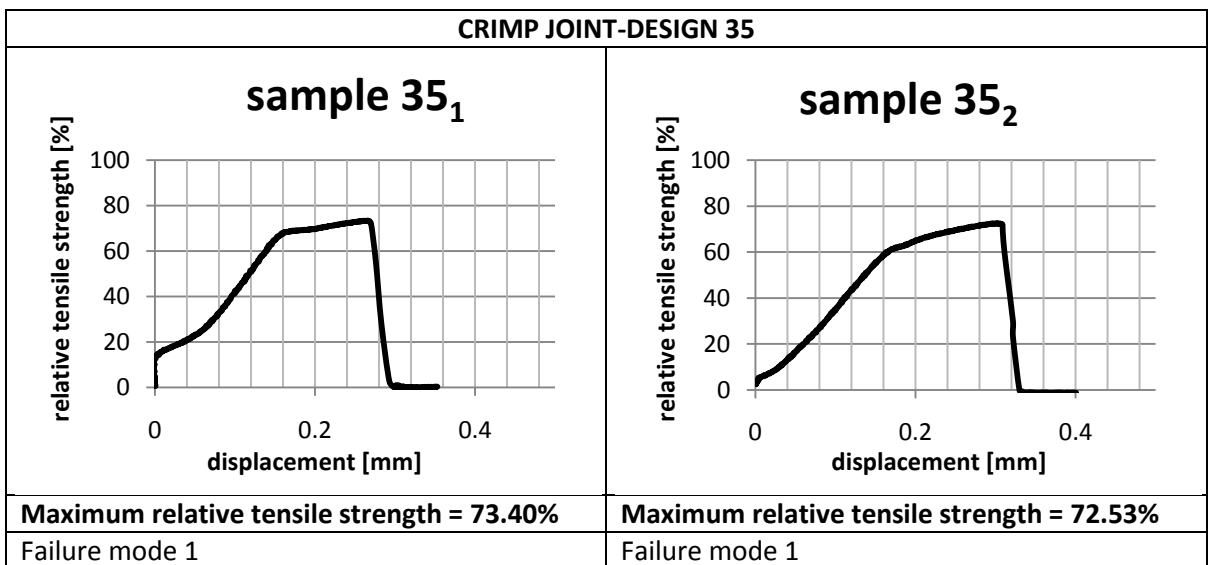
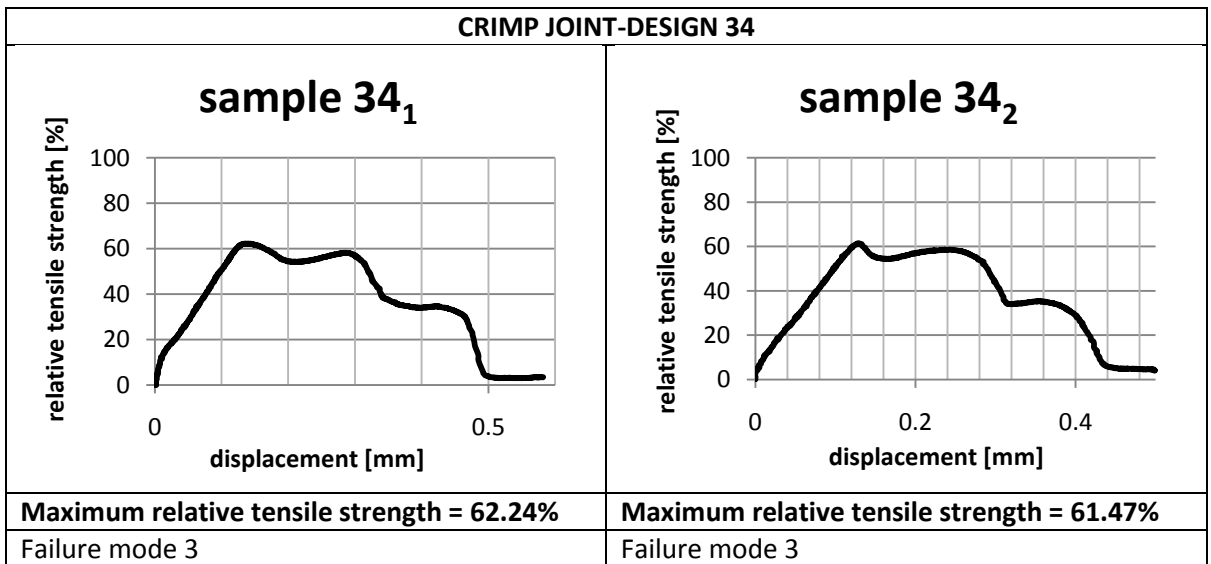
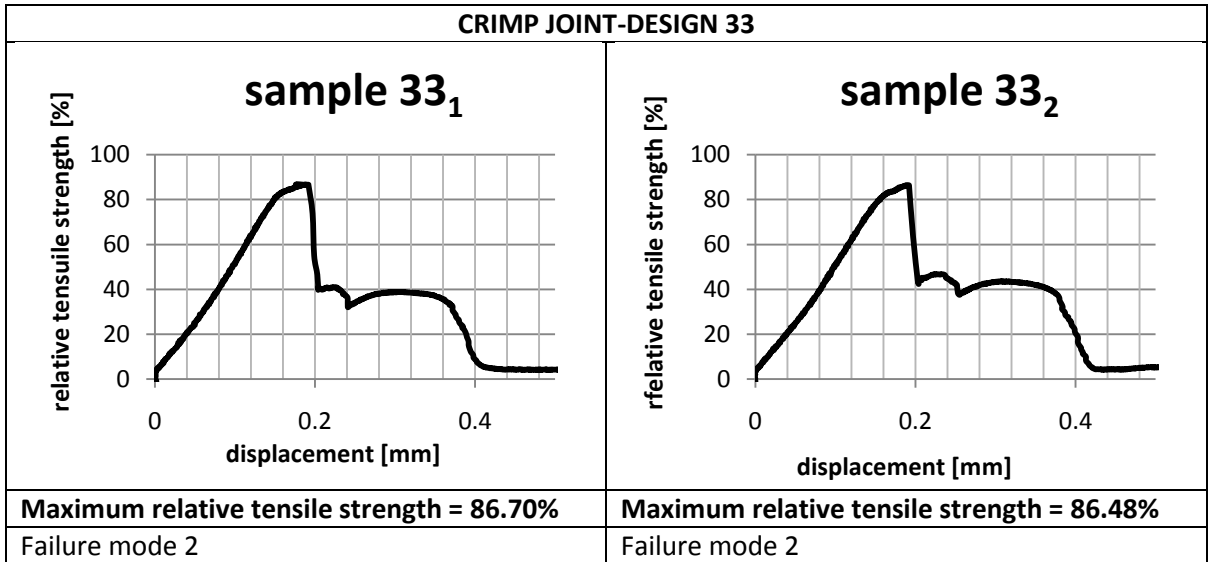








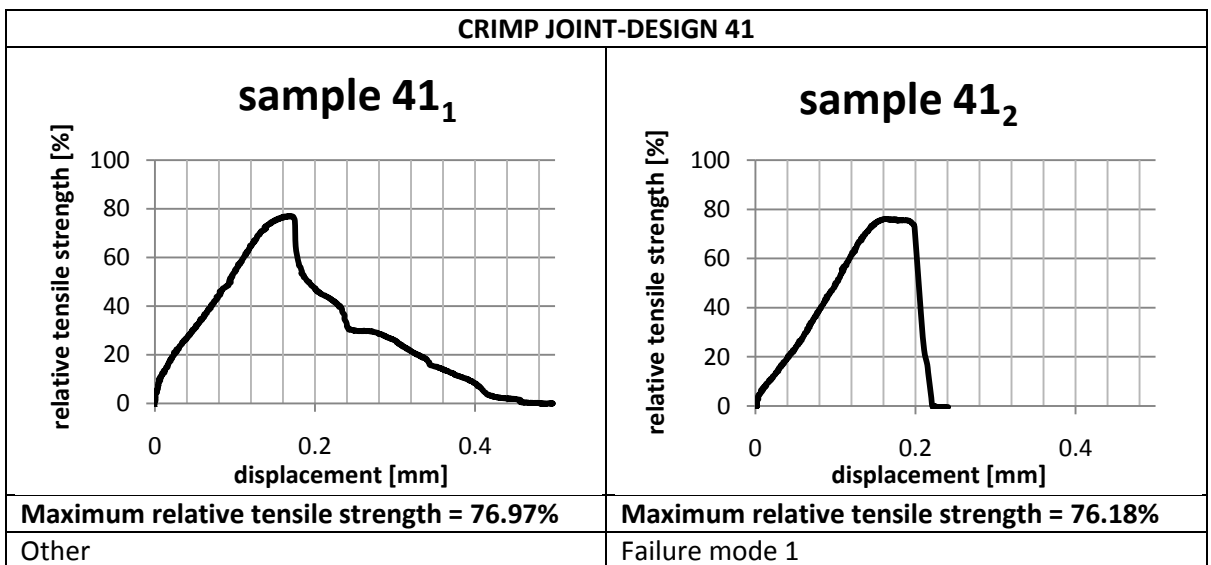
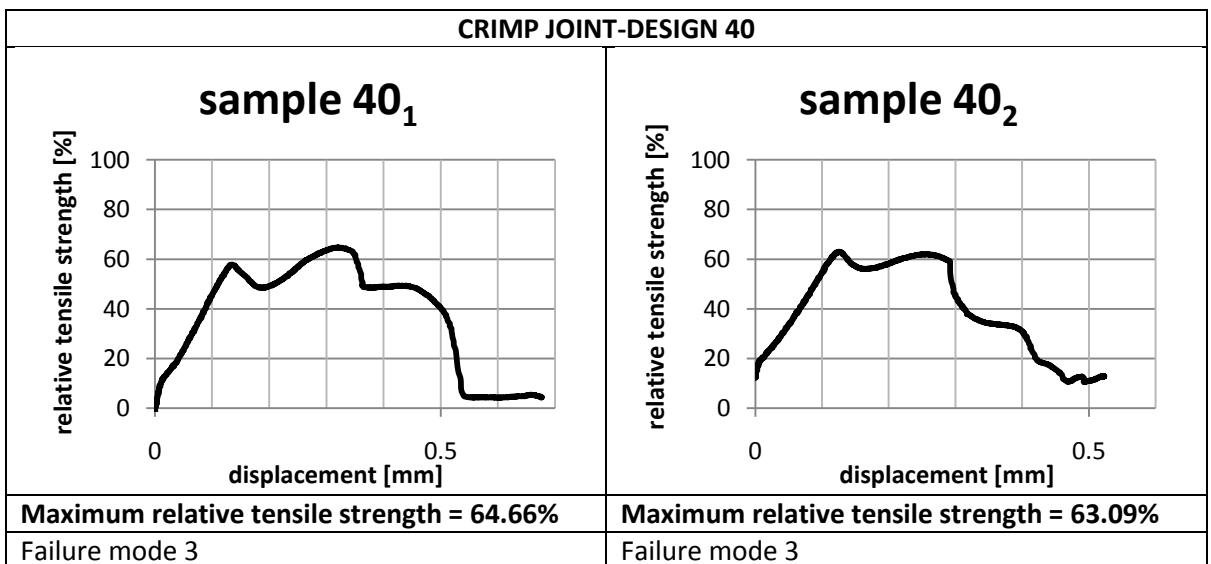
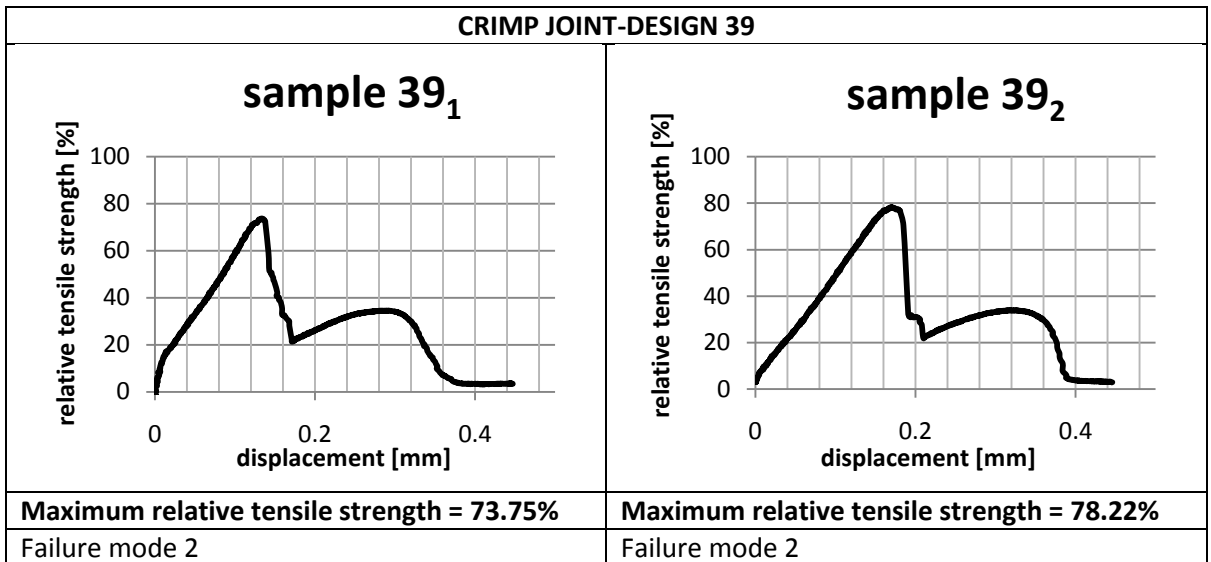


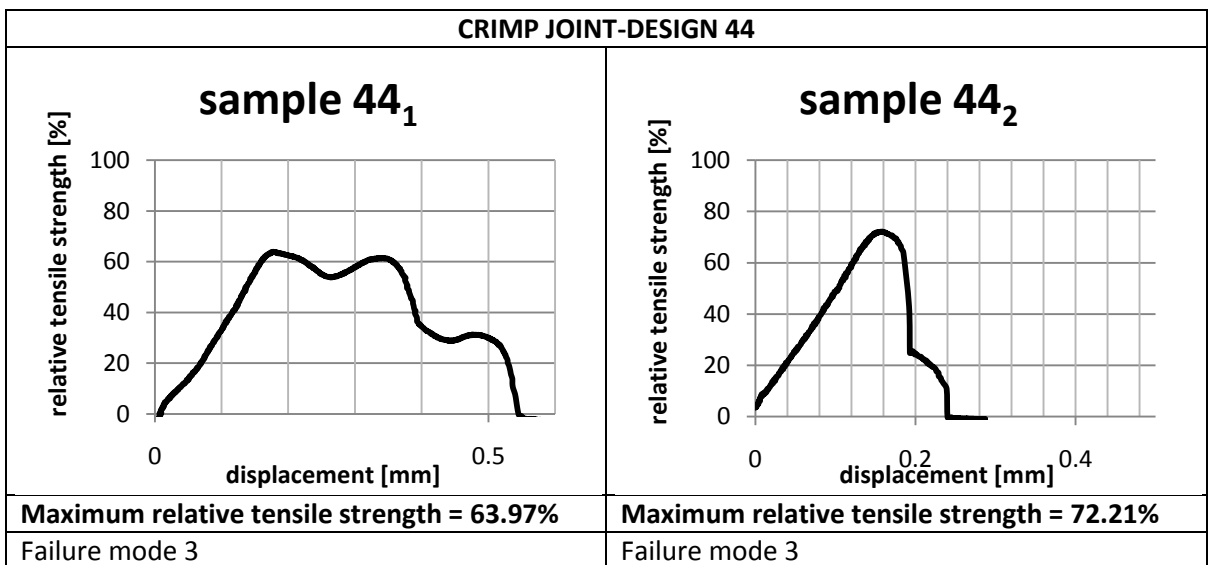
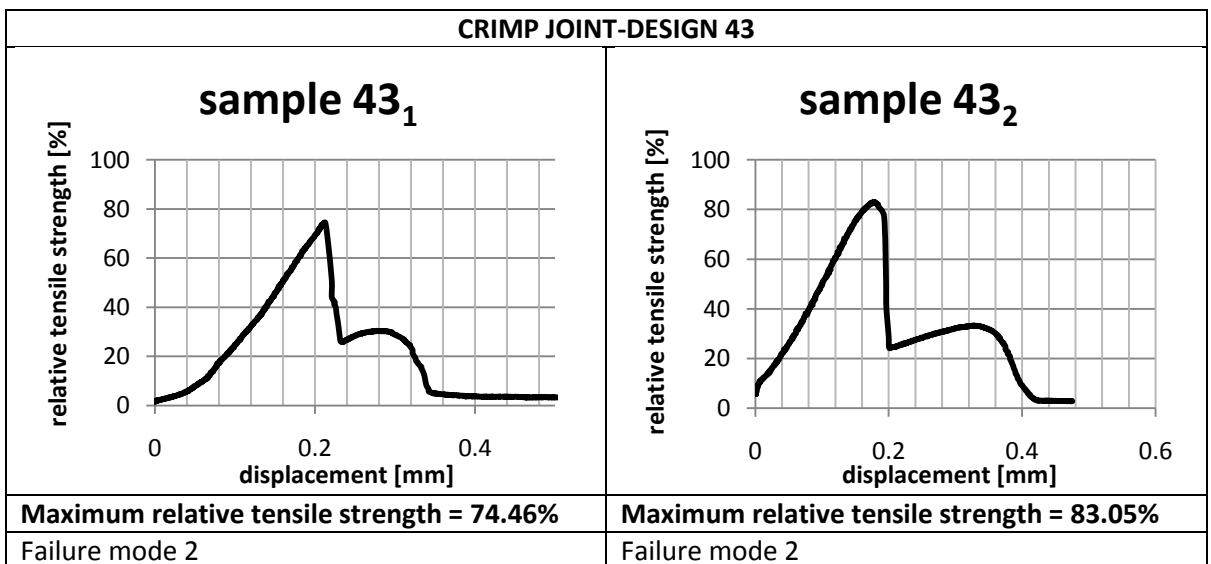
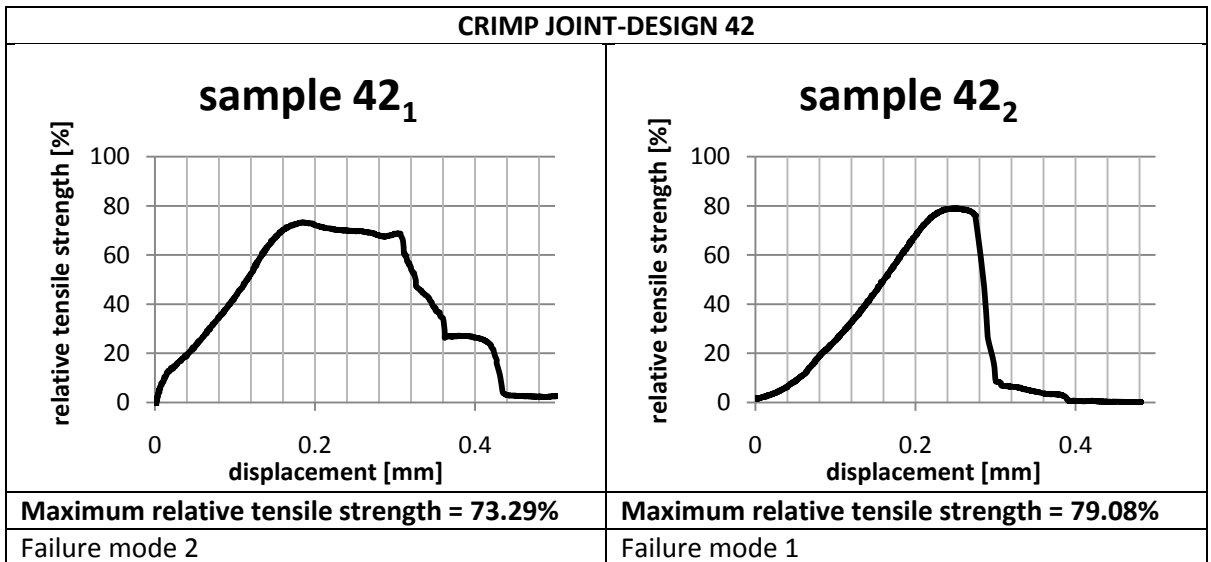


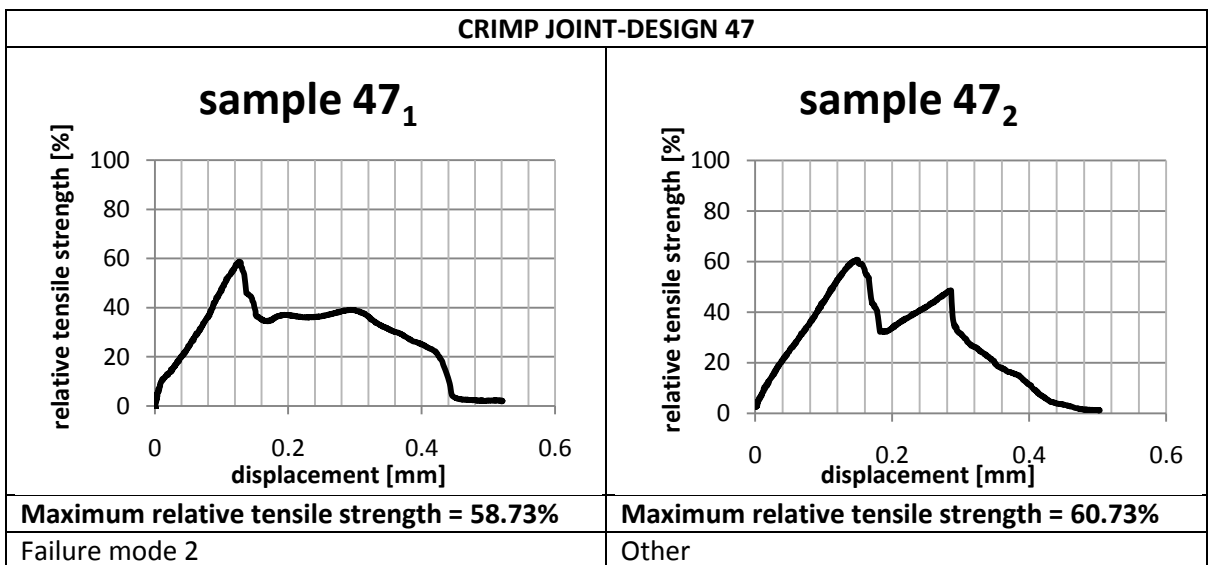
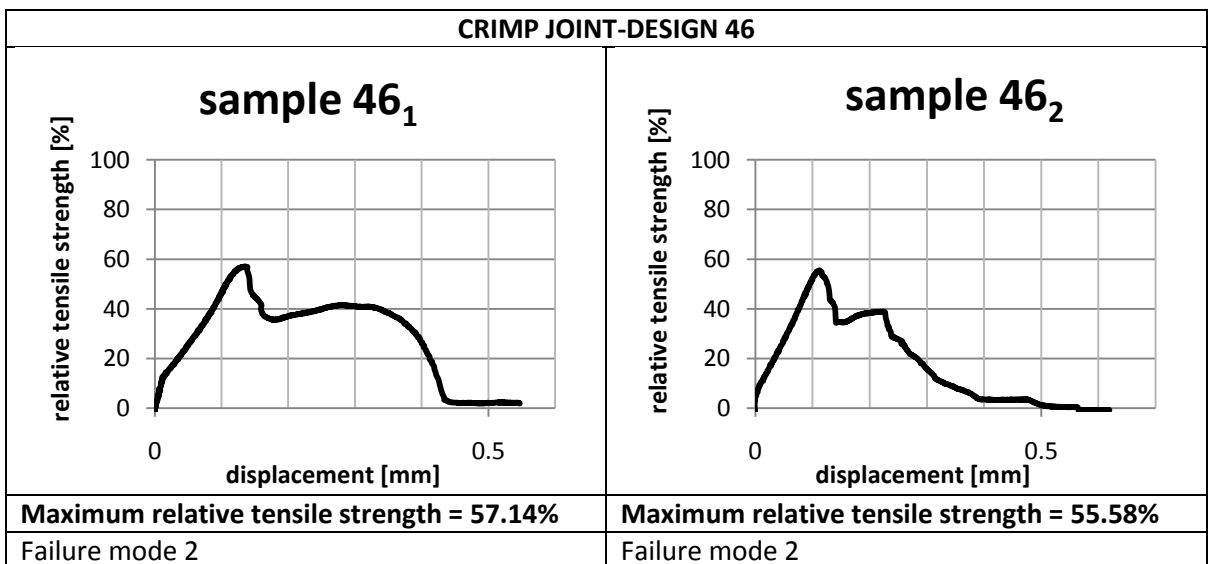
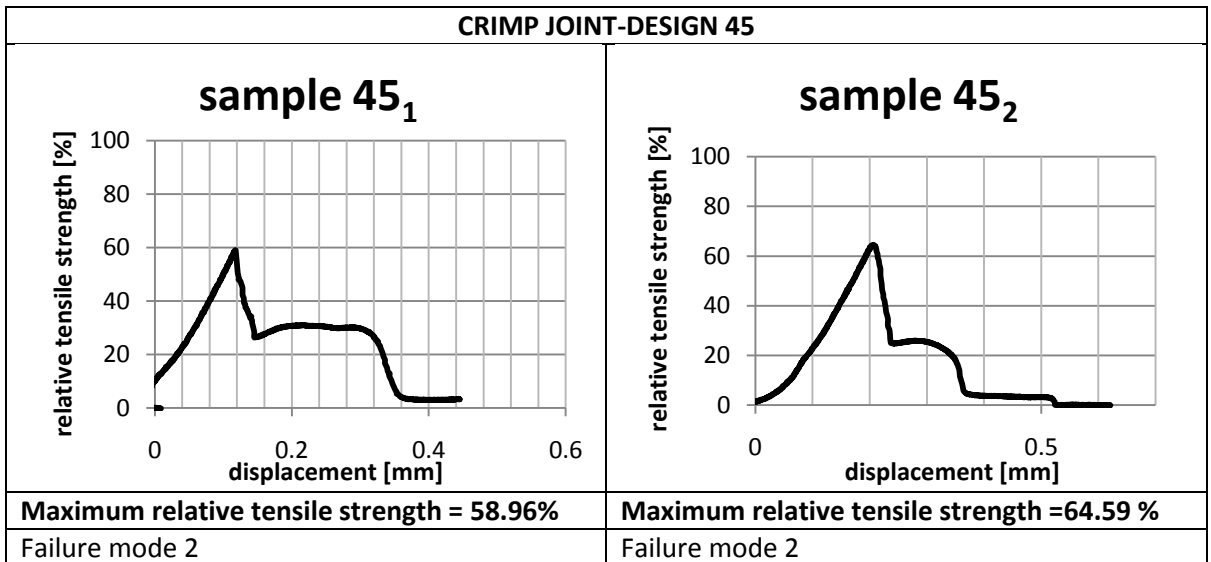
CRIMP JOINT-DESIGN 36	
<p>sample 36₁</p>	<p>sample 36₂</p>
Maximum relative tensile strength = 70.99%	Maximum relative tensile strength = 71.03%
Failure mode 3	Failure mode 3

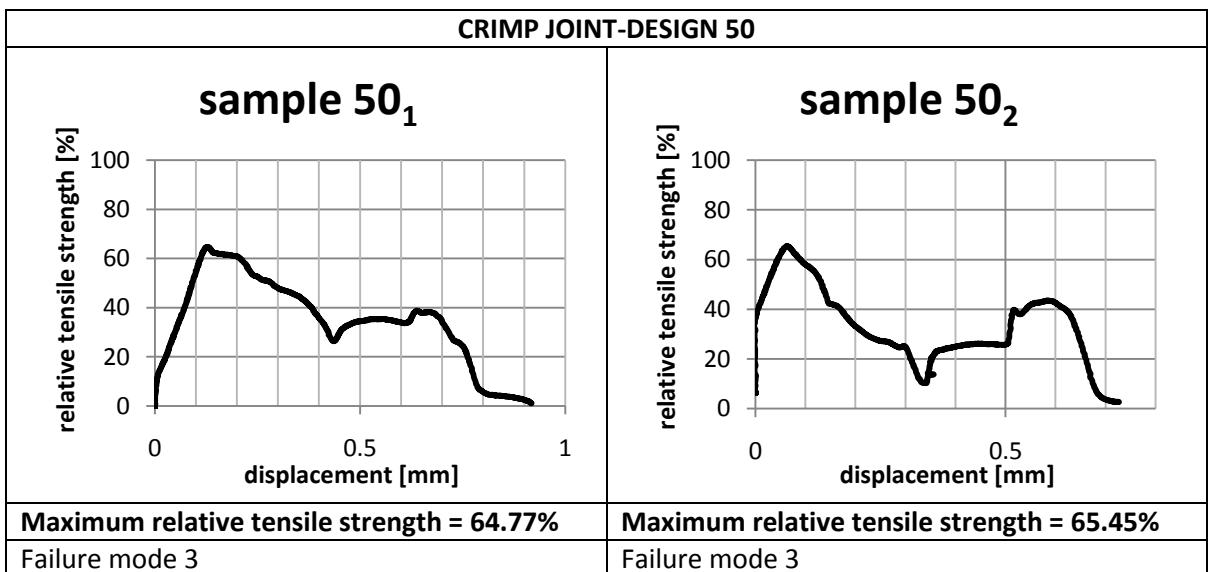
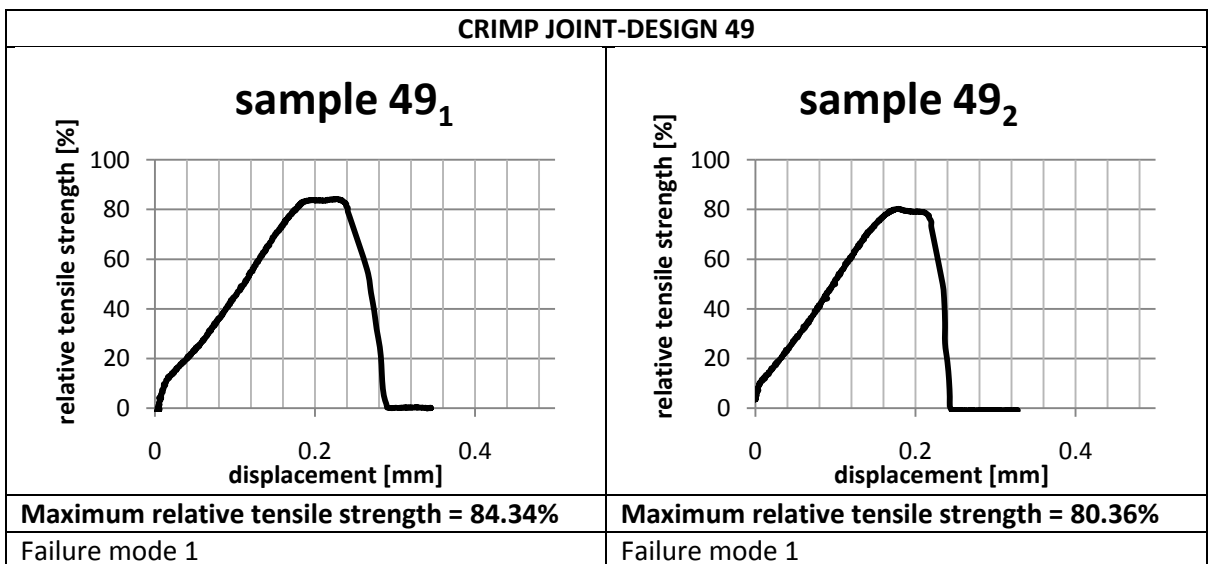
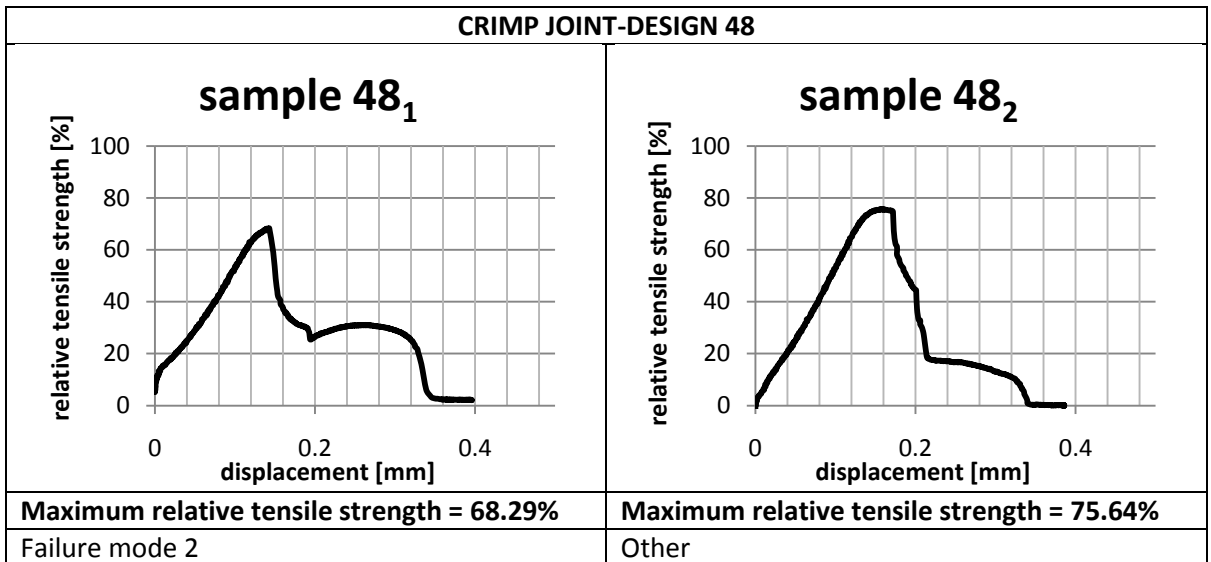
CRIMP JOINT-DESIGN 37	
<p>sample 37₁</p>	<p>sample 37₂</p>
Maximum relative tensile strength = 67.31%	Maximum relative tensile strength = 67.95%
Other	Other

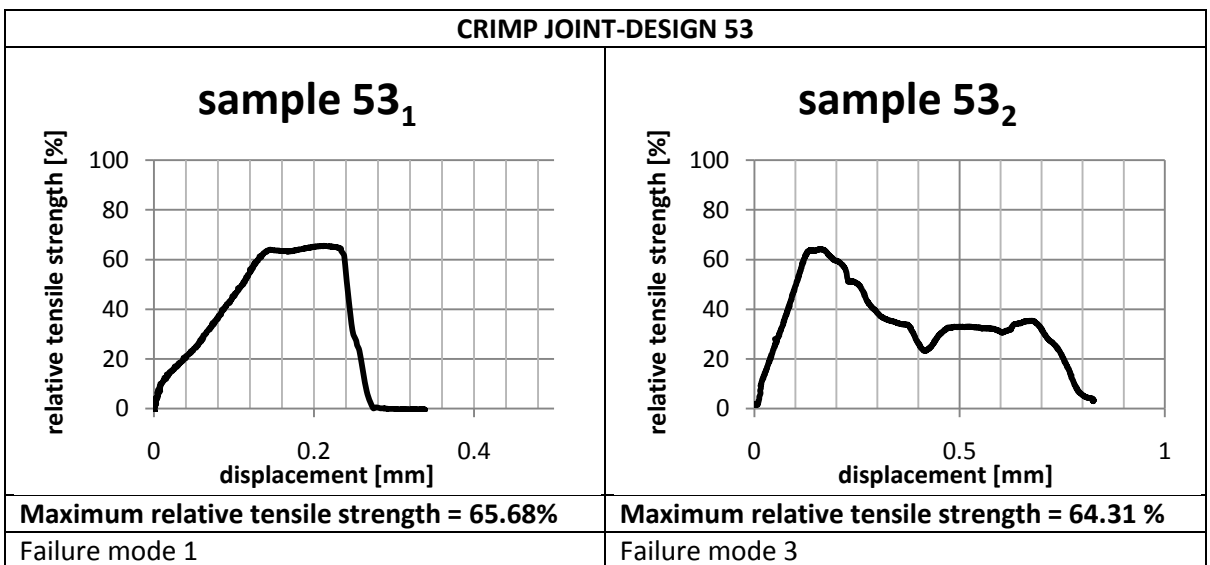
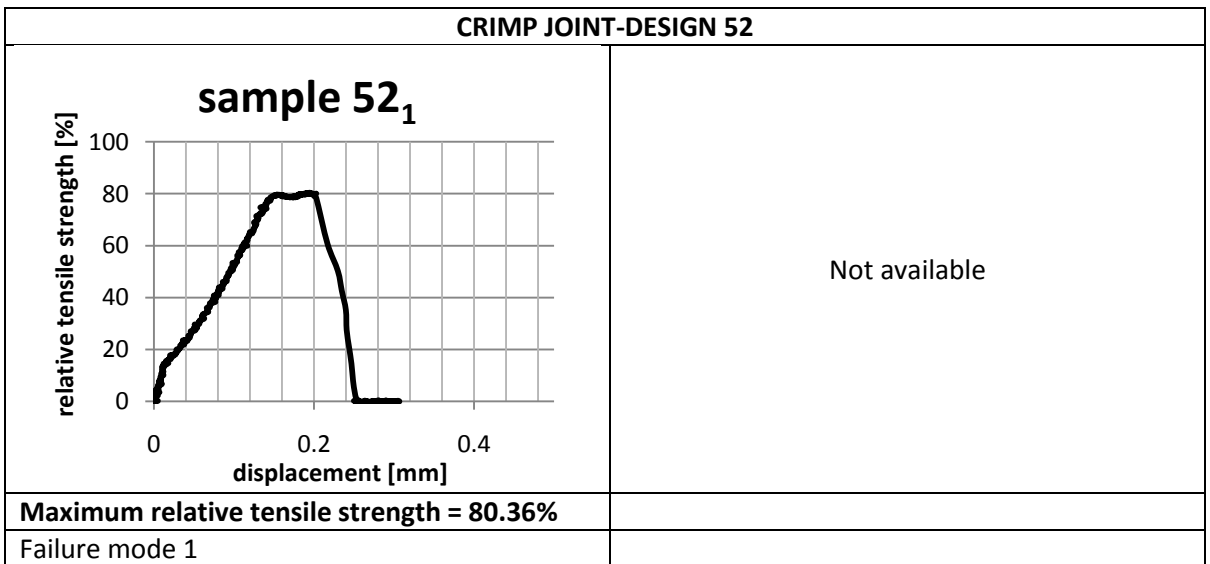
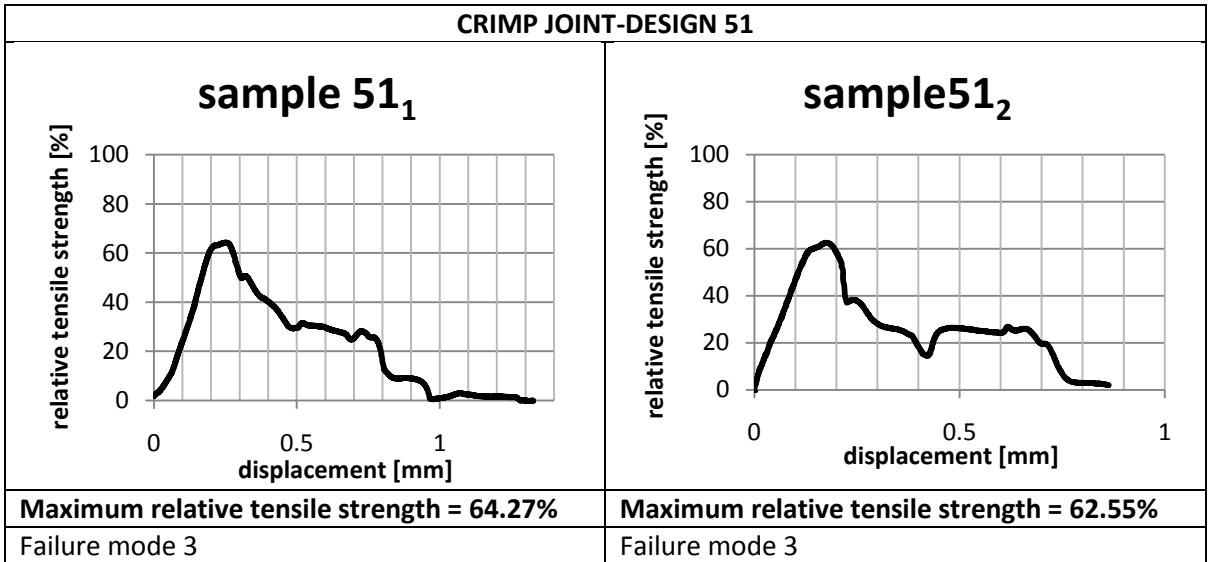
CRIMP JOINT-DESIGN 38	
<p>sample 38₁</p>	<p>Not available</p>
Maximum relative tensile strength = 72.14%	
Failure mode 3	

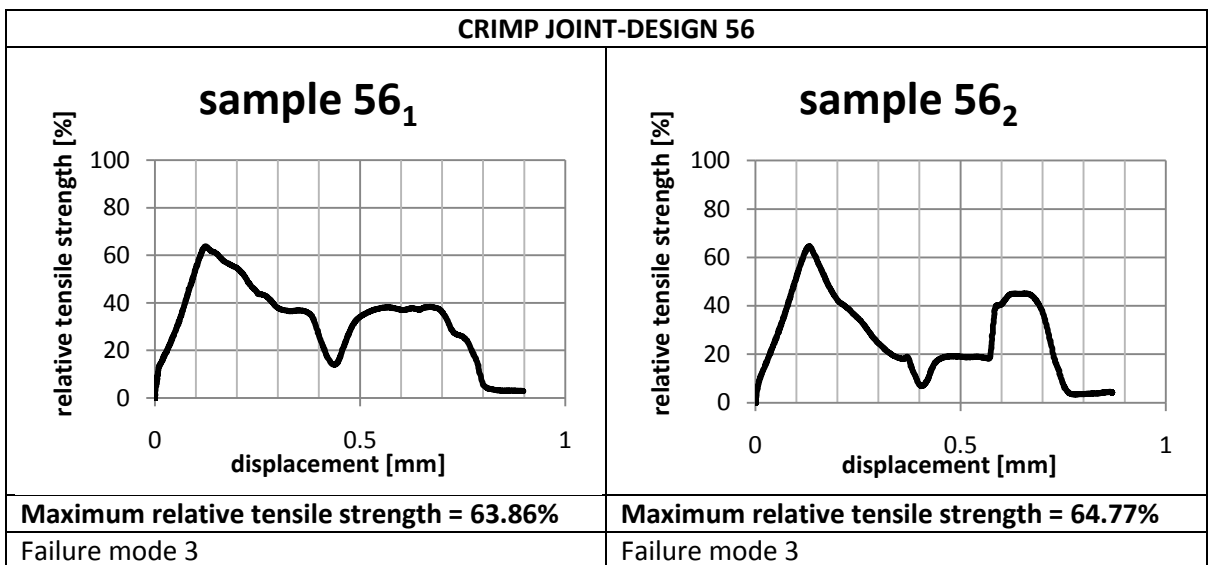
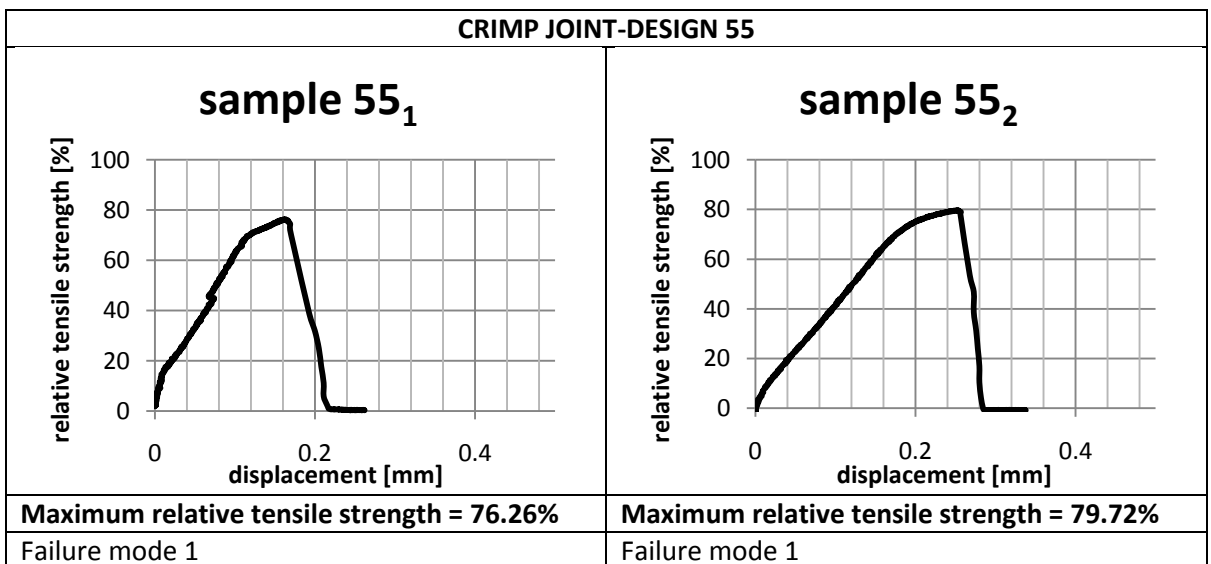
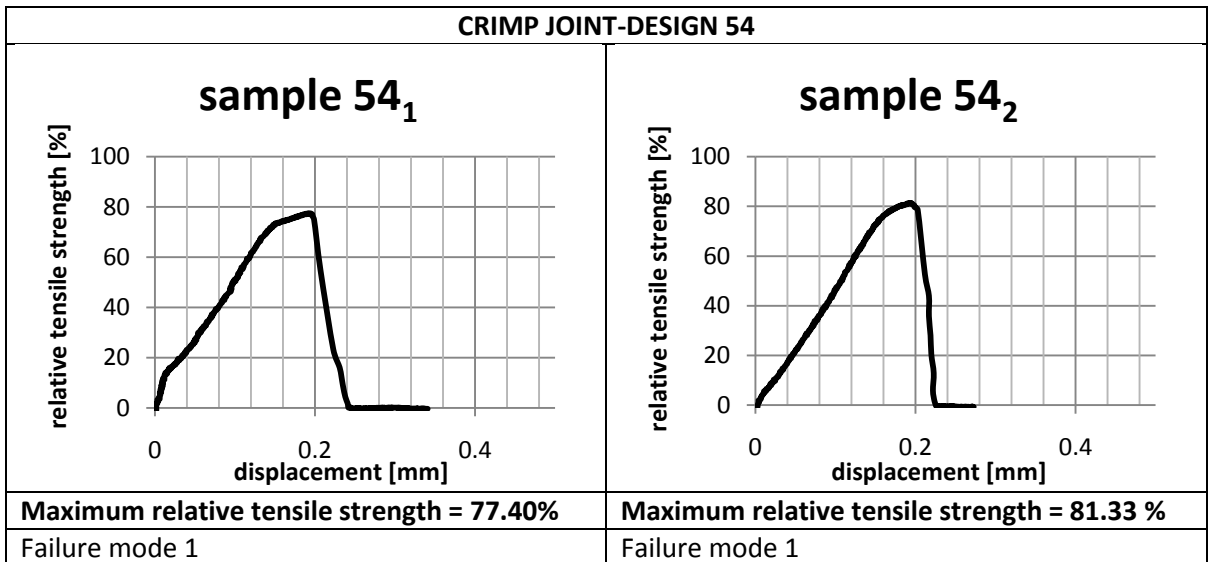


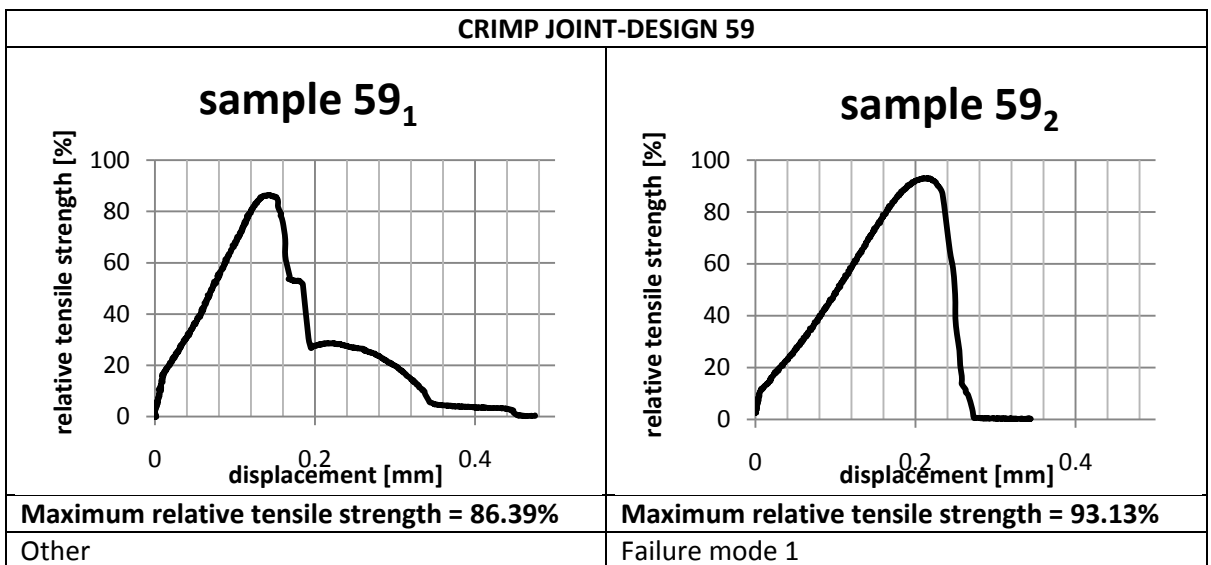
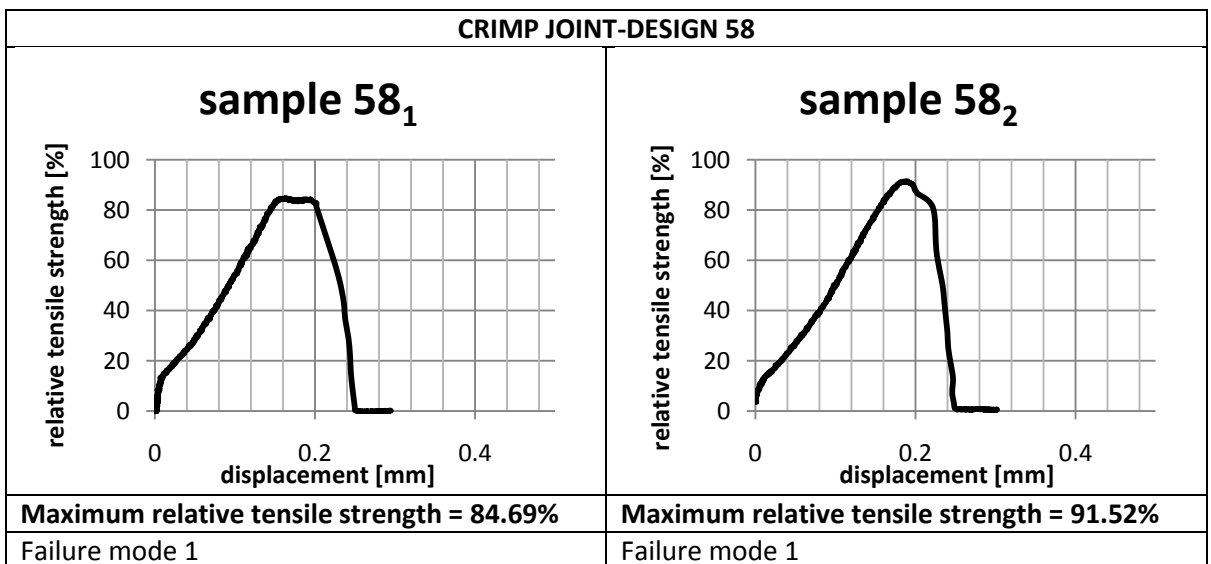
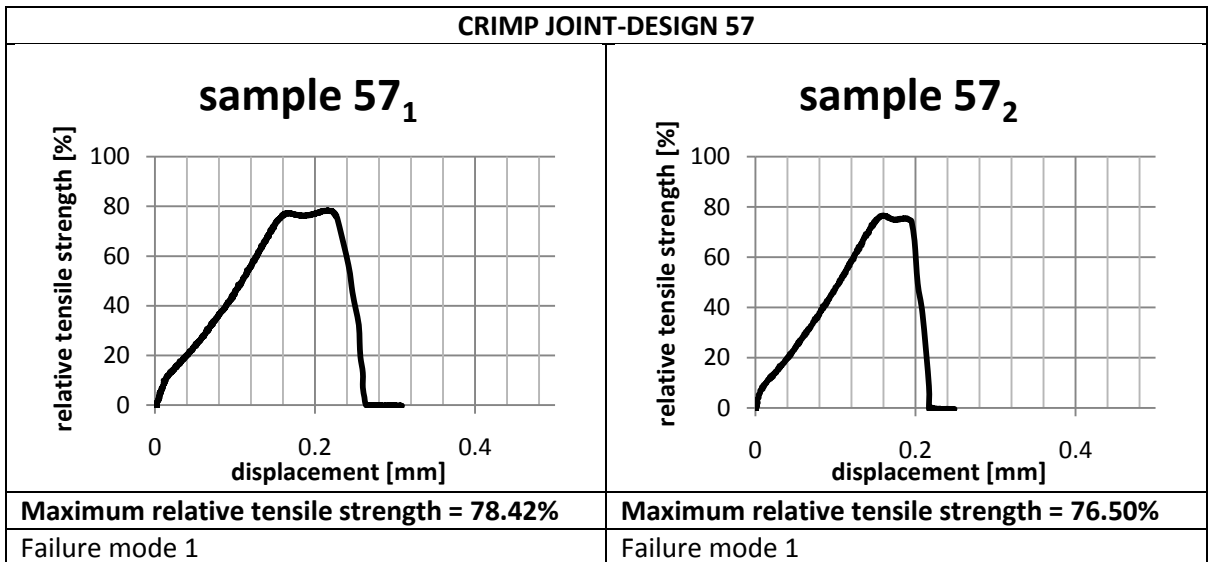


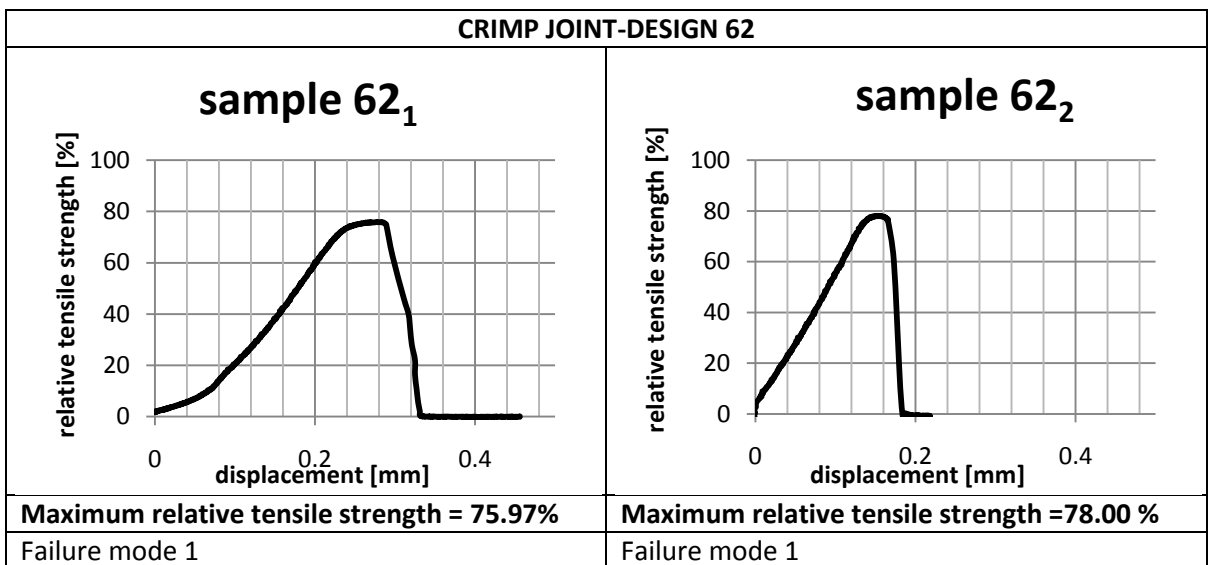
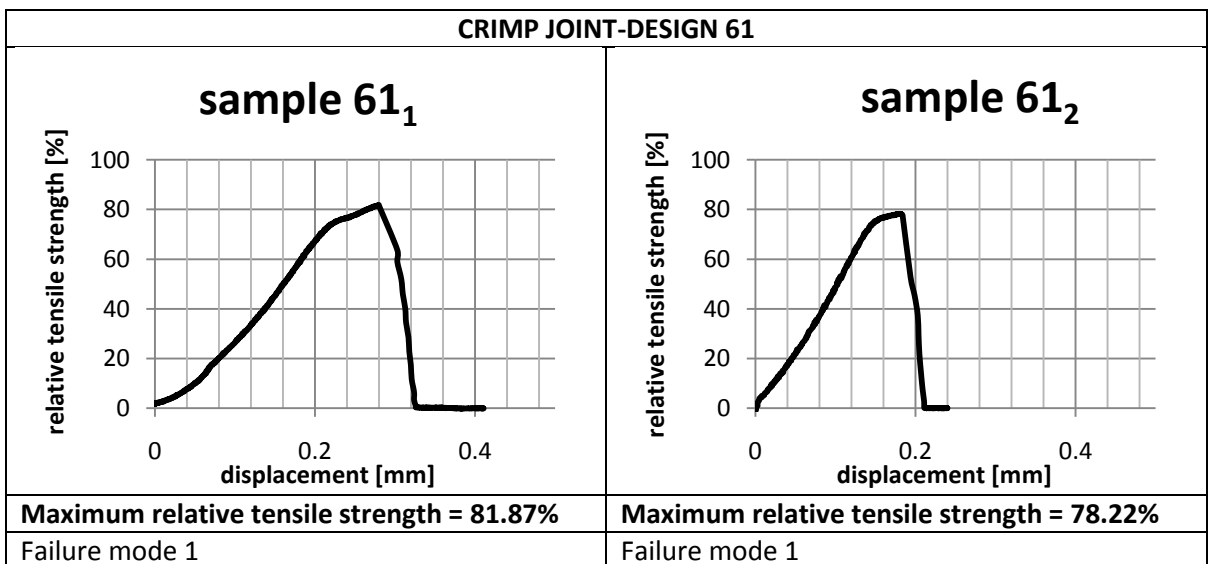
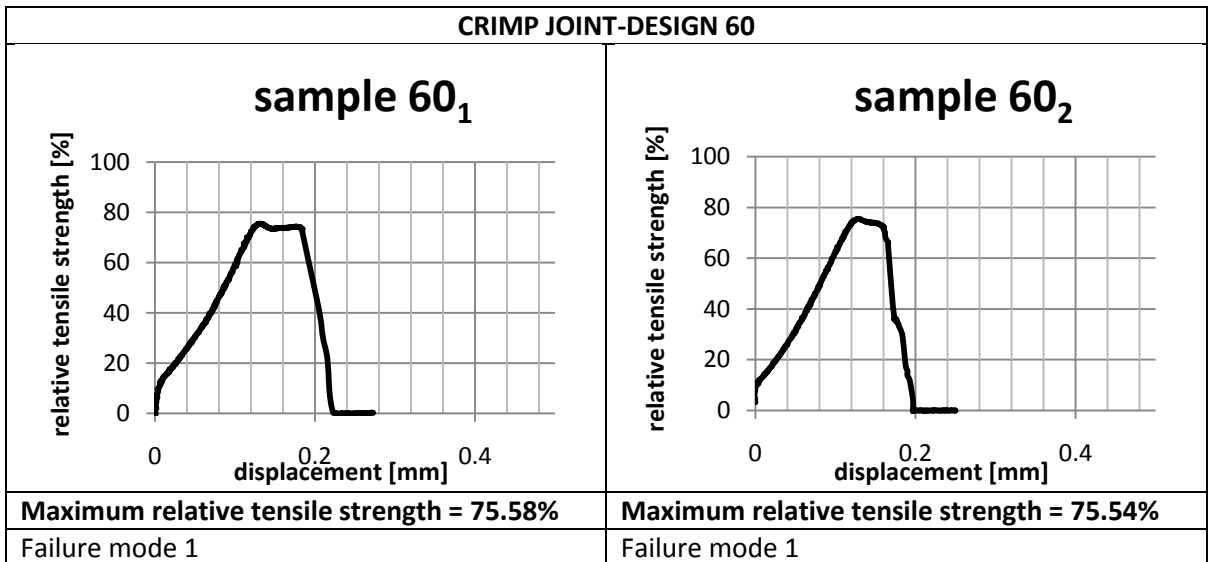


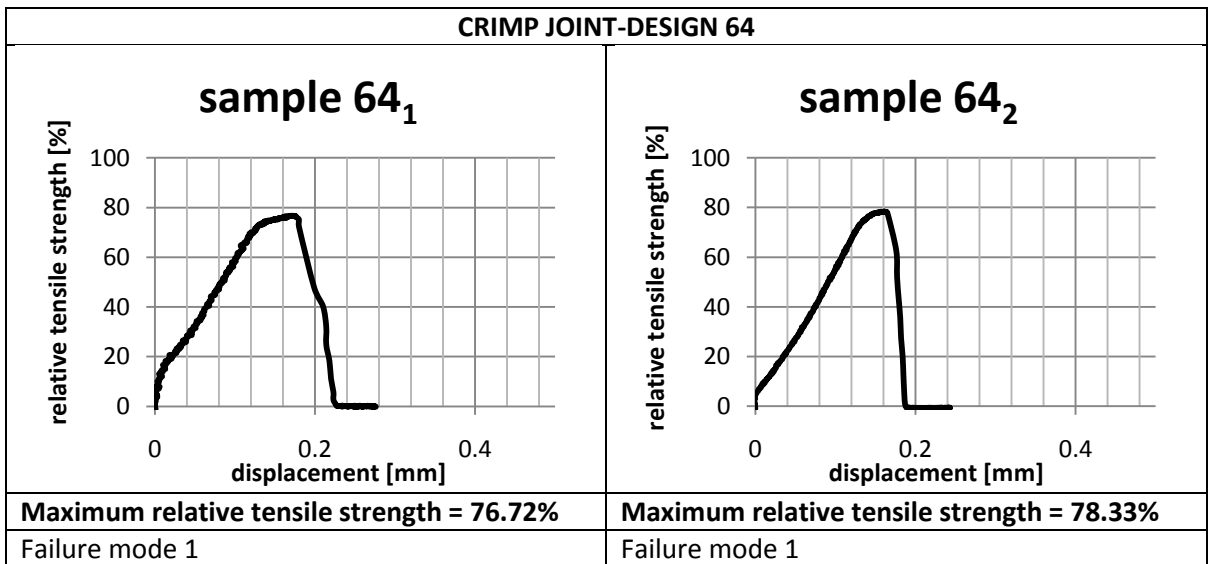
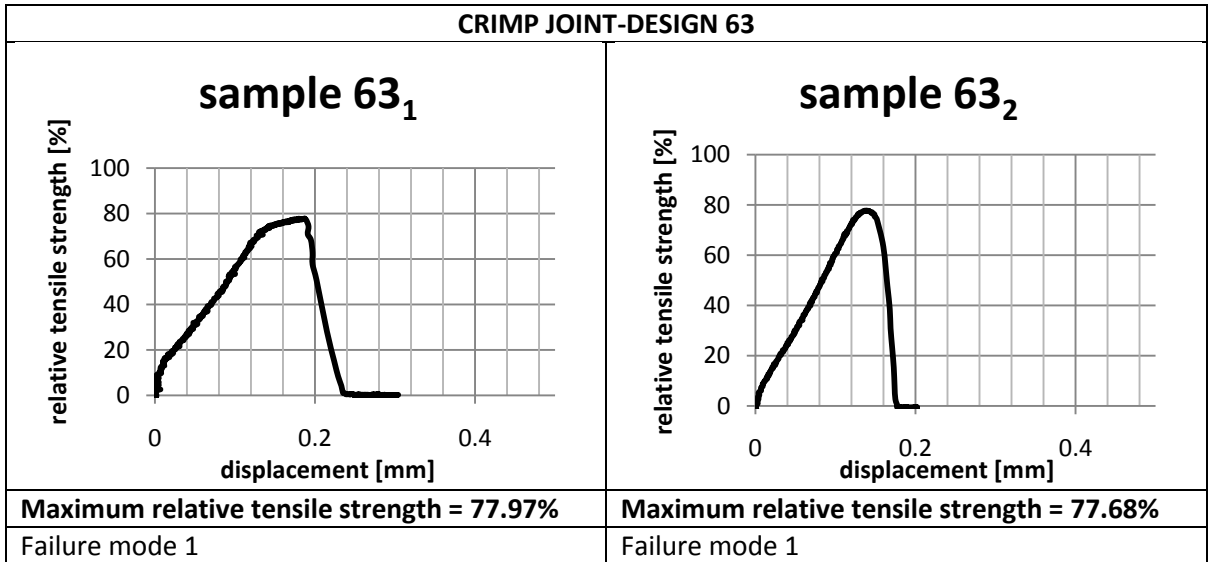












Appendix E

Lagrange strain

A strain is a normalised measure of deformation representing the displacement between particles in the body relative to a reference length. This is in general a tensor quantity. In this text, tensors will be denoted in bold.

The finite strain theory will be used here, because the material will plastically deform and hence the undeformed and deformed configurations of the continuum are significantly different (typically the engineering strains are greater than 1% [1]).

A typical tensor which is used in the finite strain theory, is the Lagrange strain tensor.

The Lagrange strain tensor \mathbf{E} is defined as [2]:

$$\mathbf{E} = \frac{1}{2}(\mathbf{F}^T \cdot \mathbf{F} - \mathbf{I})$$

Where \mathbf{F} = deformation gradient tensor

$$= \mathbf{I} + \mathbf{U}$$

\mathbf{I} = identity tensor, with components described by the Kronecker delta symbol:

$$\delta_{ik} = \begin{cases} 1, & i = k \\ 0, & i \neq k \end{cases}$$

\mathbf{U} = displacement gradient tensor

$$= \mathbf{u} \times \nabla$$

\mathbf{u} = the displacement vector which describes the motion of each point in the solid

∇ = the gradient operator

Because a tensor is a fairly abstract concept, a more familiar interpretation of \mathbf{E} will be derived. Suppose an imaginary tensile test specimen with length l_0 is marked on the deforming solid. The orientation of the specimen is arbitrary, and is specified by a unit vector \mathbf{m} , with components m_i . Upon deformation, the specimen increases in length to $l = l_0 + \delta l$. Based on the Seth-Hill interpretation of the Lagrange tensor [3], the Lagrange strain can be defined as

$$\varepsilon(m_i) = \frac{l^2 - l_0^2}{2l_0^2} = \frac{\delta l}{l_0} + \frac{(\delta l)^2}{2l_0^2}$$

This definition of strain is similar to the standard true strain definition $\varepsilon = \frac{\delta l}{l_0}$, but it contains an additional second order term. This additional term is negligible for small δl .

In other words, the Lagrange strain is the equivalent of true strain for large δl .

It can be noted that the link between the above defined Lagrange strain and Lagrange strain tensor definition is given by

$$\varepsilon(m_i) = E_{ij} m_i m_j$$

[1] Rees, D., *Basic Engineering Plasticity - An Introduction with Engineering and Manufacturing Applications*. 2006: Butterworth-Heinemann.

[2] *Lagrange strain tensor*. available from: http://solidmechanics.org/text/Chapter2_1/Chapter2_1.htm.

[3] *Lagrange strain*. available from: <http://www.mech.utah.edu/~brannon/public/strain.pdf>.

References

- [1] Faes, K., De Waele, W., *Industriële toepassingen van het elektromagnetisch puls lassen en krimpen*, in *Lastechniek*. juni 2010. p. 2 - 5.
- [2] *PULSCRIMP - Investigations on magnetic pulse crimping of tubular overlap joints with and without filler material*. available from: <http://www.innovatienetwerk.be/projects/1551>.
- [3] *PST Products*. available from: <http://www.pstproducts.com/anwendungen.htm>.
- [4] Shribman, V., *Magnetic pulse technology for improved tube joining and forming*. Tube & Pipe Technology, November/December 2006: p. 91-95.
- [5] *Skin effect*. 2010; available from: http://en.wikipedia.org/wiki/Skin_effect.
- [6] Pulsar Ltd., *MPW 50 25 Magnetic Pulse System*, user guide.
- [7] Peihui, Z., *Joining enabled by high velocity deformation*. 2003, The Ohio State University.
- [8] Dehra, M.S., *High velocity formability and factors affecting it*, in *Materials Science and Engineering*. 2006, Ohio State University. p. 336.
- [9] Hammers, T., *et al.*, *Influence of Mandrel's Surface and Material on the Mechanical Properties of Joints Produced by Electromagnetic Compression*. Steel Research International, 2009. **80**(5): p. 366-375.
- [10] Broekaert, F., De Ketele, M., *An exploratory study into the feasibility of magnetic pulse forming*, in *Mechanical construction and production*. 2009, Gent. p. 284.
- [11] Winkler, R., *Hochgeschwindigkeitsbearbeitung*. VEB Verslag Technik, Berlin, 1973.
- [12] Mühlbauer, A., von Finckenstein, E. (1967) *Magnetumformung rohrförmiger Werkstücke*. Bänder Bleche Rohre 8 (2) **86-92**.
- [13] Weddeling, C., Woodward, S., Marré, M., Nellesen, J., Psyk, V., Tekkaya, E., Tillmann, W., *Influence of groove characteristics on strength of form-fit joints*. Journal of Materials Processing Technology, 2010.
- [14] Schulze, V., Barreiro, P., Löhe, D., *Investigation of the Influence of Process Parameters on the Structure and the Mechanical Properties of Joints Produced by Electromagnetic Compression*. Advanced Materials Research, 2006. **10**: p. 79-88.
- [15] Padmanabhan, M., *Wrinkling and Springback in Electromagnetic Sheet Metal Forming and Electromagnetic Ring Compression*. 1997, Ohio State University,.
- [16] Weber, A., *The cold welding process is being used for more and more high-volume applications*, in *Assembly Magazine*. August 2002.

- [17] Wilson, M.N., Srivastava, K.D., *Design of efficient flux concentrators for pulsed high magnetic fields*, in *The review of scientific instruments*. 1965: Berkshire, England.
- [18] Haiping, Y., et al., *Effect of field shaper on magnetic pressure in electromagnetic forming*. *Journal of Materials Processing Technology*, 2005. **168**(2): p. 245-249.
- [19] Pulsar (2008) *Coil/field shaper designing (company guidelines)*.
- [20] Bahmani, M.A., K. Niayesh, and A. Karimi, *3D Simulation of magnetic field distribution in electromagnetic forming systems with field-shaper*. *Journal of Materials Processing Technology*, 2009. **209**(5): p. 2295-2301.
- [21] Yu Hai, P. and F. Li Chun, *Effects of coil length on tube compression in electromagnetic forming*. *Schools of Materials Science and Engineering*, 2007.
- [22] *Wrijvingscoefficient*. 2010; available from: <http://nl.wikipedia.org/wiki/Wrijvingsco%C3%ABffici%C3%ABnt>.
- [23] *Coefficient of friction*. available from: <http://www.engineershandbook.com/Tables/frictioncoefficients.htm>.
- [24] *Measurement of Residual Stress by X-ray Diffraction*. available from: <http://www1.chm.colostate.edu/Files/Residualstress.pdf>.
- [25] Young-Bae Park, H.-Y.K., Soo-ik Oh, *Design of axial/torque joint made by electromagnetic forming*. *Thin-Walled Structures*, 2005. **43**(5): p. 826-844.
- [26] Bühler, H., von Finckenstein, E., *Fügen durch Magnetumformung*. *Werkstatt und Betrieb* 101, 1968: p. 671-675.
- [27] Golavashchenko, S. *Methodology of design of pulsed electromagnetic joining of tubes*. in *Proceedings of the TMS Symposium "Innovations in Processing and Manufacturing of Sheet Materials"*. 2001. New Orleans, LA, USA.
- [28] Park, Y., Kim, H. , Oh, S., *Design of axial/torque joints made by electromagnetic forming*. *Thin-walled structures* 43, 2005: p. 826-844.
- [29] Bühler, H., von Finckenstein, E., *Bemessung von Sickenverbindungen für ein Fügen durch Magnetumformung*. *Werkstatt und Betrieb* 104, 1971: p. 45-51.
- [30] Läßle, V., *Einführung in die Festigkeitslehre*, in *Vieweg Verlag*. 2006.
- [31] *Magneform*. available from: <http://www.magneform.com/>.
- [32] *Material Data Sheet 11 S Mn 30*. available from: <http://quickmetall.eu/en/Werkstoffdatenblatt.aspx?Werkstoff-Nr=1.0715&layout=print>.
- [33] *EMI Shielding Principles*. available from: http://www.chomerics.com/tech/Shielding_methods.htm.
- [34] *Material Data Sheet Beryllium Copper*.

- [35] *Amsler 60 ton tensile test bench.* available from: http://www.tribology-fatigue.ugent.be/05_a_amsler60ton.shtml.
- [36] *Emmigi - application and use of aluminium.* available from: <http://www.emmegi.se/Sezione.jsp?idSezione=227&idSezioneRif=225>.
- [37] *Material Data Sheet EN AW-6060.*
- [38] *Internal measurement.* available from: http://www.swissinstruments.com/prod_metrology_internal_micrometers.html.
- [39] *Matlab - curve fitting toolbox.* available from: http://www.mathworks.com/help/toolbox/curvefit/bq_5ka6-1_1.html#bq_5kwr-3.
- [40] Filip and Michael, ... 2009.
- [41] *Material Data Sheet CuCrZr.* available from: http://www.abmkupral.hu/download/Elmedur/Elmedur_X_b_E.pdf.
- [42] Altekar, M., *et al.*, *Assay Optimization: A Statistical Design of Experiments Approach.* Journal of the Association for Laboratory Automation, 2006. **11**(1): p. 33-41.
- [43] Bahloul, R., *et al.*, *Sheet metal bending optimisation using response surface method, numerical simulation and design of experiments.* International Journal of Mechanical Sciences, 2006. **48**(9): p. 991-1003.
- [44] Verstraete, M., *et al.*, *Parameter study of a friction welding process for pipelines using Design of Experiments.* 2011.
- [45] Schmidt, S., Launsby, R., *Understanding Industrial Designed Experiments.* 4th ed.
- [46] *Statistical Power Analysis.* available from: <http://www.epa.gov/bioiweb1/statprimer/power.html>.
- [47] Bowker, A.H., *Lieberman Engineering Statistics.* 1972, Englewood Cliffs, New Jersey: Prentice-Hall Inc.
- [48] *statistical software package MINITAB.* available from: www.minitab.com.
- [49] Lichtenberger, R., Schreier, H., *Efficient Optimization of Airbags by the Measurement of the Time Resolved Strain Distribution on Airbag Covers.*
- [50] *VIC-3D 2010.* available from: <http://www.correlatedsolutions.com/>.
- [51] *Bevel Gears.* available from: <http://science.howstuffworks.com/transport/engines-equipment/gear4.htm>.

